Growth and characterization of InN and In-rich InGaN alloys by migration-enhanced plasma-assisted MOCVD

vorgelegt von
Diplom-Physiker
Daniel Seidlitz

von der Fakultät II - Mathematik und Naturwissenschaften
der Technischen Universität Berlin
zur Erlangung des akademischen Grades

Doktor der Naturwissenschaften
- Dr. rer. nat. -
genehmigte Dissertation

Promotionsausschuss:
Vorsitzender: Prof. Dr. Thomas Möller
Gutachter: Prof. Dr. Axel Hoffmann
Gutachterin: Prof. Dr. Janina Maultzsch

Tag der wissenschaftlichen Aussprache: 6. August 2019

Berlin 2019

Zusammenfassung

Im Rahmen dieser Arbeit werden die strukturellen und optoelektronischen Eigenschaften von Indiumnitrid (InN) und Indiumgalliumnitrid (InGaN) untersucht und vorgestellt. Des Weiteren beschreibt die Arbeit den Herstellungsprozess von Gruppe III-Nitriden mittels einer neuartigen Wachstumstechnik namens Migrations-verstärkter Plasma-assistierter Metallorganischer Chemischer Gasphasenabscheidung (Migration-enhanced plasma-assisted metalorganic chemical vapor deposition, MEPA-MOCVD).

MEPA-MOCVD ist eine Erweiterung der Niederdruck-MOCVD. In diesem neuartigen Konzept generiert eine radiofrequente Plasmaquelle reaktive Stickstoff-Teilchen, welche im Gegensatz zur konventionellen MOCVD Ammoniak als Ausgangsstoff ersetzen. Die Motivation, MEPA-MOCVD von InGaN zu erforschen, ergibt sich einerseits aus dem vielversprechenden Potential der ternären Gruppe III-Nitride als sehr geeignetes Materialsystem für die Herstellung von Leuchtdioden und für Anwendungen in der Photovoltaik. Das Wissen über das InGaN Materialsystem und deren Eigenschaften ist nicht vollständig erforscht, zum Beispiel ist das Krümmungsverhalten der Bandlücke Gegenstand kontroverser Diskussionen. Andererseits ist MEPA-MOCVD ein Ansatz, die gegenwärtigen Herausforderungen der typischen Wachstumsverfahren zu überwinden. Zur Zeit sind die Wachstumstechnologien zur Produktion von InGaN mit einem Indiumgehalt bis zu 25 - 30% und ausreichender Materialqualität für die Herstellung von Bauteilen limitiert. Diese Arbeit diskutiert die aktuellen Wachstumsprobleme von InN und InGaN in Anbetracht der Vor- und Nachteile der typischen sowie alternativen plasma-assistierten Wachstumsprozeduren.

Der Hauptteil dieser Arbeit ist in zwei Fragestellungen aufgeteilt. Zuerst wird die Entwicklung und Optimierung des MEPA-MOCVD Prozesses untersucht, um Gruppe III-Nitride-Schichten zu stabilisieren, deren Kristallqualität zu verbessern und vergleichbare Wachstumsraten wie mit der konventionellen MOCVD zu erzielen. Daher werden das Reaktordesign und die Fähigkeiten des MEPA-MOCVD Prozesses detailliert vorgestellt. Das Einfahren und die Optimierung des Prozesses erfordert vielfache Wiederholungszyklen verschiedener Wachstumsserien in Abhängigkeit der Prozessparameter wie Wachstumstemperatur, Reaktordruck sowie der Komposition der reaktiven Stickstoff-Teilchen und deren kinetischer Energie, um Gruppe III-Nitride zu stabilisieren. Während der Einfahrprozedur wird eine zeitliche Modulation der Stickstoffplasma-Teilchen und der metallorganischen Ausgangsstoffe eingeführt, um den Prozessparameterbereich zu erweitern und potentielle Reaktionen zwischen den Stickstoff-Teilchen und metallorganischen Ausgangsstoffen zu verhindern. Die Anwendung einer gepulsten Zufuhr der reaktiven Stickstoff-Teilchen und metallorganischen Ausgangsstoffe führt zum erfolgreichen Wachstum von stabilisiertem InN und InGaN bei einer Temperatur von 775°C. Mit konventioneller MOCVD ist die Herstellung von InN und InGaN nicht möglich, da es bei dieser Temperatur zur Desorption der Indiumatome kommt. Es besteht eine Wissenslücke, um die reaktiven Stickstoff-Teilchen mit der Gasphasenchemie und den Wachstumsbedingungen in Verbindung zu setzen. Ein Zusammenhang zwischen Prozessparametern, reaktiven Stickstoff-Teilchen und Filmeigenschaften wird in einer Wachstumsserie bei verschiedenen Drücken beobachtet, welche eine signifikante Verbesserung der InN Filmqualität ergibt. Die Halbwertsbreite der E_2(high) Mode, ein Maß für die Kristallqualität, verringert sich von 20 cm^{-1} bei 4.7 Torr auf 10 cm^{-1} bei 2.8 Torr. Die qualitative Verbesserung geht zu Lasten der InN-Schichtdicke, welche von 200 nm auf 50 nm

abnimmt. Es kommt zum Ätzen der abgeschiedenen Schicht aufrund einer höheren Konzentration hochenergetischer Teilchen, welche anhand von Plasmaemissionsspektroskopie (PES) bestätigt wird. Die Korrelation von Echtzeit, in-situ PES mit den ex-situ Schichteigenschaften kann Kontrollmechanismen für die MEPA-MOCVD ermöglichen. Ähnliche Wachstumsraten wie mit konventioneller MOCVD werden allerdings nicht erzielt. Die Produktion von hochqualitativen Gruppe III-Nitriden mit vergleichbaren Wachstumsraten erfordert daher weitere Prozessoptimierungen.

Der zweite Teil der Arbeit befasst sich mit der Machbarkeit Indium-reiches InGaN mittels MEPA-MOCVD zu wachsen. Der Indiumgehalt der InGaN-Proben beträgt 26%, 46%, 69%, 86% and 92%, bestimmt mittels Ramanspektroskopie und Röntgendiffraktometrie. Raman-Mapping deutet auf sehr hohe Homogenität der Proben hin, da die Abweichung vom Durchschnittswert des Indiumanteils nur ±1% beträgt. Allerdings weisen die Proben eine starke Verbreiterung der A_1(LO) Phononmode auf, was ein Anzeichen für nanoskopische Inhomogenitäten und ein gegenwärtiges Problem bei der Herstellung von Indium-reichen InGaN-Schichten sowie InGaN Quantenfilmen ist. Untersuchungen mit TERS und optischer Rasternahfeldnanoskopie (scattering-type scanning near-field infrared nanoscopy, s-SNIN) zeigen unabhängig voneinander nanoskopische Phasentrennungen mit übereinstimmender Größenordnung an der Oberfläche der InGaN-Schichten auf. Im Gegensatz zu s-SNIN erlaubt TERS die Quantifizierung der kompositionellen Fluktuationen. Zusätzlich werden mit TERS neue verstärkte Nahfeldmoden C_1 and C_2 in InN-Schichten entdeckt, welche nicht mit den klassischen Fernfeld-Ramanmoden übereinstimmen. Bei diesen Moden handelt es sich vermutlich um Kombinationen der A_1(TO) Phononmode mit dem akustischen Phononenzweig am Symmetriepunkt M oder K. Diese Kombinationsmoden treten unabhängig vom Wachstumsverfahren auf und ermöglichen die Identifizierung von InN-Nanoclustern in zwei- und dreidimensionalen InGaN-Strukturen.

Abstract

This thesis investigates and presents the structural and optoelectronic properties of indium nitride (InN) and indium gallium nitride (InGaN) alloys. Furthermore, this work describes the synthesis of group III-nitride alloys using a novel growth technique named migration-enhanced plasma-assisted metalorganic chemical vapor deposition (MEPA-MOCVD).

MEPA-MOCVD is an extension of low-pressure MOCVD. In this novel concept, a radio-frequency plasma source generates reactive nitrogen species replacing ammonia as a precursor in contrast to conventional MOCVD. On the one hand, the motivation to explore MEPA-MOCVD of InGaN comes from the promising potential of ternary group III-nitrides as a high-suitable material system for the fabrication of light emitting diodes (LEDs) and photovoltaic applications. The InGaN material system is not fully understood, and some properties such as bandgap bowing are still under discussion. On the other hand, MEPA-MOCVD is an approach to overcome the present growth limitations faced by typical deposition techniques. In the current state-of-the-art, growth technologies are limited to the production of InGaN alloys with an indium content up to 25 - 30% and sufficient material quality for device fabrication. This work discusses the present growth challenges of InN and InGaN by considering the advantages and disadvantages of common as well as alternative plasma-assisted growth procedures.

The major part of this work is separated into two objectives. First, the development and optimization of the MEPA-MOCVD growth process to stabilize group III-nitride layers and improve their crystalline quality with similar growth rates as in conventional MOCVD are studied. Thus, the reactor design and the capabilities of the MEPA-MOCVD growth process are described in detail. The running-in and the optimization of the process require multiple iterations of different growth series as a function of process parameters such as growth temperature, reactor pressure as well as the composition of the reactive nitrogen species and their kinetic energies to stabilize group III-nitride alloys. During the running-in procedure, a temporal modulation of the nitrogen plasma species and the metalorganic precursors is introduced into the MEPA-MOCVD process to extend the process parameter window and avoid potential gas-phase reactions between nitrogen and metalorganic precursors. Utilizing a pulsed metalorganic and nitrogen precursor supply established the growth of stabilized InN and InGaN at a temperature of 775°C. The synthetization of InN and In-rich InGaN layers is not possible with conventional MOCVD at 775°C due to desorption of indium atoms at this temperature. Furthermore, there is a lack of knowledge to link the reactive nitrogen species to the gas-phase chemistry and the growth conditions. A correlation between process parameters, reactive nitrogen species, and layer properties is observed in a growth series at various reactor pressures revealing a significant enhancement of the InN film quality. The full width at half maximum of the E_2(high) mode (measure for crystalline quality) narrowed from 20 cm^{-1} at 4.7 Torr to 10 cm^{-1} at 2.8 Torr. The qualitative improvement comes at the expanse of the InN film thickness reducing from 200 nm to 50 nm due to the etching of the deposited layer by an increased number of high-energetic species as verified by plasma emission spectroscopy. The correlation of real-time in-situ PES results with the ex-situ layer properties can enable control mechanisms for the MEPA-MOCVD growth process. However, similar growth rates as in conventional MOCVD are not accomplished. The production of high-quality group III-nitrides and comparable deposition rates require further process optimization.

The second part is about the feasibility to grow In-rich InGaN films by MEPA-MOCVD. The indium contents of the InGaN samples are 26%, 46%, 69%, 86% and 92% determined by Raman spectroscopy and X-ray diffraction. Based on Raman mapping, all InGaN samples appear to have a high compositional homogeneity, because the deviation from the average indium fraction is only ±1%. However, a strong broadening of the A_1(LO) phonon modes indicates nanoscopic inhomogeneities, a current growth challenge in the fabrication of InGaN layers and also present in InGaN multiquantum wells. Investigations with tip-enhanced Raman spectroscopy (TERS) and scattering-type scanning near-field infrared nanoscopy (s-SNIN) reveal independently nanoscopic phase separations with matching dimensions at the surface of the InGaN layers. In contrast to s-SNIN, TERS allows the quantification of the compositional fluctuations. In addition, TERS detects new enhanced near-field signals C_1 and C_2 in thin InN films which are not in agreement with the known far-field Raman modes. These modes result from an additive combination of the A_1(TO) phonon mode and the acoustic branch at the symmetry point M or K. The C_1 and C_2 feature appear independent of the growth technique and enable the identification of InN clusters in two- and three dimensional InGaN structures.

Publications

1 **Optoelectronic and structural properties of InGaN grown by Migration-Enhanced, Plasma-Assisted MOCVD**
D. Seidlitz, M. K. I. Senevirathna, Y. Abate, A. Hoffmann and N. Dietz
SPIE Conf. Proc. 9571, 14th Int. Conf. SSL & LED-based Illum. Systems (2015)

2 **Nanoscopy of Phase Separation in $In_xGa_{1-x}N$ Alloys**
Y. Abate, D. Seidlitz, A. Fali, S. Gamage, V. Babiicheva, V.S. Yakovlev, M. I. Stockman, R. Collazo, D. Alden and N. Dietz,
ACS Applied Materials & Interfaces 8 (35), 23160-23166 (2016)

3 **Effect of AlN buffer layers on the structural and optoelectronic properties of InN/AlN/Sapphire heterostructures grown by MEPA-MOCVD**
I.M.K. Senevirathna, D. Seidlitz, A. Fali, B. Cross, Y. Abate and N. Dietz
Proc. SPIE 9954, 15th Int. Conf. on SSL and LED-based Illum. Systems (2016)

4 **Surface and optical properties of indium-rich InGaN layers grown on sapphire by migration-enhanced plasma assisted metal organic chemical vapor deposition**
Chi Zhang, Yao Li, Yingda Qian, Yuanlan Liang, Devki N. Talwar, Shih-Yung Huang, Qingxuan Li, Daniel Seidlitz, Nikolaus Dietz, Dong-Sing Wuu, Ian T. Ferguson, Xiang Lu, Lingyu Wan, Kaiyan He and Zhe Chuan Feng
Materials Research Express 6 (1), 016407, (2018)

Contents

1 Introduction

The first chapter discusses the motivation and the objectives of this thesis to investigate the group III-nitride material system due to their promising potential for novel devices and applications. For almost three decades, group III-nitrides semiconductors such as Gallium nitride (GaN), Indium nitride (InN) and aluminum nitride (AlN) and their alloys have raised a high interest in research because of their attractive structural and optoelectronic properties. These outstanding characteristics make the group III-nitride alloys a promising material system with the potential for numerous electronic and optoelectronic applications and devices. First, this chapter briefly recaps the most important steps in the historical progress of the group III-nitride semiconductors. The second part gives a closer look at the potential and applications of the group III-nitrides. The last part of the introduction outlines the content of the different chapters.

1.1 History of group III-nitrides

This section gives a short historical timeline of major and important steps in the development of group III-nitrides with the focus on InN, GaN, and InGaN. Maruska et al. reported the first epitaxial growth of single GaN crystals on sapphire by Hydride Vapor Phase Epitaxy in 1969 [1], while first MOCVD growth of GaN was reported in 1971 by Manasevit [2]. In 1970, MacChesney et al. suggested based on their theoretical thermodynamic equilibrium calculations that the InN growth surface at higher growth temperatures can be stabilized by utilizing high-pressure nitrogen [3]. In 1972, Hovel and Cuomo used plasma active nitrogen species to grow InN and GaN in polycrystalline form by radio-frequency (rf) sputtering. The n-type InN films had a carrier concentration of (5-8) x 10^{18} cm^{-3} and a Hall mobility of 250 ± 50 cm^2 V^{-1} s^{-1} [4]. Tansley and Foley presented measurement results of rf-sputtered polycrystalline InN films. At room temperature, the films have the highest reported electron mobility of 2700 cm^2 V^{-1} s^{-1} and lowest carrier concentration of 5 x 10^{16} cm^{-3} [5] and an InN bandgap energy of 1.9 eV [6]. In the late 1980s, Amano made significant progress in GaN crystal quality by embedding an AlN buffer layer [7]. Amano also realized p-type GaN with magnesium (Mg) doped GaN films grown by MOVPE [8]. In 1989, the work of Wakahara showed epitaxial growth of InN by microwave-excited MOCVD for the first time. InN was deposited on sapphire using trimethylindium and plasma-activated nitrogen precursors [9]. The first blue emitting LED was fabricated in 1993 by Nakamura et al. utilizing a double-heterostructure of GaN and InGaN [10]. The InGaN films were grown by MOCVD with a peak emission wavelength of 440 nm. In 2014, Akasaki, Nakamura and Amano have been awarded jointly the Nobel Prize in physics for the development of efficient blue light-emitting LEDs, which enabled bright and energy-efficient white lighting.

In 2002, the discovery of the very narrow bandgap of InN due to the much-improved quality of single crystalline InN films grown by MBE [11] and PAMBE/MOMBE [12] renewed and rapidly increased the interest in InN research. These high-quality InN films showed significantly lower bandgap energies in contrast to the state of art the InN bandgap energy of 1.9 eV [13] at that time. Multiple groups reported very narrow bandgap energies of InN at 1.0 eV – 0.7 eV [14], 0.9 eV [12], 0.7 eV [15] and finally 0.64 eV [16]. The discovery of the low InN bandgap energies extends the range of optoelectronic applications of the InGaN material system from the ultraviolet (UV) region at 3.4 eV into the near-infrared (NIR) region

(0.64 eV), enclosing the complete visible spectrum. Though much research has been done on InN in the past 25 years, it is still less understood than GaN and AlN. The revision of the bandgap and the experienced inconsistent properties of InN films depending on the different growth methods have led to a controversial discussion about the interpretation of the electrical and structural properties of InN.

1.2 Potential applications of the group III-nitride material system

The group III-nitrides and their alloys are direct bandgap semiconductors. The bandgap energies of the group III-nitride binaries are 0.7 eV for InN [17], 3.4 eV for GaN [18] and 6.2 eV for AlN [18], respectively. Compositions of GaN with InN and/or AlN allow simpler bandgap engineering from the UV to the IR while the bandgap remains direct. This key feature of the group III-nitride material system is an important technological advantage compared with the conventional III-V compound semiconductors that consist of both the direct and indirect bandgap materials as for example Gallium phosphide (GaP) or Aluminum arsenide (AlAs). Therefore, the ternary and quaternary group III-nitride alloys such as InGaN, AlGaN, and AlGaInN allow a continuous tuning of the bandgap energy from 6.2 eV to 0.7 eV as a function of the alloy composition. The wide bandgap range covers the entire visible range which makes group III nitrides suitable for optoelectronic applications and devices for solid state lighting (SSL) such as light emitting diodes (LEDs) and laser diodes (LDs). Green and blue emitting LDs and LEDs based on GaN and InGaN active layers stand out in particular due to their high brightness [19, 20]. LEDs emitting green and blue light have become technologically relevant and are already commercially used in traffic signals, transportation vehicle exterior and interior lighting, as well as backlighting in liquid crystal display (LCD) TVs and computer screens [21]. In 2016, the LED lighting market reached a revenue of nearly 4 billion US dollars and the perspective revenue will more than triple in 2022 to 13.8 billion dollars [22].
Another well-known commercial application is the Blu-Ray technology which utilizes blue GaN LDs and has become a part of everyday life for more than a decade. Recent studies show that the LED and lighting segment together with Laser segment represent nearly half of the intellectual property (IP) of group III-nitride semiconductors [23]. Power devices account for another quarter of IP, which makes it the second major group of group III-nitride applications after LEDs. Further applications of group III-nitrides and especially for InN and InGaN are photovoltaic (PV) devices and multi-junction solar cells [24]. The continuous bandgap engineering over the full solar spectrum allows potential growth of multi-junction solar cells. The solar cells consist of multiple absorber layers with varied absorption edge. Thus, each layer absorbs a different wavelength range of the solar spectrum which enables an optimization of the solar cell efficiency [25]. PV device performance can be further enhanced by nanostructural engineering of the material (e.g. nanotubes) to increase optical path length and provide light trapping [26]. InN and InGaN alloys are also applicable as aerospace solar cells because they exhibit a superior resistant against high-energy particles [27] and as photoelectrodes for water splitting [28, 29]. The chemical bonding in group III-nitride semiconductors is very strong. Therefore, group III-nitrides possess a high melting point, chemical stability, resistance to radiation damage and a high-current degradation threshold. These properties make group III-nitrides semiconductors suitable for high-temperature operation. The high thermal conductivity, electron mobility and saturation velocity of group III-nitrides also make them useful for high-voltage power and high-speed electronics as well as optoelectronic devices. [30, 31]. High power applications are the second highest segment in the IP landscape of group III-

nitride semiconductors [22]. Among the group III-nitrides, InN possesses the highest mobility (400 - 3280 $cm^2\ V^{-1}\ s^{-1}$ for InN layers [32, 33]) and saturation velocity due to its very small effective mass [34]. Thus, the high electron mobility in indium-rich alloys enables ultra-fast electronics operating in the THz regime [35, 36]. The list of devices based on the properties of group III-nitride semiconductors continues in the development of chemical and biosensors [37, 38], thermoelectric devices [39], UV and IR detectors [40] and nuclear detection [41].
From an environmentally point of view, group III-nitride alloys do not contain toxic elements in found in compound semiconductors such as Gallium arsenide (GaAs) which require arsenic for their fabrication.

1.3 Thesis objective and outline

Currently, the $In_xGa_{1-x}N$ material quality with a moderate Indium content below 30% is sufficient for commercial device fabrication [27].However, the internal quantum efficiency (IQE) of these films drops significantly towards 550 nm ('green gap') [21, 42, 43]. In-rich $In_xGa_{1-x}N$ materials with an indium content more than 0.3 encounter a quality limitation due to present challenges in their formation. One major challenge in the growth of In-rich $In_xGa_{1-x}N$ are the vastly different partial pressures of volatile constituents which result in a wide growth temperature gap ($\geq$ 300 K) between the group III-nitride binaries InN and GaN. In conventional MOCVD, InN growth is presently limited to a growth temperature below 600°C, while high-quality GaN is grown between 950°C to 1100°C. AlN with a good crystalline quality requires higher growth temperatures above 1100°C.
Conventional growth techniques fabricate GaN and Ga-rich InGaN at high temperatures. The bond between Ga and N is stronger than the In-N bond which results in a low dissociation temperature for InN. Thus, MOCVD growth to attain higher Indium incorporation in InGaN has to take place at lower temperatures to reduce Indium absorption. However, the formation of high-quality In-rich InGaN at low temperatures is difficult due to poor adatom diffusion. The partial pressure difference can also cause stoichiometric instabilities as well as point defect chemistry.
Additionally, the group III-nitrides are not a lattice matched system. The lattice mismatch between InN and GaN (~ 11 %) induces local strain which can cause structural defects such as threading dislocations (TD). Additionally, there is no native lattice-matched substrate available for group III-nitrides. The growth of non-matching substrates further increases the high dislocation density, which affects the optoelectronic and mechanical layer properties.
Another major challenge in the growth of InGaN is nanoscale lateral compositional inhomogeneities at the growth surface, which can lead to bulk phase segregations and reduce the heterostructural quality. An interaction of thermodynamic effects, strain, and miscibility between InN, GaN and the substrate cause these nonuniform distributions of segregated atoms. These compositional fluctuations of the Indium content are in the nano- to micrometer range. Spinodal decompositions during MOCVD growth of InGaN epilayers within the miscibility gap contribute to the phase separations. The solid phase miscibility gap in InGaN originates from the large difference in the interatomic spacing of GaN and InN [44, 45]. The radius of the Ga atom is smaller than the atomic radius of Indium which adds to the epitaxial layer strain. Phase separations affect the bandgap of the alloy and limit the optical and electronic internal device efficiency [46].

Migration-enhanced plasma-assisted metalorganic chemical vapor deposition (MEPA-MOCVD) is an approach to stabilize the growth surface by kinetic means of the metalorganic (MO) and plasma-excited nitrogen precursors and reduce the partial pressure difference between InN and GaN. This enables deposition of InN and GaN in the same growth regime with the potential to fabricate In-rich InGaN epilayers.
The goal of this thesis is to optimize the crystal quality of binary and ternary group III-nitride semiconductors grown by Migration-enhanced plasma-assisted-MOCVD. The study of the growth parameter window assesses to optimize the fabrication of high-quality InN, GaN and In-rich InGaN films and nanostructures. The analysis of the structural, optoelectronic and morphological properties of the group III-nitrides depending on the growth conditions contributes to a better understanding of the growth mechanism in low-pressure plasma-assisted MOCVD. Real-time monitoring of plasma active species enables to identify the active nitrogen species which promote the growth of group III-nitride films. The correlation and comparison of ex-situ structural, morphological and optoelectronic layer properties and in-situ metrology further enhances the understanding of the growth mechanism and allows to potentially control the growth process of MEPA-MOCVD.

This thesis consists of seven chapters. The first chapter provides a brief overview of the historical progress in fabrication and the high interest in research for applications due to the potential of group III-nitride alloys.
Chapter two discusses the basic fundamentals of the group III-nitride material system. The main focus is on the crystallographic structure, the polarity and polarization and the Raman structure of hexagonal wurtzite group III-nitrides.
Chapter three outlines the experimental characterization methods to investigate the structural, morphological and optoelectronic properties of the InN, GaN and InGaN films and nanostructures grown by MEPA-MOCVD.
The fourth chapter gives a state of the art overview of the most common and major growth methods for the fabrication of group III-nitride materials. The advantages and drawbacks of the various growth techniques, which manifest in different group III-nitride properties, are compared in consideration to crystal quality and film thickness as well as growth parameters such as growth temperature. Present challenges in the growth of In-rich InGaN alloys are also in the focus of this chapter.
Chapter five follows with a detailed description of the Migration-enhanced plasma-assisted MOCVD system which was utilized to grow InN, GaN and In-rich InGaN epilayers on sapphire substrates. Therefore, this chapter gives elaborate insight into the technological characteristics of the reactor design and the growth mechanism, including growth kinetics and the conditioning of the plasma-activated nitrogen precursors via growth parameters.
Chapter six presents analytical results of the optoelectronic, structural and morphological properties of the InN and InGaN films grown by MEPA-MOCVD. The last section of the sixth chapter discusses the outcome of these analysis and gives an interpretation in regard to the growth process parameters to evaluate how the growth conditions can optimize the crystal quality and improve the film thickness. The seventh chapter summarizes and evaluates the important results of this work and presents resulting conclusions and outlook of ongoing and future research projects.

2 Basic fundamentals of group III-nitride semiconductors

2.1 Introduction

This chapter summarizes the basic material properties of group III-nitrides including the wurtzite crystal structure, the bandgap as well as the polarity and polarization. A special focus is on the theoretical background of the phonon structure in group III-nitrides.

2.2 Crystal structure of group III-nitrides

Group III-nitrides crystallize in either hexagonal wurtzite (α-phase) or cubic zinc blende crystal structure (β-phase). Under very high-pressure conditions, a transition from the wurtzite to rock salt structure has been reported for InN (~12 GPa) [27], GaN (~47 GPa) [47] and AlN (~16.6 GPa) [48]. The wurtzite crystal structure is the thermodynamically stable phase compared to the metastable zinc blende. In group III nitrides, the hexagonal wurtzite and cubic zinc blende differ only in the stacking sequence of the nitrogen and the group III metal sublattices. Therefore, stacking faults can cause both, a hexagonal and cubic phase in epilayers. For the remainder of this work, the hexagonal wurtzite crystal structure of group III nitrides and their properties are discussed. The hexagonal wurtzite crystal structure consists of two interpenetrating hexagonal close-packed (hcp) sublattices; one is related to the nitrogen and the other one to Ga (In or Al respectively) atoms. For binary group III nitrides, the alternating stacking sequence is ABAB along the c-axis [0001] direction. The wurtzite crystal structure belongs to the space group $P6_3mc$ (C^4_{6V}). Each group III metal atom has four bonds to nitrogen atoms and vice versa, which results in a tetrahedron. In an ideal wurtzite structure, the tetrahedral angle between nearest neighbors is 109.47°. The lattice parameter *a* and *c* and the parameter u describe the hexagonal unit cell (red box in Figure 2.1).

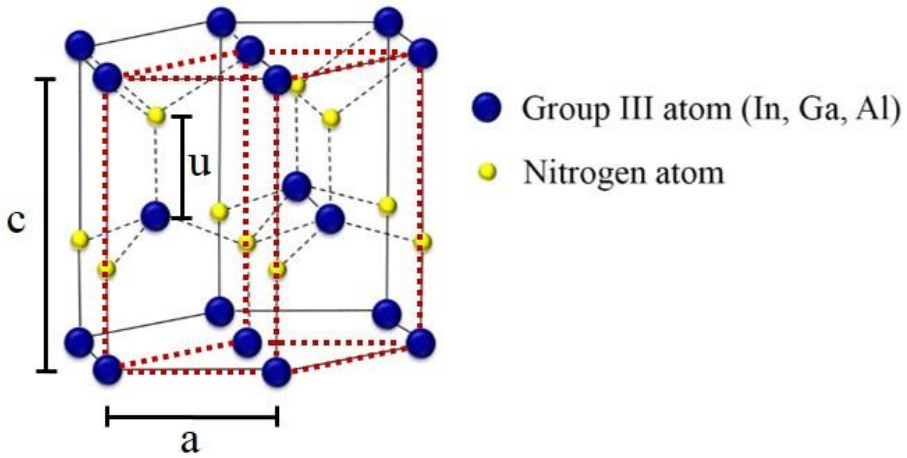

Figure 2.1: Schematic illustration of a group III nitride wurtzite crystal structure with the lattice parameters *a* and c. The unit cell is highlighted by the red dotted lines. The group III metal atoms In, Ga or Al (blue) are positively charged and the nitrogen atoms (yellow) are positively charged.

The lattice parameter *a* is the edge length of the basal hexagon. The lattice parameter *c* is perpendicular to the hexagon and defines the height of the hexagon prism. In an ideal wurtzite lattice structure, the sublattices are displaced from each other by 5/8 of the c-axis lattice parameter and the ratio of the lattice constants *c* and *a* is $c/a = (8/3)^{1/2} = 1.633$. The lattice constant ratio correlates to the parameter *u* which defines the bond length between the nitrogen anion and the metal cation along the c-axis. Hence, the sublattices are displaced by 5/8, the parameter *u* is 3/8 = 0.375. GaN, InN, and AlN have a slightly smaller lattice constant ratios than the ideal value (see Table 2.1). As mentioned, before the lattice constant ratio and the bond length parameter have a strong correlation. A lower *c*/*a* ratio means an increase of the parameter *u*, while the four tetrahedral distances remain nearly the same due to the distortion of the tetrahedral angles [18]. The lattice constant ratio *c*/*a* has another correlation with the difference between the electronegativities of the group III metal cation and the nitrogen anion. In group III nitrides, the larger electronegativity of the nitrogen anion (3.04) relative to the lower electronegativity of the group III metal cations Ga+ (1.81), In+ (1.78), and Al+ (1.61) leads to a deviation of the ideal wurtzite structure. The strong ionic bond between group III metal and nitrogen moves the atoms from their neutral electric position, which generates a dipole moment. This gives rise to an internal electric field along the c-axis in the wurtzite structure resulting in a large spontaneous polarization along the c-axis. The polarization will be discussed in detail in the next section. The ionic radii of the group III metal cations, as well as their bonding energy with nitrogen, have large differences. As a result, the group III nitrides have different lattice constants, spontaneous polarization and bandgap energies [29].

Parameter	GaN	InN	AlN
Lattice constant *c* (Å)	5.186	5.685	4.9808
Lattice constant *a* (Å)	3.189	3.517	3.112
c/*a* ratio (ideal = 1.633)	1.62606	1.616	1.60054
u (ideal = 0.375)	0.3789	0.377	0.3869
Spontaneous polarization (C/m^2)	-0.029	-0.032	-0.81

Table 2.1: Lattice parameters for GaN, AlN [49] and InN [50] as well as spontaneous polarization values [51].

2.3 Bandgap of binary and ternary group III-nitrides

Ternary group III-nitride material systems such as AlGaN and InGaN allow simpler direct bandgap engineering from 0.64 eV for InN to 3.4 eV for GaN and further to 6.1 eV for AlN. This wide direct bandgap covers a wavelength span from the deep UV to the IR. The wide direct bandgap is maintained over the whole range compared with conventional III-V compound semiconductors, that consist of both, direct and indirect band-gap materials (e.g. GaP and AlAs). Figure 2.2 displays the bandgaps of the wurtzite (wz) and cubic zinc-blende (zb) group III-nitride crystals as a function of the lattice parameter.

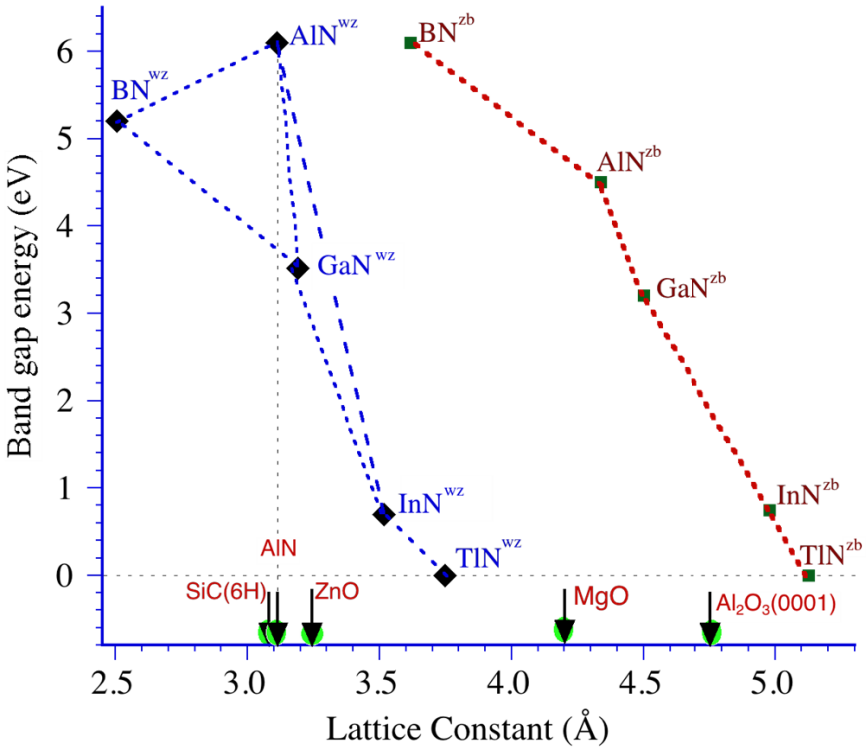

Figure 2.2: Bandgap energy of wurtzite (wz) and cubic zinc-blende (zb) group III-nitride compounds as a function of the lattice constant at RT. Lattice constants of typically used substrates for the growth of group III-nitride epilayers are added.

The wide direct bandgap range of the $In_xGa_{1-x}N$ material system covers a large part of the solar spectrum including the entire visible range (Figure 2.3) and make $In_xGa_{1-x}N$ alloys highly suitable for light emitting diodes (LEDs) and laser diodes as well as multijunction solar cells and photovoltaic applications. Compared to the other group III-nitride binaries, InN exhibits the lowest electron effective mass due to its narrow bandgap, which results in high electron mobility. The high electron mobility is another advantage of indium-rich InGaN alloys because it enables ultra-fast electronics operating in the THz regime. The bandgap energies and additional basic parameters of the wurtzite group III-nitride binaries GaN, AlN and InN are listed in Table 2.2.

Parameters	**GaN**	**InN**	**AlN**
Bandgap energy (eV)	3.43[a]	0.64[b]	6.14[a]
High-frequency dielectric constant ε_∞	5.4[c]	6.7[d]	4.6[c]
Thermal expansion coefficient c ($\times 10^{-6}\,K^{-1}$)	3.17[c]	2.9[c]	5.3[c]
Thermal expansion coefficient a ($\times 10^{-6}\,K^{-1}$)	5.59[c]	3.8[c]	4.2[c]
Thermal conductivity (W $cm^{-1}\,K^{-1}$)	1.3[c]	0.45[c]	2.85[c]

[a] Reference [52], [b] Reference [16] , [c] Reference [53] and [d] [54]

Table 2.2: Basic parameters of wurtzite GaN, InN and AlN at room temperature (RT) = 300 K.

The narrow bandgap value of 0.64 eV for InN was revised in 2002. Studies prior to that considered the bandgap value in the range of 1.9 to 2.1 eV. Progress in the synthesis of high-quality single-crystal InN layers and analysis of photoluminescence (PL) in combination with absorption spectra established the narrow bandgap energy of InN.
Based on Vegard's law, the bandgap of ternary alloys depends linear on the composition which correlates to the molar fraction *x* of the constituent elements and the bandgap energies of the end-members at a given temperature. However, instead of a linear relation, empirical results showed a non-linear behavior for the bandgap of ternary group III-nitrides:

$$E_g\left(A_xB_{1-x}N\right) = x \cdot E_g\left(B\right) + \left(1-x\right)E_g\left(A\right) - b \cdot x \cdot \left(1-x\right) \tag{2.1}$$

with *b* as the bowing parameter. In case of ternary $In_xGa_{1-x}N$, equation (2.1) is as follows:

$$E_g^{In_xGa_{1-x}N} = x \cdot E_g^{GaN} + \left(1-x\right)E_g^{InN} - b \cdot x \cdot \left(1-x\right). \tag{2.2}$$

Different values for the bowing parameter *b* of $In_xGa_{1-x}N$ have been reported in literature such as 1.43 eV [55] 1.36 eV [28] or 1.65 eV [56]. There is also a discussion if a single bowing parameter is sufficient to describe bandgap of the entire composition range Figure 2.3 displays the strain-free bowing of the $In_xGa_{1-x}N$ bandgap energy based on equation (2.18) and using the bandgap energies and bowing parameter from reference [56]. Bandgap bowing also occurs in the ternary group III-nitrides $Al_xGa_{1-x}N$ [49] and $In_xAl_{1-x}N$ [57]. The various experimental and theoretical bowing parameters vary significantly and are still under discussion.

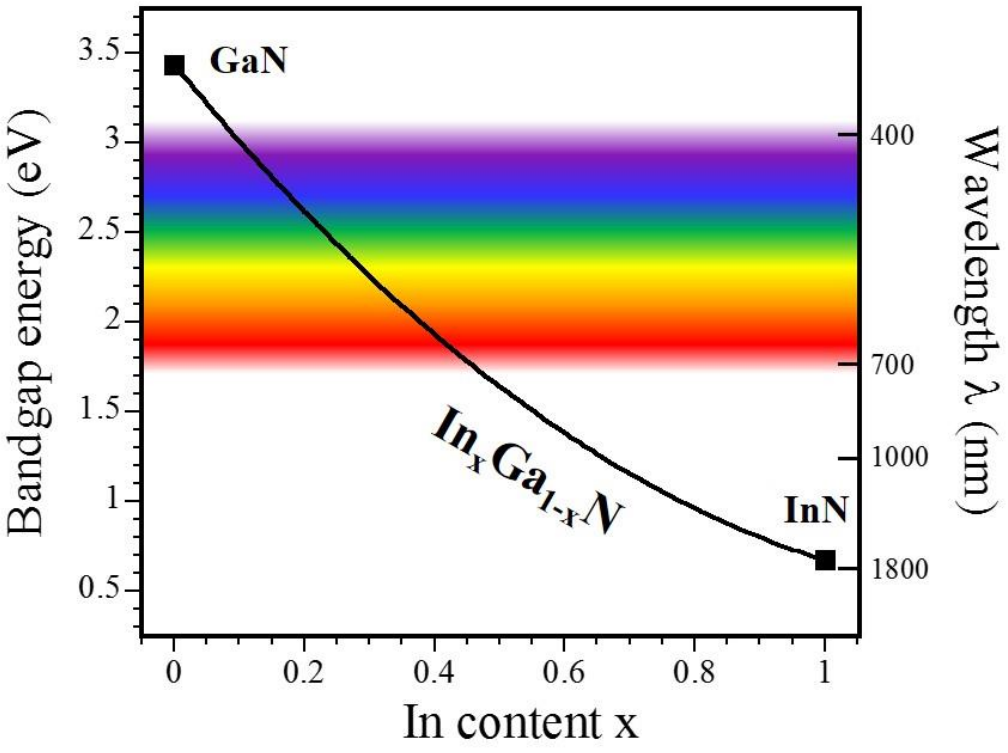

Figure 2.3: Strain-free bandgap energy of $In_{1-x}G_xN$ and the corresponding emission wavelength as a function of In-content x at RT.

Another important design parameter for the fabrication of optoelectronic devices is the bandgap offset between the group III-nitride binaries. Valence-band discontinuity is present at the interface between two nitride materials as for example in heterojunctions [58]. The reported experimental values for the valence-band offset between InN and GaN show a large variation. Similar has been reported for the valence-band offset of AlN-GaN and InN-AlN. The band alignment of the ternary group III-nitrides is displayed in Figure 2.4.

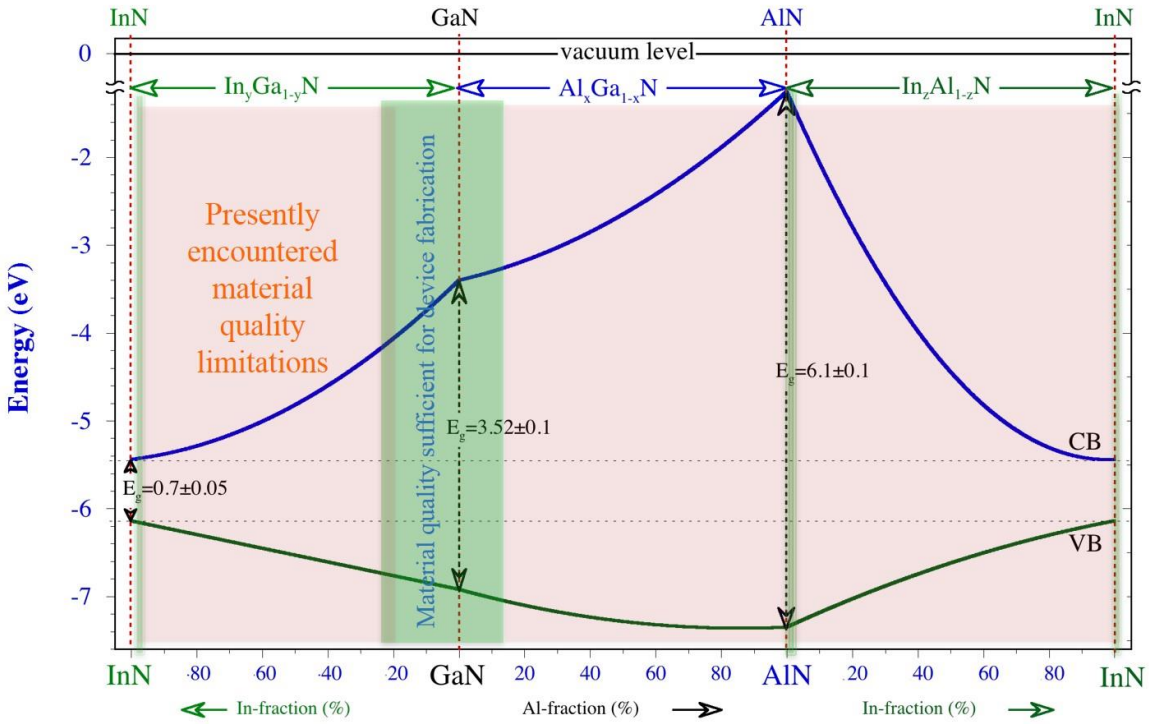

Figure 2.4: Bandgap values of the binaries InN, GaN and AlN as well as bandgap alignment of their ternary alloys. Adapted from reference [29].

2.4 Polarity and polarization

The group III-nitride wurtzite crystals exhibit strong polarity caused by two effects, the spontaneous (or pyroelectric) polarization and the piezoelectric polarization. As mentioned earlier, the nitrogen atom has a larger electronegativity as each of the group III metal atoms causing a deviation of the ideal unit cell and give rise to spontaneous polarization and with it an internal electric field along the c-axis. The spontaneous polarization for GaN, InN and AlN is also listed Table 2.1.

The wurtzite crystalline structure is non-centrosymmetric and lacks inversion symmetry which results in anisotropy and affects the structural and optoelectronic properties of the group III-nitrides. The arrangement of the hcp sublattices, describing the group III metal cations and the nitrogen anions, normal to the [0001] polar c-plane determines two distinct polarities. The polarity of the crystal is defined by the orientation of the bonds along the c-direction [0001], namely, whether the direction of the bonds is from the group III metal cation to the nitrogen anion or vice versa. Thus, two possible polarities are either III-polar (+c orientation), if the single bond faces from the group III cation to the nitrogen anion along the [0001] direction and N-polar (-c orientation), when the single bond faces from the nitrogen anion to the III-metal cation along the c-axis.

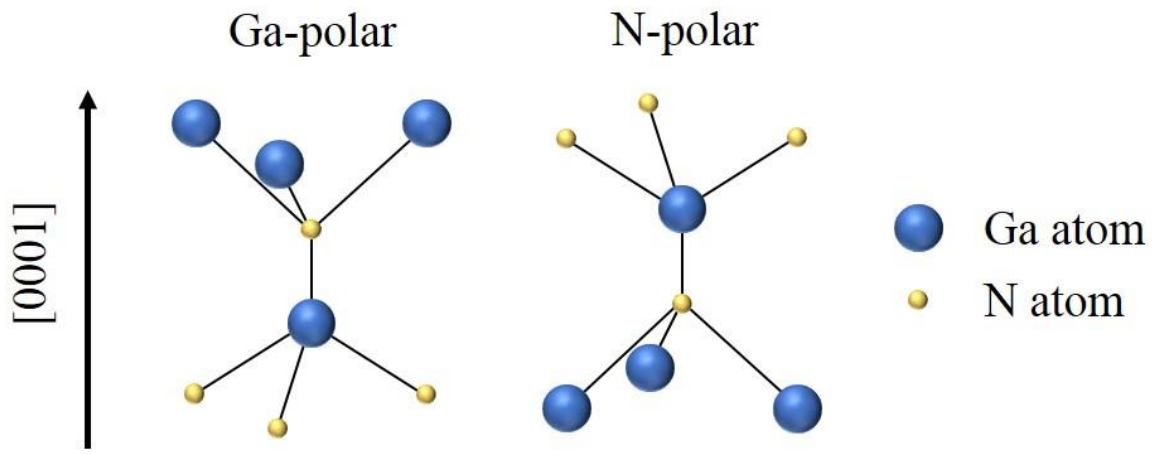

Figure 2.5: Double tetrahedrons of the ideal wurtzite crystal structure for Ga-polar (left) and N-polar (right) GaN.

For example, Figure 2.5 displays the wurtzite crystal structure of Ga-polar (left) and N-polar (right) GaN. The surface polarity refers to a direction of the crystal and should not be mistaken with the surface termination which describes a surface property. Each polar orientation can be terminated either with group III metal or nitrogen atoms. The polarity of the crystal is a challenge for the growth process of group III-nitrides. It affects the structural and physical layer properties such as surface morphology, defect density and impurity incorporation. Due to these implications, control of the polarity is essential in group III-nitride materials.

As mentioned in the previous section 2.2, the bond lengths and angles between the nearest neighbors in a wurtzite crystal with ideal lattice constants ratio c/a and ideal internal parameter u are equal. However, this is not accurate for the second nearest neighbors. Calculations showed that the distance between the second nearest neighbor in c-axis direction is 13% shorter than the distance to the other second nearest neighbors [59, 60]. The nearest and second-nearest neighbors of a center atom in a wurtzite crystal structure are highlighted in Figure 2.6.

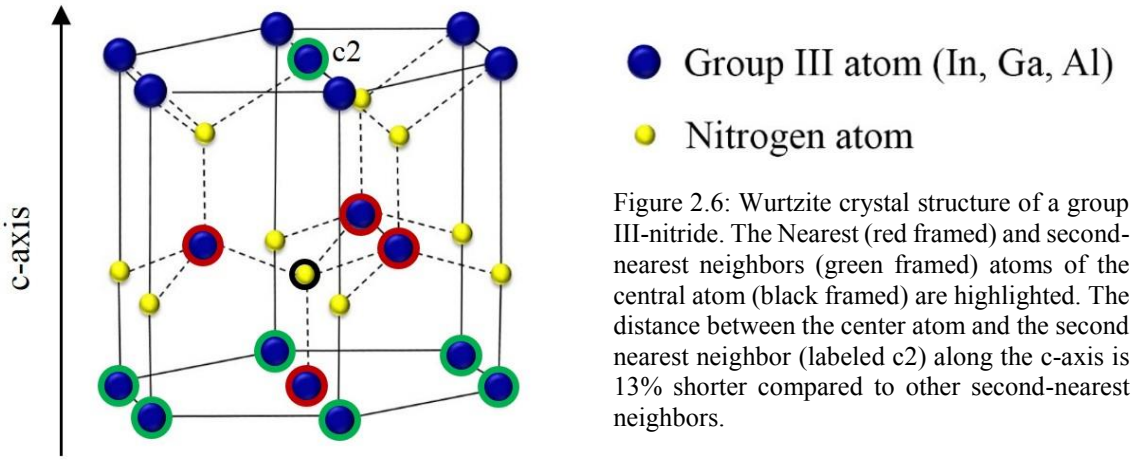

Figure 2.6: Wurtzite crystal structure of a group III-nitride. The Nearest (red framed) and second-nearest neighbors (green framed) atoms of the central atom (black framed) are highlighted. The distance between the center atom and the second nearest neighbor (labeled c2) along the c-axis is 13% shorter compared to other second-nearest neighbors.

As listed in Table 2.1, the internal parameter u of GaN, AlN and InN is larger than the ideal value. The asymmetric second-nearest neighbor interactions even in an ideal tetrahedron result in spontaneous polarization as depicted in Figure 2.7a. In the case of a non-ideal tetrahedron (Figure 2.7b), the spontaneous polarization is enhanced compared to the ideal tetrahedra

(indicated by red arrows in Figure 2.7a+b). The spontaneous polarization is different for GaN, AlN and InN. This is important for the growth of group III-nitride heterostructures such as InGaN/GaN MQWs (multi-quantum wells) or buffer layers for strain engineering. In case of a heterostructure such as GaN/AlN, the different spontaneous polarizations of GaN and AlN induce a built-in electrostatic field in the heterostructure. Furthermore, the lattice mismatch of both binaries leads to compressive strain in the growth plane and relaxation in the growth direction. In Figure 2.7c, the relaxation is expressed by a larger distance between the nitrogen and the group III metal atom, which corresponds to a larger internal parameter *u*. The compressive strain (in this case) causes a piezoelectric polarization superimposed to the spontaneous polarization.

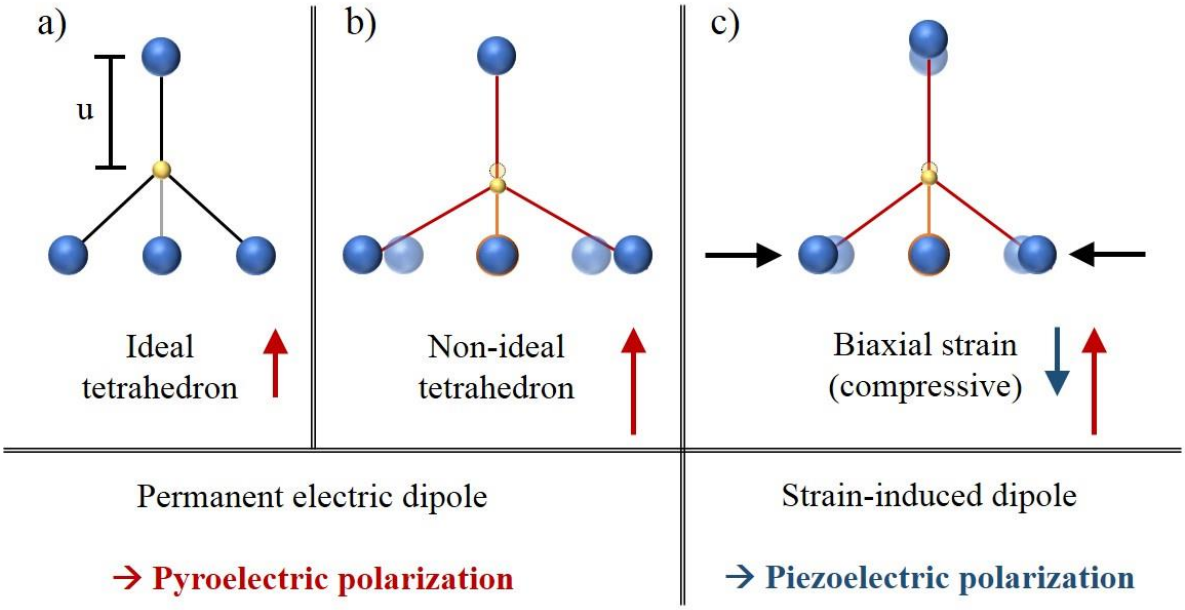

Figure 2.7: Ideal (a) and non-ideal tetrahedra (b,c) in wurtzite group III-nitride crystals. The blue spheres represent the metal (Ga, In, Al) atoms and the yellow spheres the nitrogen atoms. Deviation from the ideal tetrahedron amplifies the spontaneous polarization indicated by red arrows (b). The piezoelectric polarization (blue arrow) is due to biaxial (compressive) strain (c). The schematic illustration is adapted from [61].

Piezoelectric polarization is induced by any deformation of the hexagonal unit cell by strain or stress and superimpose with the spontaneous polarization. The direction of the piezoelectric polarization depends on the induced strain. The total macroscopic or net polarization ΔP is the combination of spontaneous and piezoelectric polarization. The direction of the net polarization correlates to the polarity and the biaxial strain [18] as given in Table 2.3.

Biaxial strain \ **Polarity**	**Ga-polar**	**N-polar**
Tensile	[0001]	$[000\bar{1}]$
Compressive	$[000\bar{1}]$	[0001]

Table 2.3: Direction of net polarity depending on polarity and biaxial strain [18].

Control of the strain in polar group III-nitrides is crucial, because the built-in piezoelectric field has an immense effect on the optoelectronic properties. The strength of the internal electric field is in the order of a few MV/cm. Inside of quantum well LED structures, the electric field can cause a spatial separation of electron and holes to opposite ends of the well, leading to a shift of the emission wavelength and a reduction of the internal quantum efficiency of the LED. The shift in the emission spectrum the spatial separation of the charged carriers is called quantum-confined Stark effect (QCSE).

2.5 Lattice mismatch and strain

In this work, InN and $In_xGa_{1-x}N$ layer are epitaxial grown on sapphire substrates. The large lattice mismatch between group III-nitride alloys and the sapphire substrate lead to strain in the deposited layer. If the film thickness is below a distinct critical layer thickness, the layer is pseudomorphically strained. Above the critical layer thickness, the introduction of defects leads to a relaxation of the layer strain. There are two types of lattice strain or mismatch f, namely compressive and tensile, which depend both on the unstrained lattice constants of the layer a_l and the substrate a_s, as expressed in the following equation:

$$f = \frac{\Delta a}{a_s} = \frac{a_l - a_s}{a_s}. \tag{2.3}$$

Compressive strain arises when the lattice constant of the layer a_l is larger than the lattice constant of the substrate a_s as shown in Figure 2.8a. In case of tensile strain, it is vice versa as illustrated in Figure 2.8b.

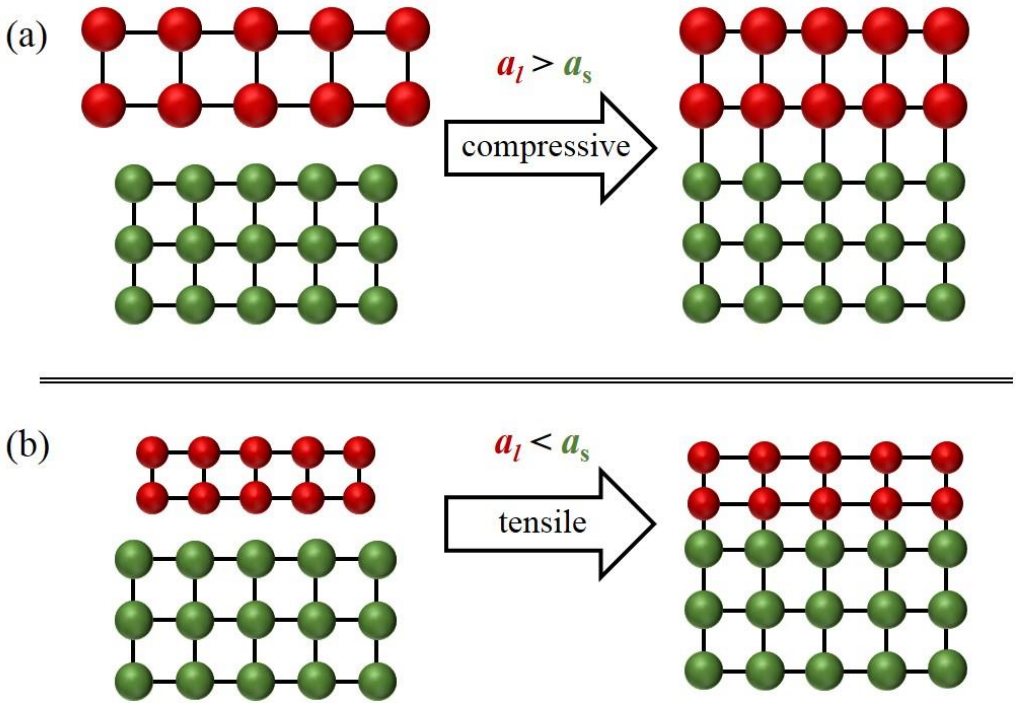

Figure 2.8: Compressive (a) and tensile (b) strained layers (red atoms) on a substrate (green atoms).

2.6 Phonon modes of InN, GaN and InGaN

In this thesis, Raman spectroscopy is one of the main characterization methods. It is a powerful and non-destructive tool which provides information about the crystalline ordering, stress and composition of semiconductor compounds. Therefore, understanding and identification of Raman-active modes and their symmetries is necessary to analyze the Raman spectra of the binary and ternary group III-nitrides investigated in this work.
Raman spectroscopy relies on the Raman Effect, which describes the inelastic scattering of light due to an elementary excitation. The effect had been theoretically predicted by Smekal in 1923 [62]. However, Raman spectroscopy is named after Sir C.V. Raman, who first experimentally discovered the effect of inelastic light scattering in liquids in 1928 [63]. For his discovery Raman was awarded the Nobel Prize in Physics in 1930.

2.6.1 Raman effect

Apart from reflection, absorption and transmission, incident light can be scattered by a material surface. The scattered light is divided into an elastically scattered part, called Rayleigh scattering and an inelastic scattered part. The percentage of inelastic scattered light is very small compared to the elastic scattered light. In the Rayleigh scattering process, the elastically scattered photon has the same energy (frequency) as the incident photon (see center of Figure 2.9). In contrast, the inelastic scattered photons have a different energy than the incident photons. Inelastic scattering in crystals can either generate or annihilate an elementary excitation. The generation and annihilation of excitations are called Stokes and Anti-Stokes process, respectively. Elementary quantized excitations are for example phonons, plasmons or phonon polaritons. This section discusses the Raman scattering of monochromatic light (photons) by lattice phonons in semiconductor crystals. In a periodic structure, phonons are elementary excitations of lattice vibrations.

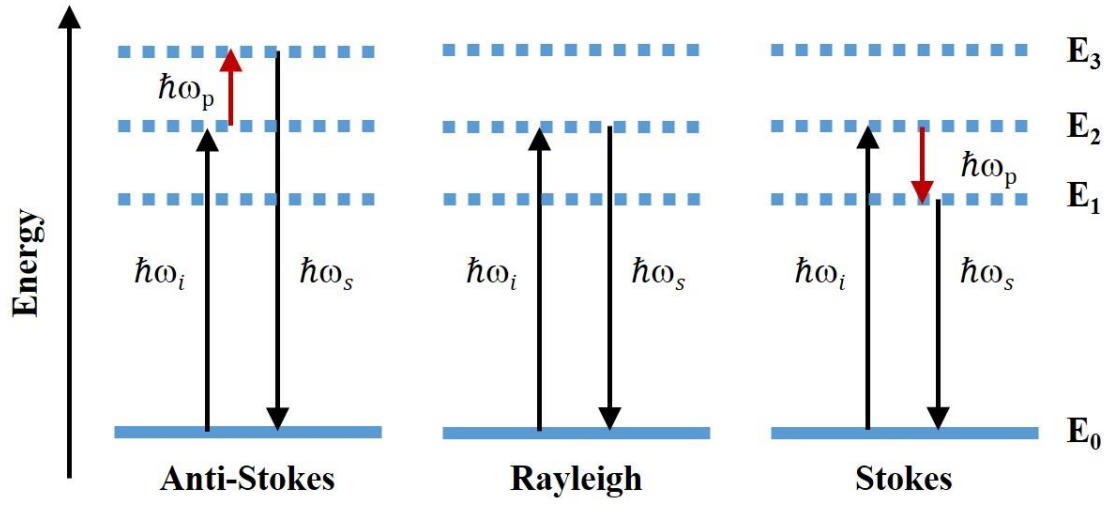

Figure 2.9: Schematic illustration of Rayleigh, Stokes and anti-Stokes scattering. $\hbar\omega_i$ is the energy of the incident photon, $\hbar\omega_s$ is the energy of the scattered photon scattered and $\hbar\omega_p$ is the energy of the scattered photon.

Figure 2.9 schematically illustrates Rayleigh scattering as well as Stokes and anti-Stokes scattering in a first-order Raman process. For all three cases, the energy of the incident light

(photon) is absorbed and leads to an excitation from an initial electronic ground state E_0 to an excited state E_2.

In case of Stokes Raman process, a phonon is created, and the scattered light has a lower energy than the incident light. In the anti-Stokes Raman process, a phonon is absorbed, and the scattered light has a higher energy than the incident light. For both processes applies the conservation of energy and momentum:

$$\hbar\omega_s = \hbar\omega_i \pm \hbar\omega_p \tag{2.4}$$

$$\vec{k}_s = \vec{k}_i \pm \vec{q}\ . \tag{2.5}$$

Equations (2.4) and (2.5) correspond to the first-order Raman scattering. The positive sign describes the creation of a phonon in the Stokes process, while the negative sign corresponds to the absorption of a phonon in the anti-Stokes process. In general, the Raman effect can be described by a semi-classic (macroscopic approach) and a quantum-mechanical approach. A detail description of both approaches can be found here [64]. First, the semi-classical approach is considered through the phenomenological description of the Raman process. The electromagnetic wave of the incident light

$$\vec{E}(\vec{r},t) = \vec{E}_i\left(\vec{k}_i,\omega_i\right)\cos\left(\vec{k}_i\cdot\vec{r}-\omega_i t\right) \tag{2.6}$$

induces a polarization field in the interacting solid medium [64]:

$$\vec{P}(\vec{r},t) = \vec{P}_i\left(\vec{k}_i,\omega_i\right)\cos\left(\vec{k}_i\cdot\vec{r}-\omega_i t\right). \tag{2.7}$$

The frequency and wave vector of the polarization are the same as those of the incident electromagnetic wave. The polarization and the electromagnetic wave are connected by the material specific electronic susceptibility χ:

$$\vec{P}\left(\vec{k}_i,\omega_i\right) = \chi\left(\vec{k}_i,\omega_i\right)\vec{E}_i\left(\vec{k}_i,\omega_i\right). \tag{2.8}$$

Inserting equation (2.8) into equation (2.7) yields:

$$\vec{P}_0(\vec{r},t) = \chi_0\left(\vec{k}_i,\omega_i\right)\vec{E}\left(\vec{k}_i,\omega_i\right)\cos\left(\vec{k}_i\cdot\vec{r}-\omega_i t\right). \tag{2.9}$$

The atomic displacements (vibrations) in a semiconductor crystal are quantized into phonons and can be expressed by a plane wave in normal coordinates:

$$\vec{Q}(\vec{r},t) = \vec{Q}\left(\vec{q},\omega_p\right)\cos\left(\vec{q}\cdot\vec{r}-\omega_p t\right) \tag{2.10}$$

with wave vector $\vec{q}$ and phonon frequency ω_p.

The atomic vibrations affect the susceptibility. Due to the adiabatic approximation that the frequency of the vibrations is much smaller than the electronic frequencies, the susceptibility χ can be expressed as a function of $\vec{Q}$. Compared to the lattice constant, the amplitudes of these atomic vibrations are smaller and the susceptibility χ can be expand as a Taylor series:

$$\chi\left(\vec{k}_i,\omega_i,\vec{Q}\right)=\chi_0\left(\vec{k}_i,\omega_i\right)+\left(\frac{\partial\chi}{\partial\vec{Q}}\right)_0\vec{Q}\left(\vec{r},t\right)+... \tag{2.11}$$

with χ_0 as the electric susceptibility of the medium without fluctuations caused by atomic displacements.

Substituting equation (2.11) into (2.9), the polarization can be written as

$$\vec{P}\left(\vec{r},t,\vec{Q}\right)=P_0\left(\vec{r},t\right)+P_{ind}\left(\vec{r},t,\vec{Q}\right). \tag{2.12}$$

The polarization consists of two terms. The first term P_0 describes the in-phase vibration of the polarization with the incident radiation, meaning energy and momentum are the same as the incident light (Rayleigh scattering)

$$\vec{P}_0\left(\vec{r},t\right)=\chi_0\left(\vec{k}_i,\omega_i\right)\vec{E}\left(\vec{k}_i,\omega_i\right)\cos\left(\vec{k}_i\cdot\vec{r}-\omega_i t\right). \tag{2.13}$$

The second term $\vec{P}_{ind}$ is the polarization induced by the phonons

$$\vec{P}_{ind}\left(\vec{r},t,\vec{Q}\right)=\left(\frac{\partial\chi}{\partial\vec{Q}}\right)_0\vec{Q}\left(\vec{r},t\right)\vec{F}_i\left(\vec{k}_i,\omega_i\right)\cos\left(\vec{k}_i\cdot\vec{r}-\omega_i t\right). \tag{2.14}$$

The induced polarization $\vec{P}_{ind}$ in terms of wave vector and frequency is

$$\begin{aligned}\vec{P}_{ind}\left(\vec{r},t,\vec{Q}\right)&=\left(\frac{\partial\chi}{\partial\vec{Q}}\right)_0\vec{Q}\left(\vec{q},\omega_p\right)\cos\left(\vec{q}\cdot\vec{r}-\omega_p t\right)\times\vec{E}_i\left(\vec{k}_i,\omega_i\right)\cos\left(\vec{k}_i\cdot\vec{r}-\omega_i t\right)\\&=\frac{1}{2}\left(\frac{\partial\chi}{\partial\vec{Q}}\right)_0\vec{Q}\left(\vec{q},\omega_p\right)\vec{E}_i\left(\vec{k}_i,\omega_i\right)\cos\left[\left(\vec{k}_i+\vec{q}\right)\cdot\vec{r}-\left(\omega_i+\omega_p\right)t\right]\\&\quad+\frac{1}{2}\left(\frac{\partial\chi}{\partial\vec{Q}}\right)_0\vec{Q}\left(\vec{q},\omega_p\right)\vec{E}_i\left(\vec{k}_i,\omega_i\right)\cos\left[\left(\vec{k}_i-\vec{q}\right)\cdot\vec{r}-\left(\omega_i-\omega_p\right)t\right].\end{aligned} \tag{2.15}$$

Equation (2.15) presents the two components of the inelastic scattering, if the partial derivative of the susceptibility is non-zero. The inelastic scattering consists of two terms. Each term in equation (2.15) is represented by a wave with shifted wave vectors and shifted frequencies that correspond to the scattered photon like in equations (2.4) and (2.5). The first term indicates the anti-stokes process and the second term indicates the Stokes process. In the Stokes process a phonon is generated and the scattered light has a lower wave vector (momentum) and frequency (energy) compared to the incident light. This expressed by the differences $\left(\vec{k}_\mathrm{i}-\vec{q}\right)$ and $\left(\vec{\omega}_\mathrm{i}-\vec{\omega}_p\right)$. The anti-Stokes process describes the annihilation of a phonon. The frequency $\left(\vec{\omega}_\mathrm{i}+\vec{\omega}_p\right)$ and the wave vector $\left(\vec{k}_\mathrm{i}+\vec{q}\right)$ are increased with respect to the incident light. From equation (2.4) follows that the difference between the incident photon frequency ω_i and the scattered photon frequency ω_i is equal to the phonon frequency and is referred to as Raman frequency or Raman shift. The change in energy can be measured by Raman spectroscopy. Equation (2.15) considers only first-order Raman scattering processes that include the conservation of frequency and wave vector. The wave vector conservation results in a much smaller wave vector $\vec{q}$ (~10^6 cm^{-1}) of phonons compared the photon wave vectors within the Brillouin zone ($\pi/a \approx 10^8$ cm^{-1}). Thus, the dimension of $\vec{q}$ allows only first-order Raman-

scattering of phonons in the center of the Brillouin zone. By extending the Taylor series in equation (2.11), second or higher order Raman scattering can be considered.

The scattered intensity I_S calculated from equation (2.15) is proportional to

$$I_s \propto \left| e_i \cdot \left(\frac{\partial \chi}{\partial \vec{Q}} \right)_0 \vec{Q}\left(\omega_p\right) \cdot e_s \right|^2 . \tag{2.16}$$

with e_i and e_s denoted as the polarization of the incident and scattered light, respectively. Considering the atomic displacement of a given phonon, the partial derivatives of the susceptibility in equation (2.16) are defined as second order tensor, known as Raman tensor $\Re$.

$$\Re = \left(\frac{\partial \chi}{\partial \vec{Q}} \right)_0 \vec{Q}\left(\omega_p\right). \tag{2.17}$$

The Raman tensor $\Re$ correlates the induced polarization in the crystal with the polarization of the incident light. In case of phonons, the frequency difference between incident and scattered light can be neglected ($\omega_i \approx \omega_s$) and the Raman tensor becomes a symmetric tensor.

Hence, equation (2.16) can be written as

$$I_s \propto \left| e_i \cdot \Re \cdot e_s \right|^2 . \tag{2.18}$$

Equation (2.18) determines under which polarizations e_i and e_s, and the choice of scattering geometry Raman active phonon modes can be observed. Each phonon mode is described by an individual component $(\partial\chi/\partial\vec{Q})_0$ of the Raman tensor. Therefore, each tensor can be derived by group theory from the symmetry of the crystal and the vibrational modes (phonon). The symmetry of Raman active phonons is determined by the Raman selection rules.

In the quantum mechanical approach of Raman scattering, a phonon is considered as a quasiparticle that describes lattice vibrations. In this microscopic theory, electrons mediate the Raman scattering of visible photons by phonons. The scattering process consists of a three steps sequence. First, an incident photon with the energy $\hbar\omega_i$ excites the semiconductor and creates an electron-hole pair (exciton). The system transfers from the initial state |i⟩ into a virtual state |a⟩. The electron-photon coupling is described by the Hamiltonian H_{eR}. In the second step, the electron-hole pair scatters to another state |b⟩ by either creating (Stokes) or annihilating (anti-Stokes) a phonon. In the last step, the electron-hole pair recombines radiatively from this state |b⟩ by the emission of the scattered photon to the final state |f⟩, again via electron-photon interaction H_{eR}.

The probability P_{ph} of the Raman scattering process is given by [64]:

$$P_{\text{ph}} = \left(\frac{2\pi}{\hbar} \right) \left| \sum_{a,b} \frac{\langle i | H_{eR} | a \rangle \langle a | H_{eP} | b \rangle \langle b | H_{eR} | f \rangle}{\left[\hbar\omega_i - \left(E_a - E_i \right) \right] \left[\hbar\omega_s - \left(E_b - E_f \right) \right]} \right|^2 \delta\left(\omega_i - \omega_p - \omega_s \right), \tag{2.19}$$

whereas ω_i and ω_i are the frequencies of the incident and scattered photon and $E_{i,\,a,\,b,\,f}$ are the energies of the different states. The Hamiltonian H_{eP} represents the interaction between electrons and optical phonon interaction. The electron – phonon interaction can occur via two

mechanisms, the deformation potential interaction and the Fröhlich interaction. The deformation potential interaction is the change of bond lengths and/or angles. The Fröhlich interaction is described later in this chapter.

2.6.2 Optical phonon modes in group III-nitrides

Group theory predicts the Raman active and the infrared (IR) active phonon modes of the crystal structure. As mentioned in section 2.2, the wurtzite crystalline structure of group III-nitride belongs to space group C^4_{6v} (or $P6_3mc$). The space group includes elements which represent the translation, rotation and reflection operations. These symmetry operations reproduce the wurtzite crystal structure onto itself.

The space group of the wurtzite structure contains symmetry operations divided into the following six classes [64]: $E, C_2, 2C_3, 2C_6, 3\sigma_d, 3\sigma_v$.

- $\{E\}$ identity
- $\{C_2\}$ a two-fold rotation (by 180°) about the *c*-axis followed by a vector translation of (0, 0, *c*/2)
- $\{C_3, C_3^{-1}\}$ three-fold rotations about the *c*-axis
- $\{C_6, C_6^{-1}\}$ six-fold rotations about the *c*-axis followed by a vector translation of (0, 0, *c*/2)
- $\{3\sigma_d\}$ three symmetry planes perpendicular to $\vec{a}_1, \vec{a}_2$ and $\vec{a}_1$+$\vec{a}_2$, respectively, with a translation of (0, 0, *c*/2)
- $\{3\sigma_v\}$ three symmetry planes perpendicular to σ_d planes

The symmetries of a given group can be used by determining the number of inequivalent irreducible representations and their characters. One property of a group is that its number of inequivalent irreducible representations is equal to the number of classes [65]. Table 2.4 displays the character table of the irreducible representations of the C_{6v} group.

C_{6v}	E	C_2	$2C_3$	$2C_6$	$3\sigma_d$	$3\sigma_v$	Basis functions	Optical active
A_1	1	1	1	1	1	1	z, $x^2 + y^2$, z^2	IR, Raman
A_2	1	1	1	1	-1	-1	R_z	
B_1	1	-1	1	-1	-1	1	$x^3 - 3xy^2$	Silent
B_2	1	-1	1	-1	1	-1	$y^3 - 3yx^2$	Silent
E_1	2	-2	-1	1	0	0	(R_x, R_y), (xz, yz), (x, y)	IR, Raman
E_2	2	2	-1	-1	0	0	(x^2 - y^2), (xy)	Raman

Table 2.4: Character table for point group C_{6v} at the Γ point [65].

In the first column are the six irreducible representations A_1, A_2, B_1, B_2, E_1 and E_2 of the symmetry point group C_{6v}. The irreducible representations are characterized by the six classes. Additionally, the column labeled 'basis functions' lists the linear, quadratic and rotational functions (R_i), which transform according to each representation. The last column in Table 2.4 shows the phonon optical activity indicated by the basis functions. Phonons represented by linear basis functions are IR active and can be detected via IR absorption spectroscopy. Quadratic basis functions indicate Raman active phonon modes, and Raman scattering can be measured by Raman spectroscopy.

The wurtzite crystal structure has $N = 4$ atoms in the unit cell and the atoms can move in the x-, y- and z-direction of the Cartesian coordinate system. This leads to a total number of $3 \times N = 12$ possible phonon modes at the Γ-point. The phonon modes are described by the irreducible representations using the Mulliken (or chemical) notation:

$$\Gamma_{total} = 2A_1 + 2B_1 + 2E_1^{(2)} + 2E_2^{(2)}. \tag{2.20}$$

As given in column 2 of the character table above (Table 2.4), the E_1 and E_2 phonon modes are degenerated twice or 2-dimensional (indicated by the superscript '2' in equation (2.20). The phonon modes A_1, A_2, B_1 and B_2 are single degenerated or 1-dimensional which adds up to a total of 12 phonon modes in equation (2.20). The phonon modes are separated into three acoustical and nine optical phonon modes:

$$\Gamma_{total} = \Gamma_{ac} + \Gamma_{opt} = \left(A_1 + E_1^{(2)}\right) + \left(A_1 + 2B_1 + E_1^{(2)} + 2E_2^{(2)}\right). \tag{2.21}$$

One of the A_1 and a set of the $E_1^{(2)}$ modes are acoustical phonon modes. For k = 0, the acoustic phonon modes represent only a uniform translation of the entire crystal (all atoms move in the same direction), and the optical phonons remain:

$$\Gamma_{opt} = A_1 + 2B_1 + E_1^{(2)} + 2E_2^{(2)}. \tag{2.22}$$

The nine optical modes consist of A_1(LO), B_1(low) and B_1(high), two E_1(TO), two E_2(low) and two E_2(high) modes. The B_1 and the E_2 modes are distinguished into 'high' and 'low', corresponding to their energy. The B-modes are neither Raman nor IR active and are called silent modes [64]. Considering the basis functions shown in Table 2.4, the remaining Raman active optical modes are:

$$\Gamma_{opt} = A_1 + E_1 + 2E_2. \tag{2.23}$$

The Atomic displacements of the optical phonon modes in wurtzite group III-nitride crystals are depicted in Figure 2.10.

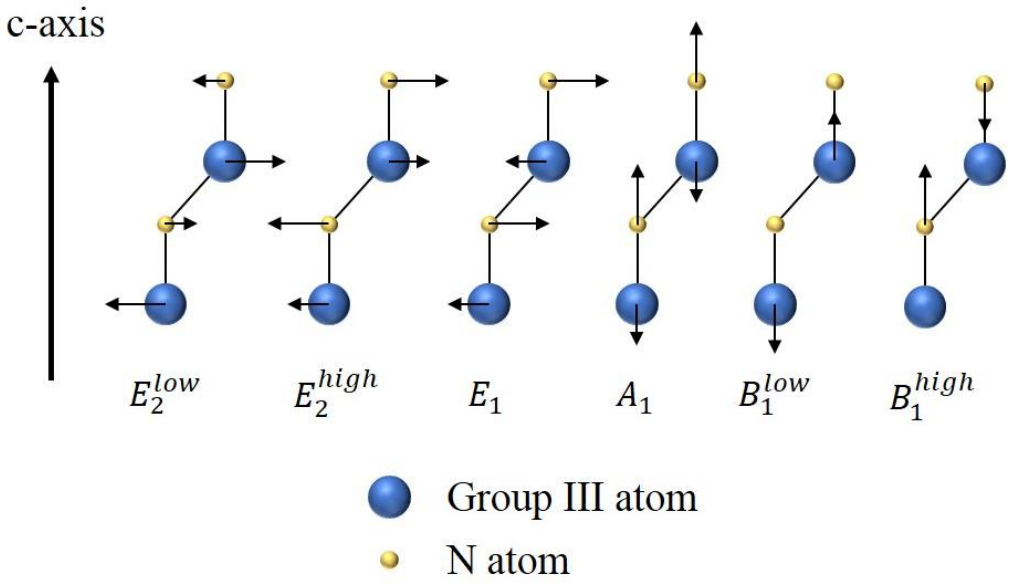

Figure 2.10: Atomic displacements of the optical phonon modes in wurtzite group III-nitride crystals [66].

The vibrations of the A_1 and both B_1 phonon modes are parallel to the *c*-axis. In case of the B_1 modes, the 'low' modes belong to the vibrations of the group III atoms and the 'high' modes describe the nitrogen vibrations. The atomic displacements of the E_1 and E_2 phonon modes are in the plane perpendicular to the *c*-axis. In E_2 modes, the atomic oscillation of both cations (and respectively both anions) in the primitive cell is in opposite direction as can be seen in Figure 2.10. Thus, the resulting electric dipole is zero and the E_2 modes are non-polar phonon modes. In case of the A_1 and E_1 modes, both cations move in the same direction, but contrarily to the displacement of both anions, resulting in an electric dipole. Hence, the A_1 and E_1 are called polar modes. The long-range Coulomb interaction of the net dipole moment induces a macroscopic field, resulting in a splitting of the polar modes A_1 and E_1 into longitudinal optical (LO) and transversal optical (TO) modes. LO-modes propagate parallel to the vibration direction, while TO-modes propagate perpendicular. Due to the long-range nature of the Coulomb interaction, an additional restoring force is present in LO phonon modes. Therefore, the frequency of LO phonons ω_{LO} is higher than the frequency of the TO modes ω_{TO}. The magnitude of the LO-TO-splitting is expressed by the Lyddane-Sachs-Teller relation as the ratio of low and high frequency dielectric constants of the material:

$$\frac{\varepsilon_0}{\varepsilon_\infty} = \frac{\omega_{LO}^2}{\omega_{TO}^2} . \tag{2.24}$$

According to equation (2.18), the intensity and therefore the observation of Raman-active modes depends on the direction of both, the incident e_i and scattered polarization e_s under the following condition:

$$I_s \propto \left| e_i \cdot \Re \cdot e_s \right|^2 \neq 0 . \tag{2.25}$$

The selection rules for the Raman scattering derive from the Raman tensor. Considering equations (2.17) and (2.25), the individual components $(\partial\chi/\partial\vec{Q})_0$ of the Raman tensor must be non-zero for phonon mode to be Raman-active. Derivates of the components in the form of bilinear combinations of x, y and z (= x^2, y^2, z^2, xy, xz, yz) [67] are different from zero and

comply with equation (2.25). This can be verified from the character table of the wurtzite crystal structure (Table 2.4). The Raman-tensors for the optical active modes in equation (2.23) are described by 3 × 3 matrices:

$$A_1(z)=\begin{pmatrix} a & & \\ & a & \\ & & b \end{pmatrix},\ E_1(x)=\begin{pmatrix} & & c \\ & & \\ c & & \end{pmatrix},\ E_1(y)=\begin{pmatrix} & & \\ & & c \\ & c & \end{pmatrix}$$

$$E_2^{(1)}(x)=\begin{pmatrix} d & & \\ & -d & \\ & & \end{pmatrix},\ E_2^{(2)}(y)=\begin{pmatrix} & d & \\ d & & \\ & & \end{pmatrix}. \tag{2.26}$$

Table 2.5 lists the Raman selection rules of Raman-active phonons in group III-nitrides for different measurement configurations. The 'A' indicates which Raman active modes can be observed for a given scattering configuration. For simplification, the scattering configurations (geometries) are given in the Porto notation, which consists of a combination of four coordinates:

$$a(b,c)d\,. \tag{2.27}$$

The first coordinate (a) corresponds to the incident light propagation direction. The second and third index describe the polarization of the incident (b) and scattered light polarization (c). The last coordinate (d) gives the direction of the detected light. In this work, Raman spectroscopy is carried out in backscattering geometry.

Scattering geometry	**Raman active modes**					
	E_2**(low)**	A_1**(TO)**	E_1**(TO)**	E_2**(high)**	A_1**(LO)**	E_1**(LO)**
$z(xx)\bar{z}$	A			A	A	
$z(xy)\bar{z}$	A			A		
$x(yy)\bar{x}$	A	A		A		
$x(zz)\bar{x}$		A				
$x(yz)\bar{x}$			A			

Table 2.5: Selection rules for first order Raman-active modes in wurtzite group III-nitrides.

Table 2.6 displays the frequencies of the Raman-active phonon modes of the wurtzite group III-nitride binaries GaN, AlN and InN. The phonon frequencies are extracted from literature. Though in Table 2.5 can be seen that the E_1(LO) mode is not measurable in any backscattering geometry, in contrast to the other modes, multiple groups have reported the observation of the E_1(LO) mode for the three group III-nitrides AlN, GaN and InN, even in high-quality crystals

[68-71]. The E_1(LO) is only seen in the symmetry-forbidden $x(zz)\bar{x}$ configuration. A possible explanation for the occurrence of this mode is the intraband Fröhlich interaction. In general, the Fröhlich interaction is an electron-phonon interaction. To describe the Fröhlich interaction, we turn again towards the already mentioned LO phonons. The LO phonons result in a macroscopic polarization, which subsequently creates a macroscopic electric field. This long-range electric field leads to a coupling of the LO phonons with the electrons. The Coulomb interaction between the long-range electric field and the electronic structure is called Fröhlich interaction. The Fröhlich mechanism specifically takes place in polar semiconductors. A detailed explanation of the Fröhlich mechanism can be found in reference [64]. Another elementary excitation that can take part in the Raman scattering process are plasmons. Plasmons are collective oscillations of the free electron density in a sample. These collective free charge oscillations produce a macroscopic electric field that couples with the long-range longitudinal electric field of the LO phonons and so-called longitudinal-optical phonon-plasmon coupled modes (LOPCMs) are formed. The free charge density strongly influences the line shape and frequency of the LOPCMs. Investigation of the coupled modes by Raman spectroscopy allows determination of the free carrier concentration in doped semiconductors.

Phonon mode	**GaN**	**AlN**	**InN**
E_2(low)	144 cm^{-1}	248.6 cm^{-1}	87 cm^{-1}
A_1(TO)	531.8 cm^{-1}	611 cm^{-1}	447 cm^{-1}
E_1(TO)	558.8 cm^{-1}	670.8 cm^{-1}	476 cm^{-1}
E_2(high)	567.6 cm^{-1}	657.4 cm^{-1}	488 cm^{-1}
A_1(LO)	734 cm^{-1}	890 cm^{-1}	586 cm^{-1}
E_1(LO)	741 cm^{-1}	912 cm^{-1}	593 cm^{-1}
Reference	[72]	[72]	[69]

Table 2.6: Phonon frequencies of first order active Raman modes in wurtzite GaN, AlN and InN. The frequencies are experimentally observed at room temperature.

2.6.3 Effect of strain on optical phonon modes

Raman spectroscopy is one of the main characterization methods to analyze the structural properties of the InN and In-rich InGaN samples studied in this work. This section gives a short overview about the interpretation of a Raman spectrum and especially the effect of strain of the optical phonon modes.

A Raman spectrum is characteristic for each material. The positions of a Raman peak is associated to a specific vibrational mode of the material. The phonon frequencies are like a fingerprint, that allows the identification of the sample material. Also, the shape of peak is of importance. The full width at half maximum (FWHM) of the E_2(high) phonon mode indicates the crystal quality. The narrower the FWHM of the E_2(high) mode, the better the crystal quality of the material. In contrast, a broad Raman peak is an indication of disorder such as point defects for example.

Residual strain and doping can lead to deviations (shift) of the phonon frequencies listed in Table 2.6. The direction and the amount of the shift provides information about the residual strain. In general, strain can induce a shift and a splitting of phonon modes. In case of uniaxial strain along the c-axis or biaxial strain in the growth plane, only a phonon shift takes place because the hexagonal symmetry of the crystal is maintained [18]. As mentioned in section 2.5, heteroepitaxial grown group III-nitrides layer can be biaxially strained in the growth plane (c-plane) due to the mismatch of the lattice parameters and thermal expansion coefficient between film and substrate. For example, phonon frequencies of thin epilayers are different compared to phonon frequencies of bulk crystals. Strain leads to a change of the phonon frequencies via the deformation potentials because strain affects the bond lengths and/or angles. The shift of the non-polar E_2(high) mode is typically analyzed for the determination of residual layer strain [73, 74]. The polar A_1 and E_1 modes depend on the angular dispersion and subsequently their frequencies depend on the scattering configuration [68]. Furthermore, the LO-phonons interact with the free charge carrier density. A red-shift of the E_2(high) to lower frequencies corresponds to tensile strain, whereas an increase of the E_2(high) phonon frequency indicates compressive strain [75].
In conclusion, Raman spectroscopy can identify the composition and crystal quality of the grown group III- alloys based upon their phonon frequencies and their linewidth, respectively. Furthermore, changes of the phonon frequencies may provide information about strain, lattice disorder or defects.

3 Characterization Methods

3.1 Introduction

This chapter describes the experimental setups of the ex-situ characterization methods to investigate the structural, morphological and optoelectronic properties of the group III-nitrides grown by MEPA-MOCVD. The structural properties like crystal quality and the composition are determined by micro-Raman spectroscopy and high-resolution X-ray diffraction (HR-XRD). Information about the surface morphology of the InGaN samples is contributed by atomic force microscopy (AFM).
Nanoscopic investigations of the ternary InGaN alloys is performed by scattering-type scanning near-field infrared microscopy (s-SNIN) and tip-enhanced Raman spectroscopy (TERS). Both methods have the advantage of a high-spatial resolution below the diffraction limit which makes s-SNIN and TERS highly suitable for the investigation lateral nanoscale compositional fluctuations in ternary group III-nitride alloys.

3.2 Atomic force microscopy

Atomic force microscopy (AFM) is a characterization technique with a high-spatial resolution to measure the topography and roughness of a sample surface on an atomic scale [76]. The surface topography of semiconductor materials allows for example conclusions about the growth mode. In this work, a Park XE-100 AFM-system is utilized to study the surface morphology of the InGaN samples. A typical AFM setup consists of a micro-machined flexible cantilever with a very sharp cone-shaped or pyramid-shaped tip to measure the sample surface as depicted in Figure 3.1. A laser beam is aligned onto the backside of the cantilever. The light of the laser is reflected at the cantilever's backside onto a position sensitive photodetector (PSPD). Atoms at the tip apex interact with atoms at the sample surface causing a deflection or bending of the cantilever. The deflection or bending of the cantilever depends on the distance between the tip and sample surface and can be either a repulsive or an attractive interatomic force. The deflection of the cantilever results in a change of the laser beam's reflection angle, and thus changing the location where the reflected laser beam enters the PSPD. The deflection itself is too small to be resolved. A PSPD consists of four cells (quad-cell) as depicted in Figure 3.1. The relation between the upper quadrants and the lower quadrants corresponds to the topographic information:

$$\text{Topographic information} = \left(A + C\right) - \left(B + D\right). \tag{3.1}$$

Quantification of the cantilever deflection enables imaging of the surface morphology. To map a sample's surface morphology, a piezoelectric tube scanner moves the sample horizontally in x- and y-direction as well in the vertical direction z. From the signal change of the probe deflection can be determined if a convex or concave area is measured, which serves as a feedback loop to control the vertical movement and maintain a constant distance between the probe tip and the sample surface during the scan.

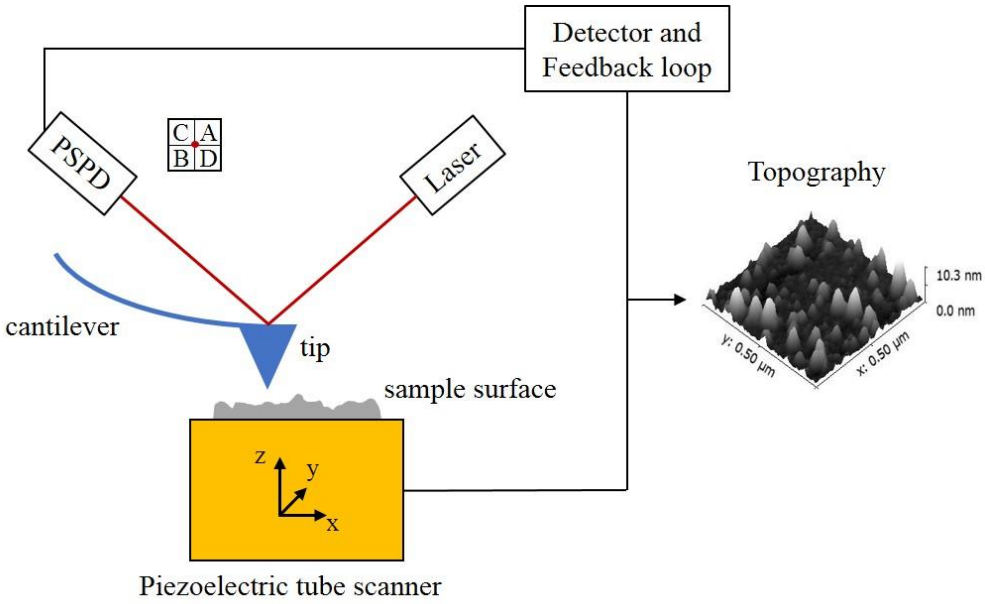

Figure 3.1: Basic configuration of a typical AFM.

In general, AFM operation is carried out in three imaging modes, namely contact, tapping or non-contact mode.

In Contact mode, the cantilever tip is in soft physical contact with the surface. Strong repulsive forces lead to a deflection of the cantilever. The topography is measured either via the deflection of the cantilever or using the feedback loop to keep the cantilever at a constant position. To avoid damage of the tip, contact mode is used at a very narrow distance between the apex of the tip and the surface, in which the repulsive interaction force is dominant.

In the non-contact mode, the separation between the tip and the surface is relatively larger compared to the contact mode. Due to the long-range van de Waals interaction, the attractive force becomes dominant between the cantilever tip and the surface. However, direct measuring of the cantilever deflection is not possible because the attractive force is very low in the non-contact regime. Instead, the cantilever vibrates at or near its resonant frequency with a constant amplitude. The attractive interaction force causes a shift of the cantilever's oscillation frequency. This frequency shift is spatially dependent and thus variations of the attractive force interacting with the tip lead to an instant modulation of the oscillation frequency [77]. By adjusting the tip-surface distance, the feedback loop corrects this frequency change and represents a topographic map of the sample surface.

In tapping mode, the cantilever is vibrating with a constant amplitude while there are no interacting forces with the surface. The tip is lowered shortly until it almost has or rather contacts the surface. When the tip approaches the surface, the cantilever is affected by interacting forces causing a change of the oscillation amplitude. The amplitude of the oscillation is the feedback parameter. During a scan, the cantilever height is adjusted to keep its oscillation amplitude constant, resulting in an image of the sample morphology. The alternatively lowering and lifting of the tip avoids dragging of the sample by the tip reducing possible damage. Due to the intermittent contact between the vibrating cantilever and the sample surface, tapping mode is called as intermittent or dynamic force mode. The non-contact and tapping mode are called dynamic modes in contrast to the static contact mode.

3.3 Raman spectroscopy

In this work, Raman spectroscopy is one of the main characterization techniques to examine the structural properties of the binary and ternary group III-nitrides grown by MEPA-MOCVD. In the previous chapter under section 2.6, the Raman effect and the selection rules for wurtzite group III-nitrides are thoroughly described. In this section, the experimental setup is explained. Raman scattering provides structural information about the crystal quality and stress in the layer. Furthermore, the composition of InGaN can be evaluated from the frequency of the A_1(LO) phonon mode using the modified random element isodisplacement (MREI) model that predicts a linear dependence of the A_1(LO) phonon frequency as a function of the indium or gallium concentration, respectively [78].

Raman spectroscopy is carried out at Technical University of Berlin (TUB) using commercial Raman systems and at Georgia State University (GSU), where a customized Micro-Raman spectrometer is utilized. Both setups measure Raman spectra in backscattering geometry at room temperature. For resonant Raman scattering experiments, the $In_xGa_{1-x}N$ are probed with excitation wavelengths of 457 nm, 532 nm and 633 nm.

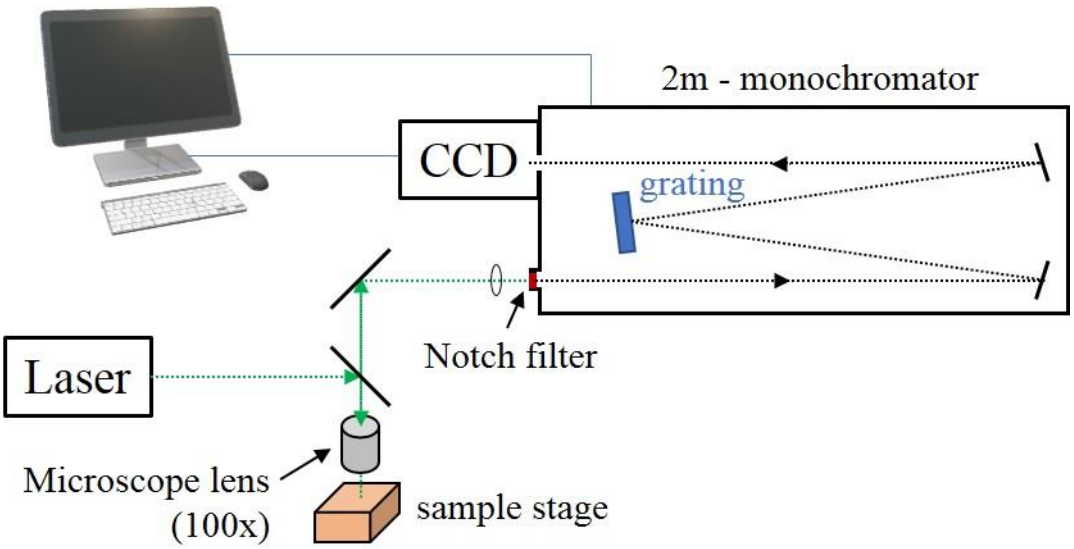

Figure 3.2: Experimental setup and optical path of the Raman spectrometer at GSU.

Figure 3.2 shows the schematic layout of the custom experimental Raman spectroscopy setup, which basically consists of a monochromatic light source, a 2-meter monochromator with a dispersing element (grating), and a detector. A frequency-doubled Nd:YAG laser with a wavelength of 532 nm (energy = 2.33 eV) and an output power of 500 mW is utilized as a light source. The laser light is focused on a sample using a beam splitter and a confocal microscope lens with 100x magnification factor. The scattered light from the sample is collected by the microscope lens. This design provides Raman spectroscopy in the backscattering geometry configuration. The scattered light passes through the beam splitter and is directed to the monochromator by a mirror. A lens focuses the scattered light into the monochromator entrance slit. A notch filter in front of the entrance slit suppresses the intense Raleigh-scattered light from entering the monochromator and ensures transmission of the scattered light into the monochromator. Alternative solutions to suppress the laser line are an interference filter or a

pre-monochromator. Compared to a notch or interference filter, a pre-monochromator is flexible and can be continuously adjusted to the applied excitation wavelength. In Figure 3.2, the monochromator (McPherson Model 2062) is a Czerny-Turner spectrometer with a 2.0-meter focal length. The first mirror in the back of the monochromator reflects the scattered light onto the grating where it is dispersed. In this work, a grating with 1800/mm and a resolution of 0.04 nm was used to measure Raman spectra of the group III-nitride films. The grating is interchangeable, allowing to vary the resolution and spectral range of the Raman spectrometer. The Raman spectrometer is equipped with a liquid nitrogen cooled charged-coupled device (LN/CCD) camera at the exit slit to detect the inelastically scattered light. The very low-level intensity of the scattered light requires long integration times and makes liquid nitrogen cooled CCDs an ideal detector. A custom LabVIEW program controls the rotation of the grating, captures the data from the CCD detector and displays the Raman spectrum as photocurrent intensity as a function of the frequency shift.

At TUB, fully integrated Raman systems are used for Raman spectroscopy. The LabRAM HR-800 Raman spectrometer by Horiba Jobin Yvon consists of a monochromator, a confocal microscope and a CCD detector. The Horiba-LabRAM system is equipped with two different excitation sources, a He-Ne-laser with an emission wavelength at 633 nm and a Nd:YAG laser with an excitation wavelength of 532 nm. The high-stability BX41 confocal microscope (Olympus) is coupled with the spectrometer system and has a revolving nosepiece to switch between objectives of 10x, 50x and 100x magnification. The microscope objective focusses the laser beam on the sample and also collects the Raman signal in a backscattering configuration. The LabRAM spectrometer has a much shorter monochromator (800 mm focal length spectrograph) compared to the 2m-monochromator at GSU. The shorter monochromator results in an increased light signal and thus requires shorter integration times. Similar to GSU setup, the commercial Raman systems utilize a corresponding notch filters to reject the selected laser excitation line and a grating as the dispersive element and. A spherical mirror in the spectrometer focuses the diffracted light onto a CCD. Raman spectra are measured with the 100x objective. The sample x-y-stage is fully motorized, enabling spatially resolved Raman mapping. In the scope of this work, micro-Raman map scans over an area of 10 µm x 10 µm were carried out to investigate the uniformity of InGaN epilayers with different compositions. Further Raman scattering experiments with an excitation at 458 nm are performed at a similar Horiba Raman spectrometer.

3.4 Tip-enhanced Raman spectroscopy

One present challenge in the growth of InGaN is nanoscale lateral compositional inhomogeneities at the growth surface. These phase separations can cause bulk phase segregations and reduction of the heterostructural quality. Another consequence of phase separations are fluctuations of the band gap energy. The suppression of these phase separation is difficult due to the different partial pressures of the constituents. The investigation of these nanoscale compositional inhomogeneities at the growth surface requires a nanoscale spatial resolution below the diffraction limit to correlate the chemical information with the morphological information.

Conventional Raman spectroscopy contributes a lot of information about the material properties such as crystalline ordering, stress and chemical composition, but the resolution *R* is restricted by the Abbe diffraction limit due to the usage of an optical microscope:

$$R = \frac{\lambda}{2NA}, \tag{3.2}$$

λ is the wavelength of the probing light and NA being the numerical aperture. The numerical aperture is a function of the refractive index n of the medium between lens and sample (typically air with n = 1) and α is half the angular aperture of the objective:

$$NA = n \cdot \sin\alpha. \tag{3.3}$$

For practical application, the resolution is approximately half of the excitation wavelength of the light source ≈ λ/2. In conventional Raman spectroscopy, the resolution limit is generally around 200 - 400 nm for visible light, which is not sufficient to distinguish nanostructures and/or nanoscale lateral compositional inhomogeneities in ternary InGaN alloys. A potential solution to study nanoscale fluctuations is the optical near-field technique tip-enhanced Raman spectroscopy (TERS). TERS combines Raman spectroscopy with the morphological characterization and high-spatial resolution (≈ 10 nm) of AFM to enable simultaneous determination of physical and chemical information at a nanoscale range far below the diffraction limit [79, 80].

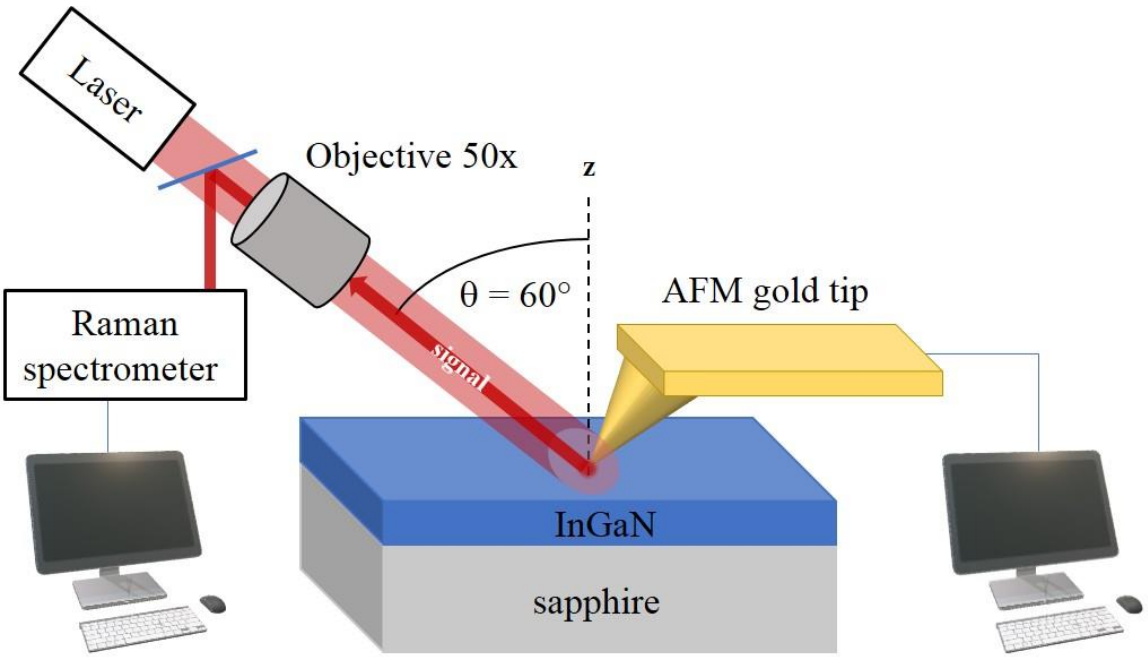

Figure 3.3: Schematic design of the experimental TERS setup.

Figure 3.3 schematically displays the experimental setup for TERS. The side illumination enables TERS on opaque samples such as group III-nitride alloys. Other configurations include the microscope below the sample or the use of parabolic mirrors [81].

In this work, the utilized TERS setup is a combination of two commercially available systems, the beforementioned AFM/STM Park XE-100 instrument and the LabRAM HR-800 Raman spectrometer (see previous sections 3.2 and 3.3). A three-stage system controls a long-distance microscope objective to couple the Raman spectrometer and the AFM/STM instrument. The objective has a magnification factor of 80x and is tilted in a 60 degrees angle with respect to the z-axis as depicted in Figure 3.3. The focus of the objective is on the cavity between tip apex and the sample surface in a confocal excitation and detection configuration. A He-Ne-laser at 632.8 nm is used to illuminate the bulk gold tip produced by electrochemical etching of a gold wire with a 50 µm diameter. The detailed procedure is described in references [82, 83].

An accurate description of the TERS principle, in particular, the interaction between near-field and material is not completely understood and still under discussion. In principle, the electromagnetic field of the incident laser light is locally confined to a nanoscale enhanced near-field at the tip apex. This enhanced electromagnetic field interacts with sample leading to local enhancement of the Raman near-field scattering from the sample. The tip-enhanced Raman scattered signal is converted back to the far-field and collected by the optics and CCD detector of a commercial Raman system [84]. Shi et al. describe the TERS mechanism based on the physical concept of optical antennas. In this concept the tip functions as an antenna that couples the far-field to the near-field at the tip apex. The tip-antenna converts the propagating electromagnetic wave of a laser source in the far-field to a localized and enhanced near-field and back to the far-field where it is detected. This article and other TERS review articles in recent years [79, 84-87] mostly mention two mechanisms generating the localized and enhanced electromagnetic near-field at the tip apex: (a) the excitation/interaction of localized surface plasmons (LSPs) and surface plasmon polaritons (SPPs) in metallic nanostructures and (b) the lightning rod effect.

First, the contribution mechanism of surface plasmon resonances is discussed. By illuminating the gold AFM tip, the photons of the incident laser light excite localized surface plasmons (LSPs) and surface plasmon polaritons (SPPs) at the tip apex due to its confined geometry on a nanoscale level. The quasiparticles LSPs and SPP coexist in the gold tip [84]. Considering the interaction of SPPs to the generation of the strongly confined and enhanced near-field is a quantum mechanical approach suggested by Poliani et al [88]. LSPs are non-propagating excitations of the conduction electrons of metallic nanostructures coupled to the electromagnetic field [89] and the confinement of LSPs by a curved nanostructure leads to significant electromagnetic enhancement. Efficient or optimally resonant excitation of the localized surface plasmons (LSPs) requires that the plasmon resonance wavelength (or frequency) of the tip material matches with the appropriate laser wavelength. Gold tips are used for an excitation wavelength of 633 nm. However, for excitation at 532 nm, silver tips have a better plasmon resonance than gold tips. Surface plasmon polaritons are surface electromagnetic waves, that arise due to the coupling between electromagnetic fields and oscillations of the conductor's electron plasma or in other words photons coupled to plasmons [89, 90]. SPPs have a dispersion relation and propagate along the surface in contrast to the non-propagating LSPs. They are generated by diffraction on a surface feature [90]. In the case of TERS, the tip apex represents a subwavelength metallic feature that breaks the surface translation symmetry of a planar interface and allows the generation of SPPs [91]. LSPs and SPPs interact in the following way. A SPP can be excited by the decay of a LSD and vice versa. Therefore, LSPs act as a localized point source for excitation and annihilation of SPPs [88].

The electromagnetic field associated with the SPPs has a strong evanescent electromagnetic field component perpendicular to the surface in the non-propagating direction [92] which corresponds to the aforementioned evanescent field. This evanescent field can be considered as a nanoscale light source [84]. Approaching a sample in very close vicinity of the tip causes an alteration of the evanescent field associated with the SPPs, enabling a new decay channel for the SPPs. In this new channel, the photon uncouples from the plasmon and tunnels inside the sample leading to an annihilation of the SPP. The photon tunneled into the sample interacts with a phonon and the emitted photon is detected in the far-field [88]. With the tip very closely approached to the sample, an enhanced Raman scattering is measured which is referred to as the near-field signal. The range of the enhanced evanescence field depends on the tip-surface distance and is very small (< 10 nm) [93, 94]. The confined electromagnetic near-field interacting with the sample surface is very different compared to the electromagnetic field of the incoming light source.
The lightning rod is an additional contribution to the enhancement due to the conical shape of the gold AFM tip. The tip represents a geometrical singularity and its illumination leads to an increase of the surface charge density. This results in spatial confinement and a strong enhancement [95, 96] of the electromagnetic field at the tip apex. Thus, the lightning rod effect influences the population of LSPs and subsequently SPPs. It is a non-resonant effect because it depends on the geometries of a sharp metallic tip [85, 97].

The experimental TERS procedure is as follows. After the optical alignment of the laser focus on the tip, only the sample is moved to measure a topographic image of the sample surface. Based on topographic overview a region of interest is selected for TERS measurements. The TERS measurements are performed in the AFM tapping mode feedback to avoid damage of the tip and to control the tip-surface distance to enable signal enhancement. As mentioned before the range of the enhanced field is very small. The evanescent field decays exponentially in all directions resulting in a high lateral resolution of a few nanometers. The incident light is not entirely focused on the tip but also on the sample surface generating a far-field Raman signal. In this case, the obtained signal consists of a near-field and a far-field component. By retracting the tip from the sample the evanescent field and subsequently the tip-enhanced signal disappears leaving the far-field signal. The subtraction of the spectrum with the tip retracted from the tip-engaged spectrum results in the pure tip-enhanced near-field Raman spectrum.
In comparison to far-field Raman spectroscopy that detects Raman-active modes in a ‘large’ volume, near-field Raman scattering in TERS only measures the top few monolayers due to its high-resolution in the nanoscale range. The enhancement in TERS depends on multiple experimental factors such as tip geometry, the sample material and the tip-sample distance for example. Another factor that is often mentioned is the incoming light polarization, though it has been shown that the enhanced near-field Raman signal is largely independent of light polarization due to a breakdown of the far-field Raman selection rules for TERS [88]. The geometry of the tip has a crucial role in the enhancement and the resolution making it difficult to reproduce TERS measurements. On the other hand, an interlaboratory study by different research groups demonstrated suitable reproducibility and comparability of TERS measurements [98]. Further challenges in TERS are the drift of the sample and thermal drift of the focus spot due to warming up of the laser.
However, TERS is on the way to be an established characterization method for the investigation on a nanoscale level.

3.5 Scattering-type scanning near-field infrared nanoscopy

Another technique to investigate nanoscale lateral inhomogeneities is the scattering-type scanning near-field infrared nanoscopy (s-SNIN). Similar to TERS, s-SNIN utilizes the high-spatial resolution of an AFM tip in simultaneous combination with chemical identification. The apex of the AFM metal tip is in the range of a few nanometers (10 - 15 nm), resulting in a high-spatial resolution far below the diffraction limit, which is required to study local nanoscale compositional fluctuations.

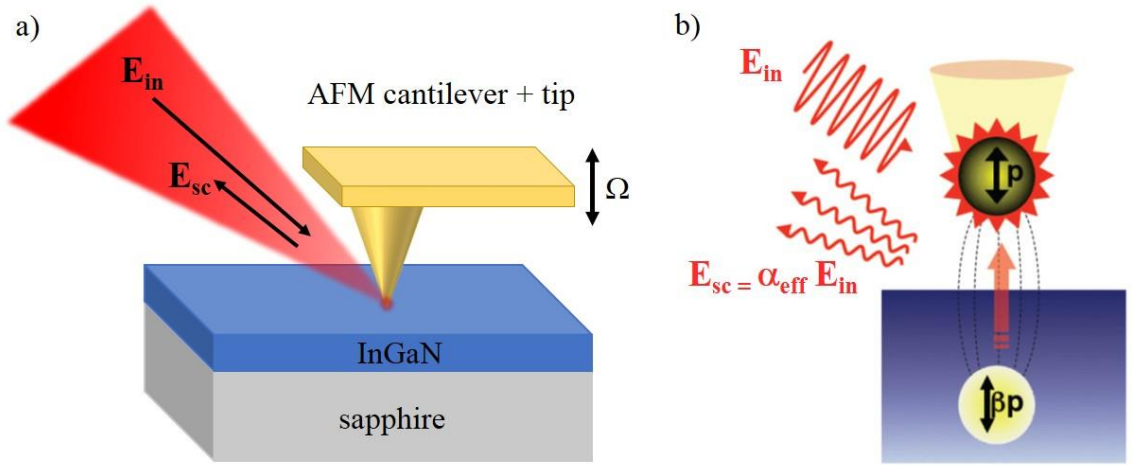

Figure 3.4: Schematic illustration of the s-SNIN experimental setup. IR laser illuminates vibrating AFM tip (a). Due to the interaction between tip-dipole and sample-dipole interaction the tip-scattered light is altered (b).

Figure 3.4a displays the principle of s-SNIN. A focused infrared (IR) laser beam ($\lambda = 10.5$ µm) illuminates the platinum-iridium (PtIr) coated AFM tip, which oscillates at the cantilever's resonance frequency Ω during a topographic scan. The angle of incidence is 45° with respect to the sample surface. The metallic-coated tip serves as an IR antenna and converts the incident radiation into a nanolocalized and enhanced near-field at the tip apex. The presence of the sample surface affects the enhanced near-field. As depicted in Figure 3.4b, the electromagnetic wave induces an electric dipole field along the metal tip, which itself induces an image dipole on the sample surface. The image dipole contains information of the dielectric constant of the surface material. Consequently, the near-field interaction between tip dipole and image dipole leads to an alteration of the scattered IR light. Due to the vibration of the AFM tip, the near-field scattering is modulated at harmonics of the tip resonance frequency $n\Omega$ (where $n > 1$), allowing electronic filtering against the background scattering [99]. Thus, the scattered light contains local information about the optical properties of the sample surface. The scattered light from the tip-surface interface is measured by an interferometric detection system in the far-field, imaging the IR near-field amplitude and phase of the optical contrasts correlated to the dielectric function of the sample material. Therefore, s-SNIN enables simultaneous profiling of the sample's chemical composition combined with its surface morphology on a nanoscale map [100].

3.6 X-ray diffraction

X-ray diffraction (XRD) is a non-destructive characterization tool to evaluate structural layer properties such as crystalline ordering, strain, defect densities and phase composition. XRD is based on the Bragg diffraction, which describes the diffraction of light or an electromagnetic wave respectively, from a periodic structure such as atoms in a crystal lattice. To interact with the atoms, the wavelength of the incident electromagnetic wave has to be in the same order of magnitude as the interatomic spacing *d* between adjacent lattice planes. In solid crystals, the distance between adjacent lattice planes is in the angstrom range, which requires eligible wavelengths from the X-ray spectrum. X-ray radiation exhibits a high penetration depth and can probe a large volume of the crystal. Typically, a diffractometer utilizes a monochromatic X-Ray radiation source.

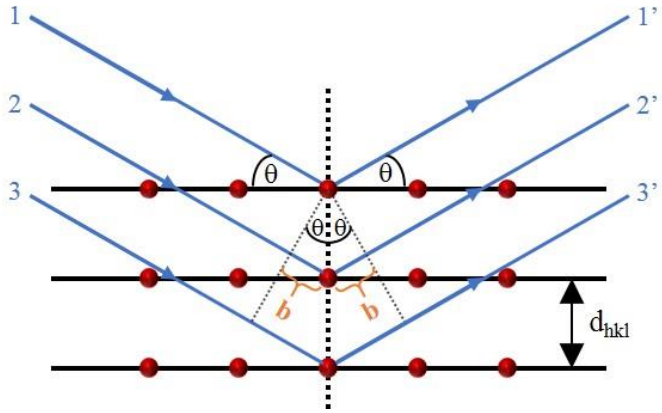

Figure 3.5: Schematic depiction of the relationship between Bragg diffraction and the crystal lattice. Adapted from reference [101].

Figure 3.5 schematically illustrates the Bragg diffraction in a periodic crystal structure. The incident X-rays are scattered at different atomic planes of a crystal. Constructive interference produces a diffraction pattern corresponding to the atomic arrangement of the crystal structure. The geometric conditions for constructive interference are also depicted in Figure 3.5. The path-length difference between beam 1 and 2 is twice the phase shift *b*. To constructively interfere, the path-length difference must be an integer multiple of the incident wavelength λ:

$$2 \cdot b = n \cdot \lambda \,, \tag{3.4}$$

where n is the order of diffraction. Using the geometric relations, the phase shift *b* can be expressed by the incident (reflection) angle θ and the interplanar spacing d_{hkl} of two adjacent lattice planes:

$$b = d_{hkl} \cdot \sin(\theta) \,. \tag{3.5}$$

Substituting equation (3.5) into equation (3.4) results in Bragg's law [102]:

$$n \cdot \lambda = 2 \cdot d_{hkl} \cdot \sin(\theta) \,. \tag{3.6}$$

Constructive interference of monochromatic X-rays only takes place at particular angles of the incidence.
In this study, a high-resolution X-ray diffractometer (PANalytical X'Pert PRO MRD) was used to investigate the structural quality and composition of the InGaN films with the copper Cu K_α wavelength = 1.54184 Å as the X-Ray radiation source. Due to the high sensitivity, the $\omega - 2\theta$ operation mode is very suitable to measure the lattice constant and provides information about the composition and strain. Figure 3.6 depicts the scan geometry in the high-resolution XRD. In general, the angle of incidence with respect to the normal of the sample is denoted as ω. In the $\omega - 2\theta$ operation mode a signal is only detected when the Bragg condition is satisfied. The separation of the Bragg diffraction peaks corresponding to the substrate and the InGaN film in a symmetric (00.2) Omega - 2theta ($\omega - 2\theta$) scan allows determining the composition of the InGaN layers [103].

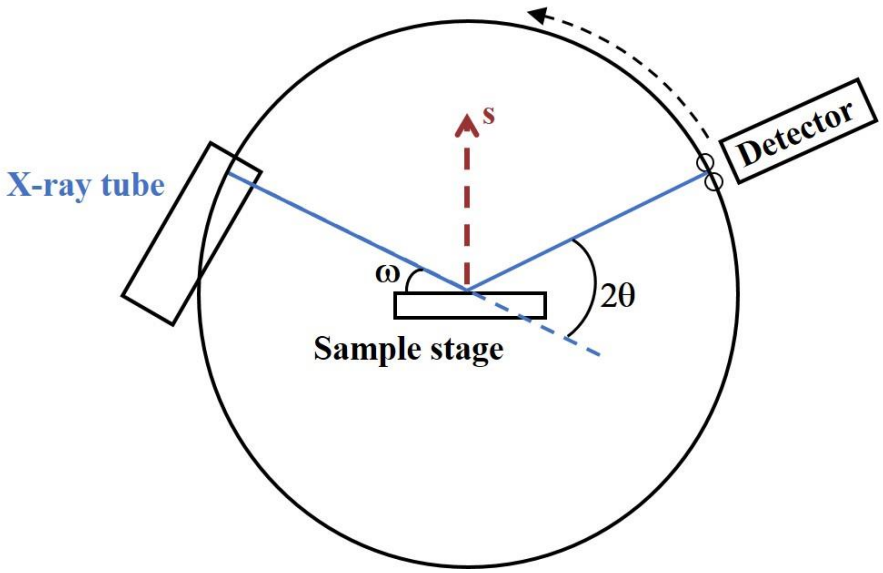

Figure 3.6: Scan geometry in HR-XRD. S represents the scattering vector.

4 Crystal growth techniques for the fabrication of group III-nitrides

4.1 Epitaxy and challenges of group III-nitrides growth

Various growth methods for group III-nitrides have been developed and established. This chapter gives an overview about epitaxy in general and follows with a brief description of the epitaxial growth processes for the deposition of GaN, InN, AlN films and their ternary alloys such as InGaN and AlGaN. The major growth techniques are Metalorganic Chemical Vapor Deposition (MOCVD), Superatmospheric MOCVD, Hydride Vapor Phase Epitaxy (HVPE), Molecular Beam Epitaxy (MBE) and Atomic Layer Deposition (ALD). MOCVD, MBE, and ALD are also discussed as plasma-assisted growth techniques. The mentioned growth techniques vary significantly in growth temperature regimes and operate at vastly different reactor pressures ranging from the superatmospheric to very low pressures in the ultra-high vacuum (UHV) range. Furthermore, the growth processes differ in their device and industrial relevance.

Sections 4.2 - 4.6 describe the reactor design, growth procedure and parameters for each of the previously mentioned growth techniques. The different growth process possesses distinct advantages which promote distinct properties of the grown crystal. Important layer properties such as crystal quality and deposition rate (film thickness respectively) as well as the drawbacks of each growth techniques are discussed.

Epitaxy derives from the combination of the two Greek words epi and taxis, meaning above/on and ordered arrangement, respectively. Translated to crystal growth it stands for the overgrowth of an ordered and oriented crystalline structure on another substrate crystal surface. The process of depositing an epitaxial layer on a substrate of the same chemical composition is named homoepitaxy. The advantage of homoepitaxial growth is a lower defect density and doping control due to the lattice match, thermal match and same surface chemistry. In contrast, the deposition of a crystalline layer on a substrate which is a different material, is denoted as heteroepitaxy. Bandgap engineering and optoelectronic structures, such as InN/GaN heterostructures, in which the InN/GaN interface is a p-n heterojunction and can realize a 2-dimensional electron gas (2DEG), requires heteroepitaxy for example.

The growth conditions such as temperature, precursor ratio as well as substrate have a strong influence on the morphology and the structure of the epitaxially grown layers. Depending on these growth parameters, the growth process can follow different growth modes, which results in different structures and morphologies of the deposited epilayers. In general, the homo- or heterogenous growth of a thin film on a substrate can follow three main growth modes depending on the growth temperature, the lattice mismatch between layer and substrate, the supersaturation of the crystalline phase and the adhesion energy. Figure 4.1 illustrates the three growth modes, which are (a) layer-by-layer (or Frank van der Merwe) [104], (b) layer-plus-island (or Stranski-Krastanov) [105] and (c) island growth (or Vollmer-Weber) [106]. The growth of epitaxial layers depends on the interaction between adatoms and the surface. The growth modes are distinguished by considering the composition of the free energies of the film, substrate and the interface.

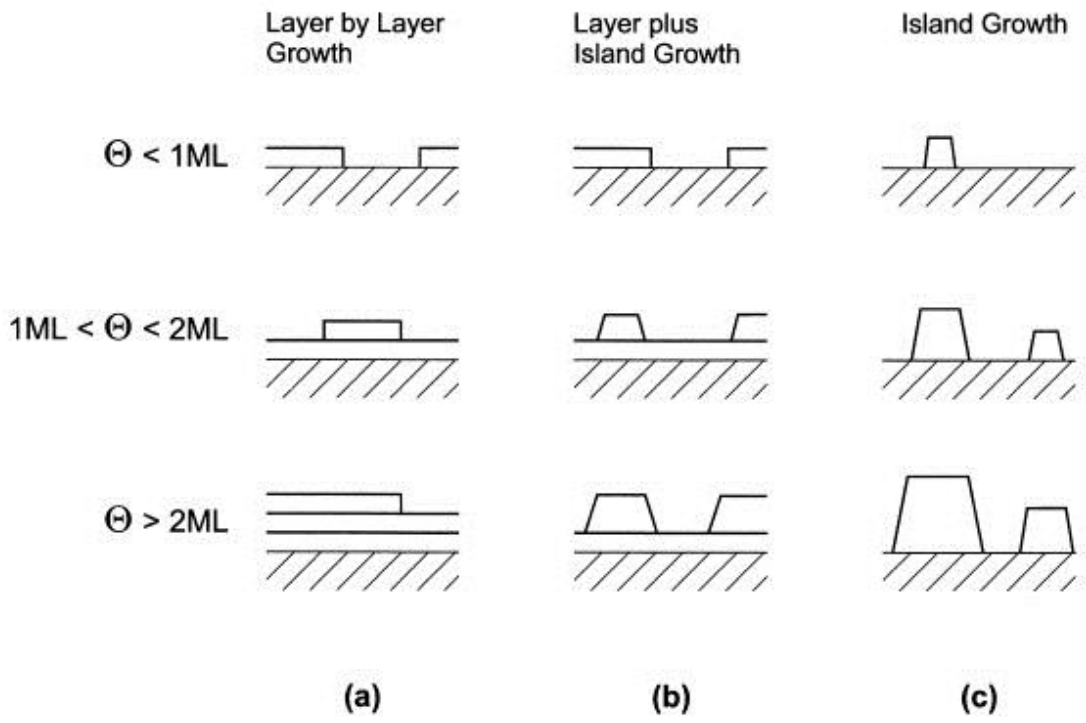

Figure 4.1: Schematic illustration of general growth modes [107]: layer-by-layer or Frank-van der Merve, FM (a), layer plus island or Stranski-Krastanov (b) and island or Vollmer-Weber (c).

In case of the layer-by-layer growth mode (Figure 4.1a), the interaction between layer adatoms and surface is stronger than between adjacent adatoms and the lattice mismatch between substrate and deposited material is relatively small. The sum of the layer and interface free energy is smaller than the substrate free energy [107].

$$\Delta\sigma = \sigma_l + \sigma_i - \sigma_s \leq 0 \tag{4.1}$$

with free energy $\sigma_{l,i,s}$ ... layer, interface, substrate.

This condition favors complete wetting of the substrate or previous layer, respectively. Due to the preferred adsorption at the surface, a smooth and complete layer with uniform thickness is formed. The formation of the subsequent layer starts after the completion of the previous layer. Therefore, layer-by-layer growth is two-dimensional (2D).
For island growth (Figure 4.1c), the interaction between neighboring adatoms is stronger than the interaction of adatoms with the surface in contrast to layer-by-layer growth. This leads to the aggregation of atoms and subsequently to the formation of three-dimensional (3D) clusters or islands. Vollmer-Weber or island growth occurs when $\Delta\sigma > 0$. The islands can grow until the substrate is fully covered. These layers show a rougher surface morphology compared to films grown by the layer-by-layer mode.
The layer plus island or Stranski-Krastanov growth is a combination of the layer-by-layer and island growth mode. This growth mode occurs in case of a significant lattice mismatch, but a strong adhesion between surface and deposited material. Because of the strong adhesion, $\Delta\sigma$ stays below zero and one or a few monolayers are formed by layer-by-layer growth until a certain thickness is reached. The critical thickness highly depends on the free energies and lattice parameters of the layer and the substrate. With increasing thickness, the layer free energy

increases linearly, and the lattice mismatch causes a gradual accumulation of internal stress. When the critical thickness is reached, the internal strain energy compensates the surface-species interaction. $\Delta\sigma$ becomes larger than zero and the growth mode changes from 2D layer to 3D island growth. In Figure 4.1b, the island formation starts after the completion of one monolayer. The growth of semiconductor nanostructures such as quantum dots occurs under Stranski-Krastanov growth mode for example [108].

4.2 Hydride Vapor Phase Epitaxy (HVPE)

In general, HVPE utilizes hydrides, such as ammonia and halides as group III precursors to synthesize group III-nitride alloys. HVPE systems consist of a quartz reactor with a multiple zone furnace as a heating system. HVPE reactors can be either in a horizontal or vertical design.

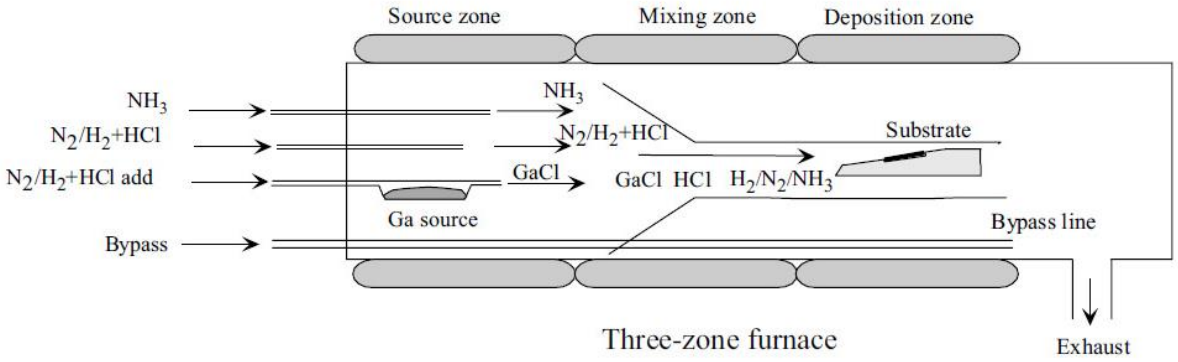

Figure 4.2: Schematic layout of a three-zone HVPE reactor for GaN growth [109].

Figure 4.2 displays a schematic diagram of a horizontal three-zone HVPE reactor for GaN growth. The first zone in a three-zone furnace is the source zone, which contains the metal source. In the center zone, the gases are homogeneously mixed and transferred to the deposition zone where the substrate is located. All zones are kept at different temperatures enabling independent control of the partial pressures of the precursors. In the source zone at temperatures between 800 - 900°C, hydrogen chloride (HCl) passes over a liquid metal Ga source through a quartz tube and forms the halide GaCl:

$$2\mathrm{Ga}(\mathrm{l}) + 2\mathrm{HCl}(\mathrm{g}) \rightarrow 2\mathrm{GaCl}(\mathrm{g}) + \mathrm{H}_2(\mathrm{g}). \tag{4.2}$$

An inert carrier gas, typically N_2, H_2, Ar or their mixtures, transports the GaCl to the deposition zone. A separate quartz line supplies ammonia directly to the reactor chamber to prevent parasitic growth reactions between GaCl and the ammonia. For GaN, the growth temperature range in the deposition zone is between 950 - 1150°C, which is comparable to MOCVD growth. The following thermodynamic growth reactions describe the formation of GaN. The growth reaction is close to thermal equilibrium, similar to MOCVD:

$$\mathrm{GaCl}(\mathrm{g}) + \mathrm{NH}_3(\mathrm{g}) \Leftrightarrow \mathrm{GaN}(\mathrm{s}) + \mathrm{HCl}(\mathrm{g}) + \mathrm{H}_2(\mathrm{g}). \tag{4.3}$$

Industrial and laboratory reactors have multiple reactor zones. The additional zones can be used for doping or as another metal source to form ternary group III-nitride alloys. The thermal

stability and high purity of halides (chlorides) enable high growth rates up to 100 µm/h and high crystal quality. GaN boules thicker than 6 mm are grown by vertical HVPE [110]. HVPE is a well-understood and developed growth technique with large scale manufacturing of GaN templates, which are used to produce group III-nitride laser. The drawback of the high growth rates is the difficulty to control the film thickness using HVPE. The growth of layer structures with sharp interfaces and very thin quantum wells, which are necessary for LED production are not possible and make HVPE not suitable for device production. Other drawbacks of HVPE are the high dislocation density, large gas consumption, and hazardous by-products such as NH_4Cl which condense and clog the exhaust [18]. HCl is a side product of the reaction between GaCl and ammonia and is a highly corrosive gas, which can degrade the reactor equipment. HVPE of InN utilizes indium trichloride ($InCl_3$) instead of indium chloride (InCl). The growth reaction between $InCl_3$ and ammonia is more effective than InCl [111] because the equilibrium constant of the reaction between $InCl_3$ and NH_3 is higher than the equilibrium constant between InCl and NH_3 [112]. AlN growth by HVPE using AlCl as a precursor is difficult because it reacts with the hot quartz walls of the HVPE reactor and causes damage of the quartz [113]. An alternative is aluminum trichloride ($AlCl_3$) because it is less reactive with quartz in the source zone. Conventional HVPE of AlN on sapphire using $AlCl_3$ has been successfully demonstrated [112].

4.3 Molecular Beam Epitaxy (MBE) and plasma-assisted MBE

In contrast to MOCVD and HVPE, molecular beam epitaxy is a non-thermodynamic equilibrium growth method, in which the surface reaction kinetics determine the growth process.

In MBE, the growth reactions take place under high vacuum or ultra-high vacuum (UHV) with a base pressure of 10^{-10} Torr or less, while the operating reactor pressure range is between 10^{-6} - 10^{-9} Torr. In an UHV environment, the mean free path length of the particles exceeds the geometric dimensions of the reactor chamber minimizing the interaction between particles. Another advantage of UHV is the reduced incorporation of impurities during growth. Effusion (or Knudsen) cells supply the metal precursors by evaporation. The evaporated atoms and molecules form a molecular beam with the heated substrate as the target. Due to UHV, the molecules (atoms) transit ballistically to the growth surface without collision. Therefore, the utilization of a carrier gas is not required. Each metal precursor is contained and heated in a separate cell. The effusions cells containing the metalorganic precursors as well as the doping material are aligned at the substrate as depicted in Figure 4.3. The nitrogen supply is via a gas source such as nitrogen or ammonia. The precursor beams impinge on the heated substrate surface, where the atoms or molecules are adsorbed. The atoms move on the surface due to diffusion until they bond to the surface at a thermodynamically favorable site, whereas molecules dissociate. The substrate is rotated to improve the homogeneity.

The UHV allows in-situ monitoring with reflection high-energy electron deflection (RHEED), which is the most popular analysis technique. As depicted in Figure 4.3, the RHEED electron gun directs electrons/electron beam on the epitaxial surface of the sample at a very small angle (< 3°). A phosphor screen detects the diffracted electrons. Only the top atoms of the epitaxial sample surface diffract the incident electrons. The diffracted electrons interfere constructively at specific angels depending on the positions of the atoms at the surface. The interference pattern contains direct information about the state of the growth surface and enables accurate growth control at a monolayer level.

MBE operates at lower growth temperatures compared to MOCVD by providing highly reactive precursor species. Mechanical shutters can quickly activate or shut down the molecular beams enabling the growth of abrupt and sharp interfaces, which is another benefit of MBE.
Plasma-assisted MBE (PAMBE) consists of a conventional MBE growth chamber combined with a nitrogen plasma source such as an electron cyclotron resonance (ECR) source or radio-frequency plasma source. The plasma source replaces an effusion cell (see Figure 4.3). The plasma source dissociates the nitrogen molecules to form reactive nitrogen precursor species. PAMBE of device-quality nitride structures occurs at much lower temperatures (by 200 - 300°C) compared to MOVPE [114]. PAMBE growth temperature ranges for GaN and InN are 650°C to 750°C [18, 115, 116], and 450 to 550°C [117], respectively.

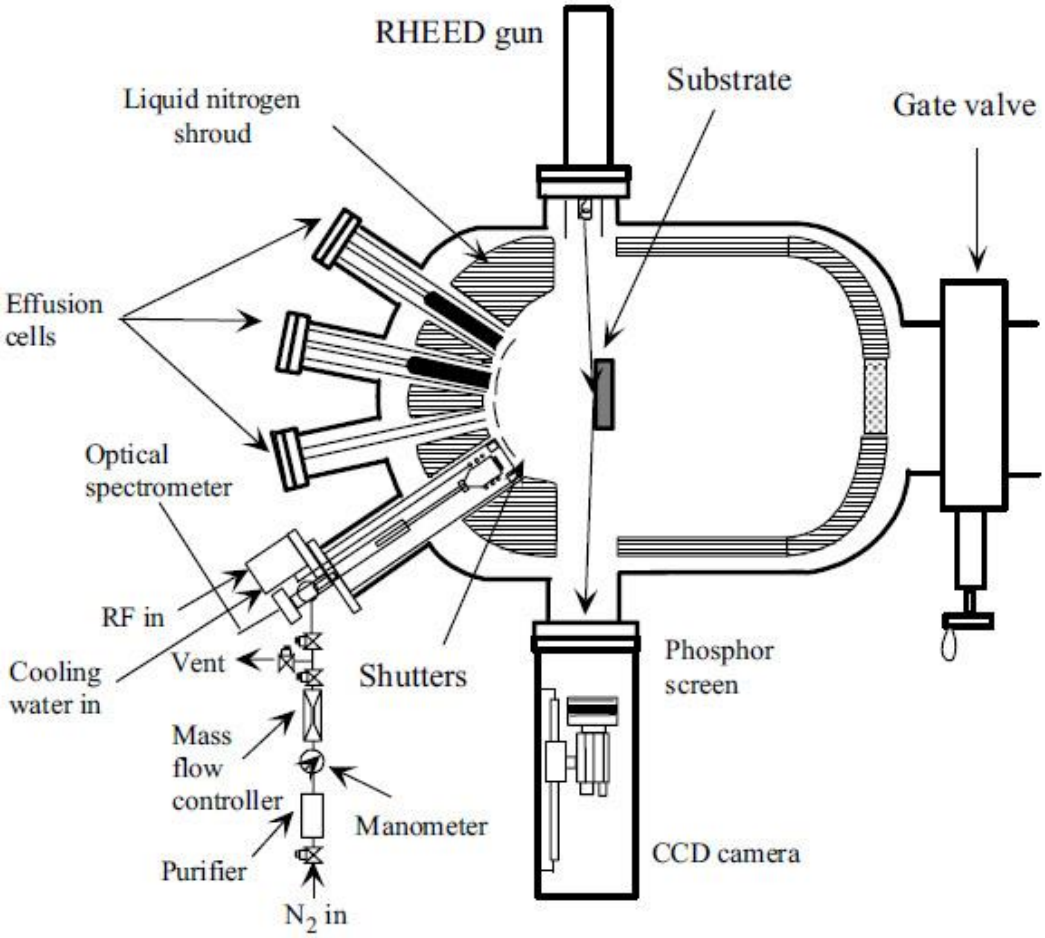

Figure 4.3: Schematic view of a PA-MBE reactor chamber [18].

A drawback of MBE compared to MOCVD are the low growth rates, commonly between a few hundred nanometers up to one micrometer per hour, though growth rates above two micrometers per hour (2.6 µm/h) have been reported [116, 118]. Also, the operation of the MBE reactor under UHV conditions is expensive and limits MBE for mass production and commercial use.

4.4 Atomic Layer Deposition (ALD) and plasma-enhanced ALD

The principle of Atomic Layer Deposition has two origins. In the 1960s proposed under the term ‘molecular layering’ by Aleskovskii and Kol’tsov. The second origin is from Finland by Suntola et al. in 1977 introducing the process as Atomic layer Epitaxy [119].
Atomic layer deposition is a vapor phase deposition technique for the fabrication of thin films. Figure 4.4 illustrates a schematic of an ALD process in general. The precursors for each element are pulsed in an alternating sequence. In contrast to conventional MOCVD, only a single gaseous precursor at a time is injected into the reactor and reacts with the substrate. This self-terminating gas-solid reaction is called ‘half-reaction’ [120]. The selected duration of the precursor pulses provides sufficient reactive fragments to saturate the substrate surface after a fully adsorption and formation of no more than one monolayer at the growth surface. This growth mechanism is called a self-limiting process. For the removal of any volatile by-products and excess precursors, the substrate surface is subsequently purged with an inert carrier gas (typically N2 or Ar). Therefore, one process cycle consists of at least four steps. One layer of the desired material requires one complete cycle. The process steps repeat until the desired film thickness is reached. ALD requires lower temperatures in comparison to MBE and MOCVD because the adsorbed atoms have a longer surface reaction time to find the lattice position which results in better crystal quality of the deposited film]. ALD enables thickness control by deposition of precise atomic layers with a sub-angstrom resolution [121], tunable film composition with high film uniformity as well as conformality based on the sequential and self-limiting half-reactions. The drawback of the layer by layer process is the significantly lower growth rates in comparison to MOCVD [122, 123].

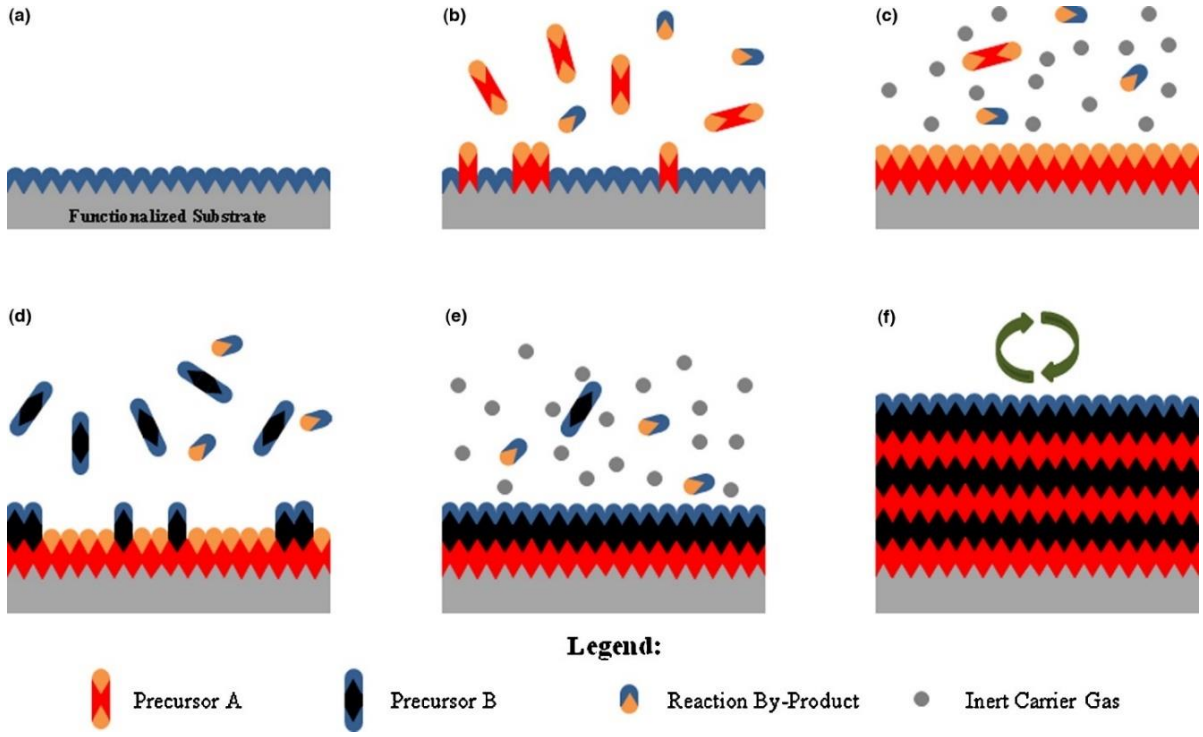

Figure 4.4: Schematic of ALD process steps: (b) Precursor A is pulsed and reacts with surface. (c) Purge of excess precursors A and volatile by-products with inert carrier gas. (d) Precursor B is pulsed and reacts with surface (e) Purge of excess precursors B and volatile by-products with inert carrier gas. (f) Cycle of sequence steps b-e are repeated until desired material thickness is achieved.

The introduction of plasma-assisted ALD (PA-ALD) or plasma-enhanced ALD (PE-ALD) enables growth at reduced substrate temperatures [123]. A plasma source delivers high reactive species to the growth surface and therefore, less thermal energy is required. In PE-ALD, the substrate is exposed to plasma generated species in one half-reaction. Equivalent to Figure 4.4, the plasma reactants would be precursor B. In the recent years, the group III-nitride binaries AlN, InN and GaN as well as ternary InGaN have been grown successfully in the growth temperature range between 180 - 350°C by Hollow cathode plasma-assisted ALD (HCPA-ALD) [121, 124, 125].

4.5 MOCVD

Metalorganic chemical vapor deposition (MOCVD), also referred to as Metalorganic vapor phase epitaxy (MOVPE) is a widely used growth method in the industry for the fabrication of group III/V compound semiconductors. Industrial MOCVD systems are designed for commercial mass manufacturing and high productivity. For example, Veeco's EPIK 868® MOCVD system accommodates 124 x 4-inch wafers for the mass production of GaN based LEDs, lowering the manufacturing cost per wafer by 20% compared to previous reactor generations [126].
First published in 1968, Manasevit reported epitaxial growth of Gallium arsenide (GaAs) utilizing MOCVD. Unlike MBE, MOCVD uses gaseous metalorganic precursors. Standard metalorganic precursors are trimethylgallium (TMG), trimethylindium (TMI) and trimethylaluminum (TMA). Ammonia is typically used as the nitrogen precursor.
In conventional MOCVD, the growth process of group III-nitrides relies on vapor transport of metal organic precursors and ammonia to a heated substrate. The MO possess a relatively high vapor pressure that allows transport to the substrate via a carrier gas. Chapter 5 provides a detailed description of the vapor transport, the control mechanism of the precursor supply and the pyrolysis of the metalorganic precursors which is identical in MOCVD and plasma-assisted MOCVD.
MOCVD of group III-nitrides occurs at similar temperatures as HVPE, but higher than compared to MBE. The reactor pressure range in MOCVD is between 1 - 700 millibar to provide laminar flow conditions. Because the growth of semiconductor compounds is not conducted under UHV conditions as in MBE, MOCVD requires extremely high purity of all the involved gases and chemicals.

There are two major types of MOCVD reactors, the horizontal flow channel and the vertical closed coupled showerhead (CCS) reactor. Figure 4.5 shows a schematic diagram of a MOCVD reactor. The most important parts of a MOCVD reactor are the gas injection inlets for the metalorganic and nitrogen precursors, a heating element and a rotating susceptor (wafer carrier). The reactor chamber walls are water-cooled to avoid overheating.

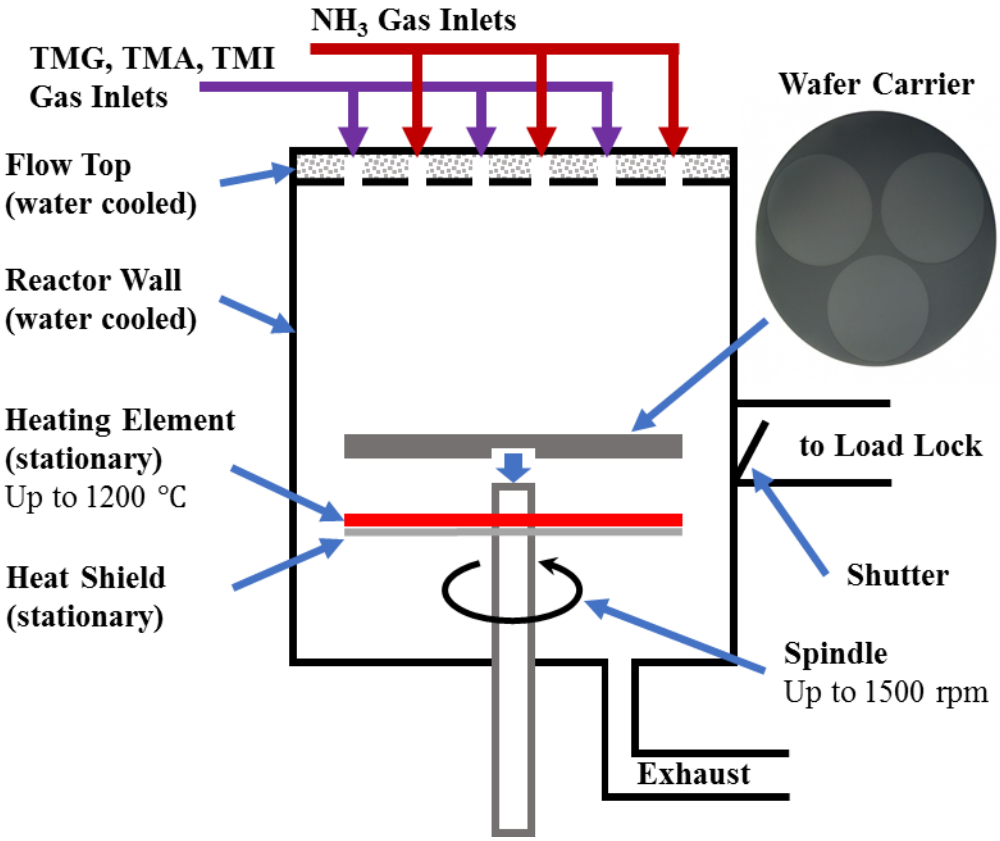

Figure 4.5: Schematic diagram of a MOCVD reactor used at Georgia State University.

In MOCVD, the growth takes place under near-thermodynamic equilibrium conditions in contrast to MBE. A heater under the substrate susceptor (wafer carrier) enables the conditions for a. The Metalorganic precursors are delivered into the reactor via vapor transport by a carrier gas such as hydrogen (H_2), nitrogen (N_2) or Argon (Ar). The ammonia is directly supplied into the reactor chamber. MOCVD growth process is the decomposition of the precursors above the heated substrate surface and consists of several steps. The decomposition process of a showerhead MOCVD is depicted in Figure 4.6 and can be basically divided into a thermodynamic, kinetic, hydrodynamic and mass transport component.

In a closed coupled showerhead reactor, the showerhead flange is very close to the substrate. The MO precursors and the ammonia are injected vertically into the gas phase. The small holes of the showerhead ensure a uniform distribution of the MO and ammonia. In the gas phase is a mixture of precursors and carrier gases. The carrier gas has an important role because it determines the hydrodynamics of the gas phase. In Figure 4.6, TMG or $(CH_3)_3Ga$ is used as the metalorganic precursor. A stationary boundary layer forms along the substrate surface, separating the substrate surface from the reactant gas flux. In the next step, the precursors diffuse through the boundary layer towards the substrate surface (mass transport). During the diffusion, the precursors decompose partially and totally by pyrolysis [127].

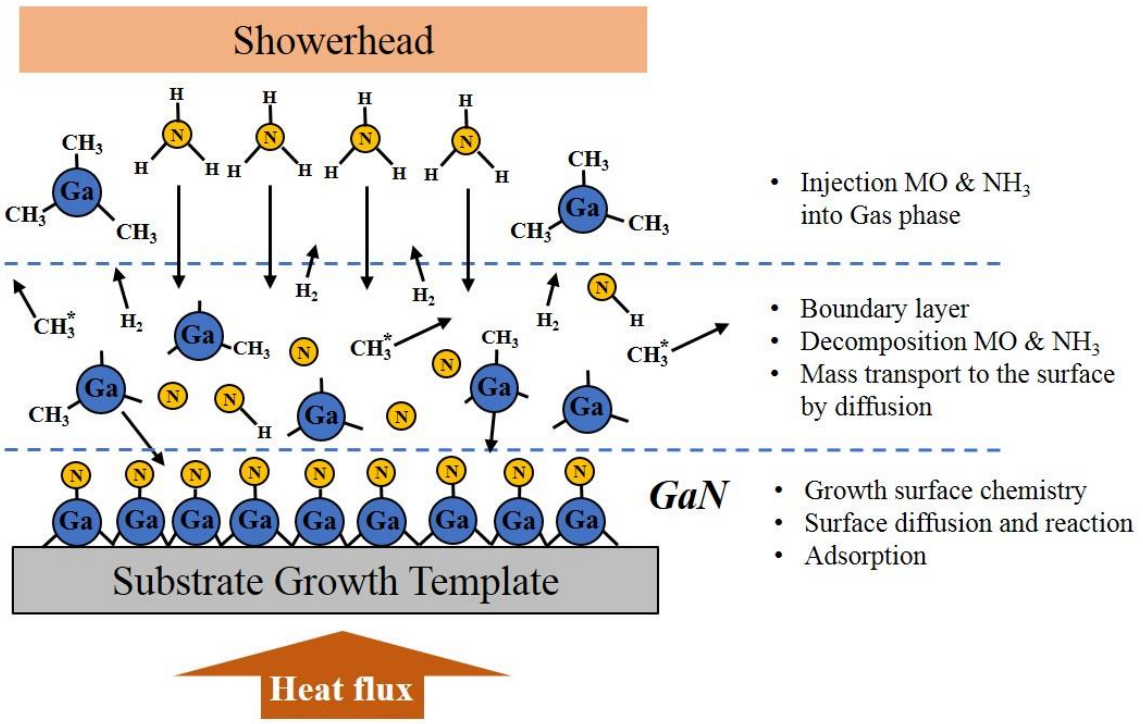

Figure 4.6: Schematic drawing of the MOCVD growth process in a vertical flow system.

Surface kinetics describe the epitaxial process. These kinetic processes on the surface are adsorption, diffusion, surface reactions and incorporation. The species can either react with the surface as well as other surface species or desorb. Adsorbed group III metal atoms are mobile and move kinetically across the surface (diffusion) until they are incorporated. The metal can either react with nitrogen, become immobile and form new nuclei or find a potential minimum like a step. In Figure 4.6, the Ga-atoms and the nitrogen atoms bond and form a crystalline layer at the substrate surface. The growth (deposition) is a reversible equilibrium reaction, and the kinetics describe at which rate. If the system is a non-equilibrium state, the thermodynamic driving force tends to restore the equilibrium by driving the system to a phase transition from vapor into solid resulting in the deposition of the desired crystal [128]. The amount to restore the equilibrium (supersaturation) corresponds to the maximum quantity of the crystallized solid or growth rate, respectively. The driving force of the reaction is defined by the thermodynamics and controls the direction of the overall growth process reaction. It can be quantitatively expressed by the Gibbs free energy:

$$\Delta G = -RT\ln(1+\sigma), \tag{4.4}$$

with σ as the supersaturation, that can be expressed by normalizing the input partial pressure of Ga and the equilibrium vapor pressure of Ga as following:

$$\sigma = \frac{P_{\mathrm{Ga}}^{0} - P_{\mathrm{Ga}}}{P_{\mathrm{Ga}}}, \tag{4.5}$$

with P_{Ga}^{0} as the input partial pressure of Ga species and P_{Ga} is the equilibrium vapor pressure of Ga.

The simplified growth chemistry reaction at the vapor-solid interface is [129]:

$$\mathrm{Ga(g) + NH_3(g) \leftrightarrow GaN(s) + \frac{3}{2} H_2(g)} \tag{4.6}$$

with corresponding equilibrium constant: $K_{GaN} = \frac{a_{GaN} P_{H_2}{}^{3/2}}{P_{Ga} P_{NH_3}}$,

where a_{GaN} is the activity of GaN, P_{Ga} is the equilibrium vapor pressure of Ga, P_{H_2} and P_{NH_3} are the partial pressures of H_2 and NH_3.

Intentionally creating and maintaining the supersaturation ensures the proceeding of the crystal growth. Supersaturation is a measure for the magnitude of the deviation from the thermodynamic equilibrium and is more suitable than the V/III ratio to evaluate the growth by MOCVD. In the case of the GaN growth reaction, the driving force depends on the partial pressure of hydrogen to drive the reaction towards GaN in terms of supersaturation. Since hydrogen is a by-product of the GaN growth reaction, using hydrogen as a carrier gas has an influence on the equilibrium of the chemical reaction. Therefore, the choice of carrier gas influences the supersaturation [130].

However, the role of hydrogen during the InN deposition is different. The equilibrium constant K of InN is rather small compared to the equilibrium constant of GaN. Considering the InN growth reaction which is analog to the GaN growth reaction [131]:

$$\mathrm{In(g) + NH_3(g) \leftrightarrow InN(s) + \frac{3}{2} H_2(g)}, \tag{4.7}$$

an increase of hydrogen leads to a decrease of the driving force and drives the reaction to the left resulting in a decreased InN deposition. Furthermore, hydrogen influences the vapor-solid interface and affects the inhomogeneous composition during the $In_xGa_{1-x}N$ deposition [130]. InN and InGaN growth require nitrogen or a mixture of nitrogen and hydrogen as carrier gas. Adsorbed species which are not incorporated desorb. Gaseous by-products and CH_3-radicals diffuse back through the boundary layer into the laminar main flow away from the growth zone to the exhaust. Incomplete decomposition of the precursors makes the reactions during the growth more complex. Carbon, hydrogen and adducts of the methyl- and ethyl groups are present above growth surface and can be incorporated, which results in non-intentional doping. During the MOCVD growth process, all these steps occur simultaneously. The process steps adsorption, desorption and the surface kinetics depend mainly on the temperature above the substrate surface as well as the precursor flow rates.

The temperature dependence of the growth rate is differentiated into three regimes as shown in Figure 4.7. At low temperatures, the kinetics of the chemical reactions in the gas phase and on the substrate surface limit the growth. Additionally, the thermal decomposition rate of the precursors is less at lower temperatures. This region (I) is kinetically limited. With increasing growth temperature, the cracking of the precursors at a given precursor injection becomes more efficient and the growth rate increases. At some temperature point, all the precursors are decomposed, and the growth rate is constant. In this intermediate temperature section (II), the diffusive mass transport across the boundary layer is independent of the growth temperature. The growth reaction proceeds fast enough, and the and growth rate depends on the transport

rate of the precursor species to the growth surface. The system has a large supersaturation and is in a near thermodynamic equilibrium condition [127]. The growth rate is mass-transport limited in the intermediate temperature range and can be controlled by the precursor input flux. In the third part (III), the growth rate reduces with increasing temperature, because the desorption increases. At high temperatures, the desorption process overtakes the adsorption, and thermal etching dominates instead of deposition. The growth rate is thermodynamically limited.

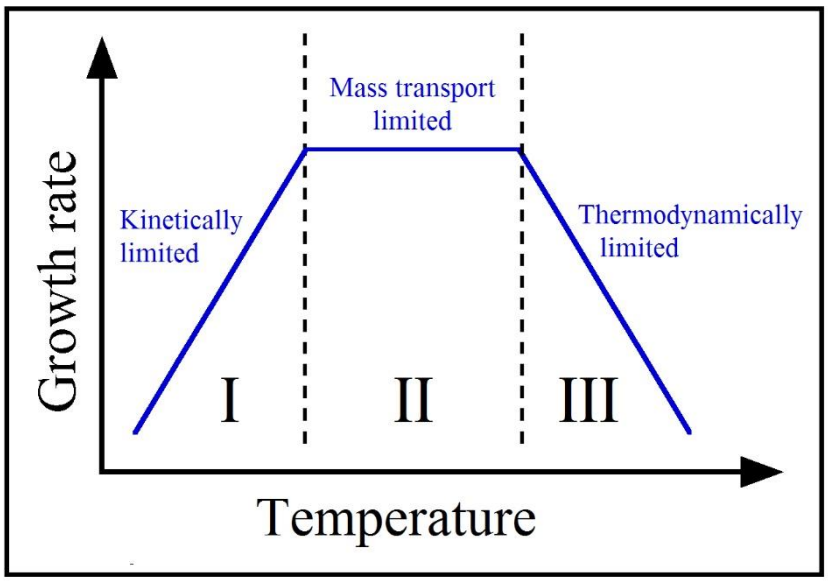

Figure 4.7: Temperature dependence of the growth rate.

4.6 High-pressure pressure chemical vapor deposition (HPCVD)

High-pressure CVD is the expansion of the MOCVD process in the direction of the superatmospheric reactor pressure regime. Therefore, HPCVD is also denoted as superatmospheric MOCVD. In general, HPCVD takes place at a higher reactor pressure to stabilize the growth surface at higher temperatures. This concept of HPCVD is based on the suggestions of McChesney et al. to utilize elevated nitrogen pressure at higher growth temperatures to stabilize the growth surface of InN [3]. Theoretical calculations of the thermodynamic equilibrium predicted a significant increase of the dissociation temperature as a function of reactor pressure. Therefore, stabilization of group III-nitrides at higher temperatures in a high-pressure nitrogen atmosphere is a possible method of single crystal growth. The superatmospheric pressure regime faces some challenges in comparison to low-pressure MOCVD systems. At superatmospheric pressures, the mean free path of the particles reduces, which leads to an increase of the metalorganic precursor interactions in the gas phase and above the growth surface. The increasing gas phase densities involve an increase in parasitic reactions between the precursor fragments and the formation of adducts. The control of the gas phase chemistry becomes critical and is approached by temporal and spatial separated injection of the precursors to minimize the gas phase reactions. Additionally, the surface boundary layer decreases with increasing reactor pressure.

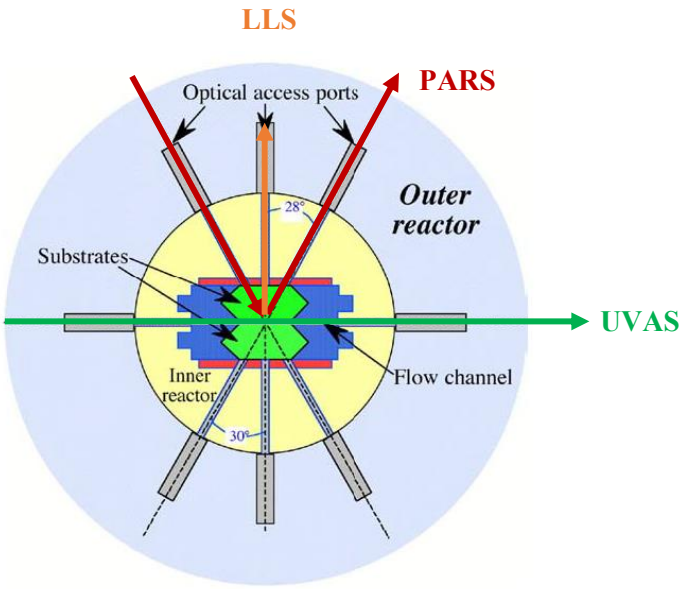

Figure 4.8: Schematic cross section of HPCVD reactor including optical characterization methods UVAS (green), LLS (orange) and PARS (red) [132].

Figure 4.8 shows a schematic cross-section of the HPCVD reactor implemented at Georgia State University. The HPCVD system consists of a narrow horizontal reactor flow channel to consider the reduction of the boundary layer to achieve optimal utilization of the precursors. The reactor possesses multiple optical viewports which enable real-time in-situ monitoring of gas phase reactions, surface morphology as well as structural and optoelectronic film properties. Ultraviolet absorption spectroscopy (UVAS) horizontally through the flow channel traces the temporal alternating precursor injection and their decomposition. Principal angle reflection spectroscopy (PARS) assess the crystalline quality and surface roughness. PARS utilize a He-Ne-laser with an excitation wavelength of 633 nm. The incident angle of the laser light is 28° from the normal of the substrate (red arrows in Figure 4.8) and close to the principal angle of reflection. This minimizes the perpendicular polarized component of the light.
Laser light scattering (LLS) monitors changes of layer thickness and dielectric constant during growth by measuring the scattered light of the same laser through an optical viewport perpendicular to the normal of the substrate. Both optical characterization methods, PARS and LLS, are obtained through the substrate backside (Figure 4.8).
The partial pressures of the group III-nitride materials are very different. HPCVD is an approach to stabilize the partial pressure differences which reduces the temperature gap between binary group III-nitrides. Therefore, stabilization of the partial pressures in the superatmospheric pressure regime enables growth of ternary group III-nitrides and heterostructures. HPCVD has accomplished the growth of InN and In-rich InGaN with promising results [29, 133-135].

4.7 Growth challenges of InN and In-rich InGaN layers

In the current state of the art, low-pressure MOCVD is a growth technique to successfully produce InGaN compositions with In-incorporation up to 30% and sufficient crystal quality for commercial device applications such as LEDs and LDs. However, the epitaxial growth of InN and In-rich $In_xGa_{1-x}N$ ($x > 0.3$) materials with high-crystal quality encounters several challenges.

4.7.1 Growth temperature gap between InN and GaN

Nitrogen is very volatile, and its equilibrium vapor pressure over the growth surface of InN is several orders higher than AlN and GaN [136]. Additionally, the InN dissociation temperature is much lower than that of AlN and GaN. The In-N bonds are weaker than the Ga-N and Al-N bonds, and thus require less thermal energy to break. Furthermore, the In-N bond energy is smaller than the energies of the In-In and N-N bond, which can lead to stoichiometric instabilities [137]. In case of InN, the dissociation of InN sets in at about 550°C, limiting the InN growth temperature to below 600°C.

Different challenges at low and high temperatures restrict the temperature growth window of InN from 450°C to 600°C. The cracking efficiency of the ammonia depends on the growth temperature. At low temperatures, ammonia has a lower cracking efficiency which results in less active nitrogen species. Shortage or not sufficient amount of active nitrogen precursors leads to the formation of In droplets on the surface [117, 138]. At higher temperatures, the decomposition of ammonia is more efficient, but on the other hand, InN can thermally decompose because of its low dissociation temperature. Also, due to the higher cracking efficiency, more hydrogen is formed. As mentioned in section 4.5, hydrogen decreases the InN growth rate or even cause thermal etching of the grown InN. For $In_xGa_{1-x}N$ deposition, an increased amount of hydrogen leads to a decrease in the In-incorporation in the solid phase [130].

Due to the limitation of the InN growth temperature between 450 to 600°C, growth parameters such as V/III ratio and reactor pressure are of importance. The low InN growth temperature range involves a low decomposition rate of ammonia, and therefore higher amounts of ammonia are required to supply sufficient reactive nitrogen species. A higher ammonia input corresponds to a higher V/III ratio and potentially suppresses the formation of In droplets and increases the growth rate.

The vastly different partial pressures of the binaries InN and GaN result in a wide gap (~300°C) between their growth temperatures making the formation of In-rich InGaN alloys difficult using low-pressure MOCVD. At elevated temperatures during InGaN growth, thermal decomposition of Indium limits the In-content of the InGaN alloy. On the other hand, at lower temperatures, the crystal quality of the material reduces. The wide temperature gap between the InN and GaN growth regime is a motivation to explore growth methods that narrow the temperature gap and enable the fabrication of high-quality In-rich InGaN materials.

4.7.2 Substrate issues

The lack of lattice-matched and thermally compatible substrates for the deposition of group III-nitrides is a present growth challenge. In general, the heteroepitaxy of wurtzite group III-nitrides utilizes different substrates such as sapphire (Al_2O_3), silicon carbide (SiC) and cubic silicon (Si) being the most common.

Sapphire is the most commonly used substrate for the growth of wurtzite group III-nitrides. The high crystal and surface quality, as well as temperature stability, are the main advantages of sapphire substrates. Sapphire is commercially available in a variety of wafer diameters from two inches up to six inches at relatively low costs. Due to its bandgap of 9.0 eV, sapphire is transparent for most of the group III-nitride bandgaps. The lack of absorption and excellent transmission is highly suitable for group III-nitride based devices such as detectors and back illumination in LEDs [18].

Like sapphire, silicon (111) is also available in large diameters. For example, the lattice mismatch between Si and InN of 8% is much smaller than the lattice mismatch between sapphire and InN (26%). Furthermore, utilizing Si (111) as a substrate enables the possible integration of group III-nitrides into the well-established silicon technology [139]. So far, the growth on silicon is very challenging and not well understood, particularly for AlN and InN. Compared to the properties of sapphire, SiC possesses better heat transport and smaller lattice mismatch. Though, high-quality single crystalline SiC substrates are expensive due to their difficult fabrication.
However, all these substrate materials have a lattice mismatch as well as differences in the thermal expansion coefficient with the group III-nitrides. The lattice and thermal mismatch between the group III-nitrides and these substrates lead to a high dislocation density (10^9 - 10^{10} cm^{-2}) [137], and biaxial strain. Further effects are mosaicity and wafer bowing. The choice of the substrate strongly influences the growth and the crystalline structure of the overgrown group III-nitride epilayers by determining the crystal orientation, polarity as well as the surface morphology and defect density of the layer. Despite the lattice mismatch and thermal expansion coefficients between the group III-nitrides and the substrate, also the abundance and the costs of the substrate must be taken into consideration to determine the suitability of a substrate. Other group III-nitrides are also possible as substrates because they have the same wurtzite crystal structure, and smaller lattice and thermal mismatch compared to sapphire. Due to the tremendous progress in the bulk crystal growth of AlN and GaN in recent years, both have become commercially available as substrates, while InN bulk crystals are not available. However, the growth and preparation of bulk AlN and GaN crystals are challenging. The substrates have a small diameter (2 inches) and are not cost-effective for mass production [140].

The different lattice and thermal properties of the substrate and the group III-nitrides require growth procedures and suitable growth conditions to grow group III-nitrides epilayers on foreign substrates and furthermore improve the crystalline quality. Another concept to address the lattice mismatch between sapphire and group III-nitrides is the introduction of a thin AlN nucleation or buffer layer. The AlN buffer layer serves as a transition from the oxide to the nitride chemistry. The decoupling of the lattice mismatch leads to strain relaxation reducing defects and improving the crystalline quality of the overgrown epilayer. Alternatively, the nitridation of the sapphire substrate before the group III-nitride growth is a concept to reduce the lattice mismatch. In principle, the nitridation mechanism consists of the diffusion of nitrogen atoms into the sapphire substrate, where they substitute oxygen atoms bonded to aluminum atoms [141].

4.7.3 Phase separations

Another challenge of $In_xGa_{1-x}N$ growth is the solid-phase miscibility gap. The large lattice mismatch of 11% between the two binaries InN and GaN leads to InGaN crystal lattice strain. For the strain reduction in the material, phase separations and spinodal decomposition can occur forming subsets with varying In composition. The dimensions and the ordering of the phase separation and spinodal decomposition are different. Phase separations lead to the formation of In-rich areas surrounded by a depleted Ga-rich matrix. The In-rich islands dimensions reach up to the micrometer scale. In contrast, the spinodal decomposition takes place in the atomic range, with compositional variations on a nanoscopic scale. Ho and Stringfellow calculated the binodal and spinodal lines of the $In_xGa_{1-x}N$ material system in dependence of the deposition temperature [44]. Their calculations are based on a modified

valence-force-field model that allows lattice relaxation beyond the first nearest neighbors. Figure 4.9 displays the binodal and spinodal composition of the entire $In_xGa_{1-x}N$ composition range as a function of the growth temperature.
Inside the dashed (spinodal) curve the InGaN material is thermodynamically unstable for the given temperatures. In this region, a solution of InN and GaN separates into areas or phases with distinctly different chemical compositions affecting the physical properties of the material. Outside of the solid (binodal) curve, InGaN exists in a thermodynamically stable phase. Between the solid and the dashed line the material phase is metastable. As indicated in Figure 4.9, the $In_xGa_{1-x}N$ material system is immiscible over most of the compositional range at typical growth temperatures in conventional MOCVD. This large solid-miscibility gap leads phase separation, a significant growth challenge for In-rich InGaN alloys.

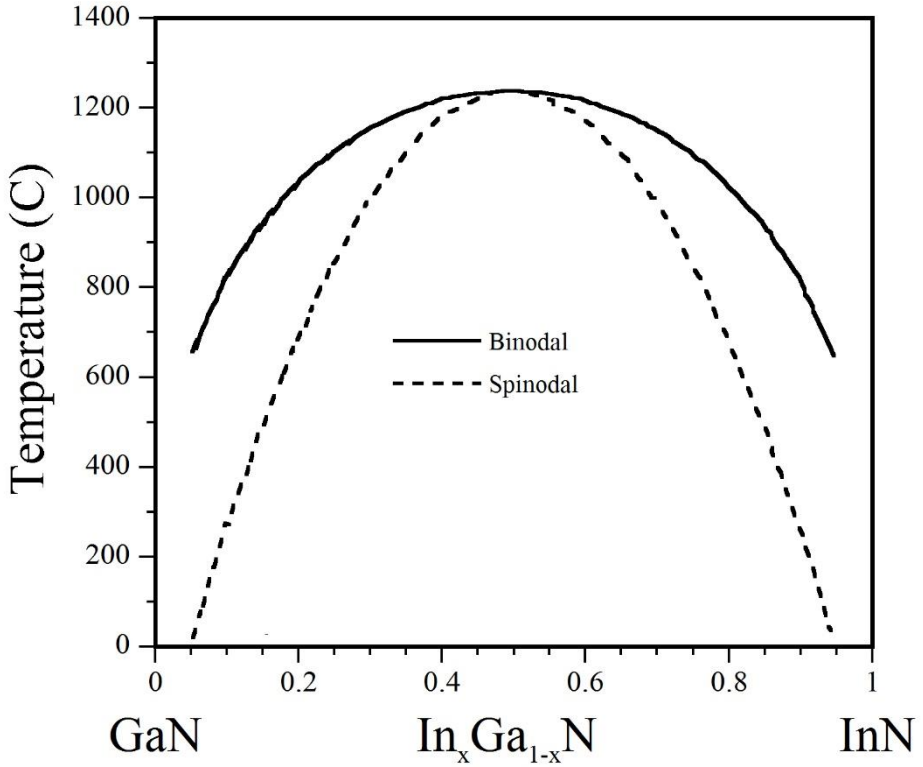

Figure 4.9: Phase diagram of the $In_xGa_{1-x}N$ material system. Binodal (solid) and spinodal (dashed) curves from calculations by Ho and Stringfellow [44].

Phase separations in In-rich InGaN are a significant problem for the fabrication of LEDs emitting in the visible spectrum from the green to red and solar cells. Nanoscale lateral compositional inhomogeneities at the growth surface can lead to bulk phase segregations and reduction of the heterostructural film quality.

Novel concepts need to be explored to address the present challenges for InGaN alloys with higher In-incorporation. Migration-enhanced plasma-assisted (MEPA-) MOCVD is an approach to reduce the partial pressure difference between InN and GaN and enable growth of the binaries in the same growth regime. The concept of MEPA-MOCVD is to replace the ammonia with plasma-activated nitrogen species and use their kinetic energies to stabilize the growth surface chemistry and narrow the temperature gap between InN and GaN. The following chapter will describe in detail the concept and the design of the MEPA-MOCVD system used in this study.

5 Deposition of group III-nitrides by MEPA-MOCVD

5.1 Introduction

In this thesis, the group III-nitride alloys InN and different compositions of $In_xGa_{1-x}N$ were grown at low pressures utilizing a custom-built Migration-enhanced plasma-assisted metalorganic chemical deposition system (MEPA-MOCVD).
This chapter describes in detail the concept of the MEPA-MOCVD growth system and how this approach addresses the challenges in In-rich InGaN growth, mentioned in the previous chapter. First, the setup and the properties of the MEPA-MOCVD reactor and the plasma source are introduced including the in-situ metrology methods to study the composition of the plasma-activated nitrogen species. The transport of the MO precursors to the reactor as well as the excitation and conditioning of the plasma-generated nitrogen precursors is described thoroughly. From this follows a description of the migration-enhance plasma-assisted growth process considering the growth kinetics to stabilize the growth surface chemistry. Results of the UV-absorption spectroscopy and the plasma emission spectroscopy verify the tailoring of the nitrogen precursors as a function of growth parameters.

5.2 MEPA-MOCVD reactor design

The MEPA-MOCVD system is a combination of a customized Emcore showerhead MOCVD reactor and a radio-frequency (RF) hollow cathode plasma source (by MEAglow^{TM}). The plasma source is installed on top of the showerhead flange. Figure 5.1 shows a schematic layout of the MEPA-MOCVD system. This section will go into detail about the capabilities of the reactor and the hollow cathode plasma source.
The reactor system consists of two stainless steel chambers, a growth chamber for the deposition of group III-nitrides and the loadlock station with a gate valve between them. The purpose of the loadlock station is to transfer samples into and out of the reactor main chamber under vacuum conditions using a fork-lift connected with a transfer-arm. Therefore, the reactor chamber is maintained under vacuum conditions between growth runs and not exposed to the atmosphere or any other contamination. A water-cooled turbo-molecular pump (THU 510 from Pfeiffer Vacuum) in combination with a roughing pump station evacuates the reactor chamber to a base pressure of 10^{-8} – 10^{-9} mbar. During growth operation, the reactor is pumped by a roughing pump enabling low growth pressure between 0.5 and 5 Torr. A butterfly valve, an exhaust valve controller, located in the exhaust line between the reactor chamber and the roughing pump regulates and maintains a constant reactor pressure during film growth. The heater assembly below the substrate carrier provides a growth temperature range from 200°C to 1100°C. The showerhead flange, the reactor base, reactor walls, and the hollow cathode plasma source are water-cooled to prevent overheating.
The substrate carrier of the MEPA-MOCVD reactor is suitable for a single 4-inch diameter wafer (1x4”) or three substrates with a two-inch diameter (3x2” configuration) with a rotation velocity between 5 to 50 rpm to promote homogeneous deposition group III-nitride films.

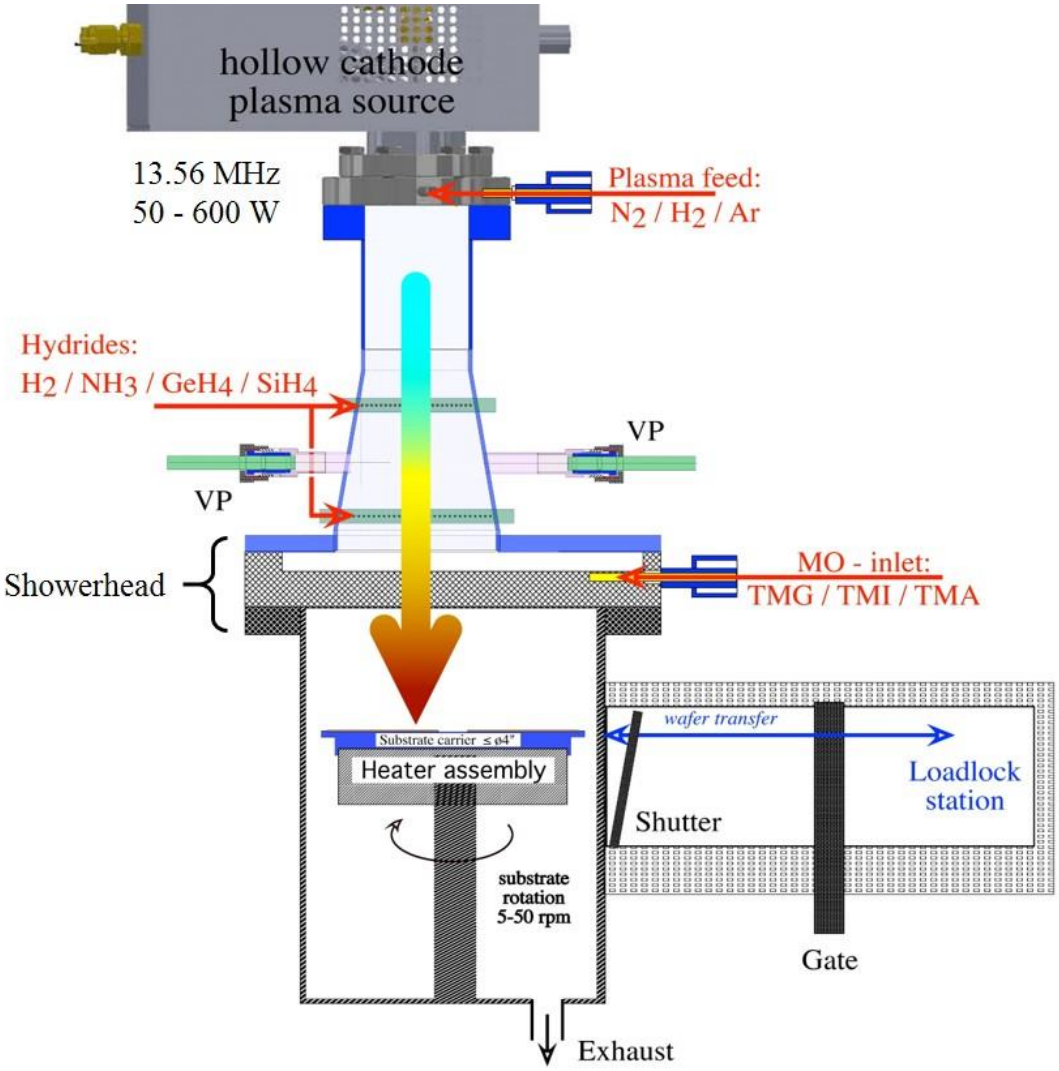

Figure 5.1: Schematic MEPA-MOCVD reactor design.

The metalorganic precursors, Trimethylindium (TMI), Trimethylgallium (TMG) and Trimethylaluminum (TMA) are supplied via the showerhead, while the reactive nitrogen precursors are generated in the hollow cathode and directed downstream towards the substrate. Added provisions to the showerhead flange allow spatial separation close to the growth surface between the metalorganic and plasma-activated precursors. Sections give a detailed description of the MO precursors, their properties and the transport mechanism into the reactor and the generation and conditioning of the plasma excited nitrogen fragments, respectively. Between the hollow cathode and the showerhead are two injection ports to admix hydrides such as hydrogen and ammonia into the plasma downstream. Another purpose of these ports is doping. Dopants such as silane (SiH_4) or germane (GeH_4) can also be mixed into the plasma downstream via the inlet ports for the hydrides in Figure 5.1.

Two optical viewports (VP) on opposite sites (between the two hydrides inlet rings) allow real-time monitoring of the active species by plasma emission spectroscopy (PES) and UV-absorption spectroscopy. Both viewports have fused silica rods (light green) inside to transmit light in and out of the reactor. A window on the same level as the substrate carrier allows PES also above the growth surface. The in-situ metrology characterization methods PES and UVAS are described later in this chapter.

All major process control parameters such as mass flow controllers, pressure regulators and valves are fully automated and completely computer controlled via a customized LabVIEW program. Within the scope of this thesis, the remote control of the plasma source and generation of a pulsed plasma supply mode was implemented by using the analog/digital interface of the plasma power source in combination with a DAQ device (NI-USB 6009). A self-written LabVIEW program allowed the modulation of the applied plasma power and its pulse length enabling temporal control of the nitrogen precursor supply during the growth process. A connection between the plasma pulse generation program and the MEPA-MOCVD control program allows exploring the influence range from temporally separated MO and active nitrogen precursor injection over a partial overlap to a simultaneous pulsed supply. This option enables potential control to stabilize the growth surface chemistry.

5.2.1 Hollow cathode plasma source

A radio-frequency (RF) hollow cathode plasma source (from MEAglow^{TM} Ltd.) converts the low-pressure MOCVD reactor at Georgia State University (GSU) into a MEPA-MOCVD system. The hollow cathode is the nitrogen precursor source for the deposition of group III-nitride alloys. This plasma source consists of two arrays with hollow cathode holes. One set is directly on the RF electrode, and the other one is on the ground electrode. The holes face each other, and each hole independently operates as a plasma source. A schematic diagram of the hollow cathode plasma source can be found in reference [142]. By increasing the number of holes, the plasma source can be scaled for larger deposition areas, reducing production costs and making it suitable for commercial production [142, 143]. Another advantage is that the hollow cathode plasma source is considered a nearly oxygen-free plasma source compared to inductively coupled plasma (ICP) and microwave plasma sources. ICP and microwave plasma sources use a ceramic (dielectric) window which can be damaged by excited plasma species and consequently leads to oxygen contamination [144]. In contrast, the hollow cathode plasma source has no window and is completely fabricated out of metal (molybdenum). Another windowless plasma source with low oxygen contamination is a capacitively coupled plasma (CCP) source. However, hollow cathode plasma sources produce electron densities around 9×10^{11} cm^3 [142], which is one magnitude higher compared to the electron densities of CCP sources around 10^9-10^{10} cm^3 [145].

The hollow cathode is powered by a radio-frequency (13.56 MHz) generator with a tunable output power range from 50 W up to 600 W. Under radio-frequency conditions, the cathode emits electrons that are trapped in the holes, where they oscillate back and forth due to the applied RF field. During these oscillations, the electron ionizes the nitrogen atoms via inelastic collisions. In one RF cycle, the electrons oscillate many times leading to a high electron density and subsequently a dense plasma. The hollow cathode plasma source is mounted in a remote position to provide spatial separation between plasma generation and film deposition to avoid direct contact of the plasma and the growth surface as well as the group III metalorganic precursors. In this design, the plasma itself acts as an anode. The excited plasma species are directed out of the cathode by a constant nitrogen flow through the hollow cathode. The reactive species are directed to the growth surface in the afterglow regime. This remote downstream process of reactive nitrogen precursors in combination with the spatial and temporal supply of MO precursors expands a conventional MOCVD reactor to a migration-enhanced plasma-assisted MOCVD system.

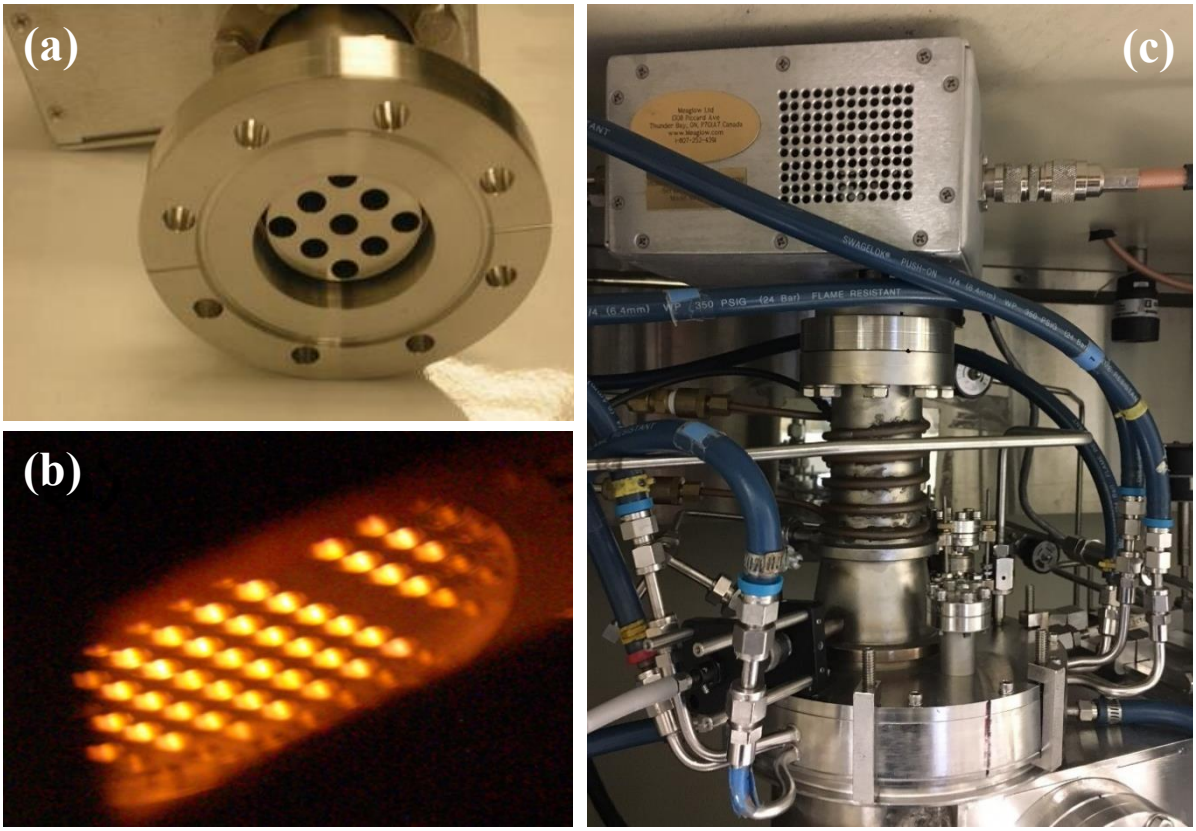

Figure 5.2: (a) Hollow cathode holes, (b) Hollow Cathode nitrogen-plasma afterglow regime monitored above growth surface and (c) MEAglow^{TM} hollow cathode on the showerhead flange of the MEPA-MOCVD system at GSU.

5.3 Real-time in-situ metrology

Real-time in-situ metrology is an important feature in MEPA-MOCVD growth and offers several advantages. UV-absorption and plasma emission spectroscopy (PES) enable a better understanding of the precursor decomposition processes and the growth mechanism. Knowledge about the kinetic energies of the reactants in the afterglow plasma region, as well as their temporal and spatial distribution, enables conditioning of the surface chemistry reactions and thus stabilization of the growth surface. Furthermore, it provides a link between the gas phase chemistry and the growth surface chemistry and allows correlation to the electrical and optical properties of the layer.

5.3.1 UV-absorption spectroscopy

Ultraviolet absorption spectroscopy has several advantages for the real-time monitoring of ammonia precursor decomposition. In MOCVD, most of the reactants such as ammonia have large absorption cross sections in the ultraviolet range [146, 147]. Additionally, radiation from the heated substrate and gas phase does not interfere with optical detection below 400 nm. UVAS systems are easy to set up and maintain compared to other common optical techniques. In this work, UVAS is used to investigate the plasma-assisted decomposition of ammonia. Figure 5.3 shows the UVAS setup. An optical fiber guides the light of a deuterium lamp to the viewport. A lens at the end of the fiber focus the light into fused silica rod and further into the reactor. The transmitted light is detected at the opposite viewport using another optical fiber and transfers the light to an USB-spectrometer (Maya2000 PRO spectrometer, Ocean Optics).

The spectrometer has a wavelength range between 200 nm to 1100 nm with a spectral resolution of 0.5 nm. Active species (N*/NHx*) increase as a function of plasma power. UV-absorption spectroscopy confirms the conversion of NH_3 to NH* molecules containing species by plasma-assisted decomposition of ammonia.

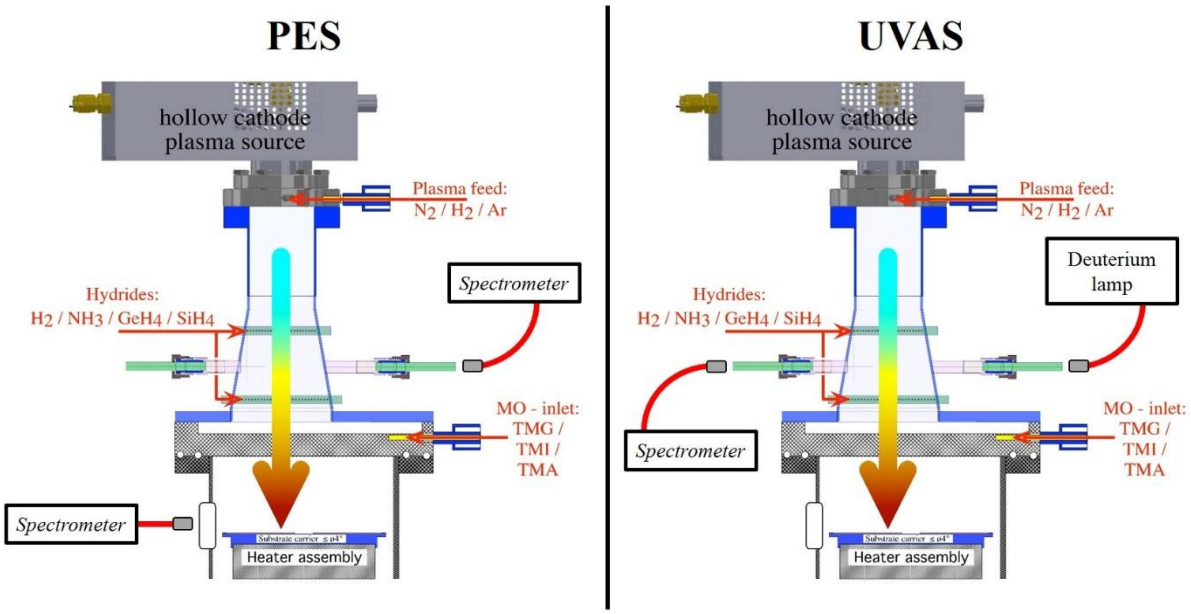

Figure 5.3: On the left are PES measurement setups near the growth surface and close to the plasma source. On the right is UVAS configuration displayed. The optical fibers with the collimating lens are indicated by the red lines with the small grey boxes.

5.3.2 Plasma emission spectroscopy

Another real-time diagnostic tool is the plasma emission spectroscopy (PES), also referred to as optical emission spectroscopy (OES). PES is non-invasive and offers the possibility to determine which species are present during the deposition of group III-nitrides by MEPA-MOCVD. Analysis of the plasma emission spectrum might assess identification and quantization of active nitrogen species which are contributing to the group III-nitride growth process. Furthermore, the plasma-activated species can be related to the electrical and optical properties of the deposited group III-nitride material. Besides the plasma activated nitrogen species, PES is also able to detect excited atomic group III metals as well as gases which are mixed into the plasma feed such as argon. As mentioned earlier, the MEPA-MOCVD system possesses the possibility to measure the plasma emission close to the hollow cathode and above the growth surface. This feature allows comparing the direct plasma with the remote plasma in the afterglow region contributing to a better comprehension of the plasma species conditioning as a function of growth parameters such as plasma power, reactor pressure and nitrogen flux through the plasma source.

For the PES close to the hollow cathode, an optical fiber with a collimating collects the light from a fused silica rod at one of the viewports and transfers it to the USB-spectrometer. The plasma emission above the growth surface is measured through a window of the reactor main chamber. A fiber with a collimating lens is positioned close to the window to collect the plasma emission signal and transfers it to the spectrometer. The shutter for the window is shortly open during PES measurements. The real-time monitoring of the plasma emission, as well as the intensity determination of the emission lines, is automated by a LabVIEW program.

5.4 Metalorganic precursor supply

The transport of the metalorganic precursors into the MEPA-MOCVD reactor is a downstream process by using a carrier gas like nitrogen or hydrogen. Hydrogen is the preferred carrier gas because of the high purity but has a crucial role in the InN and the InGaN growth. Hydrogen reduces the InN deposition rate and affects the formation of $In_{1-x}Ga_xN$ compositions [130, 148]. Therefore, purified nitrogen is used as carrier gas for InN and InGaN growth.
The MEPA-MOCVD system is equipped with three metalorganic sources, namely Trimethylindium (TMI), Trimethylgallium (TMG) and Trimethylaluminum (TMA) to grow group III-nitride alloys. These three MO compounds have the same structure consisting of a metallic atom, indium, gallium or aluminum respectively, which is bound to three methyl groups (CH_3). Figure 5.4 shows a schematic drawing of a TMG molecule. In this example, the Ga-atom (blue circle) has three bonds, one to each carbon atom (black circle) of the methyl group. The general chemical formula for the MO compounds is $(CH_3)_3M$ with M being the place holder for Ga, In and Al respectively.

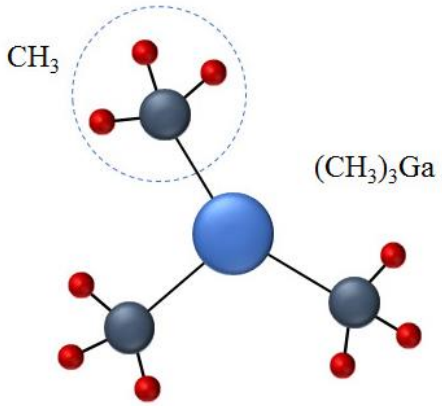

Figure 5.4: Schematic drawing of TMG molecule. The Ga-atom is indicated by blue sphere. Black and red spheres correspond to carbon and hydrogen, respectively.

The bonds between the methyl groups and the group III metal atom are the weakest ones. The required temperature to break these bonds by pyrolysis is below the growth temperature. Table 5.1 displays some physical characteristics of TMI, TMG and TMA.

Metalorganic	Appearance (RT)	Density at 30°C (g/ml)	Boiling point (°C)	Melting point (°C)
TMI	White crystalline solid	1.568	88	134
TMG	Clear, colorless liquid	1.151	56	-16
TMA	Clear, colorless liquid	0.743	127	15

Table 5.1: Physical characteristics of TMI, TMG, and TMA.

At room temperature, the metalorganic precursors TMA and TMG appear liquid, while TMI is solid. All MO are stored in sealed stainless-steel cylinders, called bubblers. For transportation of a liquid MO precursor, an inert gas is introduced at the bottom of the container, "bubbles" through the liquid and leaves with the MO through the exit pipe (Figure 5.5). In the case of TMI, a carrier gas is injected to the bubbler. The solid TMI sublimes and leaves the bubbler. The bubblers itself are kept in a temperature-controlled bath to achieve a constant vapor pressure.

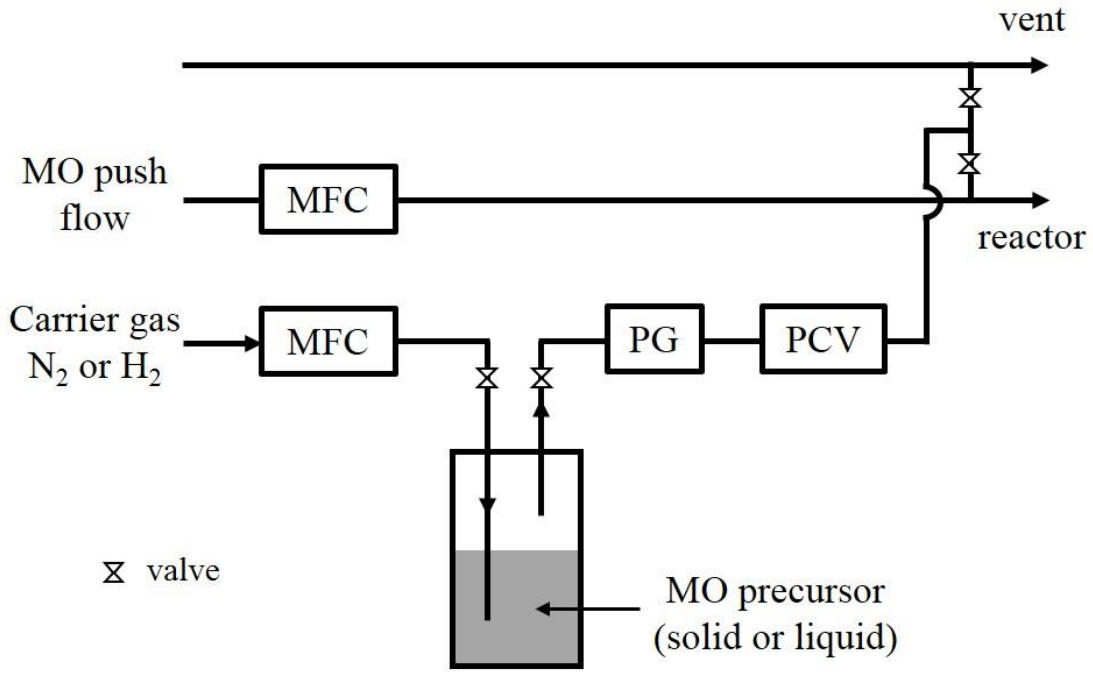

Figure 5.5: Schematic example of MO precursor transport line and reactor/vent manifold in MOCVD.

Mass flow controllers (MFC) regulate the carrier gas flow rate through the bubblers. A pressure gauge (PG) monitors the bubbler pressure $P_{bubbler}$ after the bubbler outlet while a subsequent pressure control valve (PCV) controls the bubbler pressure. The carrier gas flow rate and the bubbler pressure have to maintained to ensure a constant molar flow of the MO. The MO partial pressure (or MO vapor pressure P_{vapor}) inside the bubbler depends on the temperature of the MO. Since it is not possible to determine the temperature in the MO bubblers, the temperature of the bath (in Kelvin) is utilized to determine the MO vapor pressure:

$$P_{vapor}(\text{torr}) = 10\,\hat{}\,(B - A/T(K)). \tag{5.1}$$

A and B are the corresponding gas constants for TMI, TMG and TMA as listed in Table 5.2.

Metalorganic	Gas constant A	Gas constant B
TMI	3204	10.98
TMG	1703	8.07
TMA	2134	8.224

Table 5.2: Gas constants A and B of TMI, TMG and TMA [149-151].

The graphs in Figure 5.6 show the exponential relation between MO vapor pressure and bubbler temperature using equation (5.1) and the gas constants in Table 5.2. The molar fraction of the MO vapor through the MFC is given by the ratio between P_{vapor} and $P_{bubbler}$:

$$\text{Molar fraction} = \frac{P_{vapor}}{P_{bubbler} - P_{vapor}} \tag{5.2}$$

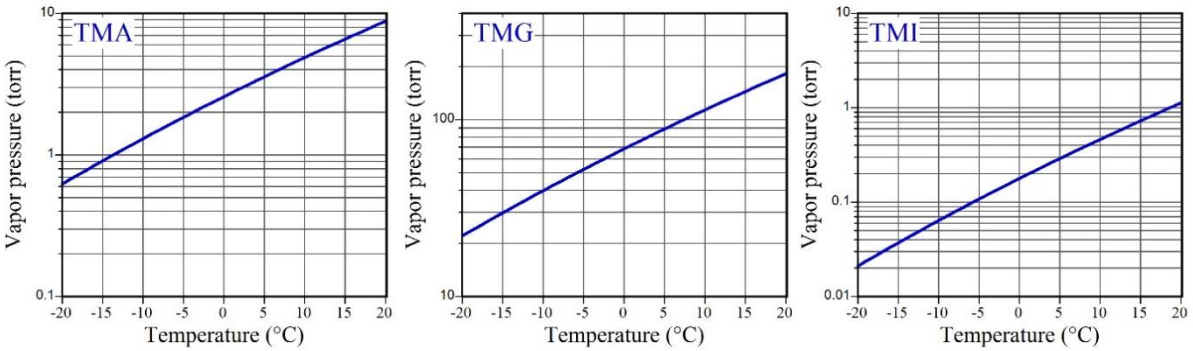

Figure 5.6: Vapor pressure curve as function of bubbler temperature for TMA, TMG and TMI.

In the MEPA-MOCVD system, all bubblers are connected to the reactor-vent switch block (as indicated in Figure 5.5). The manifold switch block allows to instantly switch the MO reactants either to the vent or the reactor chamber. The MO precursors are sent to the vent to establish a stabilized flow under a set bubbler pressure. Thus, the MO precursor is instantly accessible for deposition, when required. The rapid switching between the reactor and vent allows the formation of abrupt interfaces and the growth of complex multilayer structures.

A push flow line delivers the carrier gas transporting the MO precursor into the reactor chamber (see Figure 5.5). The push flow can be either nitrogen, hydrogen or a hydrogen/nitrogen mix and is also mass flow controlled. The LabVIEW control program automatically regulates and monitors all MFCs, pressure gauges and pressure control valves. For safety measures, the bubblers possess manual inlet and outlet valves which have to be opened before a growth run.

The rate of injected MO precursors into the reactor chamber can be evaluated based on the Ideal gas equation:

$$n \cdot R \cdot T = P \cdot V \Leftrightarrow n = \frac{P \cdot V}{R \cdot T}, \tag{5.3}$$

where n is number of moles [mol], R is the ideal gas constant = 62363.67 cm^3 torr K^{-1} mol^{-1}, T is the absolute Temperature [K], p is the absolute pressure and V is the volume.

Using the Ideal gas law, equation (5.3), the standard molar volume V_{std} for one mole of an ideal gas at standard temperature T_{std} of 273.15 K and standard pressure of 760 Torr is:

$$\begin{aligned} V_{std} &= \frac{R \cdot T_{std}}{P_{std}} \\ &= 22413.995 \text{ cm}^3 \cdot \text{mol}^{-1} . \end{aligned} \tag{5.4}$$

The standard molar volume is converted to the standard molar concentration C_{std} by:

$$C_{std} = 1/V_{std} = 44.615\ \mu\text{mol}\cdot\text{cm}^{-3}. \tag{5.5}$$

The molar flow rate is a function of the standard molar concentration C_{std}, the flow rate v_{MFC} through the bubbler (from MFC in Figure 5.5) and the molar fraction of the MO [152]:

$$\text{MO Molar flow} = 44.615\ \mu\text{mol}\cdot\text{cm}^{-3}\cdot v_{MFC}\,(\text{sccm})\cdot\frac{P_{vapor}}{\left(P_{bubbler}-P_{vapor}\right)}\cdot \tag{5.6}$$

The standard molar concentration C_{std} and the molar fraction of the MO are given by equations (5.5) and equation (5.2), respectively. The MFC flow rate is standard cubic centimeter per minute or sccm. Therefore equation (5.6) expresses the MO molar flow in micro mole per minute (μmol/min).

The MO decomposition process in this MEPA-MOCVD system is similar as in a conventional MOCVD showerhead. The MO precursors are injected into the gas phase where the thrimethyl groups thermally decompose by pyrolysis. Several groups have studied the decomposition of TMI at various temperatures and using different carrier gases. In general, TMI pyrolyzes in three consecutive homolytic fission reactions:

$$\text{In}(\text{CH}_3)_3 \rightarrow \text{In}(\text{CH}_3)_2 + \text{CH}_3, \tag{5.7}$$

$$\text{In}(\text{CH}_3)_2 \rightarrow \text{In}(\text{CH}_3) + \text{CH}_3, \tag{5.8}$$

$$\text{In}(\text{CH}_3) \rightarrow \text{In} + \text{CH}_3. \tag{5.9}$$

Jacko and Price were the first who investigated pyrolysis reactions of TMI in a toluene carrier in 1964. In their study, reactions (5.7) and (5.8) take place very rapidly by a sequential loss of the radical methyl groups resulting in monomethyl indium In-CH_3, which is very stable for temperatures below 480°C. Thus, reaction (5.9) proceeds at temperatures > 480°C and produces atomic indium [153] and was supported by real-time in-situ IR-laser spectroscopy during MOCVD [154]. In 1990, Hebner and Killeen investigated the pyrolysis of TMI in a hydrogen carrier during MOCVD by resonance fluorescence spectroscopy. They determined the temperature threshold for the formation of atomic Indium by pyrolysis of TMI at above 327°C [155]. Park et al. detected atomic indium using nitrogen as carrier gas by in-situ Raman spectroscopy during MOCVD [156]. Larsen and Stringfellow compared the decomposition of TMI using nitrogen and hydrogen as carrier gas. They discovered that the decomposition reactions take place at lower temperatures when hydrogen is used as carrier gas compared to nitrogen and proposed that in hydrogen the pyrolysis of TMI is homogeneous in the gas phase, while the pyrolysis in nitrogen is surface dependent [157]. A similar effect occurs for the decomposition of TMG. The presence of hydrogen has a strong influence on the decomposition reactions. When utilizing hydrogen as a carrier gas, the decomposition of TMG occurs at 400°C, whereas in nitrogen the decomposition proceeds at 500°C [18]. In addition to the choice of carrier gas, the growth temperature is another important factor determining the decomposition rate. The interaction with other precursors in the gas phase, as well as the substrate surface, also affects the decomposition. Furthermore, the reactor geometry and the flow conditions including pressure define the residence time of the species in heated regions.

Lower pressures result in less gas-phase reactions [128]. The pyrolysis reactions during the growth process are more complex due to incomplete decomposition leading to the formation of by-products such as polymers and adducts, e.g. [158]:

$$n\lfloor \mathrm{In}(\mathrm{CH_3})\rfloor \rightarrow \lfloor \mathrm{In}(\mathrm{CH_3})\rfloor_n (\mathrm{s}), \tag{5.10}$$

$$\mathrm{In}(\mathrm{CH_3})_3 + \mathrm{CH_3} \rightarrow \mathrm{In}(\mathrm{CH_3})_2 + \mathrm{C_2H_6}, \tag{5.11}$$

$$\mathrm{In}(\mathrm{CH_3})_3 + \mathrm{CH_3} \rightarrow \mathrm{In}(\mathrm{CH_3})_2\mathrm{CH} + \mathrm{CH_4}, \tag{5.12}$$

$$\mathrm{CH_3} + \mathrm{H_2} \rightarrow \mathrm{CH_4} + \mathrm{H}. \tag{5.13}$$

Reaction (5.13) occurs if hydrogen is the carrier gas. Incorporation of incomplete MO precursors (monomethyl indium/gallium) or adducts into the film can lead to impurities. Furthermore, the methyl groups contain hydrogen and carbon, and their incorporation can result in unintentional doping.

5.5 Plasma activation of excited nitrogen precursors

In MEPA-MOCVD, the RF hollow cathode is the source for the nitrogen precursors for the growth of group III-nitrides. Replacing ammonia with plasma-generated nitrogen species has several advantages. Plasma-assisted MOCVD in the low-pressure regime enables growth of GaN at lower temperatures compared to conventional MOCVD because the dissociation of the nitrogen molecules is independent of the growth temperature [159], in contrast to the cracking efficiency of ammonia. Lower growth temperatures also reduce wafer bowing caused by the mismatch of the thermal expansion coefficients of the substrate and grown layer [160]. Nitrogen is safer to handle and relatively cheap compared to poisonous ammonia, lowering the fabrication costs [161]. Furthermore, the replacement of ammonia results in a reduction of hydrogen in the reactor chamber benefitting the InN growth process as already mentioned in chapter 4.

In general, the radio-frequency hollow cathode creates reactive atomic and molecular nitrogen species such as N^*/N_2^* by plasma excitation and ionization of nitrogen molecules injected into the plasma feed (Figure 5.1). NH^*/NH_x^* fragments are formed by indirectly admixing hydrides such as hydrogen and ammonia into the nitrogen plasma downstream utilizing one of the two injection ports below the hollow cathode. In this case, the hydrogen and ammonia molecules are cracked by the plasma excited nitrogen species and generate excited NH^*/NH_x^* species. An alternative option to form NH^*/NH_x^* species is the direct by-mix of hydrogen into the nitrogen plasma feed. The downstream directs the plasma-activated fragments to the growth surface in the plasma afterglow regime where they interact with metalorganic (MO) precursors.

The composition of the nitrogen plasma species is a very important factor in MEPA-MOCVD because it has a significant influence on the optoelectronic and structural layer properties such as crystal quality [18]. One challenge in MEPA-MOCVD is to correlate the applied plasma power in combination with nitrogen flow through the hollow cathode to the density of the plasma activated nitrogen species and their kinetic energies to achieve a stabilized growth surface. A high density of active nitrogen species has the advantage to enhance the growth rate

but might cause possible damage to the deposited film by high-energy species. In this case, the reactor pressure plays another important role in affecting the density and the kinetic energies of the reactive nitrogen species. The gas collision rate is pressure dependent. At low pressures the plasma cloud expanses towards the growth chamber and the number of gas collisions reduces. This enables damaging species to reach the growth surface, that can result in etching of the deposited film due to their high kinetic energies. Increasing the pressure leads to a higher gas collision rate that filters the damaging energetic species before they reach the growth surface [144].

In summary, the composition of the active nitrogen-containing species ($N^*/N_2^*/NH_x^*$) reaching the growth surface is a convoluted function of a number of variables such as the applied plasma power, the nitrogen flow rate through the hollow cathode, a by-mix of hydrides and the reactor pressure. How all these parameters interact and relate to the type of species, their kinetic energies, their lifetime, their effect on growth surface stabilization and their reactivity with the MO precursors is less understood and requires further investigations. In this work, the influence of plasma power, as well as by-mix of hydrogen or ammonia on the composition of the reactive nitrogen species, is explored by PES and UVAS.

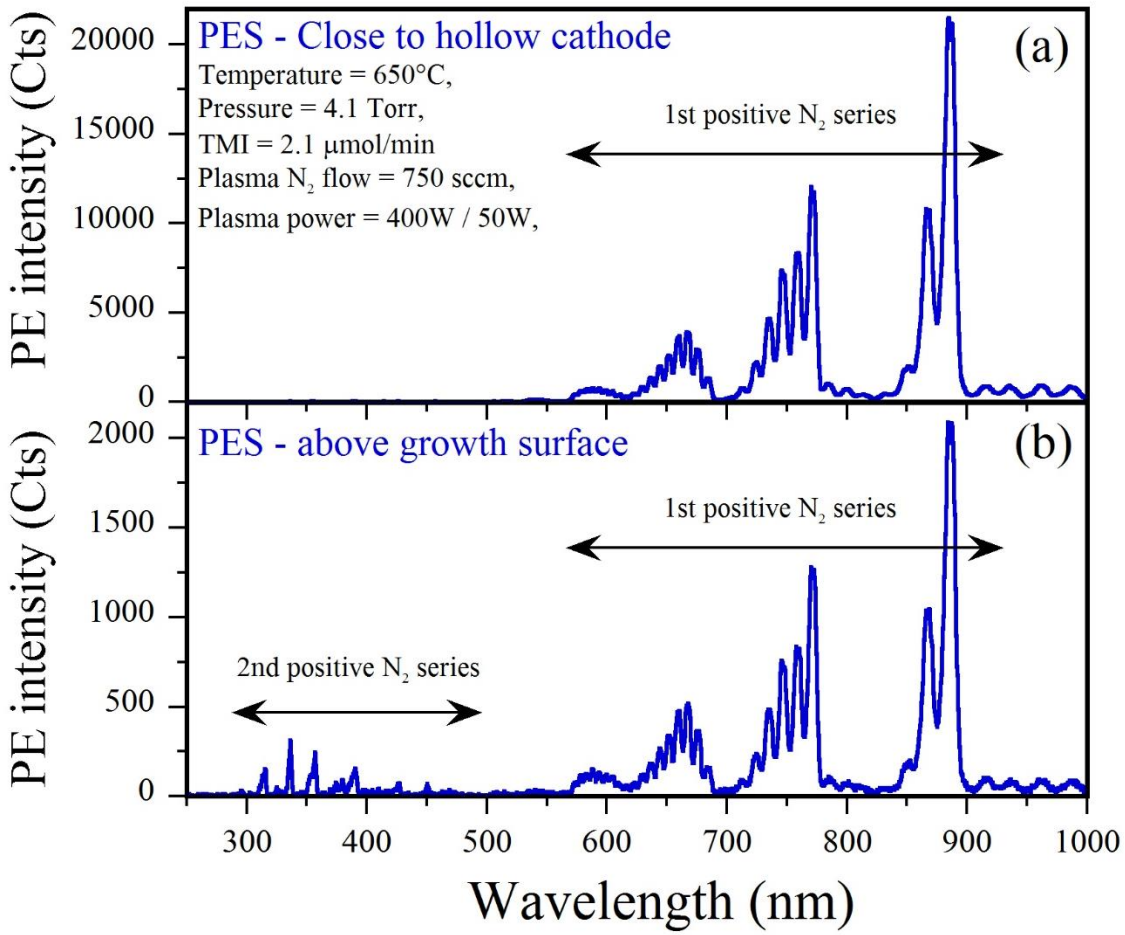

Figure 5.7: Plasma emission spectrum close to the RF hollow cathode (a) and above the growth surface (b).

Figure 5.7a and b show a plasma emission spectrum close to the hollow cathode plasma source and the corresponding above the growth surface; measured during the growth of InN by MEPA-MOCVD. The emission lines represent the energy level transitions of multiple atomic, molecular and ionic nitrogen species. In the PE spectrum close to the hollow cathode and near the growth surface, the first positive nitrogen series appearing in the wavelength range between 500 – 900 nm is dominant with five emission bands [160, 162]. The band heads are at approximately 540 nm (very weak), 580 nm, 660 nm, 750 nm and 860 nm and agree with similar results obtained by optical emission spectroscopy [163-166]. The emission lines and bands of the first positive series in the visible and near-infrared region represent energy level transitions between the following electronic states:

$$\mathrm{N}_2\left(B^3\prod_g\right)\rightarrow \mathrm{N}_2\left(A^3\Sigma_u^+\right)+h\nu \tag{5.14}$$

with $h\nu$ being the photon energy. Both electronic states correspond to the excited nitrogen molecule, though the $A^3\Sigma_u^+$ state is metastable [167]. These transitions result from the recombination of ground-state nitrogen $N(^4S)$ atoms through a three-body collision process with a third participating species M [164, 165]. The recombination process is expressed by the following sequence [168]:

$$\begin{aligned}\mathrm{N}\left(^4S\right)+\mathrm{N}\left(^4S\right)+\mathrm{M}&\rightarrow \mathrm{N}_2^*\left(^5\Sigma_g^+\right)+\mathrm{M}\\ &\rightarrow \mathrm{N}_2\left(B^3\prod_g\right)+\mathrm{M}.\end{aligned} \tag{5.15}$$

A third participating species could be for example N_2. The first line in equation (5.15) describes the excitation process by a multibody collision of two ground state nitrogen atoms and a third body species M, resulting in a highly excited nitrogen molecule. Subsequently, this excited nitrogen molecule relaxes to the electronic state $B^3\Pi_g$ at 7.4 eV via energy transfer due to collisions.

Another process that contributes to the population of the electronic states $A^3\Sigma_u^+$ and $B^3\Pi_g$ is electron impact excitation from the ground state of the nitrogen molecules [167]:

$$\mathrm{N}_2\left(X^1\Sigma_g^+\right)+e\rightarrow \mathrm{N}_2\left(A^3\Sigma_g^+\right)+e \tag{5.16}$$

$$\mathrm{N}_2\left(X^1\Sigma_g^+\right)+e\rightarrow \mathrm{N}_2\left(B^3\prod_g\right)+e. \tag{5.17}$$

Above the growth surface, the emission intensity of the first positive nitrogen system is decreased by a factor of 10 due to gas collisions in the downstream compared to the spectrum at the hollow cathode. Furthermore, various emission lines are detected in the visible and UV region between 280 nm to 450 nm. Figure 5.8 gives a closer look at these plasma emission lines. According to the literature [169-171], three different types of species are distinguished in this wavelength range. The most peaks are assigned to the second positive nitrogen series. Additionally, the ionic N_2^+ species of the first negative nitrogen series, as well as excited atomic indium, are identified.

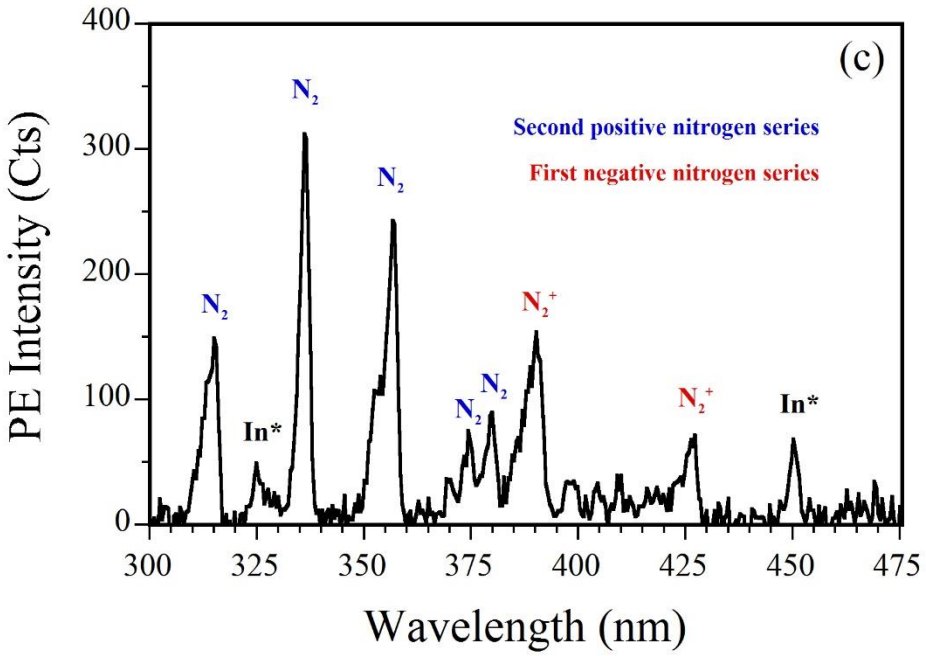

Figure 5.8: Plasma emission lines in the UV region. The most intense peaks of the second positive and first negative as well as excited NH* and excited atomic indium (In*) are marked.

The second positive nitrogen series consists of N_2 molecules with energy transitions from the electronic state $C^3\Pi_u$ at 11.1 eV to the electronic state $B^3\Pi_g$ at 7.2 eV.

$$N_2\left(C^3\Pi_u\right) \rightarrow N_2\left(B^3\Pi_g\right) + h\nu . \tag{5.18}$$

The most intense emission lines associated to the second positive series are at 315.9 nm, 337.3 nm, 357.7 nm, 375.5 nm and 380.5 nm indicated by blue labels in Figure 5.8.

The second negative nitrogen series is expressed by energy transitions of N_2^+ between the electronic states:

$$B^2\Sigma_u^+ \rightarrow X^2\Sigma_g^+ + h\nu \tag{5.19}$$

from 18.7 eV to 15.6 eV. The peaks at 391.4 nm and 428 nm (highlighted by red labels in Figure 5.8) represent the most intense transitions of N_2^+ molecular ions and belong to the first negative molecular series.

Both, the second positive nitrogen system as well as the first negative nitrogen series can be generated by direct electronic excitation and molecular ionization of ground state nitrogen molecules [172], respectively:

$$N_2\left(X^1\Sigma_g^+\right) + e \rightarrow N_2\left(C^3\Pi_u\right) + e \tag{5.20}$$

$$N_2\left(X^1\Sigma_g^+\right) + e \rightarrow N_2^+\left(B^2\Sigma_u^+\right) + 2e \tag{5.21}$$

$$N_2\left(X^1\Sigma_g^+\right) + e \rightarrow N_2^+\left(X^2\Sigma_g^+\right) + 2e . \tag{5.22}$$

Figure 5.9 displays a simplified energy level diagram including the optical transitions of the first negative system of the ionic N_2^+ molecule as well as the first and second positive system of the excited nitrogen neutral molecule N_2. The diagram includes relevant energy levels of the neutral and ionic nitrogen molecules.

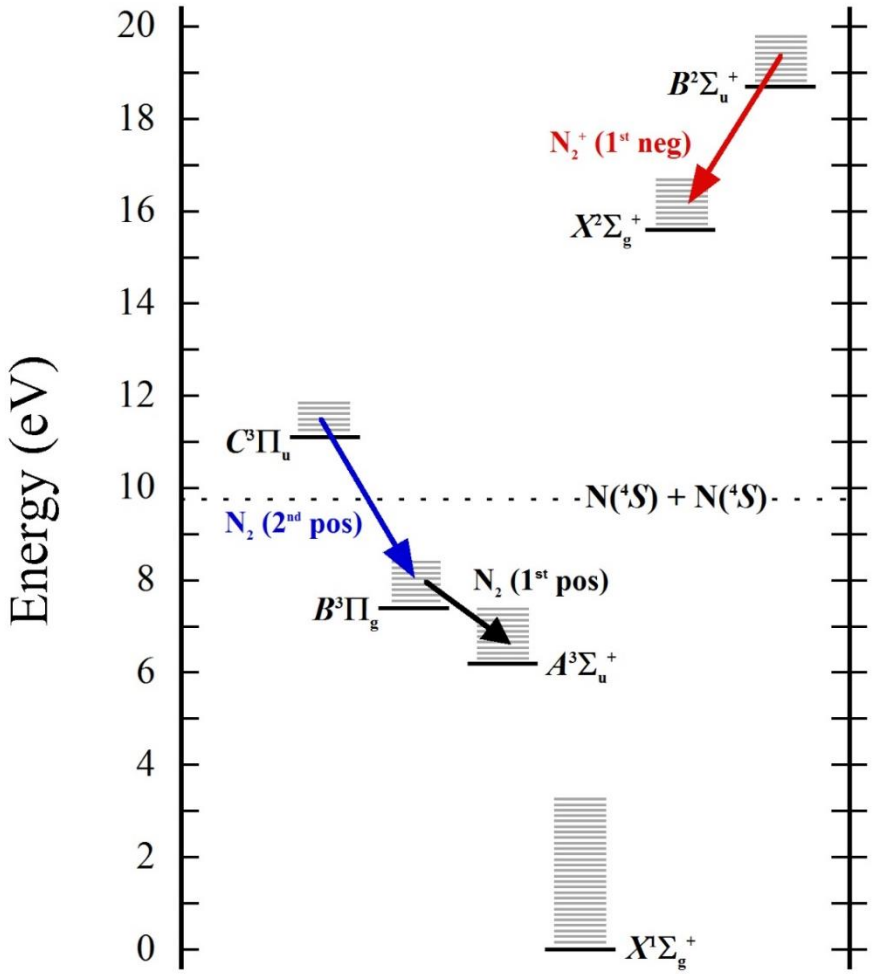

Figure 5.9: Simplified energy level diagram of nitrogen including the transitions of the first positive (black arrow), second positive (blue arrow) nitrogen molecule and first negative N_2^+ (red arrow) species. Adapted from [173]. The corresponding electronic states are labeled and indicated by thick black lines. The grey lines represent vibrational states of the nitrogen. The dashed line at 9.8 *eV* represents the energy for the dissociation of the neutral ground state $N_2(X^1\Sigma_g^+)$ given in equation (5.25).

The emission lines at 325 nm and 451 nm in Figure 5.8 are assigned to excited atomic indium (In*). These emission lines verify the decomposition of TMI resulting in the presence of atomic indium above the growth surface under the given process parameters. Indium atoms can be excited by plasma-activated nitrogen species before reaching the growth surface. The following visible transitions produce the emission doublet at 325 nm [174]:

$$5^2D_{5/2} \rightarrow 5^2P_{3/2}$$
$$5^2D_{3/2} \rightarrow 5^2P_{3/2} \tag{5.23}$$

and the 451 nm line originates from the transition between [175]:

$$6^2S_{1/2} \rightarrow 5^2P_{3/2}\,. \tag{5.24}$$

Similarly, several groups detected emission peaks of atomic Ga transitions at 403 nm and 417 nm using OES, verifying the decomposition of TMG during GaN growth by PA-MOCVD [160, 162, 176].

In summary, the optical emission spectra near the hollow cathode and above the growth surface are dominated by emission lines of the excited nitrogen molecular species. Close to the growth surface, ionic nitrogen species are also detected. As already mentioned in equations (5.16), (5.17) and (5.20) - (5.22), electronic excitation and molecular ionization generate excited neutral nitrogen and ionic nitrogen molecules. Apart from these species, the plasma source also creates ground-state atomic nitrogen N(^4S) by dissociation as well as metastable nitrogen atoms N(^2D) and N(^2P) by dissociative excitation [162, 177]:

$$\mathrm{N_2}\left(X^1\Sigma_g^+\right) + e \rightarrow \mathrm{N}\left(^4S\right) + \mathrm{N}\left(^4S\right) + e \tag{5.25}$$

$$\mathrm{N_2}\left(X^1\Sigma_g^+\right) + e \rightarrow \mathrm{N^*}\left(^2D\right) + \mathrm{N}\left(^4S\right) + e \tag{5.26}$$

$$\mathrm{N_2}\left(X^1\Sigma_g^+\right) + e \rightarrow \mathrm{N^*}\left(^2P\right) + \mathrm{N}\left(^4S\right) + e\,. \tag{5.27}$$

However, emission lines of atomic nitrogen are absent in the plasma emission spectra, indicating the efficient production of neutral nitrogen radicals by the hollow cathode. Optical emission spectroscopy in a PA-MOCVD system using a similar hollow cathode plasma source as in this work agree with this observation [142]. Apart from the mentioned excitations and dissociation reactions further competing processes are taking place in a nitrogen plasma discharge [167, 178].

5.6 Growth kinetics in MEPA-MOCVD

Figure 5.10 schematically displays the growth process of the MEPA-MOCVD system. Metalorganic precursors, in this example TMG, are injected into the gas phase above the template, where they decompose by pyrolysis due to the growth temperature. A flux of nitrogen molecules streams through the hollow cathode, where they are cracked and excited. The nitrogen flow transports the plasma active nitrogen species from the hollow cathode to the afterglow regime above the growth surface where they interact chemically with Ga atoms to form GaN. Growth process control provisions enable a temporal and spatial controlled injection of MO and plasma-excited nitrogen precursors.

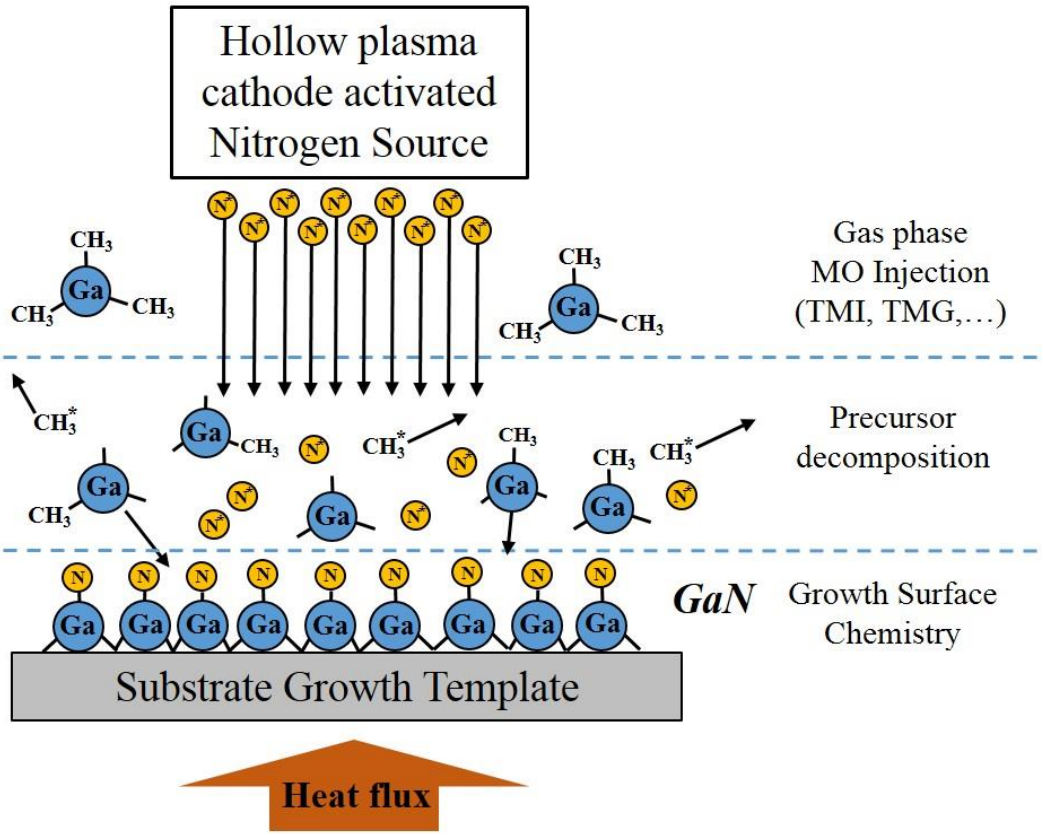

Figure 5.10: Schematic diagram of the GaN growth process in a MEPA-MOCVD system. The yellow circles that are labeled with N* are representative for the various plasma-excited species (N*, N_2*, N_2^+, etc.).

The composition of the nitrogen plasma is a complex mixture of ionic, neutral and excited nitrogen atoms as well as ionic, neutral and excited nitrogen molecules. All of these reactive species contribute directly and indirectly to the formation as well as decomposition of GaN. To discuss which species might promote the growth requires to compare the energies of the different plasma-excited nitrogen species related to the formation energy of GaN.
Newman et al. have described the chemistry in plasma-assisted MBE growth of GaN. In their study, the formation of GaN depends on plasma-activated nitrogen species at the growth surface, and the reverse reaction (decomposition) is limited by the kinetic barrier. They compared the potential energy of the various plasma-generated nitrogen species with the total energy barrier for the growth reaction of GaN as displayed in Figure 5.11. The total energy barrier is the sum of the change in Gibbs free energy for the formation of two GaN molecules

(1.9 eV) and the kinetic barrier (~ 1.3 eV) under MBE conditions [179]. As mentioned in chapter 4, the difference in Gibbs free energy describes the driving force of the GaN deposition in conventional MOCVD [129]. As displayed in Figure 5.11, the plasma-generated nitrogen species (atoms and molecules) provide considerably more than the required energy to form GaN.

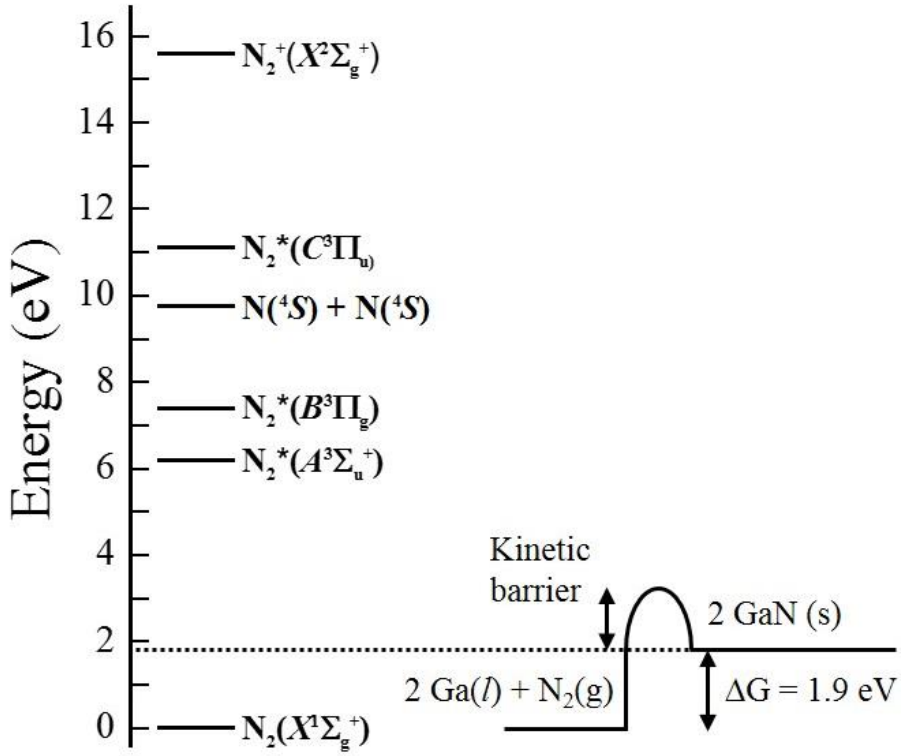

Figure 5.11: Comparison between energy levels of plasma-generated nitrogen species and energy barrier for GaN growth, adapted from [179].

In general, the growth reaction in PA-MOCVD is considered to be [160]:

$$\mathrm{Ga} + \frac{1}{2}\mathrm{N}_2^* \Leftrightarrow \mathrm{GaN}\,. \tag{5.28}$$

The growth reaction is reversible, and its direction is determined by mechanisms promoting the growth of GaN or against it.

A subset of possible GaN growth reactions as well as competing mechanisms is given in Table 5.3. The ionic N_2^+ molecule in the first growth reaction is from the $X\,^2\Sigma_g+$ state. The excited neutral nitrogen molecule N_2^* in reaction (5.28) as well as in growth reaction (2) in Table 5.3 are from one of the three electronic energy states $A^3\Sigma_u^+$, $B^3\Pi_g$ or $C^3\Pi_u$. The neutral nitrogen atom in reactions (3) and (8) is assigned to the N(^4S) state, whereas the metastable nitrogen atom in reactions (4) and (9) is either from the N(^2D) or N(^2P) state.

	Growth reactions		Competition to growth
(1)	$Ga + N_2^+ + e \rightarrow GaN + N^*$	(6)	$GaN \rightarrow Ga\uparrow + \frac{1}{2}N_2$ (decomposition)
(2)	$Ga + N_2^* \rightarrow GaN + N^*$	(7)	$Ga_{adsorbed} \rightarrow Ga\uparrow$ (desorption)
(3)	$Ga + N \rightarrow GaN$	(8)	$GaN + N \rightarrow Ga + N_2\uparrow$ or $Ga\uparrow + N_2\uparrow$
(4)	$Ga + N^* \rightarrow GaN$	(9)	$GaN + N^* \rightarrow Ga + N_2\uparrow$ or $Ga\uparrow + N_2\uparrow$
(5)	$Ga + N^+ + e \rightarrow GaN$	(10)	$GaN + N^+ + e \rightarrow Ga + N_2\uparrow$ or $Ga\uparrow + N_2\uparrow$

Table 5.3: Promoting and competitive growth reactions during GaN growth. The vertical arrows indicate the loss of either Ga or N_2 [118, 162, 180].

In the last three rows of Table 5.3 can be seen, that the atomic nitrogen species (ionic, neutral and excited) can participate in the formation (reactions 3-5) and decomposition (reactions 8-10) of GaN. The ionic and excited nitrogen molecules contribute directly to the growth of GaN as given in reaction (1) and (2). On the other hand, the reaction of Ga with a nitrogen molecular species results in the generation of atomic nitrogen, which can either take part in the growth reactions or competing reactions.

In case of the GaN growth reactions associated with atomic nitrogen species, the incorporation of the nitrogen atom into the lattice includes the release of excess energy. The energy released into the lattice can lead to GaN dissociation, desorption of Ga or the formation of point defects [118]. In contrast, the reactions (1) and (2) proceed, with one nitrogen atom of the plasma-generated nitrogen molecule forming GaN and the other one desorbs along with the excess energy.

The excited neutral nitrogen molecule at the electronic state $A^3\Sigma^+_u$ with 6.2 eV (see Figure 5.11) has the lowest potential energy and therefore should be the species with the lowest damaging potential. Another advantage of the excited nitrogen molecules at the $A^3\Sigma^+_u$ state is their relatively long lifetime in the order of seconds compared to the other nitrogen plasma species as given in Table 5.4. The long lifetime allows the N_2 ($A^3\Sigma^+_u$) species downstream from the plasma source and reach the growth surface in the afterglow regime. Due to their high energy state of 15.8 eV, the ionic nitrogen molecules N_2^+ are considered to be a possible cause for the degradation of the film quality via ion bombardment [162, 163]. A possibility to reduce the number of high-energetic plasma species and their degrading impact before they reach the growth surface is an increase of the reactor pressure. Increasing pressure causes more gas collisions of the plasma-excited nitrogen species and results in the predominantly low-energy reactive nitrogen molecules from the $A^3\Sigma^+_u$ state. Due to their low-energy and their long lifetime, the neutral excited nitrogen molecule is considered to be the major reactive precursor species in remote PA-MOCVD [176]. Thus, several authors suggested that these species are necessary for the plasma-assisted growth of high-quality GaN [142, 162] and InN [144, 161]. In PA-MBE is a controversial discussion if plasma-excited atoms [181] or molecules [115, 118,

182] are the species promoting the growth reaction. Others consider a mixture of nitrogen atoms and molecules with a negligible amount of nitrogen ions to contribute to the growth of group III-nitrides [163, 183].

Nitrogen species (electronic state)	Life time	Reference
$N_2\left(A^3\Sigma_u^+\right)$	~10^{-2} - 3.3 s	[184-187]
$N_2\left(B^3\Pi_g\right)$	3 - 13 µs	[184-186]
$N_2\left(C^3\Pi_u\right)$	36 - 40 ns	[184-186]
$N_2^+\left(X^2\Sigma_g^+\right)$	62 - 88 ns	[172, 185]

Table 5.4: Radiative lifetimes of plasma excited nitrogen molecules.

The simplified InN growth reaction is similar to the GaN growth reaction (5.28):

$$\mathrm{In} + \frac{1}{2}\mathrm{N}_2^* \Leftrightarrow \mathrm{InN} \tag{5.29}$$

with N_2^* including the states $A^3\Sigma^+_u$, $B^3\Pi_g$ and $C^3\Pi_u$ or indium reacts with the N_2^+ species associated to the $B^2\Sigma_u^+$ state:

$$\mathrm{In} + \frac{1}{2}\mathrm{N}_2^+ \Leftrightarrow \mathrm{InN}\,. \tag{5.30}$$

TMI thermally decomposes, and indium reacts with the plasma-generated nitrogen species. The reactions can proceed in the gas-phase or at the vapor-solid interface. The heat of formation (or change of enthalpy) for InN is ~ 1.2-1.4 eV [188, 189]. Consequently, the plasma-excited nitrogen atoms and molecules also possess more than sufficient potential energy for the formation of InN similar to the GaN formation.

5.6.1 Admix of hydrides

As described in chapter 4, the growth reaction in conventional MOCVD is an equilibrium reaction between Ga and ammonia as following:

$$\mathrm{Ga(g)} + \mathrm{NH_3(g)} \leftrightarrow \mathrm{GaN(s)} + \frac{3}{2}\mathrm{H_2(g)}\,. \tag{5.31}$$

Another option in MEPA-MOCVD is the admix of hydrogen or ammonia to form active NH*/NH_x* species to promote the growth of group III-nitrides. Reactive NH*/NH_x* species can be generated directly in the plasma source by the introduction of ammonia and hydrogen into the nitrogen plasma source feed. Another option is the admix of ammonia and hydrogen into the downstream of the nitrogen plasma. The plasma-excited nitrogen species crack the ammonia or hydrogen and form excited NH*/NH_x* species.

The reactive NH_x^* can react with the group III metal atom as expressed in the following growth mechanism:

$$Ga(g) + NH_x(g) \leftrightarrow GaN(s) + \frac{x}{2} H_2(g). \tag{5.32}$$

5.7 Conditioning of plasma-activated nitrogen species by process parameters

Variation of the process parameters affects the concentration of reactive nitrogen species and their kinetic energies. Optimization of the process parameters enables stabilization of the growth surface chemistry. The introduction of hydrogen or ammonia into the nitrogen feed of the plasma source or the nitrogen plasma downstream to form NH_x^* ($x \geq 1$) species is studied by in-situ PES and UVAS. Furthermore, the influence of process parameters such as plasma power and nitrogen flow through the plasma source are investigated.

5.7.1 Ammonia admix

The admix of ammonia into the downstream of the plasma-activated nitrogen species as a function of plasma power is investigated by UVAS spectroscopy. The introduction of a constant flow of 150 sccm ammonia is via the upper injection ring (Figure 5.12 on the right). The nitrogen plasma flow is 750 sccm under a reactor pressure of 2.0 Torr. UVAS is measured directly below the injection ring to determine the ammonia decomposition as a function of applied plasma power from 0 W (no plasma) to 500 W, while all other process parameters such as reactor pressure, temperature and the flow through the hollow cathode are kept constant.

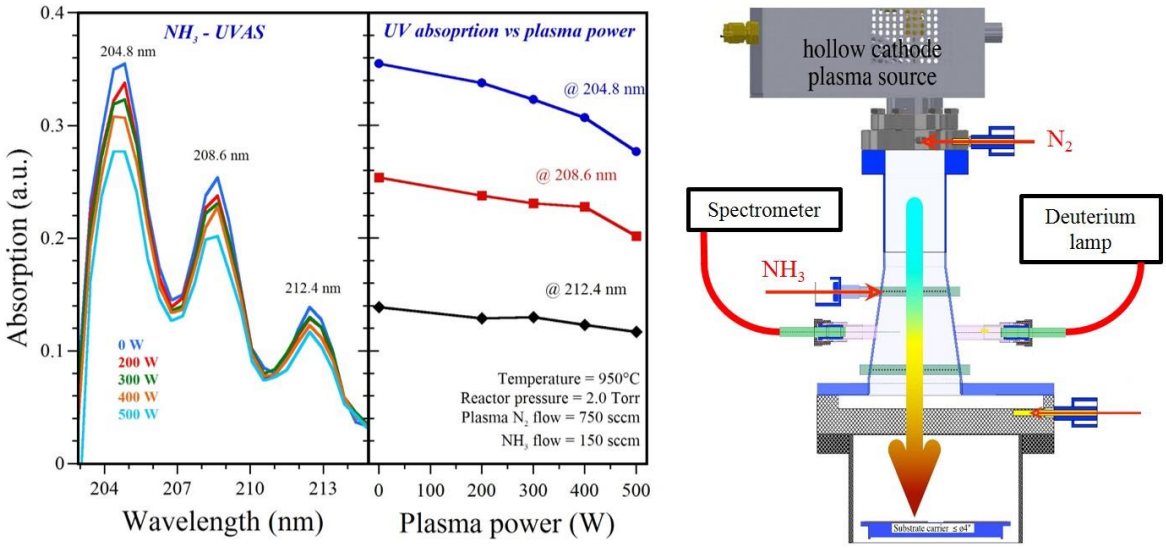

Figure 5.12: On the left UV absorption spectra of ammonia for various applied plasma power (top left). Absorption intensity as a function of plasma power (bottom left). On the right schematic view of UVAS setup and where ammonia is injected into the nitrogen plasma downstream.

The left side of the split graph in Figure 5.12 displays the UV absorption spectra as a function of the applied plasma power from 0 to 500 W in the wavelength range between 200 nm to 215 nm. All spectra show prominent absorption features at 204.8 nm, 208.6 nm and 212.4 nm in the UV range. The emission wavelength bands and the magnitude of their intensities match with the UV absorption bands of ammonia [169, 190]. Without a plasma (= 0 W), the peak intensity is the strongest and decreases with increasing plasma power. The right side of the split graph in Figure 5.12 correlates the ammonia absorption peak at 204.1 nm to the applied plasma power. The presence of plasma leads to the conversion of NH_3 to NH* containing species. At a plasma power of 500 W, the absorption has decreased by more than 20 % compared to the absorption without a plasma. With enhanced plasma power, more NH_3 molecules are converted NH* species. Thus, the reduction of the absorption intensities is an indication for plasma-assisted decomposition of ammonia.
PES offers another way to verify the creation of NH* species in the nitrogen plasma downstream. The NH* molecule has three very prominent emission lines between 336 nm and 338 nm corresponding to the following energy level transition of the triplet system [169]:

$$A^3\Pi \rightarrow X^3\Sigma^- . \tag{5.33}$$

This emission line is very close to one emission line of the N_2 molecule of the second positive series at 337.3 nm as depicted in Figure 5.13. Due to the overlap of these emission lines [191] it is difficult to distinguish between the NH* and N_2 species and ascertain quantitative information.

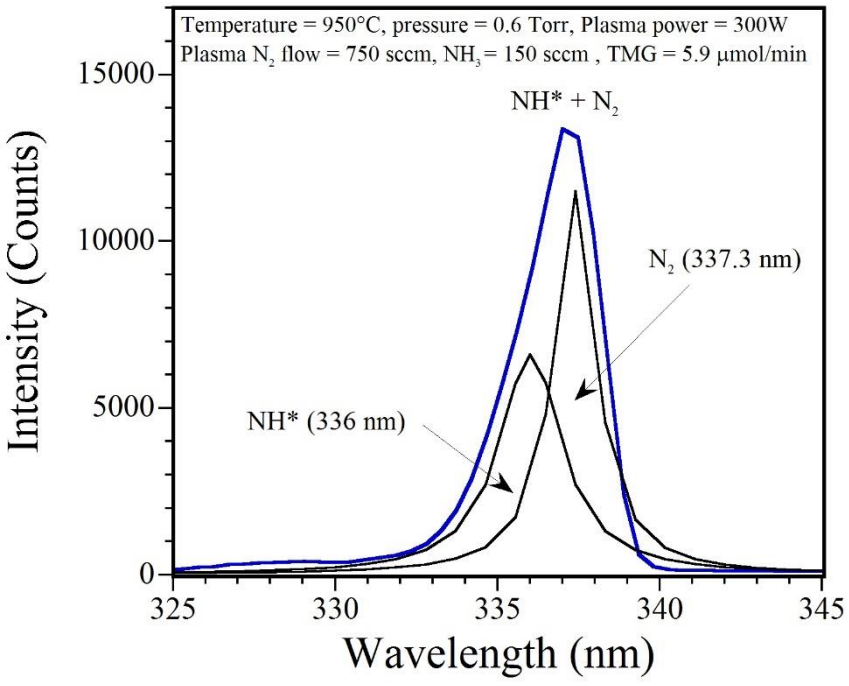

Figure 5.13: Experimental overlap (blue line) and deconvoluted (black lines) emission bands of the NH* and N_2 species.

5.7.2 Hydrogen admix

It has been reported that the admix of hydrogen into the nitrogen plasma also results in the formation of NH*/NH_x* species [160]. Various hydrogen flows are added into the nitrogen plasma downstream via the upper injection ring. PES is carried out right below the hydrogen injection port to investigate the plasma composition. A schematic layout of the experiment is given in Figure 5.14 on the right. The plasma emission is measured between 270 nm to 430 nm to cover the second positive nitrogen series including the convoluted emission line for NH* and N_2 at 337 nm. The pressure, plasma power and the nitrogen flow through the hollow cathode are kept constant.

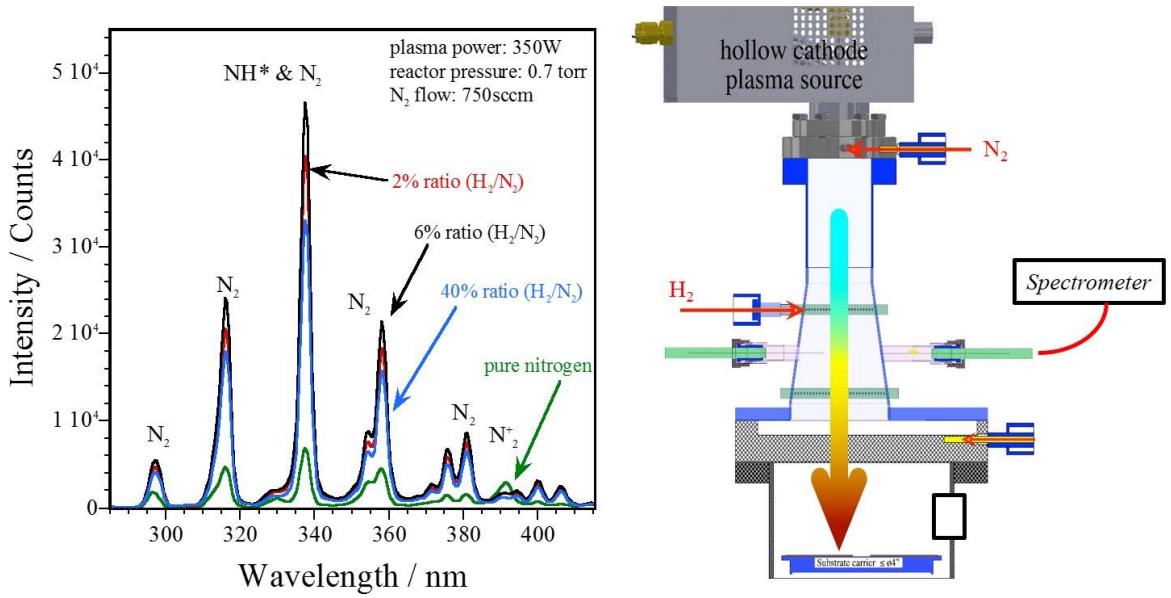

Figure 5.14: PE spectra for different hydrogen / nitrogen ratios.

Figure 5.14 on the left shows compares the optical emission of a pure nitrogen plasma with N_2-H_2 plasmas with different H_2/N_2 flow ratios. Low H_2/N_2 ratios between 2 – 6 % result in a strong intensity increases of the emission lines of the second positive N_2 system. In contrast, the emission line of the N_2^+ species at 391.4 nm almost disappears.

Compared to the enhancement of the peaks of the second positive nitrogen molecules, the intensity of the convoluted peak (337 nm) for NH* and N_2 is significantly higher as displayed in Figure 5.15. This increase might be due to the cracking of H_2 molecules and their interaction with plasma-excited nitrogen which lead to the formation of NH/NH_x species.

The decrease in N^+_2 particles can be explained by the charge transfer reaction [177]:

$$N_2^+ + H_2 \rightarrow N_2H^+ + H\,. \tag{5.34}$$

The N_2H^+ ion recombines with an electron and form NH and atomic nitrogen species:

$$N_2H^+ + e \rightarrow NH + N\left(^4S\right). \tag{5.35}$$

There are far more gas phase chemistry reactions taking place in low pressure H_2/N_2 plasma mixtures. A detailed list can be found in reference [192].

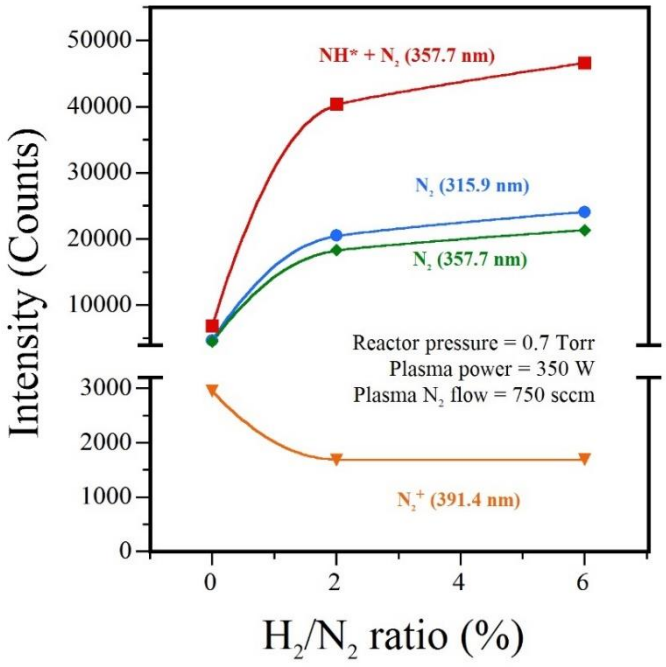

Figure 5.15: Effect of hydrogen admix on intensities of N_2, N_2^+ and NH* + N_2 emission lines.

The intensity increase of the N_2 and NH* + N_2 emission lines for a small H_2/N_2 ratio (2-6%) can be explained with the destruction of metastable N_2 states by H_2, leading to the suppression of the stepwise ionization of N_2. Instead, electron collisions excite more of the N_2 and NH states [193].

UV absorption and plasma emission spectroscopy revealed that the admix of either ammonia or hydrogen leads to the formation of NH* species, which enable another process reaction for the growth of group III-nitrides. Furthermore, the addition of ammonia and hydrogen affects the composition of the plasma-generated nitrogen species by enhancing the number of N_2 and NH* species, but also suppress the nitrogen ions N_2^+.

5.7.3 Plasma power and nitrogen plasma flow

One challenge in MEPA-MOCVD is the correlation of process parameters such as applied plasma power and flow through the hollow cathode to the composition of the plasma-excited nitrogen species and their kinetic energies at the growth surface. Analysis of the real-time time PES above the growth surface correlates the concentration of plasma active species to the applied plasma power and nitrogen flow through the plasma source. PES is measured above the growth surface as displayed in Figure 5.3.
As displayed in Figure 5.16 on the left, raising the applied plasma power leads to an intensity increase of the emission lines corresponding to the plasma-generated nitrogen species N_2, N_2^+ and NH*. More excited nitrogen molecules are observed above the growth surface with increasing plasma power. Figure 5.16 on the right shows the influence of plasma power on the excited nitrogen molecules N_2 of the second positive system and excited indium close to the growth surface. The emission line at 357.7 nm represents the nitrogen species of the second positive series, and the plasma line at 451 nm indicates excited indium. With increasing plasma power, the N_2 intensity increases linearly while the intensity of excited indium remains constant. The other nitrogen species behave similarly as a function of plasma power. At higher

plasma powers more plasma-excited nitrogen molecules are generated and transported towards the growth surface. The TMI decomposition is not affected by the plasma power due to the spatial separation between nitrogen and MO precursor injection in the used MEPA-MOCVD system. The epitaxial growth of GaN by radical enhanced MOCVD (REMOCVD), which also utilizes a plasma source to create reactive nitrogen precursors shows a similar behavior of the reactive nitrogen and MO precursors [160].

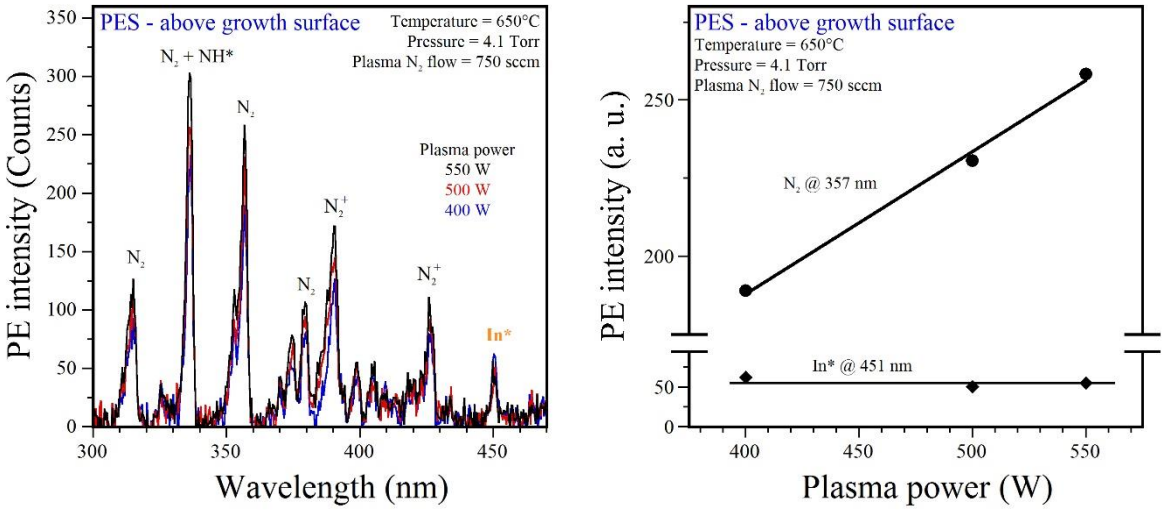

Figure 5.16: On the left, plasma emission spectra close to the growth surface for various plasma powers. On the right, emission intensity of excited indium In* at 451 nm and excited nitrogen N_2 at 357.7 nm in dependence of plasma power.

Figure 5.17 shows plasma emission spectra for various nitrogen flows through the plasma source in the range between 300 to 470 nm. The most intense peaks in this wavelength range are assigned to excited nitrogen molecules of the second positive system as well as ionic nitrogen N_2^+ at 391.4 nm and 428 nm and the overlapped N_2 + NH* peak. Additionally, excited atomic indium In* with lines at 325 nm, 410 nm and 425 nm is observed as well.

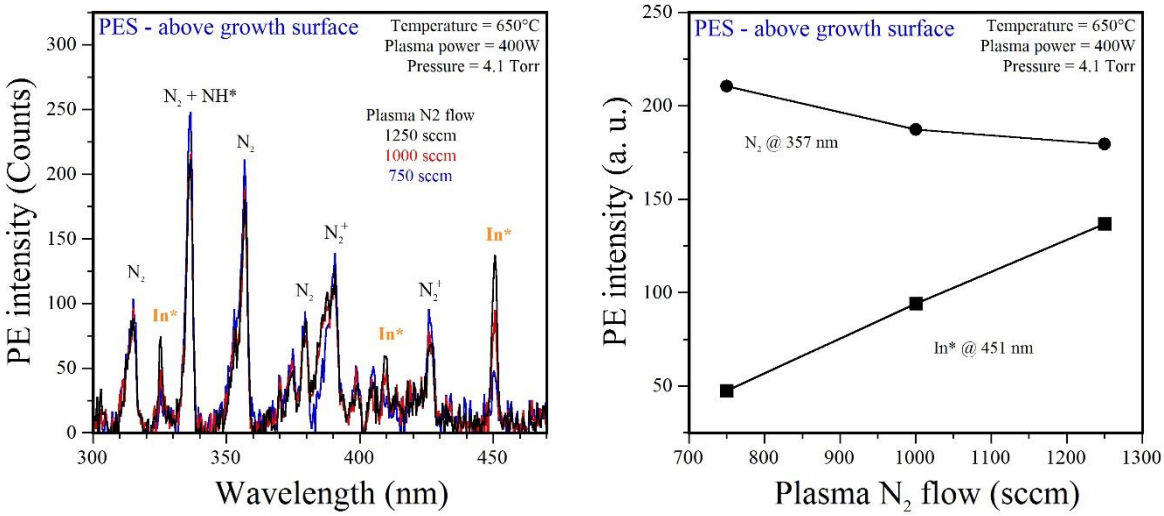

Figure 5.17: On the left, plasma emission spectra close to the growth surface as function of nitrogen flow through the plasma source. On the right, emission intensity of excited indium (line at 451 nm) and excited nitrogen (line at 357.7 nm) with plasma nitrogen flux.

An opposite influence on the nitrogen molecules and excited indium for various flows through the hollow cathode plasma source is observed compared to the variation of the plasma power. The emission intensity of excited indium increases for higher nitrogen flows while the number of nitrogen species even reduces slightly. The emission lines of related excited indium and nitrogen species show similar behavior as a function of plasma nitrogen flow. The higher flow rates result in higher kinetic energies of the plasma-generated nitrogen species leading to an enhanced excitation of thermally decomposed indium atoms in the gas phase above the growth surface. For very high nitrogen plasma flow rates, the contribution of non-excited nitrogen N_2 becomes dominant. These low energy molecules have collisions with the plasma-excited nitrogen species and further reduce their energies.

5.7.4 Reactor pressure

Reactor pressure is a particular factor in the conditioning of the plasma-generated nitrogen species and their kinetic energies during MEPA-MOCVD and how they influence the quality and thickness of the grown layer.
Thus, a series of InN films are grown by MEPA-MOCVD at different reactor pressures. The emission intensities of the reactive nitrogen species measured by in-situ PES are correlated to the crystal quality and the film thickness of the grown InN. Figure 5.18 on the left shows the intensity of the emission lines for the plasma-generated nitrogen species N_2, N_2^+ and NH* as a function of reactor pressure. The emission intensities of N2 and NH* increase steadily with decreasing pressure from 4.7 Torr. In the step from 2.8 Torr to 2.4 Torr, the intensities for the N_2 and NH* drastically increase. Due to the lower pressure, fewer collisions take place resulting in a higher concentration of activated nitrogen species. A decreasing pressure also leads to a greater flux and higher kinetic energies of the N_2 species. At 2.4 Torr the kinetic energies are too high causing etching of the deposited InN occurs agreeing with the reducing trend of the film thickness with decreasing reactor pressure (Figure 5.18 on the right).

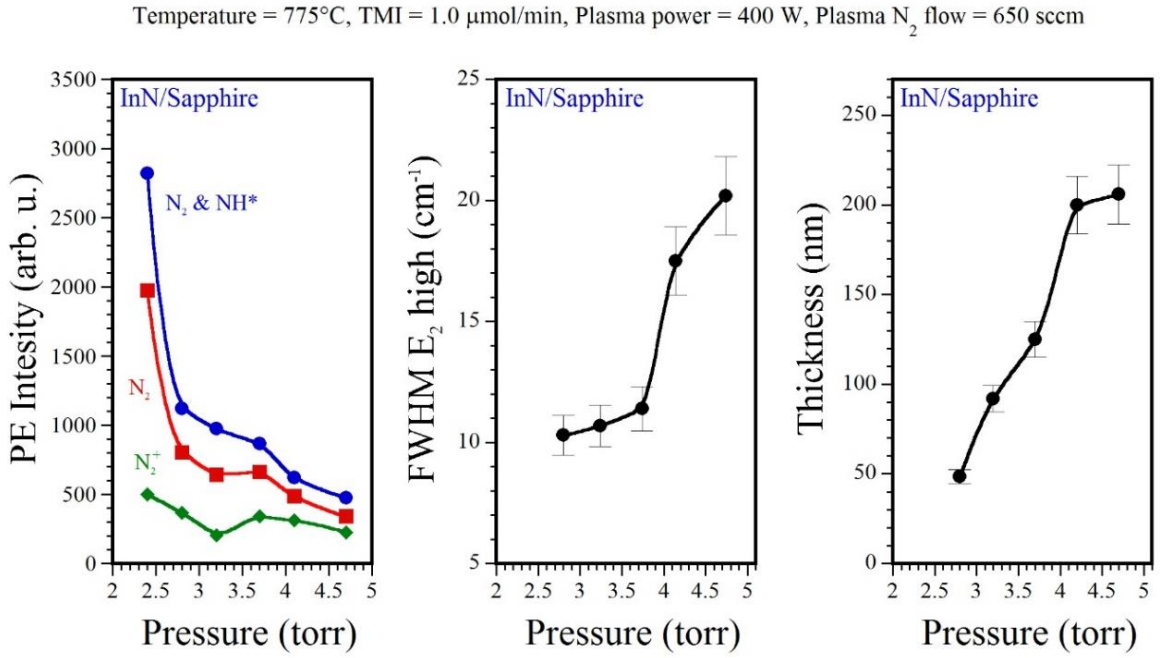

Figure 5.18: Correlation between emission intensity of plasma-excited nitrogen species to crystal quality and film thickness as a function of reactor pressure.

The decrease in the FWHM of the E_2(high) phonon mode (central graph in Figure 5.18) indicates a significant enhancement of the crystal quality with lower pressures. Since pressure also affects all the flows and especially the transport of the excited nitrogen species to the growth surface, further optimization of the growth parameters is necessary to stabilize the growth surface chemistry and enable growth of high-quality group III-nitride films. Plasma power and the nitrogen flow through the plasma source are two more process parameters that have demonstrated to tailor the generation and the number of active nitrogen. Furthermore, the introduction of hydrogen and ammonia extends the composition of the plasma-excited species.

5.8 Substrate preconditioning

All group III-nitride alloys are grown on c-plane orientated (0001) sapphire substrates with a two-inch diameter. The sapphire templates are single-side polished and have a thickness of 430 µm ± 25 µm. Simultaneously to the heat up of the reactor to 450°C, the reactor pressure is set to 3.3 Torr and maintained using the exhaust valve controller. At 450°C, the surface of the sapphire template is exposed to a hydrogen plasma with a hydrogen flow of 100 sccm and an applied plasma power of 150 W for 10 minutes to remove surface contaminations. The exposure to plasma-excited hydrogen H* at low temperatures is an effective method to clean the substrate surface.

The next chapter will describe in detail the growth process parameters for the fabrication of $In_xGa_{1-x}N$ alloys by MEPA-MOCVD. Subsequently, the structural and optoelectronic layer properties are presented and discussed considering the growth conditions.

6 Properties of InGaN layers grown by MEPA-MOCVD

MEPA-MOCVD is a growth approach to stabilize In-rich InGaN alloys while suppressing the formation of nanoscale phase segregations. In this study, a set of InGaN epilayers with high In-content over a wide compositional span ($0.3 < x < 1$) has been grown directly on c-plane sapphire substrates. The first section describes the growth process parameters and the following sections present structural, morphological and optoelectronic properties of the $In_xGa_{1-x}N$ films with different compositions. A particular focus of this research work is the investigation of nanoscale phase separations, a major challenge in the growth of ternary and multinary semiconductor alloys. Phase segregations can lead to bandgap fluctuations and limit the optical and electronic internal device efficiency. The study of nanoscopic inhomogeneities by TERS and s-SNIN contributes to a better understanding of this phenomenon and enables potential solutions to suppress phase segregations.

6.1 InGaN growth process parameters

InGaN epilayers with an estimated In-content x = [0.33, 0.5, 0.62, 0.7, 0.75] are grown on sapphire substrates by MEPA-MOCVD. The InGaN film deposition are carried out at a constant growth temperature of 775°C and a constant reactor pressure of 3.3 Torr. Figure 6.1 illustrates the modulated MO and nitrogen precursor supply of the InGaN deposition process.

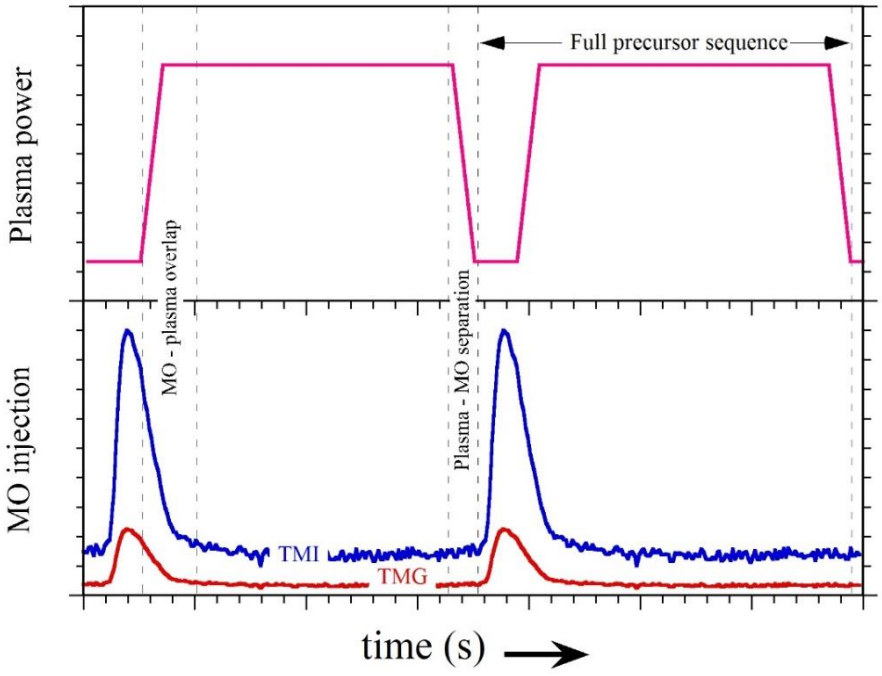

Figure 6.1: Pulsed precursor supply for InGaN growth. Red (TMG) and blue (TMI) line describe MO injection pulse. The pink line describes the modulation of the applied plasma power.

Metalorganic and nitrogen plasma precursors are delivered into the reactor in an alternating pulse sequence. The pulse sequence is split into two parts. First, TMI and TMG are injected simultaneously via the showerhead into the reactor chamber. During the pulse injection, the applied plasma power is low, which results in a small number of plasma-activated nitrogen species. Thus, a metal layer containing In- and Ga-atoms is deposited on the surface of the substrate or film, respectively. When the MO concentration reduces, the plasma power is ramped up from its low-level value to a high value (MO – plasma overlap in Figure 6.1). Due to the exposure to a high concentration of active nitrogen species, the metal layer is nitrided, which results in the formation of an InGaN layer. At the end of the pulse sequence, the applied plasma power ramps down to its value and the next precursor cycle starts. Except for a short overlap, while the plasma power is rising (MO-plasma overlap in Figure 6.1), the MO and nitrogen precursor supply are temporally separated. The temporal separation of metalorganic and active nitrogen precursors enables an increased diffusion of the adatoms on the surface. The MO pulse widths for TMG and TMI were kept constant at 1 second. The N_2 flow through the hollow cathode was 750 sccm, while plasma pulse was pulsed from 50 to 400 W. The selected plasma power range ensures a remote nitrogen plasma and minimizes possible damage of the deposited layer by ions and high-energy species which reach the growth surface. To achieve targeted $In_xGa_{1-x}N$ compositions with an indium content from 0.33 to 0.75, the TMG:TMI flow ratios per sequence were adjusted individually. The correlation for the targeted In-content depends on the ratio x = TMI / (TMG+TMI). For sample #760, a thin InN buffer layer (~20 nm) was deposited prior the InGaN growth. An overview of the set of InGaN samples grown by MEPA-MOCVD is given in Table 6.1.

Sample	**$In_xGa_{1-x}N$ composition x = TMI / (TMI+TMG)**	**Thickness (nm)**
#749	$In_{0.33}Ga_{0.67}N$	43
#751	$In_{0.50}Ga_{0.50}N$	44
#760	$In_{0.62}Ga_{0.38}N$	85
#753	$In_{0.70}Ga_{0.30}N$	86
#752	$In_{0.75}Ga_{0.25}N$	86

Table 6.1: List of $In_xGa_{1-x}N$ samples studied in this thesis. All epilayers were grown by MEPA-MOCVD at growth temperature of 775°C and a reactor pressure of 3.3 Torr. The thickness values are determined by ellipsometry and FTIR spectroscopy.

6.2 Structural properties of InGaN alloys grown by MEPA-MOCVD

One method to assess the structural properties of InGaN alloys such as crystal quality and strain is Raman spectroscopy. Furthermore, Raman spectroscopy enables to determine the In and Ga partitions of the deposited InGaN compound semiconductors due to the dependence between composition and the phonon frequencies.

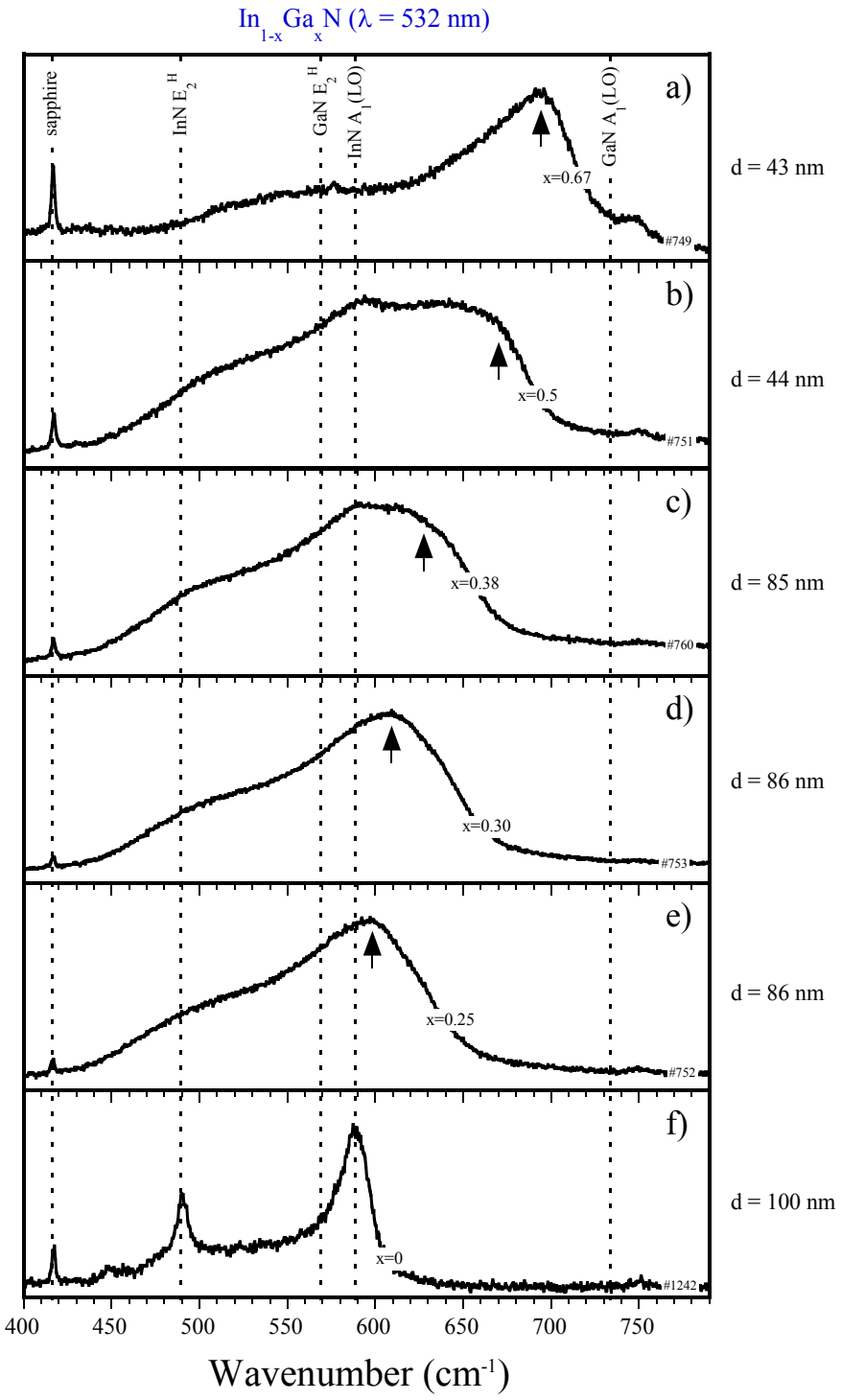

Figure 6.2: Frequency shift of A_1(LO) Raman mode in ternary $In_xGa_{1-x}N$ with increasing Ga content. For clarity, the Raman spectra are normalized. The black arrows indicate the frequency position of the InGaN A_1(LO) mode.

In this study, Raman spectroscopy was performed at room temperature in backscattering geometry with different visible excitation wavelengths λ = 457 nm, 532 nm and 633 nm. Figure 6.2 displays Raman spectra of the different InGaN alloys measured at 532 nm (= 2.33 eV) in the frequency range from 400 to 800 cm^{-1}, in which the E_2 (high) and A_1(LO) Raman modes for the complete $In_xGa_{1-x}N$ composition range ($0 \leq x \leq 1$) are located. For clarification, a Raman spectrum of the end-member InN also grown at 775°C by MEPA-MPCVD is added.

Based on the modified random-element isodisplacement (MREI) model, the E_2(high) and A_1(LO) Raman mode in InGaN alloys exhibit a one-mode-behavior. The MREI model predicts a linear frequency shift for both Raman modes between the modes of the composition end-members InN and GaN as a function of the $In_xGa_{1-x}N$ composition [78]. The one-mode behavior of InGaN has been verified by other groups [194-198]. Except for InN (Figure 6.2f), no distinct E_2(high) mode is observed in the ternary $In_{1-x}Ga_xN$ alloys which implies a low crystal quality due to disorder and disorientation as well as strain or stress. A possible cause for the strain is the lattice mismatch and different thermal expansion coefficients between the deposited InGaN layers and the sapphire substrate. Additionally, the group III-nitride material system is not a lattice-matched system (see chapter 2), which also results in strain gradients for layers above a certain thickness, depending on the composition [199]. During the growth process, strain is built-in and increases until a specific layer thickness, named critical layer thickness, is reached. Above the critical layer thickness, the film relaxes, and strain is relieved due to the introduction of dislocations. The formation of defects is energetically favored, because it is lesser than the accumulated elastic energy.

Subsequently, films above the critical layer thickness suffer high dislocation densities and defects, which propagate along the growth direction. All obtained Raman spectra (Figure 6.2) show a peak at 417 cm^{-1}, which is assigned to the A_{1g} mode of the sapphire substrate. Some Raman spectra also show a weak peak at 749 cm^{-1} which belongs to the E_g mode of sapphire. The presence of both peaks indicates a low film thickness for all samples. Analysis of FTIR spectroscopy and ellipsometry verify a low film thickness for all InGaN samples. The film thickness range is between 40 to 100 nm. InGaN layers with a Ga-content of 40% or less are twice as thick compared to Ga-rich InGaN films. According to literature, the critical layer thickness for an InGaN composition with an In-content of ~20% grown on top of a GaN buffer is less than 30 nm [200, 201]. For InGaN alloys with an Indium composition above 40%, the critical layer thickness is almost 1 nm [201, 202]. The lattice mismatch between InGaN and sapphire is much larger than the lattice mismatch between InGaN and a GaN buffer layer. Given that, it is fair to assume that, the examined InGaN layers in this thesis possess tensile strain. The thin InGaN layers #749 and #751 with a thickness below 50 nm are most likely completely strained. The thickness of the In-rich $In_xGa_{1-x}N$ samples ($x > 0.6$) might be above the critical layer thickness and exhibit a high dislocation density. Another effect of strain relaxation at the critical layer thickness is the occurrence of three-dimensional (3D) growth. The surface of thicker InGaN layers becomes three dimensional, and naturally rougher. Therefore, an increase in surface roughness could indicate strain relaxation.

To verify if the InGaN layers show a 3D growth and increased roughness, the surface morphology of each sample is studied by AFM.

Figure 6.3 displays the AFM surface morphology of the InGaN layers with an estimated In-content of 62% and 70%. As shown in Figure 6.3a-c, the surface roughness of sample #760 has a root mean square (RMS) value around 2.5 nm. Many islands with similar height are observed on the surface. Compared to sample #760, the layer surface of sample #753 is very smooth with

a RMS value below 1.5 nm. The surface topography also reveals a uniform distribution of islands with identical height but smaller than sample #753 (Figure 6.3d-f). The formation of uniform distributed islands with a low height can be an indication for 3D growth, though the surface is rather smooth. Both samples are grown under the same growth conditions with the only difference being the ratio of TMI and TMG.

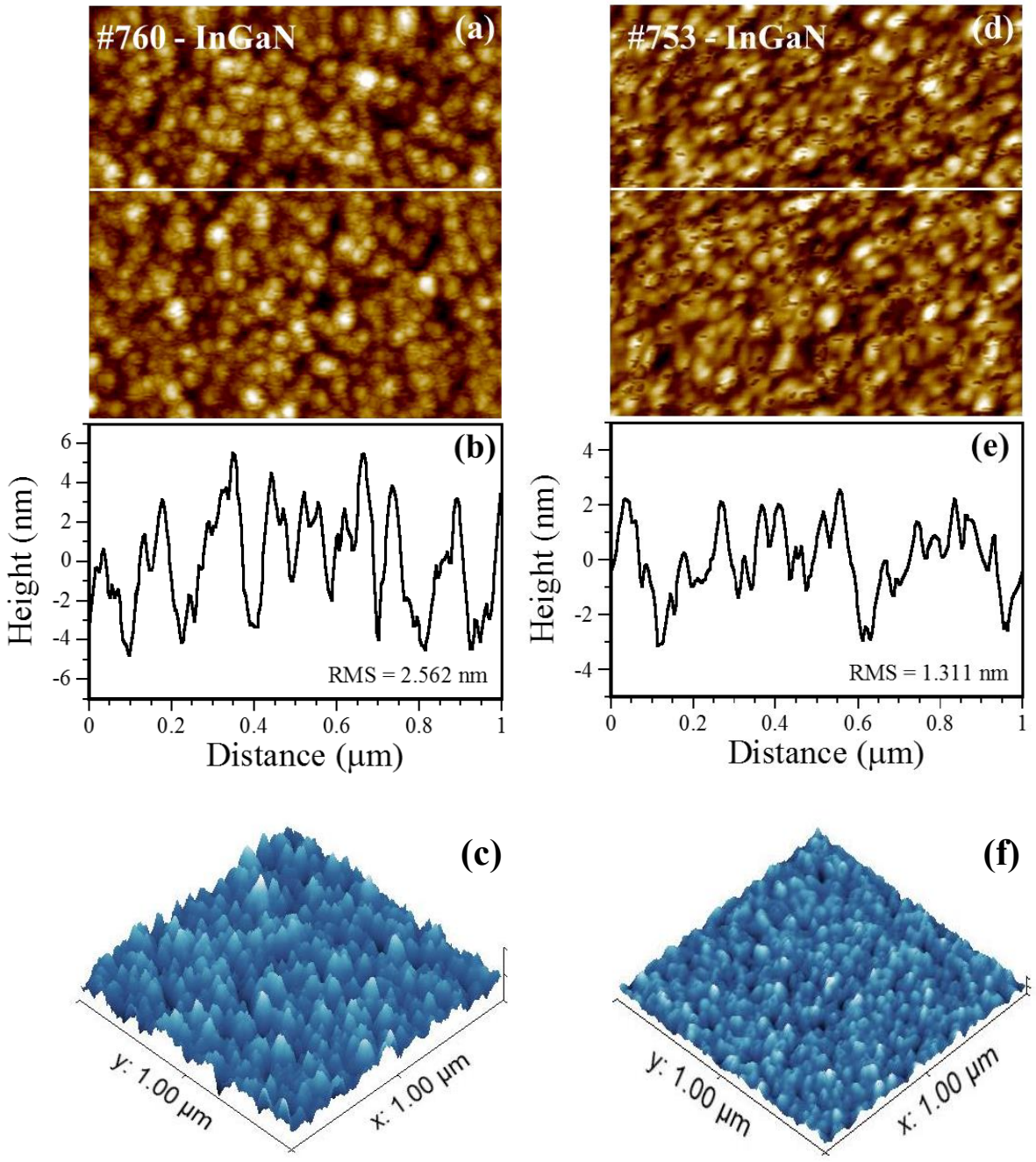

Figure 6.3: AFM surface topography of sample #760 - $In_{0.62}Ga_{0.38}N$ (a) and sample #753 - $In_{0.70}Ga_{0.30}N$ (d) with height profile (b) and (e). 3D-plot of 1 µm x 1 µm scan area (c) and (f).

6.3 InGaN composition by µRaman spectroscopy

The plot of the stacked Raman spectra in Figure 6.2 displays a systematic shift of the A_1(LO) Raman mode as a function of the InGaN composition (pointed out by small black arrows). With increasing Ga-content, the A_1(LO) mode shifts to higher frequency values as predicted by the MREI model. To investigate the homogeneity of the different InGaN compositions, µRaman mapping with an excitation wavelength of 532 nm are measured. The Raman maps have the dimensions of 10 µm x 10 µm with a step size of 1 µm in x- and y-direction. The maps on left-hand side of Figure 6.4a-e display the In-concentration for each InGaN alloy. The In-content is calculated by conversion of the A_1(LO) frequency based on the linear dependency of the MREI model. For each map, all Raman spectra are fitted by a fit function and the observed peaks are assigned to the corresponding phonon modes. The graphs on the right-hand side in Figure 6.4a-e, show exemplary how the Raman spectra are fitted for each map. Next to the sample number, the targeted $In_xGa_{1-x}N$ composition is given. On a microscopic scale, the Raman maps of all InGaN samples indicate a high compositional homogeneity with compositional fluctuations of less than ±1%. In every spectra, a very broad peak in the range of the E_2(high) mode for $In_xGa_{1-x}N$ is observed. The measured frequencies of the unnamed peaks in Figure 6.4a-e do not correspond to the evaluated composition. The frequency deviation and large width indicates crystalline disorder in the $In_xGa_{1-x}N$ layers.

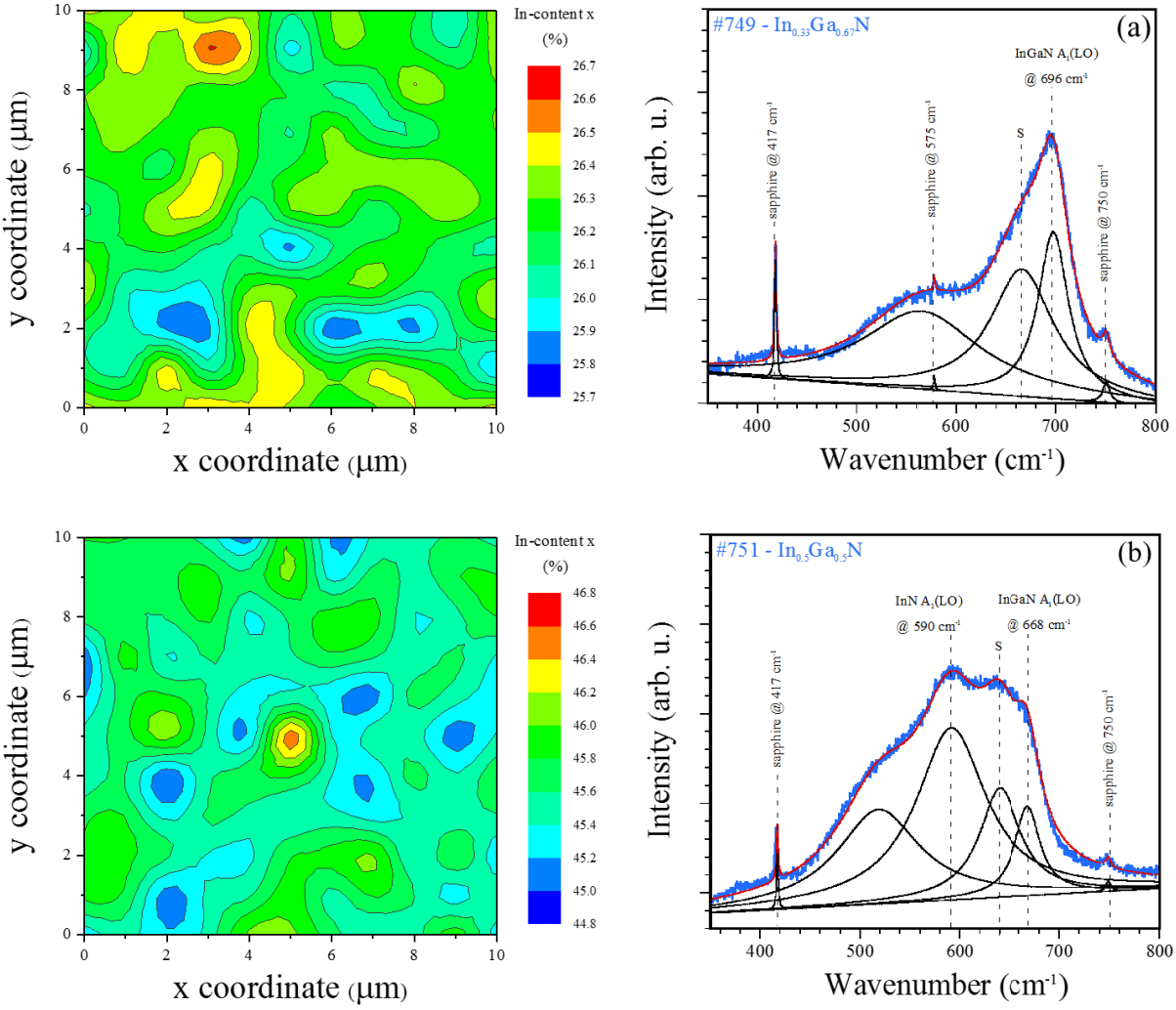

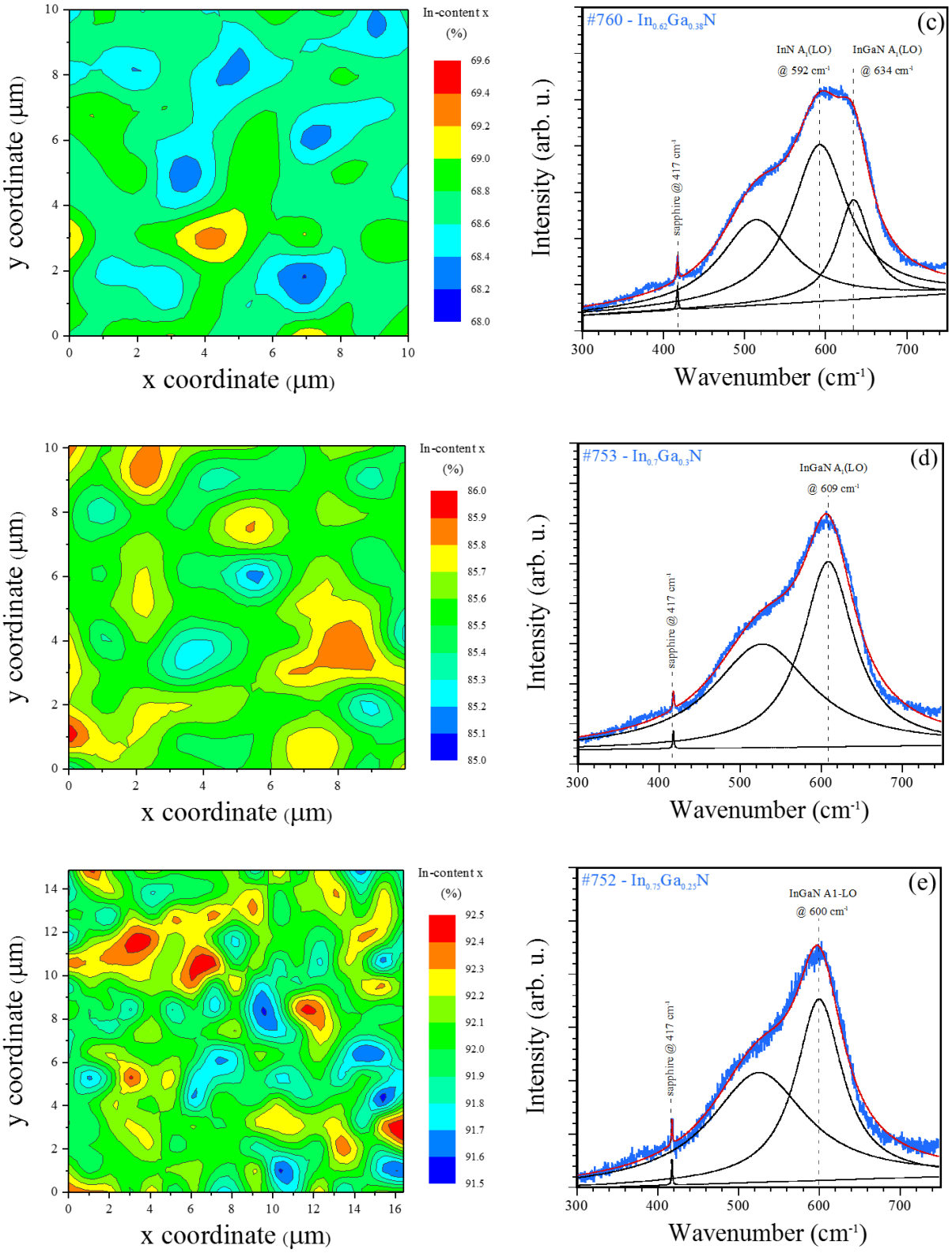

Figure 6.4a-e: Maps on the left show In-content x of $In_xGa_{1-x}N$ alloys. On the right is an example how map spectra are fitted with experimental single map spectrum (blue), fit function (red) and single fit peaks (black).

These results do not allow a conclusion about the existence of phase segregations, because the resolution of μRaman spectroscopy is not sufficient to identify nanoscopic inhomogeneities. The investigation of nanoscale phase segregations by the characterization methods TERS and SNIN with spatial resolution below the optical diffraction limit will be discussed in section 6.5.

The average InGaN composition of the entire map for each sample is plotted as a function of the input flow ratio x = TMG / (TMI+TMG) in Figure 6.5. The estimated and achieved $In_xGa_{1-x}N$ compositions are also listed in Table 6.2. On the assumption that the input MO flow ratio would result in a similar InGaN composition, a linear dependency would be expected, but instead a bowing/exponential behavior between targeted and outcome InGaN composition is found.

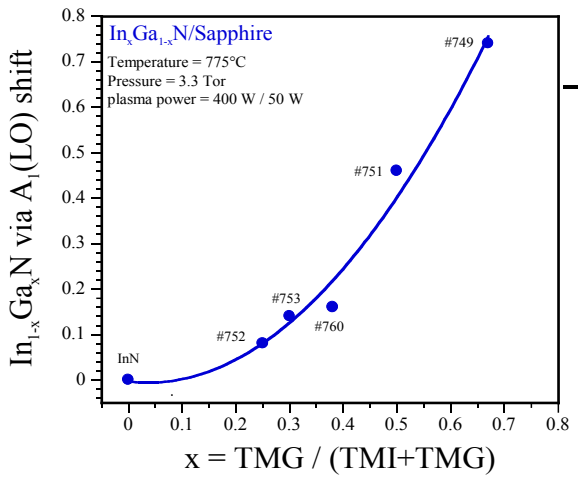

Figure 6.5: Estimated InGaN composition as a function of TMG and TMI precursor ratio.

Sample	$In_xGa_{1-x}N$ x = TMI/(TMI+TMG)	$In_xGa_{1-x}N$ by A_1(LO) shift
#749	$In_{0.33}Ga_{0.67}N$	$In_{0.26}Ga_{0.74}N$
#751	$In_{0.50}Ga_{0.50}N$	$In_{0.46}Ga_{0.54}N$
#760	$In_{0.62}Ga_{0.38}N$	$In_{0.69}Ga_{0.31}N$
#753	$In_{0.70}Ga_{0.30}N$	$In_{0.86}Ga_{0.14}N$
#752	$In_{0.75}Ga_{0.25}N$	$In_{0.92}Ga_{0.08}N$

Table 6.2: Estimated InGaN composition compared to achieved composition via A_1(LO) Raman shift.

For an estimated Gallium content of 40% and higher, the deposited InGaN layers are in reasonable range of the targeted composition with content differences between 4% - 9%. For targeted Ga-contents up to 30%, the evaluated Ga-fraction of the InGaN films is significantly lower. Instead of expected 25% and 30% Gallium content, only 8% and 14% Gallium are incorporated, respectively. Under these growth conditions, the In-incorporation is significantly more dominant than the Ga-incorporation. Furthermore, samples with high In-content (x > 50%) are twice as thick compared to the Ga-rich samples.

6.3.1 InGaN composition by high-resolution X-ray diffraction

Another technique to investigate the structural properties of the InGaN epilayers and determine the In-composition is high-resolution X-ray diffraction (HR-XRD). A Philips MRD was utilized to perform HR-XRD scans of selected InGaN layers to characterize their crystal quality and the In-concentration. Figure 6.6 displays the HR-XRD profile of the InGaN sample #752. Two Bragg peaks are observed in the 2θ - ω scan, InGaN (0002) and Al_2O_3 (0006), which correspond to the grown $In_xGa_{1-x}N$ epilayer and the sapphire substrate, respectively. The diffraction from (0002) $In_xGa_{1-x}N$ arises as a single peak and no macroscopic phase separation is observed. The peak location at 31.75° is assigned to the diffraction of the InGaN (0002) plane and provides information about the composition. Based on the assumption that Vegard's law applies, the $In_xGa_{1-x}N$ alloy composition can be calculated by determining the shift of the (0002) InGaN diffraction peak in relation to the (0006) sapphire peak. For sample #752, the InGaN layer exhibits an In-content of 0.86, which is close to 0.92 determined by μRaman mapping. The lattice parameters in InGaN depend on the In-fraction as well as strain, which can explain the difference in the alloy composition. The In-rich InGaN layer grown by MEPA-MOCVD possess a good crystallinity due to the narrow full width at half maximum (FWHM) of 0.338° (inset of Figure 6.6). The second Bragg peak at 41.475° is from the sapphire substrate.

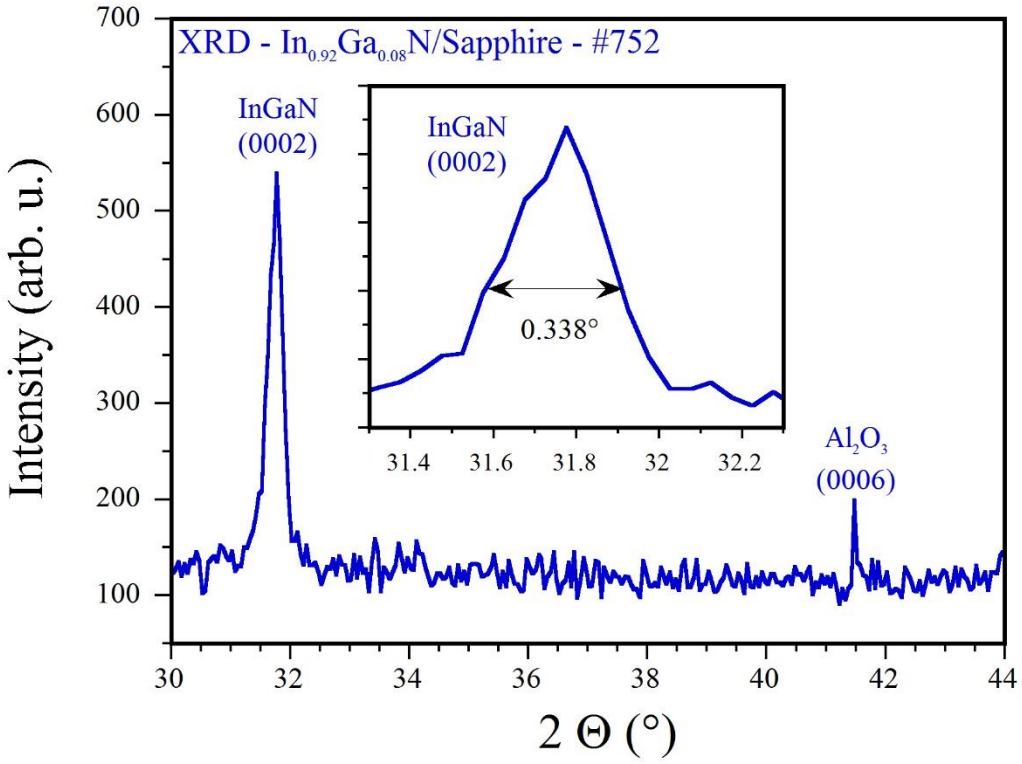

Figure 6.6: HR-XRD scan (2-theta) of $In_{0.8}Ga_{0.2}N$ sample.

The other samples with In-content x = 0.33 (#749) and 0.5 (#751) were also measured by HR-XRD and are displayed in Figure 6.7. In the HR-XRD scan of sample #751 the InGaN (0002) peak is observed at 33.11°, but the sapphire peak is not clear, which makes it difficult to obtain a precise In-content. The evaluated In-composition from HR-XRD is 43% which is in good agreement to the 46% Indium obtained by μRaman mapping. For sample #749 the InGaN composition could not be determined because, only the sapphire peak but no peak for

InGaN is visible. The HR-XRD results in this work are not sufficient to contribute to the decoupling between in-depth strain gradients and compositional inhomogeneities.

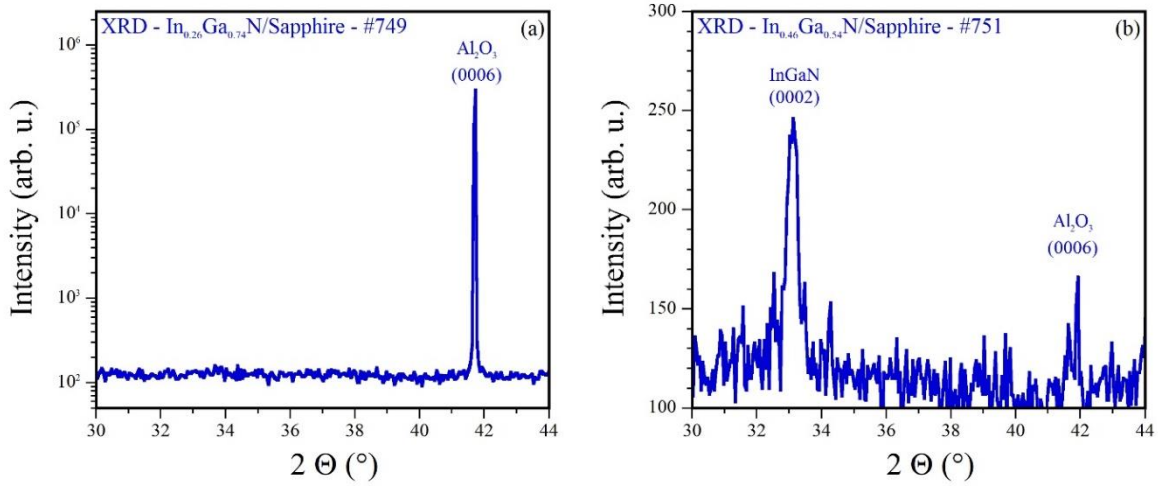

Figure 6.7: HR-XRD scan of InGaN samples #749 (a) and #751 (b).

The combination of the results from HR-XRD scans and the μRaman mapping, allows to analyze the composition dependence of the A_1(LO) frequency for the samples investigated in this work. Figure 6.8 displays the evaluated A_1(LO) phonon frequency of each InGaN samples as a function of the estimated InGaN composition. For sample #751 and #752, the In-content evaluated from the HR-XRD scans is used. The results are compared to the linear frequency behavior of the MREI model (represented by the black solid line) and values reported in literature (red circles and blue diamonds). The A_1(LO) frequencies of the $In_xGa_{1-x}N$ sample with an In-content in the $0.2 < x < 0.9$ range show a one-mode behavior and are in good agreement with the predicted linear composition dependence. The Indium-rich $In_xGa_{1-x}N$ alloys with $0.6 < x < 0.8$ are significantly downshifted compared to the MREI model predictions. The observed phonon frequency deviations can be explained by in-depth strain and/or compositional gradients. Each mode represents atomic displacements, consequently phonon frequencies are sensitive to strain. Due to the higher lattice constant of the sapphire substrate, the occurrence of tensile strain can be assumed in the InGaN films inducing a Raman shift to lower values. In contradiction to the In-rich InGaN layers, the A_1(LO) frequency of Ga-rich sample #749 is higher than the expected frequency of the MREI model but is very similar to other results reported in literature [194, 197, 198]. Considering that the Ga-rich samples #749 has a very thin layer thickness of nearly 40 nm, it can be suggested that strain strongly affects the A_1(LO) frequencies. Another possible effect to explain the phonon frequencies deviations are compositional inhomogeneities which can lead to selective resonant excitation of subsets with a particular In-concentration.

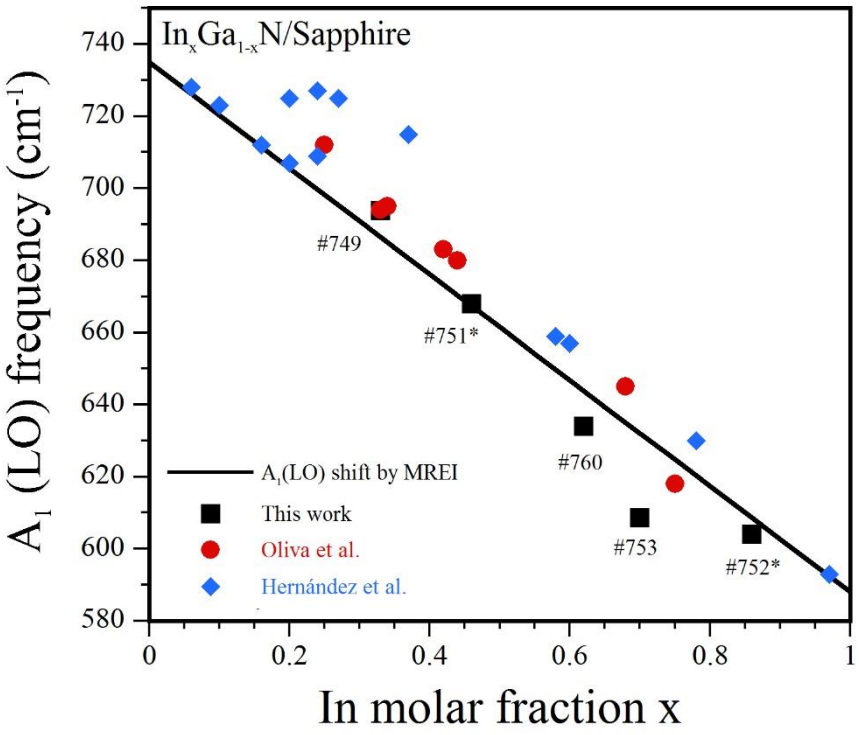

Figure 6.8: Experimental phonon frequencies of the A_1(LO) mode of each InGaN alloy (full black squares) as a function of the input In-content. For samples #751 and #752, the In-molar fraction from HR-XRD scans are used (marked with asterisk). Full red circles and blue diamonds are reported values from Oliva et al. [194] and Hernández [197]. The black solid line is the linear frequency shift predicted by the MREI model [78].

In particular, the growth method and growth conditions have an influence on the appearance of in-depth strain and composition gradients in InGaN compounds according to literature. Pereira et al. have studied strain and composition distributions in InGaN epilayers grown by MOCVD and their results showed an increase of the In composition with layer relaxation [203]. Wang et al. reported that an increased In content is accompanied with the strain relaxation of Ga-rich InGaN layers grown by MOCVD [204]. In contrast, MBE grown InGaN layers showed either a constant or even slightly reduced In content along the growth direction [205]. In-depth strain and composition gradients can be studied by resonant and non-resonant Raman spectroscopy. The influence of resonant and non-resonant excitation on the Raman scattering in InGaN layers will be discussed in the following section.

6.4 Impact of resonant and non-resonant excitation

As mentioned earlier, the phonon shift of the A_1(LO) mode in $In_xGa_{1-x}N$ materials is strongly influenced by in-depth strain and composition gradients [194, 195, 197, 199, 206, 207]. Another explanation for the phonon frequency deviations is selective resonant excitation, which has been widely reported in literature [194, 199, 208-210]. It is difficult to discriminate between in-depth strain gradients and compositional gradients, because composition and strain relaxation are generally linked. Therefore, both effects have to be simultaneously taken into account for the interpretation of Raman spectra. The probing depth or penetration depth δ in Raman spectroscopy depends on the absorption coefficient α of the $In_xGa_{1-x}N$ material composition and the laser excitation energy (wavelength):

$$\delta = 1/2\alpha \,. \tag{6.1}$$

To investigate the influence of resonant and non-resonant excitation of the A_1(LO) frequency, Raman spectra at different excitation energies between 1.96 eV to 2.71 eV were carried out. Using the absorption coefficients given by Wu et al. [55], estimated penetration depths for each excitation wavelength 457nm, 532 nm and 633 nm in correlation to the experimentally achieved InGaN compositions are listed in the following table.

Sample	$In_xGa_{1-x}N$ composition by A_1(LO)	Thickness (nm)	Probing depth of laser excitation (nm)		
			457 nm	532 nm	633 nm
#749	$In_{0.26}Ga_{0.74}N$	43	> 65	> 75	> 125
#751	$In_{0.46}Ga_{0.54}N$	43.9	> 50	> 60	> 110
#760	$In_{0.69}Ga_{0.31}N$	85	35	40	50
#753	$In_{0.86}Ga_{0.14}N$	86	25	33	40
#752	$In_{0.92}Ga_{0.08}N$	86	< 22	< 30	< 40

Table 6.3: Estimated penetration depths of Raman spectroscopy for each InGaN composition in dependence of the excitation wavelength.

In case of Raman spectroscopy of InGaN layers with different compositions using one excitation wavelength, the following correlation must be taken in consideration. An increasing Ga-content results in a higher bandgap energy while the absorption coefficient is reduced. This leads to larger probing depth and therefore a higher scattering volume. The increase of the penetration depth as a function of Ga molar fraction can be seen in the last three columns of Table 6.3. In case of measuring one InGaN composition at different excitations wavelengths two factors must be considered. First, with increasing excitation wavelength the probing depth also increases (rows in Table 6.3). Second, utilizing different laser wavelengths can lead to resonant excitation, depending on the bandgap of the investigated InGaN composition as well as compositional inhomogeneities.

Figure 6.9 illustrates Raman spectra at room-temperature excited with the 457 nm laser line. The laser energy is above the bandgap energy of the InGaN layers studied in this work. Similar to the laser excitation with 532 nm (Figure 6.2), no E_2(high) peak is observed. With increasing

Ga-content the intensity of the signal around 520 cm^{-1} decreases (indicated by black arrow in Figure 6.9). Conversely, this implies an intensity enhancement of the A_1(LO) mode because the excitation energy approaches the direct bandgap of the $In_{26}Ga_{0.74}N$ layer and the A_1(LO) is resonantly excited via the Fröhlich mechanism. The Fröhlich mechanism takes only place for longitudinal optical phonons in polar semiconductors. Longitudinal optical phonon modes accompany atomic displacements which lead to macroscopic electric fields. The Fröhlich electron-phonon interaction is a long-range Coulomb interaction between these electric fields and the electronic structure. That leads to the conclusion that the broad scattering signal at 520 cm^{-1} originates from non-polar modes. Resonant Raman-scattering (RRS) is very suitable for the investigations of small dimensional structures, for example phase separations in thin films have been evaluated by RRS [208]. Also, the influence of strain and composition on the phonon frequencies in InGaN/GaN multi quantum wells (MQWs) has been studied by RRS [210]. Overall, the Raman spectra measured with laser lines 457nm (Figure 6.9) and 532 nm (Figure 6.2) show a pronounced broadening of the A_1(LO) mode from the end-member InN with increasing Ga-content.

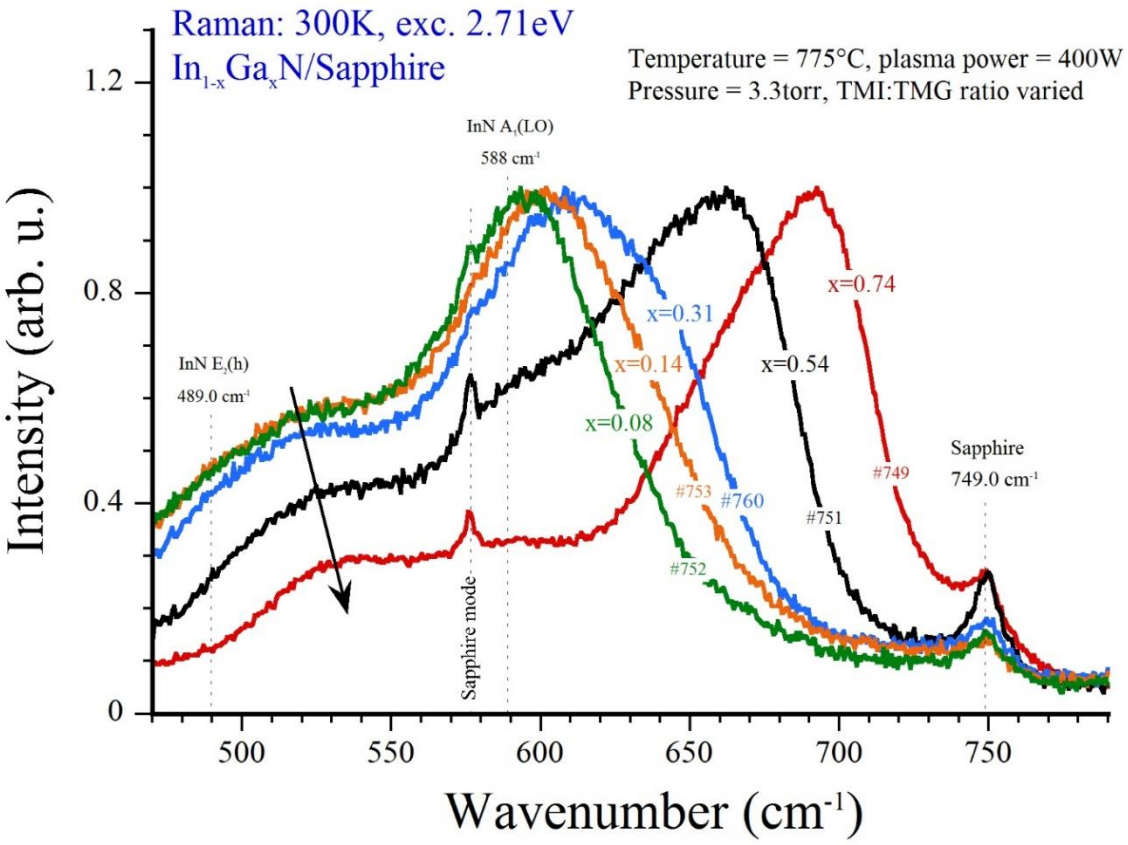

Figure 6.9: Raman spectra of the $In_xGa_{1-x}N$ layers excited with 457 nm. The spectra have been normalized for clarity.

In general, Raman spectroscopy is sensitive to disorder in atomic arrangements. Randomly arranged cations give rise to a broadening of the phonon modes. The strong broadening of the A_1(LO) mode for In content ($0.2 < x < 0.6$) is another indicator for lattice disordering and compositional fluctuations in the InGaN layers. In the latter case, the phonon peaks broaden because the scattering volume contains distributions with different In-concentrations. Furthermore, lateral compositional fluctuations cause a broadening of the Raman peaks, without affecting the A_1(LO) frequency. Last, the significant broadening of the A_1(LO) mode

can also be attributed to nanoscale phase segregations. Sample #749 shows an asymmetric broadening of the A_1(LO) mode towards lower frequency values, due to a feature mode at 665 cm^{-1} (Figure 6.4). This feature is referred to as 'S-band' in literature. In Figure 6.4b, Sample #751 shows a very broad peak which is a superposition of the InN A_1(LO) at 590 cm^{-1}, the S-band around 640 cm^{-1} and the InGaN A_1(LO) at 668 cm^{-1}. In the Raman spectra of the $In_{1-x}Ga_xN$ layers with In-content $x > 0.5$, the S-band is not observed. This feature mode below the A_1(LO) mode has been reported by multiple groups. One suggestion is that the S-band is a disordered-activated optical mode. Structural defects in the InGaN alloy induce an activation of phonon density of states which leads to Raman scattering [194, 195, 199]. Other authors discussed a possible contribution of the B_1(high) mode, which is a silent mode and Raman-forbidden for ideal wurtzite crystals. Tütüncü [211] and Kontos [195] proposed that the B_1(high) mode is activated by stoichiometric disorder and their interpretation is based on selective resonance. Kim et al. observed the B_1(high) mode in $In_xGa_{1-x}N$ alloys in the range from $0.11 < x < 0.54$ [196]. They explained the presence of the B_1(high) mode by relaxed Raman selection rules due to lattice disordering caused by randomly arranged cation species.

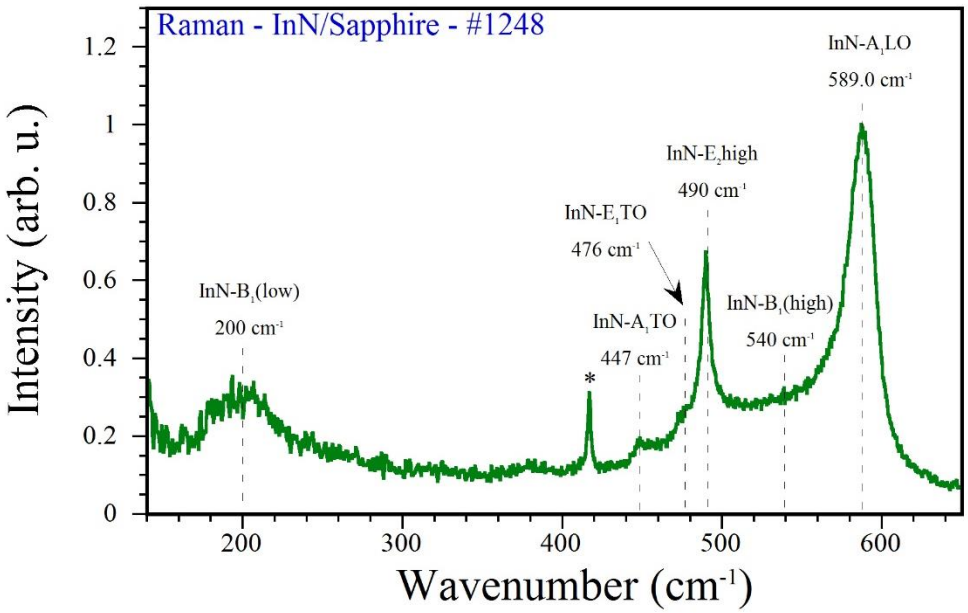

Figure 6.10: Extended Raman spectrum of InN grown by MEPA-MOCVD. The spectra are taken with an excitation wavelength of 532 nm in backscattering geometry. The mode with the asterisk is the A_{1g} mode of the sapphire substrate.

Raman spectroscopy (Figure 6.10) of InN also grown by MEPA-MOCVD at the same growth temperature (775°C) as the InGaN layers, revealed two peaks at 200 cm^{-1} and 540 cm^{-1} which are assigned to the B_1 Raman modes. Davydov et al. suggested that the B_1 modes can be observed in structurally imperfect samples, in which the wave-vector conservation law is violated and the density of vibrational states is reproduced by the Raman spectrum [212]. Inushima et al. reported similar phonon structures and assigned them to the B_1(low) and B_1(high) modes, respectively [71]. They considered the high electron density of the examined sample as an indication for numerous nitrogen vacancies. Therefore, the Raman selection rules are relaxed and the silent B_1 modes become detectable. The B_1(high) mode was also detected in InN films grown by HPCVD [133]. On the other hand, Kaczmarczyk et al. interpret the weak and broad structure at 200 cm^{-1} not as the B_1(low) silent mode, but rather as second order

processes of the acoustic phonons [213]. Talwar et al. also reported a band around 200 cm^{-1} [214], which they assigned to overtones of the TA modes either at the K or M point based on the acoustic and low-energy optical phonon dispersion relations of wurtzite InN by Serrano [215]. Additionally, the E_2(high), A_1(LO), A_1(TO) and E_1(TO) also appear in the extended Raman spectrum. The E_2(high) Raman mode has a Full width half maximum (FWHM) of 8 cm^{-1}, which indicates a reasonably good quality. On the other hand, the A_1(TO) and E_1(TO) modes are forbidden in backscattering geometry. The observation of these two modes leads to the conclusion that the InN layer contains polycrystalline regions.

To investigate the influence of resonant excitation on InGaN layers, Raman spectroscopy of InGaN sample #749 is carried out at excitation energies of 1.96 eV, 2.33 eV and 2.71 eV. The determined In-content of sample #749 is x = 0.26. Using Vegard's law for the bandgap energy of ternary $In_xGa_{1-x}N$ alloys, this composition corresponds to a bandgap value of 2.43 eV. The excitation energy of 2.33 eV and 2.71 eV are in the vicinity of the resonant direct bandgap. Figure 6.11 shows the Raman spectra of sample #749 obtained at excitation energies of 1.96 eV, 2.33 eV and 2.71 eV. For clarity, the Raman spectra have been normalized to the intensity of the A_1(LO) mode. The Raman spectrum of sample #749 with an excitation energy of 1.96 eV (= 633 nm) showed a very low scattering signal. The intensity was 15 times lower than the spectra excited with 2.33 eV and 2.71 eV. The laser energy of 1.96 eV (633 nm) is smaller than the direct bandgap of the InGaN layer. Subsequently, the transmission of the excitation energy into the layer and substrate is stronger. In contrast to the low excitation energy, the Raman spectra at higher excitation energies of 2.33 eV and 2.71 eV show an enhanced A_1(LO) peak with an almost similar intensity due to near-resonant excitation. The similar intensities can be explained that the phonon scattering resonance profile of A_1(LO) mode is strong and broad, which even leads to enhancement of the A_1(LO) mode for energies near the bandgap energy (within 200 - 300 meV) [216].

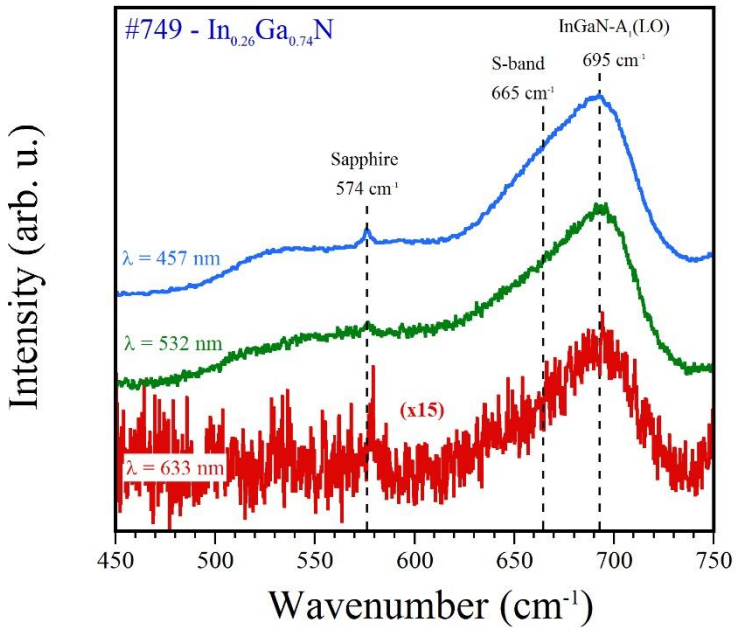

Figure 6.11: Raman spectra of InGaN sample #749 at excitation wavelengths (energies) = 633 nm (1.96 eV), 532 nm (2.33 eV) and 457 nm (2.71 eV).

As mentioned in the beginning of this section, selective resonant excitation can also have an impact on the A_1(LO) phonon mode. Oliva Vidal et al. presented a simple model that describes the influence of selective resonant excitation on the A_1(LO) frequency of $In_xGa_{1-x}N$ in dependence of the degree of compositional inhomogeneity. Their approach considers only lateral compositional fluctuations, which follow a Gaussian distribution with a standard deviation σ centered at a Indium composition x [194]. The model predicts upward (downward) frequency shifts from the resonance A_1(LO) peak frequency for near-resonant excitation above (below) the resonant bandgap energy. The extent of the shift depends on the value of σ. With increasing σ values, the upward (downward) shift from the resonance peak frequency increases and can reach a value up to 10 cm^{-1}. For lower (higher) excitation energies far away from the resonance, the shift shows a tendency towards back to the A_1(LO) frequency correlated to the average layer composition. As seen in Figure 6.11, the phonon frequency of the InGaN A_1(LO) mode is almost not affected by the near-resonant excitation. In consideration of the model by Vidal, this indicates a high compositional homogeneity and verifies the results of the µRaman maps (Figure 6.4a).

As given in Table 6.3, the penetration depths of all three excitation wavelengths used in the present work exceed the layer thickness of the Ga-rich InGaN sample (#749). Therefore, contributions from the sapphire substrate and the $In_xGa_{1-x}N$-sapphire interface which could be strained have to be taken into account. Hence the entire InGaN layer is probed for each laser line, a conclusion about in-depth strain and compositional gradients in this InGaN layer is not possible. However, the presence of the sapphire E_g mode at 574 cm^{-1} verifies a contribution from the sapphire substrate. All Raman spectra show a similar asymmetric broadening towards lower frequency values which is attributed to the S-band as discussed above. The S-band is also independent of the excitation energy. Kontos et al. have reported a resonant behavior of the A_1(LO) and the S-band for $In_xGa_{1-x}N$ in the range $0.1 < x < 0.27$ [195]. Thus, they suggested that the S-mode is related to the B_1 silent mode, which is activated by stoichiometric disorder, rather than to a defect activated point of the phonon density of states.

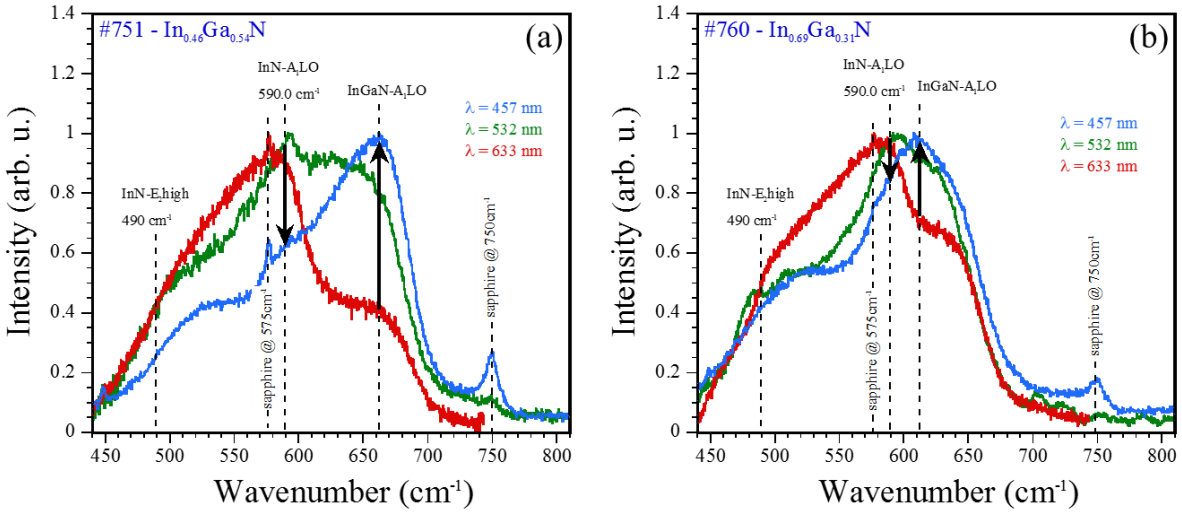

Figure 6.12: Raman spectra of sample #751 - $In_{0.46}Ga_{0.54}N$ (a) and sample #760 - $In_{0.69}Ga_{0.31}N$ (b) excited with excitation wavelengths of 457 nm (blue line), 532 nm (green line) and 633 nm (red line).

For the $In_xGa_{1-x}N$ layer with x = 0.46, the penetration depths of the laser lines are also larger than the layer thickness. In Figure 6.12a, the sapphire E_g modes at 574 cm^{-1} and 749 cm^{-1} are present in the Raman spectra. Though the whole layer is probed, the Raman spectra differ significantly. At 633 nm (red line), a broad peak is shown around 580 cm^{-1} and followed by a less intense shoulder at higher frequency values around 660 cm^{-1}. For 532 nm (green line), the

strongest peak is observed at 590 cm^{-1} and the high-frequency shoulder has a higher intensity, but the shoulder does not shift significantly. For an excitation at 457 nm (blue line), the behavior is reversed (indicated by black arrows in Figure 6.12a) with the strongest peak around 660 cm^{-1} and two weaker shoulders 590 cm^{-1} and 530 cm^{-1}, respectively. Figure 6.12b displays the Raman spectra taken at different laser lines of sample #760. It should be noted, that the layer thickness of sample #760 is well above the critical layer thickness and all three penetration depths are within the film (see Table 6.3). This ensures inelastic scattering exclusively from the InGaN layer. The spectra should only provide information about the InGaN layer. A very similar behavior of the Raman spectra as in Figure 6.12a is observed. For 633 nm and 532 nm the strongest peak is around 580 cm^{-1} and 590 cm^{-1}, respectively and both graphs have a less intense shoulder at a frequency around 620 cm^{-1}. The spectra excited at 457 nm, has the strongest peak at 610 cm^{-1} and a shoulder at 530 cm^{-1}. An interpretation for the observed scattering signal could be a response of regions with a different specific Indium content, due to selective resonant excitation. The peaks at 580-590 cm^{-1} (red and green Raman spectra) match with the A_1(LO) mode of InN and might indicate the presence of InN clusters. On the other hand, the high-frequency shoulder of the 633 nm and 532 nm spectra and the strongest peak at 457 nm in Figure 6.12 arise from the InGaN phase. Compared to the higher laser wavelengths, the InGaN phase has a stronger scattering signal at 457 nm. The InGaN phase has a low In-concentration and exhibits a higher bandgap. When the laser excitation energy reaches the range of the band gap resonance of the $In_xGa_{1-x}N$ A_1(LO) phonon mode, the material with the smaller Indium molar fraction is resonantly excited first and dominates the Raman spectrum. A comparison of the spectra excited at 457 nm shows a significant downward shift of the A_1(LO) peak frequency, due to a higher In-content of sample #760. The shoulder of the green and red Raman spectra has also shifted to a lower frequency, which verifies that this shoulder is the A_1(LO) mode of InGaN. In Figure 6.12b, the intensity of the red Raman spectrum is more intense than the one in Figure 6.12a. As mentioned earlier, the Raman scattering is only from the InGaN layer. Given that the probing depth reduces with increasing excitation wavelength, the Raman spectra in Figure 6.12b indicate the presence of InN clusters in the deeper region of the InGaN layer and towards the surface the InGaN phase becomes dominant.

The presence of the InN and InGaN phase in sample #751 and #760 can be explained by considering the phase diagram calculated by Ho and Stringfellow. Figure 6.13 shows that InN and GaN are not miscible at a growth temperature of 775°C. The intermediate InGaN compositions of samples #751 and #760 are unstable and phase separation is expected due to spinodal decomposition. Phase separation takes place by Indium atoms which separate from the InGaN lattice and form an alloy of a different composition to reduce the strain energy of the $In_xGa_{1-x}N$ alloy system, which is due to the lattice mismatch between InN and GaN of ~11% [207, 217]. Sample #749 does not show any indication for microscopic phase separation. A possible reason might be that the In-content (x= 0.26) of the $In_xGa_{1-x}N$ layer is close the region where the phase transitions from the metastable to the unstable state takes place. The InGaN samples #752 and #753 qualify for investigation of in-depth strain and compositional gradients under non-resonant conditions. The evaluated Indium molar fraction of both InGaN layers are $x = 0.86$ and $x = 0.92$, which correspond to bandgap energies of 0.91 eV and 0.81 eV, respectively. These bandgap values are far below the excitation energies of 1.96 eV, 2.33 eV and 2.71 eV. Furthermore, the penetration depths are smaller than the film thickness of both samples, which ensures Raman scattering exclusively from the InGaN layer. The estimated probing depths range between 20 nm and 40 nm and provide information about a shallow region close the InGaN surface.

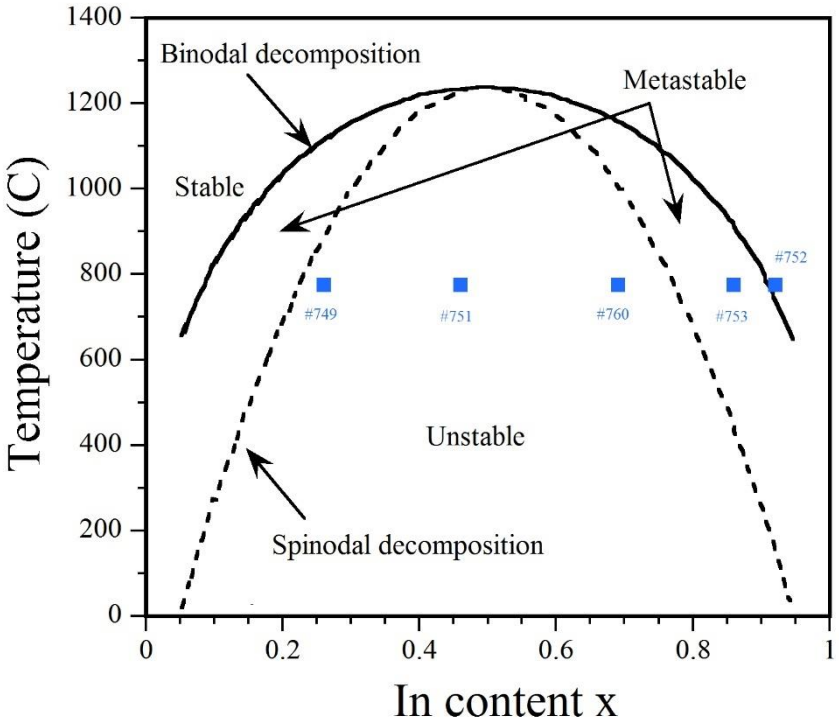

Figure 6.13: Phase diagram for InGaN based on the model of Ho and Stringfellow [44]. Blue squares indicate $In_xGa_{1-x}N$ samples of this work. Note that determined $In_xGa_{1-x}N$ composition via A_1(LO) mode is used.

As displayed in Figure 6.14a, the Raman spectra overlap. For clarity, the spectra are normalized and stacked in Figure 6.14b. At an excitation wavelength of 633nm, a peak at 592 cm^{-1} and a slightly lower shoulder at 630 cm^{-1} are distinguished (bottom of Figure 6.14b). These peaks are assigned as the A_1(LO) of InN and InGaN, respectively. The spectrum is similar as the red Raman spectra of sample #751 and #760 in Figure 6.12. According to the phase diagram (Figure 6.13), sample #753 is located in the metastable region and the observed Raman scattering is due to phase separation. The spectra in the middle (532 nm) and at the top (457 nm) of Figure 6.14b, are fitted using one peak corresponding to the A_1(LO) phonon mode of InGaN.

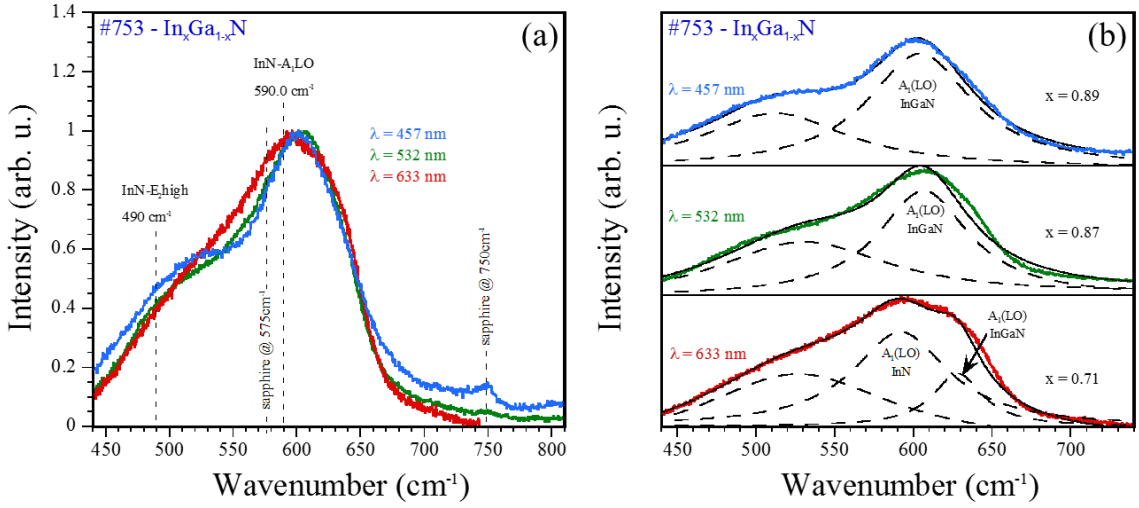

Figure 6.14: Raman spectra of #753 – $In_xGa_{1-x}N$ excited with wavelengths of 457 nm, 532 nm and 633 nm (a). Measured (colored lines) spectra and fit (black solid lines) of each spectrum and corresponding Indium fraction x (b). The dashed lines indicate the single fit peaks.

The $In_xGa_{1-x}N$ composition is nearly identical with In-concentrations of 89% and 87%. From the three Raman spectra in Figure 6.14b, a shift of the A_1(LO) phonon mode towards lower frequencies with increasing excitation wavelength is visible. The shift of the A_1(LO) mode is an indication for compositional fluctuations. The compositional inhomogeneity increases with depth, because a higher wavelength corresponds to a deeper penetration depth. Furthermore, these results indicate an increase of the indium content towards the growth surface. Phase segregation deeper in the layer or is it selective resonant excitation of In-rich domains. Two distinct regions are revealed by the non-resonant Raman measurements. The InGaN phase is dominant near the surface. Deeper in the layer phase segregation is verified.

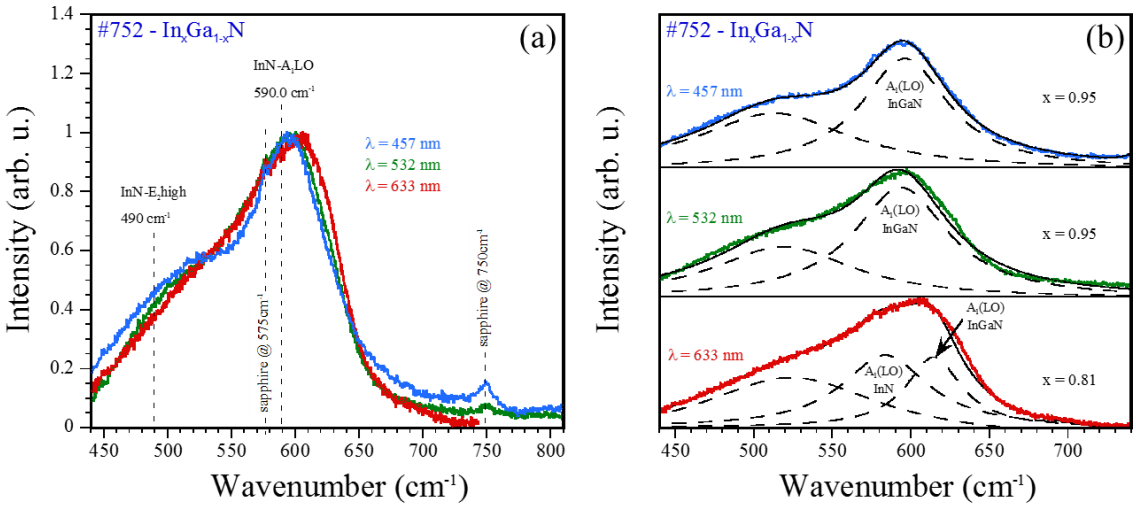

Figure 6.15: Raman spectra of #752 – $In_xGa_{1-x}N$ excited with wavelengths of 457 nm, 532 nm and 633 nm (a). Experimental (colored lines) and fitted (black solid lines) spectra with corresponding Indium fraction x (b). The dashed lines are the single peak fits.

Sample #752 has a high In-content (x > 0.85) and lies in the stable region of the phase diagram (Figure 6.13).The results of the non-resonant Raman spectroscopy of sample #752 in Figure 6.15 look similar as the previous sample. At excitation wavelengths of 457 nm and 532 nm, only the A_1(LO) phonon mode of InGaN at almost the same frequency is observed. The $In_xGa_{1-x}N$ composition is highly indium-rich with an In-fraction x = 0.95. Fitting of the Raman spectrum taken with the 633 nm laser line, yields two peaks at 596 cm^{-1} and 616 cm^{-1}. The first peak is attributed to the A_1(LO) mode of InN and the second peak is the A_1(LO) mode of InGaN. The A_1(LO) frequency is shifted by 20 cm^{-1} towards higher frequencies corresponding to an In-concentration of 81% in the $In_xGa_{1-x}N$ sample. For sample #753 the upshift of the A_1(LO) frequency is even larger with 26 cm^{-1}.

The results of the non-resonant Raman spectroscopy of sample #752 and #753 lead to the suggestion that phase separations take place deeper in the layers. Excitation with laser lines 457 nm and 532 nm, revealed that the InGaN phase becomes dominant and homogeneous towards the surface. Nonetheless, strain-effects cannot be ruled out. A deeper penetration depth reaches a more strained part of the InGaN layer and a low-frequency shift would be expected due to tensile stress. The discrimination between in-depth strain and a compositional gradient as well as selective resonant excitation is difficult. An opposite contribution of layer composition and strain to the direction of the phonon shift has been reported [194, 199]. To decouple the effect of strain and compositional inhomogeneity on the phonon frequencies more independent characterization methods such as XRD are needed.

6.5 Nanoscale phase separations in InGaN alloys

As mentioned previously, phase segregations are a major challenge in the growth of InGaN materials and a possible reason for the broadening of the A_1(LO) Raman mode as observed for the InGaN layers investigated in this work. Since the resolution of µRaman spectroscopy is not sufficient to identify nanoscale inhomogeneities, characterization methods with high-spatial resolution are required. TERS and s-SNIN are two techniques, which provide nanoscopic imaging well below the diffraction limit of the probing light and enable the study of nanoscale phase separations. Both characterization methods are described in chapter 3.

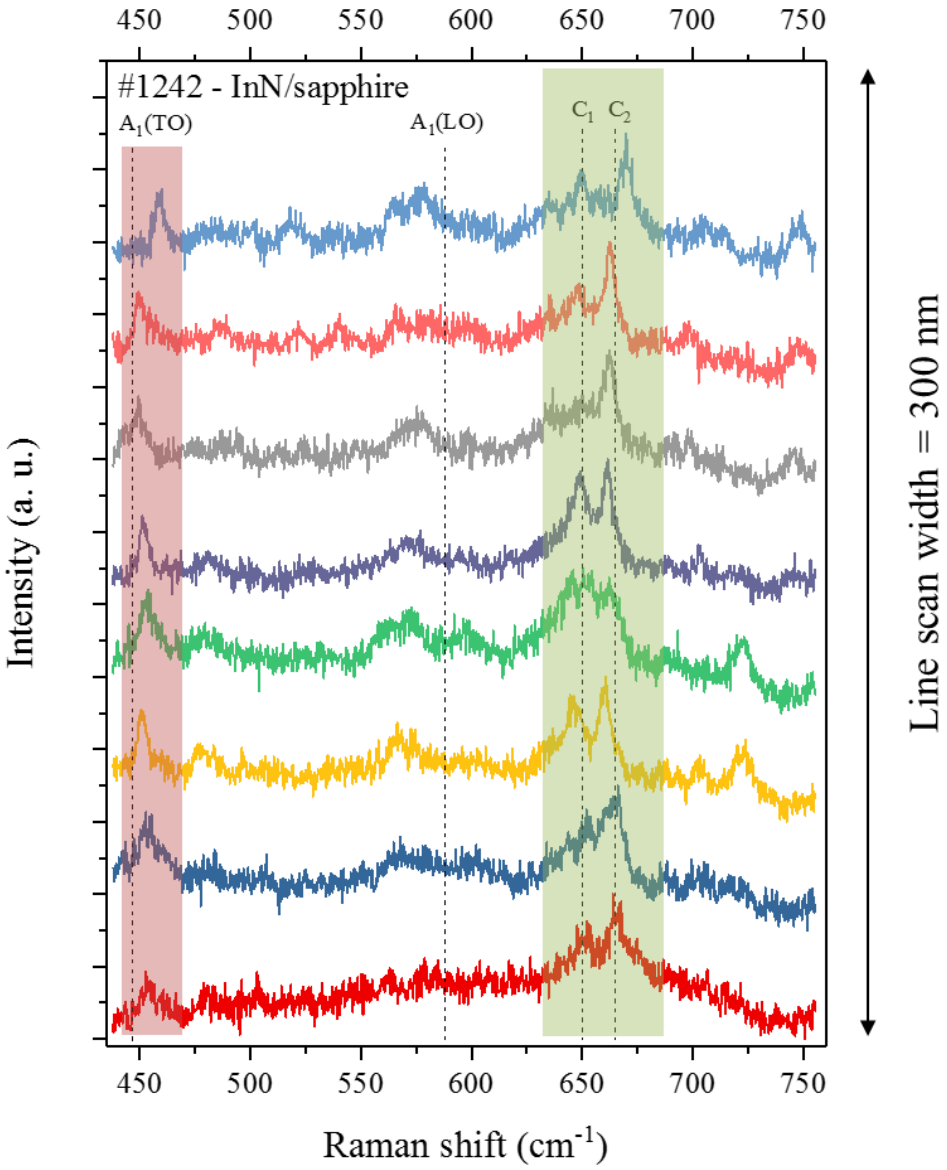

Figure 6.16: Tip-enhanced Raman spectra along the line scan of a pure InN layer. The red box highlights the A_1(TO) mode of InN. Inside the span from 630 cm^{-1} to 670 cm^{-1} (green box) two peaks named as C_1 and C_2 are observed.

First, a TERS linescan of the composition end-member InN (same InN sample as in Figure 6.2f) is carried out. Analysis of these TERS measurements will help with the interpretation of the TERS measurements of the $In_xGa_{1-x}N$ layers. The TERS spectra are taken using a He-Ne-

laser with an excitation wavelength of 632.8 nm. The linescan has a length of 300 nm with a step size of 42.85 nm. Figure 6.16 shows the consecutive TERS spectra along the line scan of the pure InN sample. For clarity the spectra are normalized and shifted. Throughout the line scan, an intense mode at 450 cm^{-1} is dominant (highlighted by the transparent red box in Figure 6.16). This mode agrees with the A_1(TO) mode of the hexagonal wurtzite InN. Additionally, a broad band between 640 cm^{-1} and 670 cm^{-1} with a duplet of modes, denoted as C_1 and C_2, is present throughout the linescan (indicated by the green box in Figure 6.16). The C_1 and C_2 peaks are very interesting, because based on the phonon dispersion curves of hexagonal and cubic InN, there are no known first-order phonon modes above 610 cm^{-1}. Furthermore, there is a relation between the frequency of the A_1(TO) mode and the C_1 and C_2 peak. Both peaks almost shift simultaneously in the same direction along the linescan (see solid lines in Figure 6.17) as the A_1(TO) phonon mode. At this point, the discussion about the origin of the C_1 and C_2 mode are part of the ongoing research. One explanation might be the combination of optical and acoustical phonons. Kaczmarcyk et al. have observed a weak peak at 678 cm^{-1} due to second-order processes in Raman-scattering experiments of hexagonal InN. They have interpreted this peak with A_1 symmetry as the sum of optical and acoustical phonons A_1(TO) + A_1(LA) near the symmetry point M or K [213]. The calculations of the InN phonon dispersion curves [69, 213, 215] lead to another assumption, namely that C_1 and C_2 are the sum of the A_1(TO) at the Γ-point and the E_2(low) and B at the symmetry point M, respectively:

$$C_1 = A_1(TO) + E_2^{\text{low}}(M) \tag{6.2}$$

$$C_2 = A_1(TO) + B(\mathrm{M}). \tag{6.3}$$

Inserting the A_1(TO) values of the TERS line scan and the frequencies of the E_2(low) = 194 cm^{-1} and the B phonon = 213 cm^{-1} at the symmetry point M (red circle in Figure 6.17 on the right) into equations (6.2) and (6.3) allows to compare the experimental and theoretical frequencies of the C_1 and C_2 mode. In this case, the plasmons carry the missing momentum to ensure the conservation of momentum.

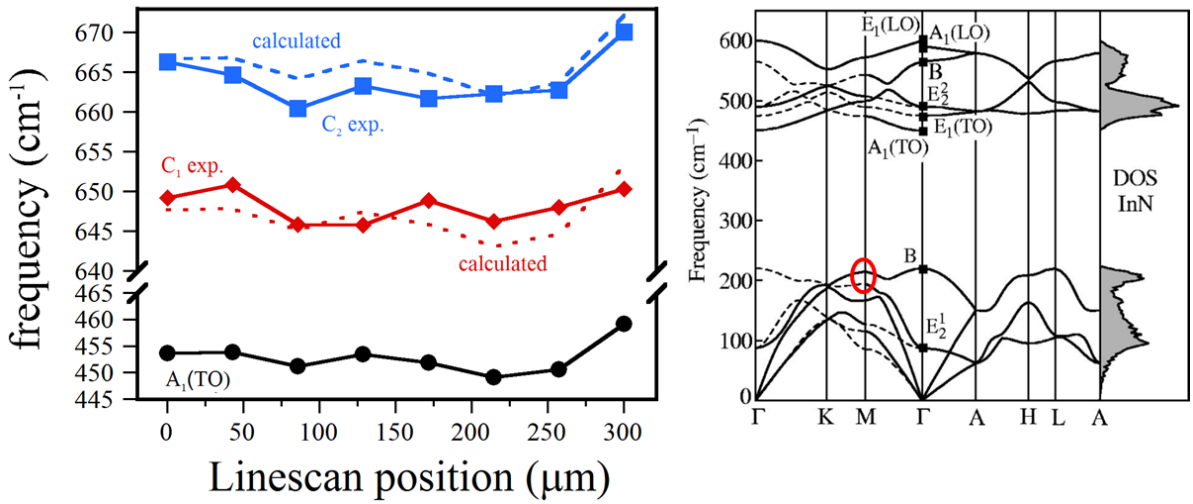

Figure 6.17: On the left is the frequency of the A_1(TO) mode (black) as well as the C_1 (red) and C_2 peak (blue) plotted along the linescan. The dashed line indicates the combination of the A_1(TO) and an acoustic mode at the symmetry point M. On the right are the calculated phonon dispersion curves and phonon density of states (DOS) function for hexagonal InN by Davydov et al. [69]. The red circle indicates the acoustic phonon branch at the symmetry point M.

The calculated values (dashed lines) are in good agreement with the experimental phonon frequencies for the C_1 and C_2 mode as displayed in Figure 6.17. The disordered band can be related to a surface optical phonon mode SO(A_1) or to a surface accumulation layer of electrons in InN [198]. Studies have estimated an accumulation layer thickness of 3 nm or less [218]. Considering the TERS probing depth of ~10 nm [219], the presence of a surface accumulation layer may affect the outcome of the near-field Raman spectra. In TERS, one has also to consider a breakdown of the *k* conservation and subsequently the breakdown of the classical Raman selection rules [88]. The necessary investigations to assign these phonon modes are part of ongoing studies. For example, a depth-dependent composition analysis using X-ray photoelectron spectroscopy (XPS) with synchrotron radiation as energy source. However, this would go beyond the scope of this thesis.

A TERS line scan of sample #760 is displayed in Figure 6.18. The total length of the line scan is 200 nm and TERS spectra were taken every 10 nm. For clarity the spectra are normalized and shifted. Along the line scan, different peaks appear (disappear) abruptly between adjacent tip-enhanced Raman spectra. These modes cannot be distinguished in far-field Raman spectroscopy.
An intense mode at 447cm^{-1} appears locally in the spectra #6 to #9 (highlighted by the blue box). This mode matches theoretically and experimentally with the A_1(TO) mode of hexagonal InN (see Table 2.6) and was also detected in the TERS linescan of the pure InN layer. The local hexagonal InN cluster has a width of 40 nm. A_1(TO) and E_1(TO) mode of hexagonal InN as well as the TO mode of cubic InN are known to show a strong intensity enhancement in TERS due to the lower bandgap energies of hexagonal InN with E_g = 0.68 eV, and cubic InN with E_g = 0.56 eV [220] compared to the bandgap of the surrounding InGaN. As consequence, InN clusters exhibit a large carrier concentration, which leads to strong coupling of surface plasmon polaritons (SPPs) and localized surface plasmons (LSPs). In addition, charge accumulation at the surface also increases the carrier concentration resulting in an increased plasmon concentration and subsequently a stronger enhancement of local InN modes. TERS enables the observation of the A_1(TO) phonon mode as well as the C_1 and C_2 modes in InN and InGaN materials because of the breakdown of the selection rules compared to classical Raman scattering. TERS identifies the presence of a local hexagonal wurtzite InN cluster at or rather close to the surface of the InGaN layer. The formation of InN clusters is due to phase segregations. Furthermore, the spectra #6 to #9, show almost no disorder in the range between 630 cm^{-1} and 670 cm^{-1} compared to the other spectra. Moreover, these spectra show a peak around 660 cm^{-1} a peak that matches with the C_2 feature. The combination of the A_1(TO) phonon mode and the C_2 peak was also observed in the pure InN sample (see Figure 6.16), indicating a pure InN cluster. In spectra #2 and #3, a Raman mode at 460 cm^{-1} is observed (purple box). This frequency is very close to the TO mode of pure cubic (zinc-blende) InN [221]. On the other hand, Kaczmarczyk et al have theoretically and experimentally verified the TO mode of cubic InN at a frequency value of 472 cm^{-1} [213]. Recently, two groups have found the TO phonon mode attributed to cubic InN at 463 cm^{-1} [222, 223]. In this case, the phonon mode at 460 cm^{-1} could be rather assigned to the A_1(TO) mode of InGaN. The frequency shift of the A_1(TO) mode depends on the In-content (or Ga-content respectively) of the InGaN compound as well as local strain. In this case, the shift of the A_1(TO) mode corresponds to an In-content of 85%, based on the MREI model. This In-concentration deviates by 16% from the average In-content of 69%, which is in the range of compositional fluctuations in nanoscale

phase separations (10-20%). Two more areas of $In_xGa_{1-x}N$ are verified by the spectra #13 to #19 and spectrum #20.

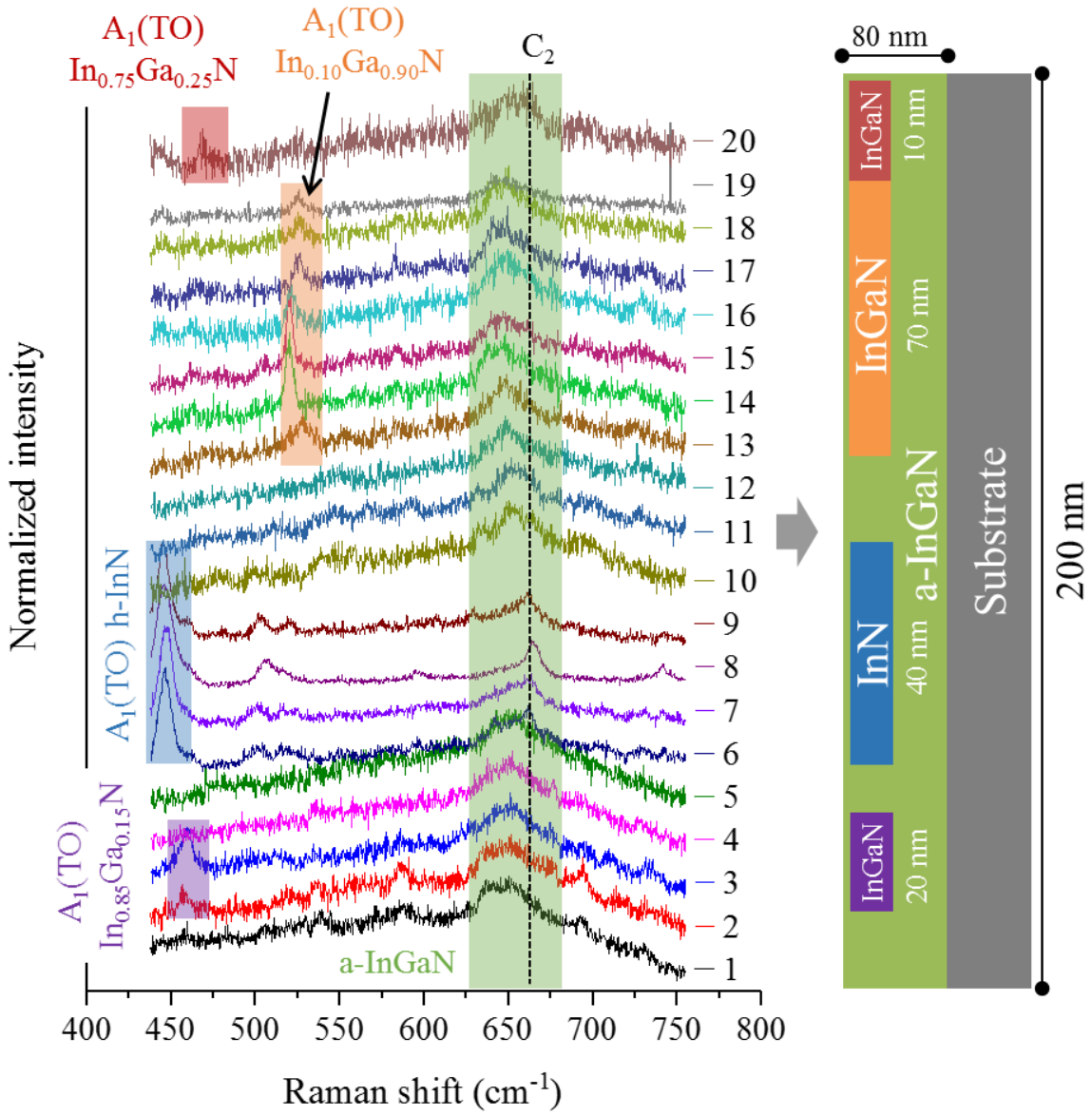

Figure 6.18: TERS Line scan of sample #760 InGaN (left). Highlighted are the A_1(TO) mode of InN (blue box), different $In_xGa_{1-x}N$ (purple, orange and red box), as well as a broad and disordered feature indicating disordered InGaN (green box). On the right is the $In_xGa_{1-x}N$ material distribution based on the assigned A_1(TO) modes of the TERS linescan (no depth profile).

In the TERS spectra #13 to #19, a peak shifting between 520 cm^{-1} to 527 cm^{-1} is observed. This peak is also due to the frequency shift of the A_1(TO) mode as a function of the InGaN composition. The average peak wavenumber of the A_1(TO) modes corresponds to an InGaN composition with an In-concentration of 10%. This value is way off compared to the average In-content of 69% as evaluated from µRaman mapping. The vast compositional discrepancy might be due to the formation of the InN cluster. As shown in Figure 6.18 on the right, the InGaN subset is next to the hexagonal InN cluster. As mentioned previously, these InN clusters are formed by phase segregations. Indium aggregates to clusters and depletes the surrounding area, which leads to lower In-concentrations than expected. In spectrum #20, the A_1(TO) is

located at 469 cm^{-1} and corresponds to an Indium content of 0.75, which is close to the average composition of the $In_{0.69}Ga_{0.31}N$ layer. As already mentioned, a broad and disordered feature between 630 cm^{-1} and 670 cm^{-1} is observed almost throughout the whole TERS line scan (indicated by green box). This Raman scattering signal originates from amorphous InGaN. The gathered information from the TERS line scan about the material's composition and their lateral dimensions is converted into a schematic material distribution of the InGaN layer surface (Figure 6.18 on the right). The penetration depth of TERS is only a few nanometers, therefore the schematic layout does not display information about the compositional depth profile of the InGaN layer.

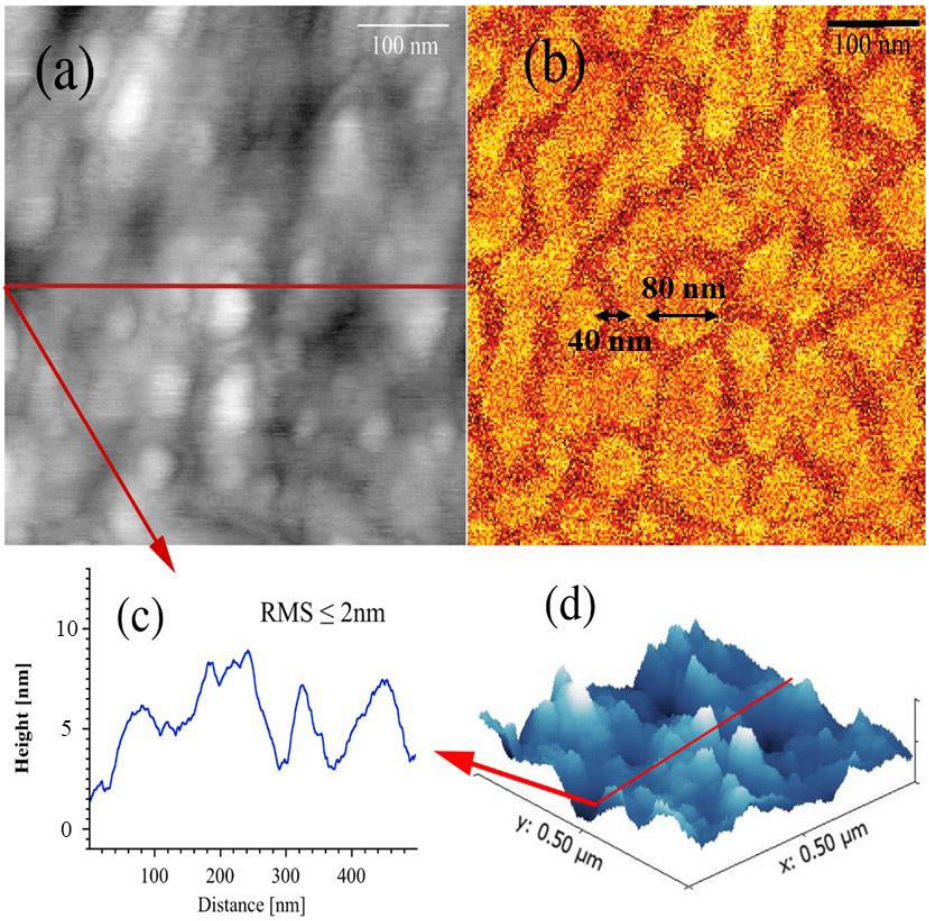

Figure 6.19: AFM surface topography (a) with height profile (c) and 3D contour plot (d) of sample #760 InGaN. The s-SNIN (b) image recorded for an excitation wavelength of λ = 10.5 µm reveals nano-scale compositional fluctuations. Figure from Reference [224].

Figure 6.19 shows a near-field amplitude image (b) and the corresponding surface topography (a) of the InGaN sample #760 measured by s-SNIN with an excitation wavelength of 10.5 µm. The s-SNIN mapping displays islands with different permittivity. As described in chapter 3, the backscattered IR signal provides a map of the dielectric constant (ε) of the sample. The amplitude contrast is related to the real part Re(ε) or refractive index of the material, respectively. Therefore, the near-field amplitude represents lateral compositional fluctuations of the InGaN growth surface indicating a strong phase separation. The surface morphology image and the height profile display (Figure 6.19c) that adjacent domains with different InGaN compositions have nearly the same height, indicating that the amplitude contrast has only a

material-specific origin. Therefore, s-SNIN verifies the presence of nanoscale inhomogeneities at the surface of the InGaN layer. In Figure 6.19b, the two black double arrows indicate the dimension of the phase separations. The size of these phase separations in the s-SNIN image matches with the size of the phase separations in the TERS line scan as seen in Figure 6.18. However, TERS provides accurate compositional information of the nanoscopic phase separations compared to s-SNIN. Reasons for these phase separations are spinodal and binodal decomposition. Ho and Stringfellow calculated the binodal and spinodal decomposition for the InGaN system on the assumption of a constant average value for the solid phase interaction parameter [44]. Based on their model, $In_{0.69}Ga_{0.31}N$ deposited at a growth temperature of 775°C is thermodynamically not stable (see also Figure 6.13), which may lead to segregation into stable In-rich and Ga-rich InGaN subsets. The stabilization of Ga-rich and In-rich domains depends on the kinetic stabilization of the growth surface by process parameters such as growth temperature, sequential precursor supply, pressure and other growth conditions. A model to quantify the nanoscale phase segregation of indium and gallium in the $In_xGa_{1-x}N$ lattice by s-SNIN, including initial results, has been discussed by Abate et al. [46].

For sample #753, a high-resolution Raman map was achieved by TERS. The dimensions of the mapped surface area are 300 µm x 300 µm, which are partitioned into 8 x 8 points.

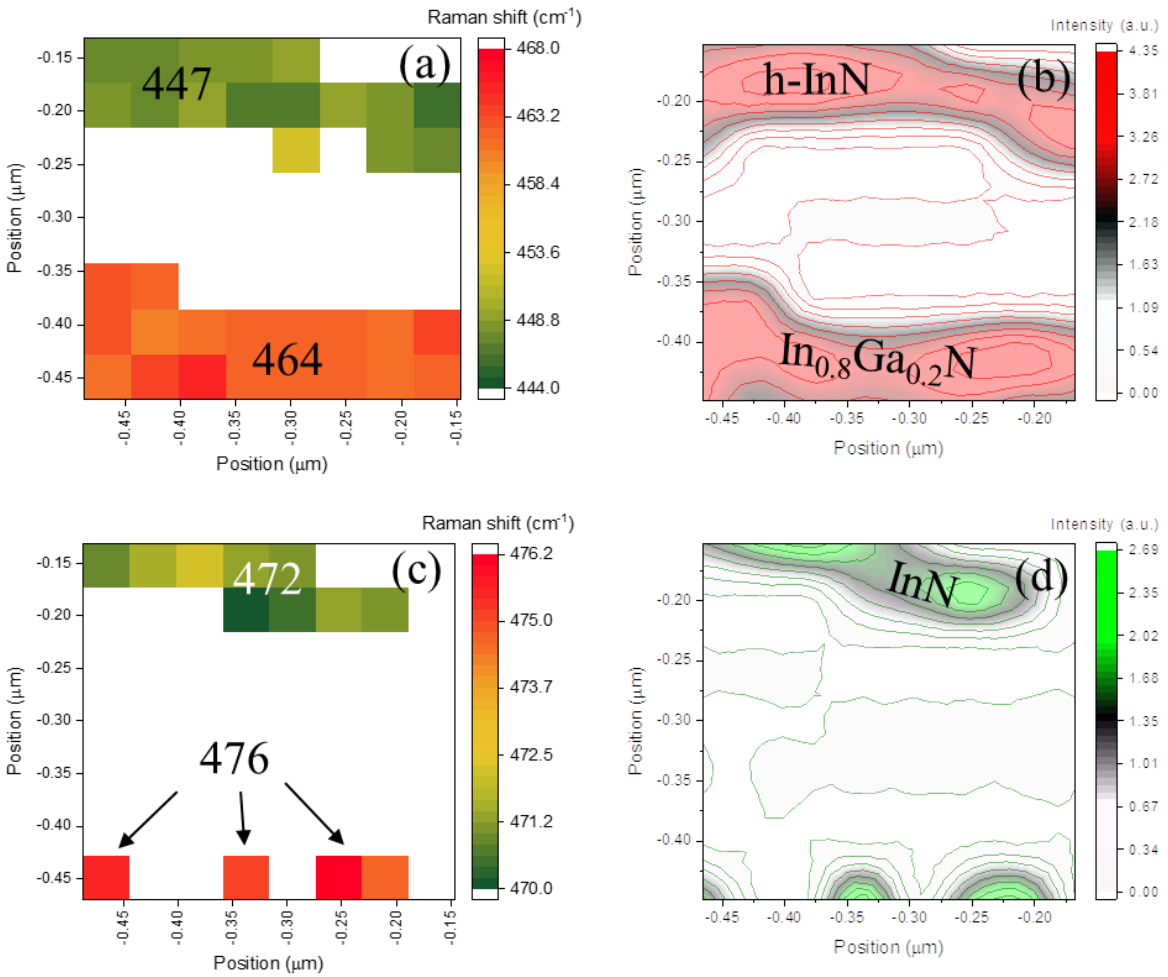

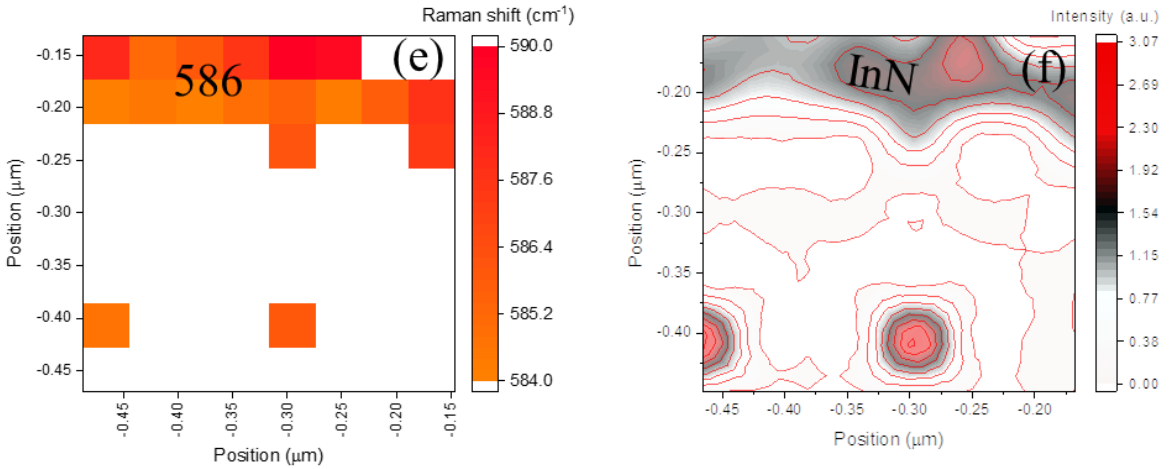

Figure 6.20: Intensity (left) and phonon frequency (right) maps of the A_1(TO) mode of hexagonal InN and $In_{0.8}Ga_{0.2}N$ (a+b), E_1(TO) mode of InN (c+d) and the A_1(LO) mode of InN (e+f).

Numerical fitting and analysis of each spectrum provides the peak positions of the multiple phonon modes and their intensities. The local distribution of these phonon frequencies and their intensities are plotted in Figure 6.20a-f. Figure 6.20a shows a color-coded map of two intense phonon modes at 447 cm^{-1} and 464 cm^{-1} and Figure 6.20b displays the corresponding intensity distribution of both modes. Both phonon modes have a similar intensity. The peak at 447 cm^{-1} is assigned to the A_1(TO) of hexagonal InN. InN is present in the upper third of the investigated layer surface. The second peak is detected in the bottom part of the TERS map and associated to the A_1(TO) mode of InGaN. Based on the MREI model, this frequency shift correlates to an Indium content x = 0.8, which is close to the average layer composition with In x = 0.86. The presence of InN in the upper part of the TERS map is verified by the presence of the InN A_1(LO) mode at 586 cm^{-1} (see Figure 6.20e and f). Figure 6.20c+d show the distribution of a phonon between 470 cm^{-1} to 476 cm^{-1}. In this span is the E_1(TO) mode of InN located and further verifies the presence of InN in the upper part of the map. The C_2 phonon mode is also detected (see Figure 6.21a+b) in the same area as the A_1(TO), E_1(TO) and A_1(LO) phonon modes of hexagonal InN. Besides theses modes, a very intense peak at 500 cm^{-1} (Figure 6.21c+d) and a band at 635 cm^{-1} (Figure 6.21e+f) are distinguished also in the area where the InN is located. The latter band can be attributed to the surface SO(A_1) mode of InN.

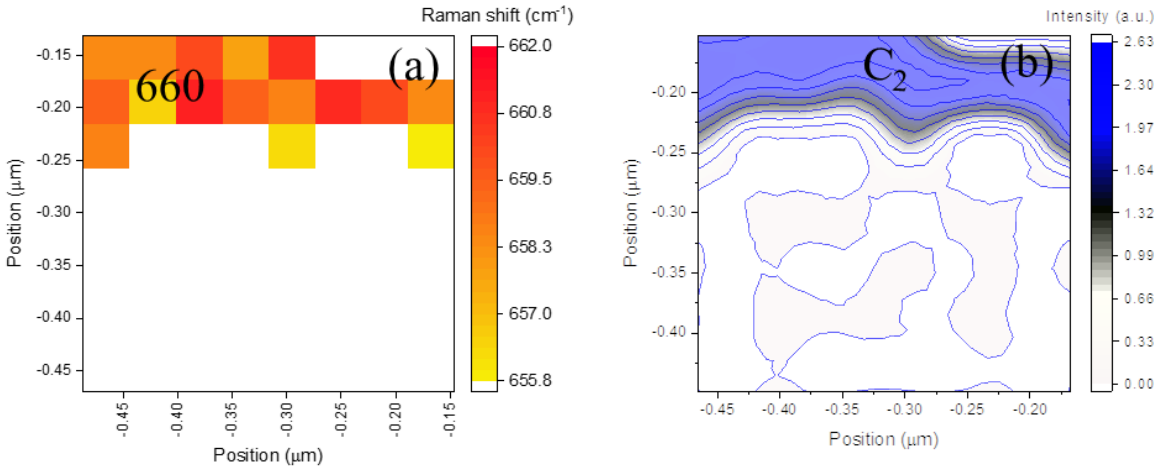

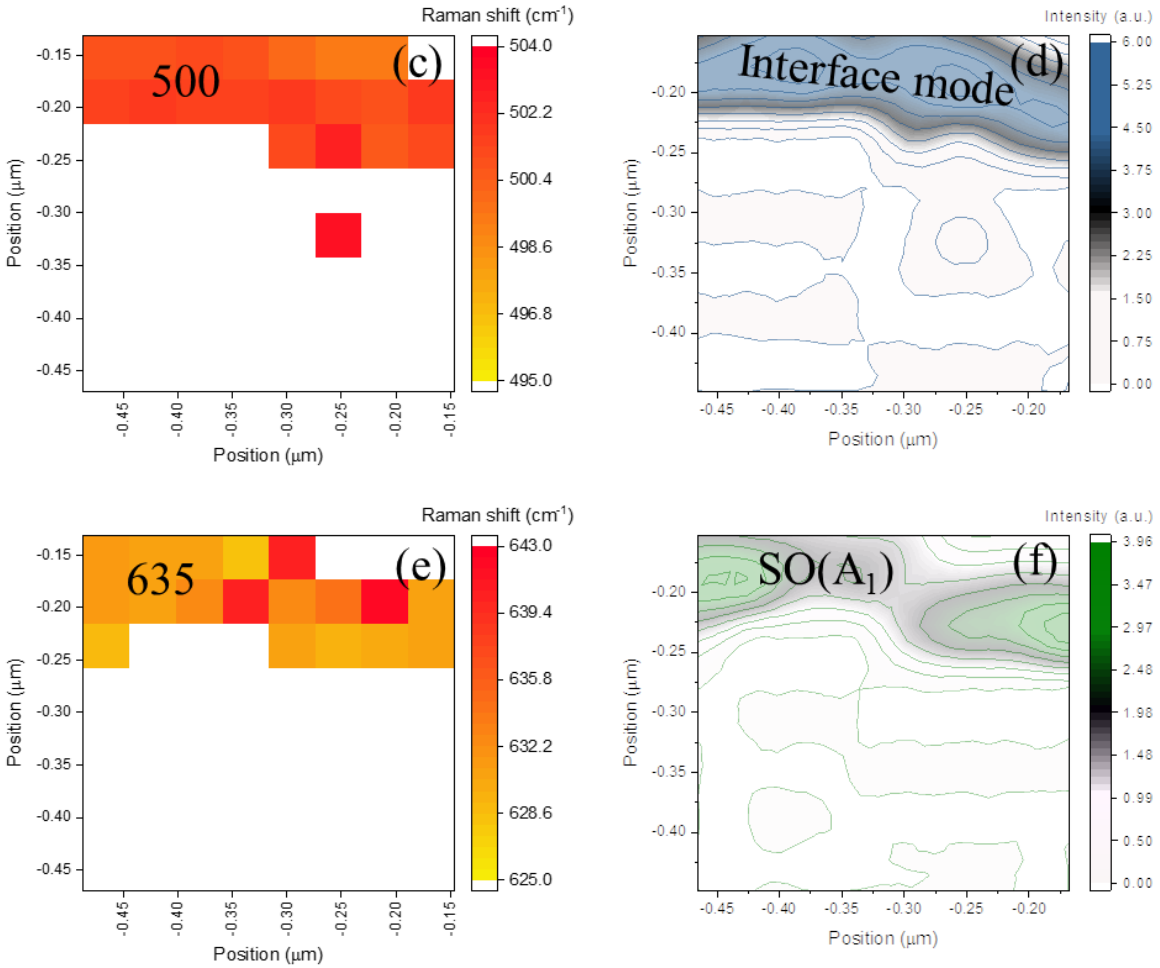

Figure 6.21: Phonon frequency and intensity map of $In_xGa_{1-x}N$ sample #753 with In x = 0.5 and 0.6 (a+b), interface mode (c+d) and SO(A_1) mode (e+f).

The assignment of the line at 500 cm^{-1} is difficult. The peak appears in the same area where the InN cluster is located, but the frequency does not match any of the known InN phonon modes. This mode is also not observed in the pure InN sample. Presumably, the 500 cm^{-1} line is linked to the interface of the InN cluster and the InGaN layer. In the spectra #6 to #9 of InGaN sample #760, a peak at 500 cm^{-1} is also observed in combination with the A_1(TO) and the C_2 mode (Figure 6.18). The enhanced peak might also be a surface mode. Thus, further investigations are necessary to assign this mode.

Further TERS measurements were performed at the surface of the InGaN layer with an intermediate composition with 46% Indium. Figure 6.22 a+b illustrate the presence of the strong TERS peak around 688 cm^{-1} and its intensity. The Raman peak is assigned as the A_1(LO) mode of the InGaN. The frequency shift corresponds to an In-content x = 0.32 and is very homogeneous with a compositional variation of ± 1%. As shown in Figure, the $In_{0.3}Ga_{0.7}N$ compound is identified over the most part of the investigated area but differs from the average determined In-content x = 0.46 by µRaman mapping. The compositional difference of 14% is in the typical range of phase separations.

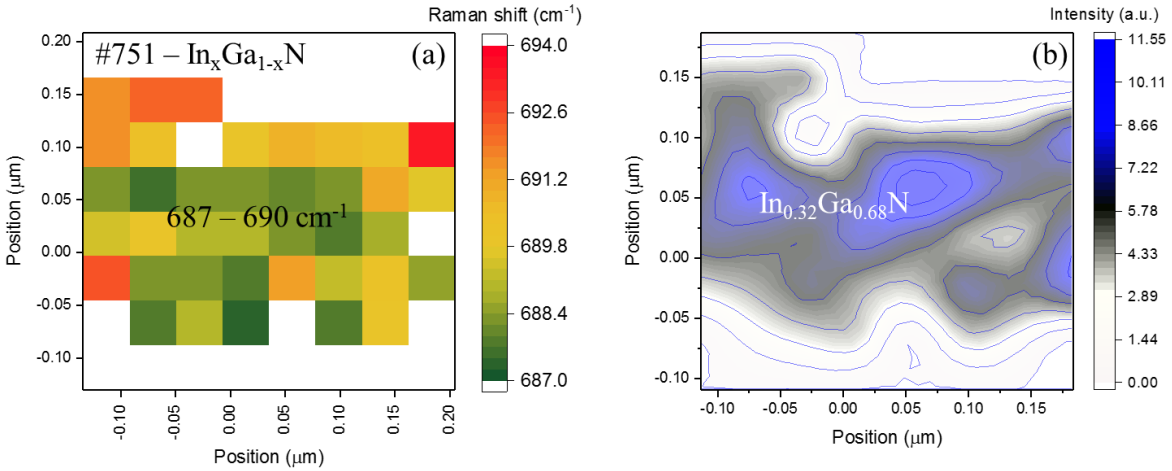

Figure 6.22: Distribution of the A_1(LO) phonon mode (a) and the corresponding intensity map of sample #751.

The discovery of the near-field modes C_1 and C_2 in thin InN contributes to the identification of InN clusters in thin InGaN films grown by MEPA-MOCVD leading to further investigations. One question is if the enhanced modes C_1 and C_2 also exist in bulk InN grown by a different deposition technique. Another question is if InN clusters are also present in 2-dimensional InGaN structures. Therefore, TERS measurements of a 2 µm thick InN sample grown by PA-MBE and a 3 nm InGaN single QW grown by MOVPE are carried out. Figure 6.23 displays the tip-enhanced spectra in the following order from top to bottom: bulk InN, thin film InN and InGaN and last the spectrum of the InGaN QW. TERS detects the C_1 and C_2 near-field modes in combination with the enhanced A_1(TO) in the InN bulk (Figure 6.23a) confirming the previous results of the InN film (Figure 6.23b). Furthermore, the C_1 and C_2 signals are also measured in the InGaN QW (Figure 6.23d) identifying localized InN clusters inside the 2-dimensional structure similar to the thin InGaN layer (Figure 6.23c). The E_2(high) mode in the tip-enhanced spectrum of the InGaN QW is due to the GaN capping layer. The single InGaN quantum well is embedded in a GaN matrix with a thin capping layer between 1 - 5 nm.

In summary, TERS reveals compositional fluctuations on a nanometer scale in InGaN layers, which appeared homogeneous by µRaman mapping. TERS detected new enhanced modes C_1 and C_2 not only in thin film and bulk InN, but also in InGaN films and single quantum well. Both modes are a combination of the A_1(TO) mode with the acoustic branch at the symmetry point M or K. The nearfield modes C_1 and C_2 are independent of the growth technique and offer identification of InN nanoclusters in the 2-D and 3-D InGaN materials.

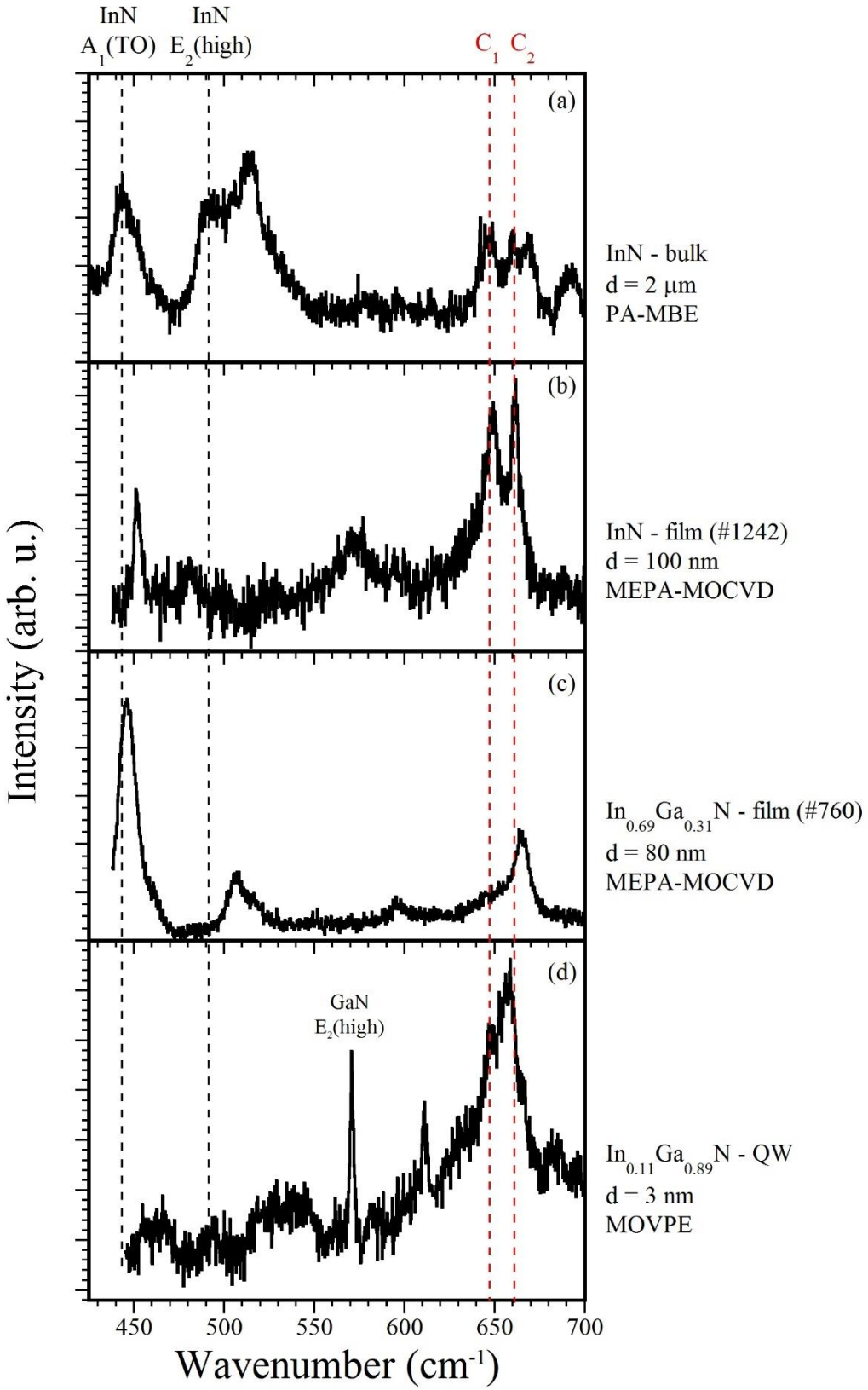

Figure 6.23: Enhanced nearfield modes C_1 and C_2 in (a) bulk InN, (b) thin film InN, (c) thin film InGaN and (d) InGaN QW.

7 Conclusion and outlook

Growth techniques such as conventional MOCVD and MBE face challenges in the growth and stabilization of quality $In_xGa_{1-x}N$ materials with an Indium content above 30% for device fabrication. To step beyond the current limitations and address these challenges alternative growth approaches have to be explored. The topic of this work is the fabrication and characterization of InN and indium-rich InGaN alloys grown by Migration-enhanced plasma-assisted (MEPA-) MOCVD, a novel approach for the growth of binary and ternary group III-nitride materials.
This chapter discusses and interprets the analytical results presented in this work regarding the applied growth parameters. It summarizes the most important results and gives an outlook on the ongoing research.

MEPA-MOCVD

The concept of MEPA-MOCVD is the stabilization of the growth surface in the afterglow regime by kinetic means. The replacement of ammonia as a nitrogen precursor by plasma-activated nitrogen species has extended the process parameter space to stabilize the growth surface. The interaction between metalorganics, reactor pressure, gas by-mix (H_2, NH_3), applied plasma power, the nitrogen flow rate through the plasma source as well as the distance to the growth surface must be considered to achieve a high flux of reactive nitrogen species and avoid damage of the deposited material. Therefore, the composition and the density of the plasma-activated nitrogen species in the afterglow regime is a convoluted function of all these variables. The applied plasma power has an influence on the type and concentration of the plasma-activated nitrogen species. At high plasma power, the consequently generated reactive nitrogen species might have a deleterious impact on the growth process. The impact of the low- and high-energy nitrogen species and their density during plasma exposure is another question that needs to be further explored. Two important variables to tailor the kinetic energies of the reactive nitrogen fragments in MEPA-MOCVD are the reactor pressure and the nitrogen flow rate through the plasma source. Both growth parameters define the number of collisions that the plasma-activated nitrogen species will undergo between the plasma source and the substrate. A growth series at various reactor pressures showed a significant improvement of the InN film quality with decreasing pressure indicated by the narrowing of the FWHM of the E_2(high) mode from 20 cm^{-1} to 10 cm^{-1}. However, the film thickness reduced from 200 nm to 50 nm with decreasing pressure. Growth at low pressures leads to fewer collisions, and more damaging species reach the growth surface, which was verified by PES. The high-energy species result in etching of the deposited film. A possible solution might be the implementation of a grid between the plasma source and the growth surface. Applying a positive or negative grid voltage allows filtering of ionized species and determination of the growth mode by initiating or suppressing the growth of nanostructures. The study of the plasma-activated species at the growth surface as a function of a DC grid voltage during the MEPA-MOCVD process is the object of ongoing research.

The optimization of process parameters like growth temperature and the precursor pulse sequence is necessary for the stabilization of the growth surface to fabricate InN and In-rich InGaN alloys of good crystalline quality. The pulse sequence of the MO and plasma nitrogen species has an influence on the layer quality and the suppression of phase segregation of the

deposited InGaN layers. To reduce potential gas-phase reactions between ionized nitrogen fragments and MO precursor fragments in the gas phase, a temporally modulated delivery of active nitrogen species and MO-precursor species towards the growth surface was utilized. As mentioned at the beginning of the previous chapter, TMI and TMG are simultaneously pulsed into the reactor and overlap shortly with the plasma exposure. This could lead to a possible interaction between MO and nitrogen precursors and the formation of adducts in the gas phase above the growth surface. Furthermore, nitrogen radicals can form bonds with ad-atoms on the growth surface and increase the probability of desorption of Indium and Gallium atoms from the surface. Enlarging the separation between the MO pulsed and the plasma exposure might be required.

At this point, there is little knowledge about which constituents of the nitrogen plasma promote the growth of group III-nitrides and how their kinetic energies and their lifetime stabilize the growth surface as a function of all these parameters. Real-time monitoring by plasma emission spectroscopy (PES) of the species in the gas phase above the growth surface can provide a possibility to engineer and control the gas phase and surface chemistry. The identification of the nitrogen species and their concentrations in correlation to the diffusion and the surface chemistry process, which drive the film growth, might enable to precisely tailor the separation or overlap of the pulsed MO and nitrogen precursor supply. In the scope of this thesis, conditioning of the plasma activated nitrogen species by variation of plasma power, nitrogen flow rate as well as by-mix of hydrides (hydrogen and ammonia) has been successfully demonstrated. UVAS verified plasma-assisted decomposition of ammonia indicated by the conversion of NH_3 to NH* containing species. PES showed that molecular nitrogen species dominate the emission of the hollow cathode plasma source in the range from 200 to 1000 nm. The multiple lines and bands are assigned to the energy level transitions of the first positive, second positive and first negative nitrogen series. The number of active nitrogen species above the growth surface is a function of plasma power. PES detected excited indium In*-species as well. However, monitoring of the emission intensities of a single peak of each nitrogen series is not sufficient for a correlation with the structural layer properties, because each nitrogen series consist of multiple peaks. A better model might be, to summarize the emission intensities for each group of plasma nitrogen species and compare them in relation to each other.

InGaN

MEPA-MOCVD has successfully demonstrated the growth of InN at an increased temperature of 775°C, way above the temperature range compared to conventional MOCVD. At growth temperatures above 630°C, the mobility of the Indium atoms is enhanced, and the Indium atoms thermally desorb from the growth surface. In MEPA-MOCVD, the kinetic energies of the plasma-activated nitrogen species stabilize the growth surface and suppress the Indium decomposition. The MEPA-MOCVD concept of stabilizing the growth surface at an increased InN growth temperature narrows the temperature gap between GaN and InN and enables the growth of In-rich InGaN. In the next step, InGaN layers with different compositions were deposited using a sequenced precursor injection. The structural and optoelectronic properties of the deposited InGaN epilayer have been analyzed by characterization methods such as Raman spectroscopy, HR-XRD, AFM as well as s-SNIN and TERS. The results of Raman spectroscopy and HR-XRD have verified that MEPA-MOCVD is a viable approach to fabricate and stabilize $In_xGa_{1-x}N$ alloys over a wide composition range ($0.3 < x < 1$). The dependency of the A_1(LO) frequency with the composition of the studied InGaN layers shows a linear behavior

in good agreement with the MREI model. μRaman mapping in the dimension of 10 μm x 10 μm yielded a high compositional homogeneity. The average composition for each $In_xGa_{1-x}N$ layer had a deviation of less than 1%. Furthermore, the topography of the sample surface shows a uniform island distribution and the surface morphologies are very smooth.
However, resonant Raman-scattering experiments showed a microscopic phase separation for $In_xGa_{1-x}N$ layers with an intermediate Indium composition between $0.4 < x < 0.65$. These phase separations can be explained by spinodal decomposition because these compositions are inside the miscibility gap at a growth temperature of 775°C. Considering the phase diagram calculated by Ho and Stringfellow, the InGaN samples with the intermediate composition are thermodynamically unstable. Overall, the Raman spectra showed a significant broadening of the A_1(LO) mode. The broadening of A_1(LO) Raman mode is an indication of nanoscale phase segregations at the growth surface. Hence the resolution of μRaman spectroscopy is not sufficient, the investigation of these nanoscale compositional inhomogeneities requires characterization methods with a high spatial resolution below the diffraction limit. The state of the art near-field spectroscopic tools TERS and s-SNIN offer a resolution of ~10-15 nm and provide a correlation of the chemical compositional and the morphological information. Based on the significant broadening for the $In_xGa_{1-x}N$ layers with intermediate, the layer with an In-content x = [0.46, 0.69 and 0.86] were selected for s-SNIN and TERS measurements. TERS and s-SNIN independently verified nanoscopic compositional inhomogeneities at the surface of the selected $In_xGa_{1-x}N$ layers grown by MEPA-MOCVD in the same growth window. The dimensions of these phase segregations observed by s-SNIN agreed with the dimensions found by TERS. While s-SNIN reveals only a difference in the material composition, TERS provides compositional information about the indium and gallium content of the nanoscale phase segregations. A domain of $In_xGa_{1-x}N$ with a low In-content enclosed by InN clusters have been identified. The vast difference between the composition of the InGaN subset and the average layer composition is due to the formation of phase segregation because the aggregation of In-atoms to form InN clusters leads consequently to a depletion of the surrounding area. For another $In_xGa_{1-x}N$ layer, phonon modes assigned to InN and InGaN are found in the same region of the TERS scan. Probably, InN at the surface buries a subset of InGaN, resulting in an interface mode that is also detected in the same area of the TERS map. In addition, TERS of a pure InN layer was also carried out. The pure near-field spectrum reveals a set of new phonon modes in the range from 625 cm^{-1} to 670 cm^{-1}, that cannot be assigned to the first order phonon modes of cubic or hexagonal InN. The analysis showed a relation between the A_1(TO) mode and the C_1 and C_2 mode. Considering calculations of the InN phonon dispersion curves lead to the assumption that these modes are an additive combination of optical and acoustical phonons at the symmetry point M or K. This two-phonon process agrees very well with the experimental frequencies of the C_1 and C_2 mode. A better understanding is crucial to ensure correct discrimination and assignment of these modes because they are located in the phonon frequency range of the A_1(LO) mode of $In_xGa_{1-x}N$. Further TERS experiments detected the C_1 and C_2 feature also in InN bulk as well as different $In_xGa_{1-x}N$ layers and in a single InGaN quantum well. The presence of these modes is independent of the growth procedure and enables identification of InN nanoclusters, which are formed due to indium segregation, in 2D and 3D InGaN structures.

In conclusion, the tremendous effort in research and the enhancement of novel growth techniques enable to address the current challenges and limitations in the growth of In-rich InGaN layers and nanostructures. The combination of real-time metrology of excited nit species with the structural and optoelectronic properties of group III-nitride alloys will help to define the growth parameter window of MEPA-MOCVD in terms of supersaturation. The state-of-the-art characterization methods TERS and s-SNIN provide nanoscale information about compositional variations as well as indium clustering due to phase segregation. TERS as a non-destructive tool with nanoscale resolution obtains chemical and morphological feedback, which is essential for the optimization of the group III-nitride growth process. Further studies are needed to evaluate to which extend compositional fluctuations can be suppressed by kinetic means using MEPA-MOCVD to produce homogeneous, high-quality In-rich InGaN structures for device fabrication. The group III-nitride material system still gives rise to new questions and challenges that fortify the interest in further research.

Bibliography

1. Maruska, H.P. and J.J. Tietjen, *The Preparation and Properties of Vapor-Deposited Single-Crystalline GaN.* Applied Physics Letters, 1969. **15**(10): p. 327-329.

2. Manasevit, H.M., F.M. Erdmann, and W.I. Simpson, *The Use of Metalorganics in the Preparation of Semiconductor Materials: IV . The Nitrides of Aluminum and Gallium.* Journal of The Electrochemical Society, 1971. **118**(11): p. 1864-1868.

3. MacChesney, J.B., P.M. Bridenbaugh, and P.B. O'Connor, *Thermal stability of indium nitride at elevated temperatures and nitrogen pressures.* Materials Research Bulletin, 1970. **5**(9): p. 783-791.

4. Hovel, H.J. and J.J. Cuomo, *Electrical and Optical Properties of rf-Sputtered GaN and InN.* Applied Physics Letters, 1972. **20**(2): p. 71-73.

5. Tansley, T.L. and C.P. Foley, *Electron mobility in indium nitride.* Electronics Letters, 1984. **20**(25): p. 1066-1068.

6. Tansley, T.L. and C.P. Foley, *Optical band gap of indium nitride.* Journal of Applied Physics, 1986. **59**(9): p. 3241-3244.

7. Amano, H., et al., *Metalorganic vapor phase epitaxial growth of a high quality GaN film using an AlN buffer layer.* Applied Physics Letters, 1986. **48**(5): p. 353-355.

8. Hiroshi, A., et al., *P-Type Conduction in Mg-Doped GaN Treated with Low-Energy Electron Beam Irradiation (LEEBI).* Japanese Journal of Applied Physics, 1989. **28**(12A): p. L2112.

9. Wakahara, A. and A. Yoshida, *Heteroepitaxial growth of InN by microwave-excited metalorganic vapor phase epitaxy.* Applied Physics Letters, 1989. **54**(8): p. 709-711.

10. Shuji, N., S. Masayuki, and M. Takashi, *P-GaN/N-InGaN/N-GaN Double-Heterostructure Blue-Light-Emitting Diodes.* Japanese Journal of Applied Physics, 1993. **32**(1A): p. L8.

11. Lu, H., et al., *Effect of an AlN buffer layer on the epitaxial growth of InN by molecular-beam epitaxy.* Applied Physics Letters, 2001. **79**(10): p. 1489-1491.

12. Davydov, V.Y., et al., *Absorption and Emission of Hexagonal InN. Evidence of Narrow Fundamental Band Gap.* physica status solidi (b), 2002. **229**(3): p. r1-r3.

13. Foley, C.P. and T.L. Tansley, *Pseudopotential band structure of indium nitride.* Physical Review B, 1986. **33**(2): p. 1430-1433.

14. Matsuoka, T., et al., *Optical bandgap energy of wurtzite InN.* Applied Physics Letters, 2002. **81**(7): p. 1246-1248.

15. Wu, J., et al., *Effects of the narrow band gap on the properties of InN.* Physical Review B, 2002. **66**(20): p. 201403.

16. Wu, J., et al., *Temperature dependence of the fundamental band gap of InN.* Journal of Applied Physics, 2003. **94**(7): p. 4457-4460.

17. Khludkov, S.S., I.A. Prudaev, and O.P. Tolbanov, *Physical properties of indium nitride, impurities, and defects.* Russian Physics Journal, 2014. **56**(9): p. 997-1006.

18. Morkoç, H., *Handbook of nitride semiconductors and devices / Volume 1, Materials properties, physics and growth*. 2008, Weinheim :: Wiley-VCH.

19. Tran, C.A., et al., *Phase separation in InGaN/GaN multiple quantum wells and its relation to brightness of blue and green LEDs.* Journal of Crystal Growth, 1998. **195**(1): p. 397-400.

20. Isamu, A. and A. Hiroshi, *Breakthroughs in Improving Crystal Quality of GaN and Invention of the p–n Junction Blue-Light-Emitting Diode.* Japanese Journal of Applied Physics, 2006. **45**(12R): p. 9001.

21. Zhu, D., D.J. Wallis, and C.J. Humphreys, *Prospects of III-nitride optoelectronics grown on Si.* Reports on Progress in Physics, 2013. **76**(10): p. 106501.

22. KnowMade. *What is the status of III-N technology?* 2017; Available from: http://www.knowmade.com/status-iii-n-technology/.

23. Yole Develloppement. *LED lighting module market with more than US$4 billion revenue, is showing attractive perspectives*. 2017; Available from: http://www.yole.fr/LED_Modules_MarketTrends.aspx#.WrjZjH8h2po.

24. Dahal, R., et al., *InGaN/GaN multiple quantum well concentrator solar cells.* Applied Physics Letters, 2010. **97**(7): p. 073115.

25. McLaughlin, D.V.P. and J.M. Pearce, *Progress in Indium Gallium Nitride Materials for Solar Photovoltaic Energy Conversion.* Metallurgical and Materials Transactions A, 2013. **44**(4): p. 1947-1954.

26. Keating, S., et al., *Effects of Substrate Temperature on Indium Gallium Nitride Nanocolumn Crystal Growth.* Crystal Growth & Design, 2011. **11**(2): p. 565-568.

27. Wu, J., *When group-III nitrides go infrared: New properties and perspectives.* Journal of Applied Physics, 2009. **106**(1): p. 011101.

28. Moses, P.G. and C.G. Van de Walle, *Band bowing and band alignment in InGaN alloys.* Applied Physics Letters, 2010. **96**(2): p. 021908.

29. Collazo, R. and N. Dietz, *Chapter 8 The Group III-Nitride Material Class: from Preparation to Perspectives in Photoelectrocatalysis*, in *Photoelectrochemical Water Splitting: Materials, Processes and Architectures*. 2013, The Royal Society of Chemistry. p. 193-222.

30. Masyukov, N.A. and A.V. Dmitriev, *Hot electrons in wurtzite indium nitride.* Journal of Applied Physics, 2011. **109**(2): p. 023706.

31. Ferreyra, R.A., et al., *Group III Nitrides*, in *Springer Handbook of Electronic and Photonic Materials*, S. Kasap and P. Capper, Editors. 2017, Springer International Publishing: Cham. p. 1-1.

32. Miller, N., et al., *Effect of charged dislocation scattering on electrical and electrothermal transport in n-type InN.* Physical Review B, 2011. **84**(7): p. 075315.

33. Xinqiang, W., et al., *High-Electron-Mobility InN Layers Grown by Boundary-Temperature-Controlled Epitaxy.* Applied Physics Express, 2012. **5**(1): p. 015502.

34. Wang, K., et al., *Selective growth of N-polar InN through an in situ AlN mask on a sapphire substrate.* Applied Physics Letters, 2014. **104**(3): p. 032108.

35. Meziani, Y.M., et al., *Terahertz investigation of high quality indium nitride epitaxial layers.* physica status solidi (a), 2005. **202**(4): p. 590-592.

36. Polyakov, V.M., et al., *Impact of n-type doping on the terahertz surface emission from c-plane InN.* physica status solidi (a), 2010. **207**(6): p. 1353-1355.

37. Pearton, S.J., et al., *GaN-based diodes and transistors for chemical, gas, biological and pressure sensing.* Journal of Physics: Condensed Matter, 2004. **16**(29): p. R961.

38. Lu, H., W.J. Schaff, and L.F. Eastman, *Surface chemical modification of InN for sensor applications.* Journal of Applied Physics, 2004. **96**(6): p. 3577-3579.

39. Na, L. and F. Ian, *III-nitrides for energy production: photovoltaic and thermoelectric applications.* Semiconductor Science and Technology, 2013. **28**(7): p. 074023.

40. Ariyawansa, G., et al., *GaN/AlGaN heterojunction infrared detector responding in 8–14 and 20–70μm ranges.* Applied Physics Letters, 2006. **89**(14): p. 141122.

41. Melton Andrew, G., et al., *Comparison of neutron conversion layers for GaN-based scintillators.* physica status solidi c, 2011. **9**(3-4): p. 957-959.

42. Phillips, J.M., et al., *Research challenges to ultra-efficient inorganic solid-state lighting.* Laser & Photonics Reviews, 2007. **1**(4): p. 307-333.

43. Auf der Maur, M., et al., *Efficiency Drop in Green InGaN/GaN Light Emitting Diodes: The Role of Random Alloy Fluctuations.* Physical Review Letters, 2016. **116**(2): p. 027401.

44. Ho, I.h. and G.B. Stringfellow, *Solid phase immiscibility in GaInN.* Applied Physics Letters, 1996. **69**(18): p. 2701-2703.

45. Stringfellow, G.B., *Microstructures produced during the epitaxial growth of InGaN alloys.* Journal of Crystal Growth, 2010. **312**(6): p. 735-749.

46. Abate, Y., et al., *Nanoscopy of Phase Separation in InxGa1–xN Alloys.* ACS Applied Materials & Interfaces, 2016. **8**(35): p. 23160-23166.

47. Perlin, P., et al., *Raman scattering and x-ray-absorption spectroscopy in gallium nitride under high pressure.* Physical Review B, 1992. **45**(1): p. 83-89.

48. Gorczyca, I., et al., *High pressure phase transition in aluminium nitride.* Solid State Communications, 1991. **79**(12): p. 1033-1034.

49. Paszkowicz, W., S. Podsiadło, and R. Minikayev, *Rietveld-refinement study of aluminium and gallium nitrides.* Journal of Alloys and Compounds, 2004. **382**(1): p. 100-106.

50. Belabbes, A., J. Furthmüller, and F. Bechstedt, *Electronic properties of polar and nonpolar InN surfaces: A quasiparticle picture.* Physical Review B, 2011. **84**(20): p. 205304.

51. Bernardini, F., V. Fiorentini, and D. Vanderbilt, *Spontaneous polarization and piezoelectric constants of III-V nitrides.* Physical Review B, 1997. **56**(16): p. R10024-R10027.

52. Vurgaftman, I. and J.R. Meyer, *Band parameters for nitrogen-containing semiconductors.* Journal of Applied Physics, 2003. **94**(6): p. 3675-3696.

53. Levinshtein, M.E., S.L. Rumyantsev, and M. Shur, *Properties of advanced semiconductor materials : GaN, AlN, InN, BN, SiC, SiGe*. 2001, New York: Wiley. xvii, 194 p.

54. Kasic, A., et al., *Effective electron mass and phonon modes in n-type hexagonal InN.* Physical Review B, 2002. **65**(11): p. 115206.

55. Wu, J., et al., *Small band gap bowing in In1−xGaxN alloys.* Applied Physics Letters, 2002. **80**(25): p. 4741-4743.

56. Sakalauskas, E., et al., *Dielectric function and bowing parameters of InGaN alloys.* physica status solidi (b), 2012. **249**(3): p. 485-488.

57. Gorczyca, I., et al., *Gap bowing in Inx Ga1–x N and Inx Al1–x N under pressure.* physica status solidi c, 2009. **6**(S2): p. S368-S371.

58. Martin, G., et al., *Valence-band discontinuities of wurtzite GaN, AlN, and InN heterojunctions measured by x-ray photoemission spectroscopy.* Applied Physics Letters, 1996. **68**(18): p. 2541-2543.

59. Ambacher, O., et al., *Electronics and sensors based on pyroelectric AlGaN/GaN heterostructures.* physica status solidi (c), 2003. **0**(6): p. 1878-1907.

60. Mattila, T. and A. Zunger, *Predicted bond length variation in wurtzite and zinc-blende InGaN and AlGaN alloys.* Journal of Applied Physics, 1998. **85**(1): p. 160-167.

61. Schliwa, A., G. Hönig, and D. Bimberg, *Electronic Properties of III-V Quantum Dots*, in *Multi-Band Effective Mass Approximations: Advanced Mathematical Models and Numerical Techniques*, M. Ehrhardt and T. Koprucki, Editors. 2014, Springer International Publishing: Cham. p. 57-85.

62. Smekal, A., *Zur Quantentheorie der Dispersion.* Naturwissenschaften, 1923. **11**(43): p. 873-875.

63. Raman, C.V. and K.S. Krishnan, *A New Type of Secondary Radiation.* Nature, 1928. **121**: p. 501.

64. Yu, P.Y., M. Cardona, and SpringerLink (Online service), *Fundamentals of semiconductors physics and materials properties*, in *Graduate texts in physics*. 2010, Springer,: Berlin ; London. p. 1 online resource (xx, 775 p.).

65. Lew Yan Voon, L.C., et al., *Terms linear in k in the band structure of wurtzite-type semiconductors.* Physical Review B, 1996. **53**(16): p. 10703-10714.

66. Zhang, J.M., et al., *Raman spectra of isotopic GaN.* Physical Review B, 1997. **56**(22): p. 14399-14406.

67. Wieting, T.J. and M. Schlüter, *Electrons and Phonons in Layered Crystal Structures*. Physics and chemistry of materials with layered structures. 1979, Dordrecht u.a.: Reidel. X, 473 S.

68. Haboeck, U., et al., *Lattice dynamics in GaN and AlN probed with first- and second-order Raman spectroscopy.* physica status solidi (c), 2003. **0**(6): p. 1710-1731.

69. Davydov, V.Y., et al., *Experimental and theoretical studies of phonons in hexagonal InN.* Applied Physics Letters, 1999. **75**(21): p. 3297-3299.

70. Behr, D., et al., *Resonant Raman scattering in hexagonal GaN.* Applied Physics Letters, 1996. **68**(17): p. 2404-2406.

71. Inushima, T., T. Shiraishi, and V.Y. Davydov, *Phonon structure of InN grown by atomic layer epitaxy.* Solid State Communications, 1999. **110**(9): p. 491-495.

72. Davydov, V.Y., et al., *Phonon dispersion and Raman scattering in hexagonal GaN and AlN.* Physical Review B, 1998. **58**(19): p. 12899-12907.

73. Kozawa, T., et al., *Thermal stress in GaN epitaxial layers grown on sapphire substrates.* Journal of Applied Physics, 1995. **77**(9): p. 4389-4392.

74. Kuball, M., *Raman spectroscopy of GaN, AlGaN and AlN for process and growth monitoring/control.* Surface and Interface Analysis, 2001. **31**(10): p. 987-999.

75. Wang, F.C., et al., *Residual thermal strain in thick GaN epifilms revealed by cross-sectional Raman scattering and cathodoluminescence spectra.* Semiconductor Science and Technology, 2007. **22**(8): p. 896-899.

76. Binnig, G., C.F. Quate, and C. Gerber, *Atomic Force Microscope.* Physical Review Letters, 1986. **56**(9): p. 930-933.

77. Albrecht, T.R., et al., *Frequency modulation detection using high-Q cantilevers for enhanced force microscope sensitivity.* Journal of Applied Physics, 1991. **69**(2): p. 668-673.

78. Grille, H., C. Schnittler, and F. Bechstedt, *Phonons in ternary group-III nitride alloys.* Physical Review B, 2000. **61**(9): p. 6091-6105.

79. Deckert-Gaudig, T., et al., *Tip-enhanced Raman spectroscopy - from early developments to recent advances.* Chemical Society Reviews, 2017. **46**(13): p. 4077-4110.

80. Stöckle, R.M., et al., *Nanoscale chemical analysis by tip-enhanced Raman spectroscopy.* Chemical Physics Letters, 2000. **318**(1): p. 131-136.

81. Kusch, P., et al., *Combined Tip-Enhanced Raman Spectroscopy and Scattering-Type Scanning Near-Field Optical Microscopy.* The Journal of Physical Chemistry C, 2018. **122**(28): p. 16274-16280.

82. Poliani, E., F. Nippert, and J. Maultzsch, *Effect of gap modes on graphene and multilayer graphene in tip-enhanced Raman spectroscopy.* physica status solidi (b), 2012. **249**(12): p. 2511-2514.

83. Eligal, L., et al., *Etching gold tips suitable for tip-enhanced near-field optical microscopy.* Review of Scientific Instruments, 2009. **80**(3): p. 033701.

84. Verma, P., *Tip-Enhanced Raman Spectroscopy: Technique and Recent Advances.* Chemical Reviews, 2017. **117**(9): p. 6447-6466.

85. Shi, X., et al., *Advances in Tip-Enhanced Near-Field Raman Microscopy Using Nanoantennas.* Chemical Reviews, 2017. **117**(7): p. 4945-4960.

86. Kawata, S., et al., *Nano-Raman Scattering Microscopy: Resolution and Enhancement.* Chemical Reviews, 2017. **117**(7): p. 4983-5001.

87. Shao, F. and R. Zenobi, *Tip-enhanced Raman spectroscopy: principles, practice, and applications to nanospectroscopic imaging of 2D materials.* Analytical and Bioanalytical Chemistry, 2019. **411**(1): p. 37-61.

88. Poliani, E., et al., *Breakdown of Far-Field Raman Selection Rules by Light–Plasmon Coupling Demonstrated by Tip-Enhanced Raman Scattering.* The Journal of Physical Chemistry Letters, 2017. **8**(22): p. 5462-5471.

89. Maier, S.A., *Plasmonics : fundamentals and applications*. 2007. xxiv, 223 pages.

90. Zayats, A.V., I.I. Smolyaninov, and A.A. Maradudin, *Nano-optics of surface plasmon polaritons.* Physics Reports, 2005. **408**(3): p. 131-314.

91. Hayashi, S. and T. Okamoto, *Plasmonics: visit the past to know the future.* Journal of Physics D: Applied Physics, 2012. **45**(43): p. 433001.

92. Novotny, L. and B. Hecht, *Principles of nano-optics*. Reprinted with corr. ed. 2007, Cambridge u.a.: Cambridge Univ. Press. XVII, 539 S.

93. Pashaee, F., et al., *Tip-Enhanced Raman Spectroscopy of Self-Assembled Thiolated Monolayers on Flat Gold Nanoplates Using Gaussian-Transverse and Radially*

Polarized Excitations. The Journal of Physical Chemistry C, 2013. **117**(30): p. 15639-15646.

94. Roth, R.M., et al., *Resonant-plasmon field enhancement from asymmetrically illuminated conical metallic-probe tips.* Optics Express, 2006. **14**(7): p. 2921-2931.

95. Bouhelier, A., *Field-enhanced scanning near-field optical microscopy.* Microscopy Research and Technique, 2006. **69**(7): p. 563-579.

96. Yeo, B.-S., et al., *Tip-enhanced Raman Spectroscopy – Its status, challenges and future directions.* Chemical Physics Letters, 2009. **472**(1): p. 1-13.

97. Yang, Z., J. Aizpurua, and H. Xu, *Electromagnetic field enhancement in TERS configurations.* Journal of Raman Spectroscopy, 2009. **40**(10): p. 1343-1348.

98. Blum, C., et al., *Tip-enhanced Raman spectroscopy – an interlaboratory reproducibility and comparison study.* Journal of Raman Spectroscopy, 2014. **45**(1): p. 22-31.

99. Richards, D., et al., *Near-field microscopy by elastic light scattering from a tip.* Philosophical Transactions of the Royal Society of London. Series A: Mathematical, Physical and Engineering Sciences, 2004. **362**(1817): p. 787-805.

100. Stiegler, J.M., et al., *Nanoscale Infrared Absorption Spectroscopy of Individual Nanoparticles Enabled by Scattering-Type Near-Field Microscopy.* ACS Nano, 2011. **5**(8): p. 6494-6499.

101. Cullity, B.D., *Elements of x-ray diffraction*. 2d ed. Addison-Wesley series in metallurgy and materials. 1978, Reading, Mass.: Addison-Wesley Pub. Co. xii, 555 p.

102. Bragg William, H. and L. Bragg William, *The reflection of X-rays by crystals.* Proceedings of the Royal Society of London. Series A, Containing Papers of a Mathematical and Physical Character, 1913. **88**(605): p. 428-438.

103. Moram, M.A. and M.E. Vickers, *X-ray diffraction of III-nitrides.* Reports on Progress in Physics, 2009. **72**(3): p. 036502.

104. Frank, F. and J. van der Merwe, Proceedings of the Royal Society of London A, 1949. **198**: p. 205.

105. Stranksi, I. and L. Krastanov, Akad. Wiss. Wien, 1937. **146**: p. 797.

106. Volmer, M. and A. Weber, Zeitschrift für Physikalische Chemie, 1926. **119**: p. 277.

107. Franchy, R., *Growth of thin, crystalline oxide, nitride and oxynitride films on metal and metal alloy surfaces.* Surface Science Reports, 2000. **38**(6): p. 195-294.

108. Pohl, U.W., *Epitaxy of semiconductors : introduction to physical principles*. Graduate texts in physics,. Springer-Verlag Berlin Heidelberg. xiv, 325 pages.

109. Ruterana, P., M. Albrecht, and J.œ. Neugebauer, *Nitride semiconductors : handbook on materials and devices*. First edition ed. 2008. xxii, 664 pages.

110. Richter, E., et al., *Growth of GaN boules via vertical HVPE.* Journal of Crystal Growth, 2012. **350**(1): p. 89-92.

111. Takahashi, N., J. Ogasawara, and A. Koukitu, *Vapor phase epitaxy of InN using InCl and InCl3 sources.* Journal of Crystal Growth, 1997. **172**(3): p. 298-302.

112. Kumagai, Y., et al., *Hydride vapor phase epitaxy of InN by the formation of InCl3 using In metal and Cl2.* Journal of Crystal Growth, 2007. **300**(1): p. 57-61.

113. Kumagai, Y., et al., *Hydride vapor phase epitaxy of AlN: thermodynamic analysis of aluminum source and its application to growth.* physica status solidi (c), 2003. **0**(7): p. 2498-2501.

114. Skierbiszewski, C., et al., *InGaN laser diodes operating at 450–460 nm grown by rf-plasma MBE.* Journal of Vacuum Science & Technology B, Nanotechnology and Microelectronics: Materials, Processing, Measurement, and Phenomena, 2011. **30**(2): p. 02B102.

115. Klosek, K., et al., *Optimization of nitrogen plasma source parameters by measurements of emitted light intensity for growth of GaN by molecular beam epitaxy.* Thin Solid Films, 2013. **534**: p. 107-110.

116. McSkimming, B.M., et al., *Plasma assisted molecular beam epitaxy of GaN with growth rates >2.6μm/h.* Journal of Crystal Growth, 2014. **386**: p. 168-174.

117. Bhuiyan, A.G., A. Hashimoto, and A. Yamamoto, *Indium nitride (InN): A review on growth, characterization, and properties.* Journal of Applied Physics, 2003. **94**(5): p. 2779-2808.

118. Myers, T.H., et al., *Influence of active nitrogen species on high temperature limitations for (0001_) GaN growth by rf plasma-assisted molecular beam epitaxy.* Journal of Vacuum Science & Technology B, 1999. **17**(4): p. 1654-1658.

119. Suntola, T. and J. Antson, *Method for producing compound thin films*. 1977, Google Patents.

120. Puurunen, R.L., *Surface chemistry of atomic layer deposition: A case study for the trimethylaluminum/water process.* Journal of Applied Physics, 2005. **97**(12): p. 121301.

121. Ozgit-Akgun, C., et al., *Hollow cathode plasma-assisted atomic layer deposition of crystalline AlN, GaN and AlxGa1-xN thin films at low temperatures.* Journal of Materials Chemistry C, 2014. **2**(12): p. 2123-2136.

122. Johnson, R.W., A. Hultqvist, and S.F. Bent, *A brief review of atomic layer deposition: from fundamentals to applications.* Materials Today, 2014. **17**(5): p. 236-246.

123. Profijt, H.B., et al., *Plasma-Assisted Atomic Layer Deposition: Basics, Opportunities, and Challenges.* Journal of Vacuum Science & Technology A: Vacuum, Surfaces, and Films, 2011. **29**(5): p. 050801.

124. Haider, A., et al., *Low-temperature grown wurtzite InxGa1-xN thin films via hollow cathode plasma-assisted atomic layer deposition.* Journal of Materials Chemistry C, 2015. **3**(37): p. 9620-9630.

125. Haider, A., S. Kizir, and N. Biyikli, *Low-temperature self-limiting atomic layer deposition of wurtzite InN on Si(100).* AIP Advances, 2016. **6**(4): p. 045203.

126. Veeco Instruments Inc. *VEECO SHIPS NEXT GENERATION MOCVD SYSTEMS TO CHINA FOR HIGH VOLUME LED PRODUCTION*. Available from: https://ir.veeco.com/news-events/press-releases/press-release-details/2017/Veeco-Ships-Next-Generation-MOCVD-Systems-to-China-for-High-Volume-LED-Production/default.aspx.

127. Stringfellow, G.B., *A critical appraisal of growth mechanisms in MOVPE.* Journal of Crystal Growth, 1984. **68**(1): p. 111-122.

128. Stringfellow, G.B., *Organometallic vapor-phase epitaxy: theory and practice*. 1999, San Diego: Academic Press. 1 Online-Ressource (xxiv, 572 S.).

129. Mita, S., et al., *Influence of gallium supersaturation on the properties of GaN grown by metalorganic chemical vapor deposition.* Journal of Applied Physics, 2008. **104**(1): p. 013521.

130. Koukitu, A., et al., *Thermodynamic study on the role of hydrogen during the MOVPE growth of group III nitrides.* Journal of Crystal Growth, 1999. **197**(1–2): p. 99-105.

131. Akinori, K., T. Naoyuki, and S. Hisashi, *Thermodynamic Study on Metalorganic Vapor-Phase Epitaxial Growth of Group III Nitrides.* Japanese Journal of Applied Physics, 1997. **36**(9A): p. L1136.

132. Woods, V. and N. Dietz, *InN growth by high-pressures chemical vapor deposition: Real-time optical growth characterization.* Materials Science and Engineering: B, 2006. **127**(2–3): p. 239-250.

133. Dietz, N., *Indium-nitride growth by High-Pressure CVD: Real-time and ex-situ characterization*, in *III-Nitride Semiconductor Materials*. 2006, Published by Imperial College Press and distributed by World Scientific Publishing Co. p. 203-235.

134. Buegler, M., et al., *Growth temperature and growth rate dependency on reactor pressure for InN epilayers grown by HPCVD.* Physica Status Solidi (c), 2011. **8**(7-8): p. 2059-2062.

135. Alevli, M., et al., *Effect of reactor pressure on optical and electrical properties of InN films grown by high-pressure chemical vapor deposition.* physica status solidi c, 2015. **12**(4-5): p. 423-429.

136. Ambacher, O., et al., *Thermal stability and desorption of Group III nitrides prepared by metal organic chemical vapor deposition.* Journal of Vacuum Science & Technology B: Microelectronics and Nanometer Structures Processing, Measurement, and Phenomena, 1996. **14**(6): p. 3532-3542.

137. Ivanov, S.V., et al., *Metastable nature of InN and In-rich InGaN alloys.* Journal of Crystal Growth, 2014. **403**: p. 83-89.

138. Oliver, R.A., et al., *The influence of ammonia on the growth mode in InGaN/GaN heteroepitaxy.* Journal of Crystal Growth, 2004. **272**(1): p. 393-399.

139. Sakalauskas, E., et al., *Optical properties of InN grown on Si(111) substrate.* physica status solidi (a), 2010. **207**(5): p. 1066-1069.

140. Ehrentraut, D. and Z. Sitar, *Advances in Bulk Crystal Growth of AlN and GaN.* MRS Bulletin, 2009. **34**(4): p. 259-265.

141. Skuridina, D., et al., *Surface and crystal structure of nitridated sapphire substrates and their effect on polar InN layers.* Applied Surface Science, 2014. **307**: p. 461-467.

142. Butcher, K.S.A., et al., *Gallium Nitride Film Growth Using a Plasma Based Migration Enhanced Afterglow Chemical Vapor Deposition System.* Japanese Journal of Applied Physics, 2012. **51**(1S): p. 01AF02.

143. Butcher, K.S.A., et al., *Initial experiments in the migration enhanced afterglow growth of gallium and indium nitride.* physica status solidi (c), 2012. **9**(3-4): p. 1070-1073.

144. Butcher, K.S.A., et al., *InN grown by migration enhanced afterglow (MEAglow).* physica status solidi (a), 2012. **209**(1): p. 41-44.

145. Lieberman, M.A. and R.W. Boswell, *Modeling the transitions from capacitive to inductive to wave-sustained rf discharges.* J. Phys. IV France, 1998. **08**(PR7): p. Pr7-145-Pr7-164.

146. Karlicek, R.F., B. Hammarlund, and J. Ginocchio, *UV absorption spectroscopy for monitoring hydride vapor-phase epitaxy of InGaAsP alloys.* Journal of Applied Physics, 1986. **60**(2): p. 794-799.

147. McCrary, V.R. and V.M. Donnelly, *The ultraviolet absorpton spectra of selected organometallic compounds used in the chemical vapor deposition of gallium arsenide.* Journal of Crystal Growth, 1987. **84**(2): p. 253-258.

148. Piner, E.L., et al., *Effect of hydrogen on the indium incorporation in InGaN epitaxial films.* Applied Physics Letters, 1997. **70**(4): p. 461-463.

149. Product data sheet, *TMIn SSG*. AkzoNobel Functional Chemicals, Chicago, USA.

150. Product data sheet, *TMGa SSG*. AkzoNobel Functional Chemicals, Chicago, USA.

151. Product data sheet, *TMAl SSG*. AkzoNobel Functional Chemicals, Chicago, USA.

152. Huang, J.-J., H.-C. Kuo, and S.-C. Shen, *Nitride semiconductor light-emitting diodes (LEDs): materials, technologies and applications*. Woodhead Publishing series in electronic and optical materials. 2013, Oxford: Woodhead Publishing. 1 Online-Ressource.

153. Jacko, M.G. and S.J.W. Price, *THE PYROLYSIS OF TRIMETHYLINDIUM.* Canadian Journal of Chemistry, 1964. **42**(5): p. 1198-1205.

154. Butler, J.E., et al., *In situ, real-time diagnostics of OMVPE using IR-diode laser spectroscopy.* Journal of Crystal Growth, 1986. **77**(1): p. 163-171.

155. Hebner, G.A. and K.P. Killeen, *Measurement of atomic indium during metalorganic chemical vapor deposition.* Journal of Applied Physics, 1990. **67**(3): p. 1598-1600.

156. Park, C., et al., *In situ Raman spectroscopic studies of trimethylindium pyrolysis in an OMVPE reactor.* Journal of Materials Chemistry, 2002. **12**(2): p. 356-360.

157. Larsen, C.A. and G.B. Stringfellow, *Decomposition kinetics of OMVPE precursors.* Journal of Crystal Growth, 1986. **75**(2): p. 247-254.

158. Buchan, N.I., C.A. Larsen, and G.B. Stringfellow, *Mass spectrometric studies of trimethylindium pyrolysis.* Journal of Crystal Growth, 1988. **92**(3): p. 591-604.

159. Cairns, R.A., *Plasma physics*. 1985, United Kingdom: Blackie.

160. Lu, Y., et al., *Epitaxial growth of GaN by radical-enhanced metalorganic chemical vapor deposition (REMOCVD) in the downflow of a very high frequency (VHF) N2/H2 excited plasma – effect of TMG flow rate and VHF power.* Journal of Crystal Growth, 2014. **391**: p. 97-103.

161. Norman, D.P., et al., *Effect of temperature and V/III ratio on the initial growth of indium nitride using plasma-assisted metal-organic chemical vapor deposition.* Journal of Applied Physics, 2011. **109**(6): p. 063517.

162. Cormac, C., B. Rod, and C. Robert, *Gas phase optical emission spectroscopy during remote plasma chemical vapour deposition of GaN and relation to the growth dynamics.* Journal of Physics D: Applied Physics, 2011. **44**(4): p. 045201.

163. Hughes, W.C., et al., *Molecular beam epitaxy growth and properties of GaN films on GaN/SiC substrates.* Journal of Vacuum Science & Technology B, 1995. **13**(4): p. 1571-1577.

164. Clay, K.J., et al., *Characterization of a-C:H:N deposition from CH4/N2 rf plasmas using optical emission spectroscopy.* Journal of Applied Physics, 1996. **79**(9): p. 7227-7233.

165. Liu, H., et al., *Growth of zinc blende-GaN on β-SiC coated (001) Si by molecular beam epitaxy using a radio frequency plasma discharge, nitrogen free-radical source.* Journal of Applied Physics, 1993. **74**(10): p. 6124-6127.

166. Mavadat, M., et al., *Determination of ro-vibrational excitations of N2(B,v') and N2(C,v') states in N2microwave discharges using visible and IR spectroscopy.* Journal of Physics D: Applied Physics, 2011. **44**(15): p. 155207.

167. Friedl, R. and U. Fantz, *Spectral intensity of the N2emission in argon low-pressure arc discharges for lighting purposes.* New Journal of Physics, 2012. **14**(4): p. 043016.

168. Partridge, H., et al., *Theoretical study of the A' 5Σ+g and C' 5Πu states of N2: Implications for the N2 afterglow.* The Journal of Chemical Physics, 1988. **88**(5): p. 3174-3186.

169. Pearse, R.W.B. and A.G. Gaydon, *The identification of molecular spectra*. 1976, London : New York: Chapman and Hall ; Wiley. viii, 407 p., [6] leaves of plates.

170. Burns Iain, S. and F. Kaminski Clemens, *Diode Laser Induced Fluorescence for Gas-Phase Diagnostics*, in *Zeitschrift für Physikalische Chemie*. 2011. p. 1343.

171. Whiddon, R., et al., *Vapor phase tri-methyl-indium seeding system suitable for high temperature spectroscopy and thermometry.* Review of Scientific Instruments, 2015. **86**(9): p. 093107.

172. Petrović, Z.L., et al., *Spatiotemporal optical emission spectroscopy of rf discharges in SF6.* Journal of Applied Physics, 1993. **73**(5): p. 2163-2172.

173. Fantz, U., et al., *Quantification of the VUV radiation in low pressure hydrogen and nitrogen plasmas.* Plasma Sources Science and Technology, 2016. **25**(4): p. 045006.

174. Safronova, U.I., M.S. Safronova, and M.G. Kozlov, *Relativistic all-order calculations of In I and Sn II atomic properties.* Physical Review A, 2007. **76**(2): p. 022501.

175. Burger, M., et al., *Spectroscopic study of the laser-induced indium plasma.* The European Physical Journal D, 2014. **68**(8): p. 223.

176. Tokuda, T., et al., *Plasma-excited organometallic vapor phase epitaxy of GaN on (0 0 0 1)sapphire.* Journal of Crystal Growth, 1997. **173**(3): p. 237-243.

177. Tatarova, E., et al., *Nitrogen dissociation in low-pressure microwave plasmas.* Journal of Physics: Conference Series, 2007. **71**: p. 012010.

178. Hiroshi, A., *Progresses in Experimental Study of N2 Plasma Diagnostics by Optical Emission Spectroscopy.* 2012.

179. Newman, N., *Chapter 4 Thermochemistry of III–N Semiconductors*, in *Semiconductors and Semimetals*, J.I. Pankove and T.D. Moustakas, Editors. 1997, Elsevier. p. 55-101.

180. Newman, N., *The energetics of the GaN MBE reaction: a case study of meta-stable growth.* Journal of Crystal Growth, 1997. **178**(1): p. 102-112.

181. Blant, A.V., et al., *Nitrogen species from radio frequency plasma sources used for molecular beam epitaxy growth of GaN.* Plasma Sources Science and Technology, 2000. **9**(1): p. 12.

182. Iliopoulos, E., et al., *Active nitrogen species dependence on radiofrequency plasma source operating parameters and their role in GaN growth.* Journal of Crystal Growth, 2005. **278**(1): p. 426-430.

183. Kikuchi, T., et al., *Role of excited nitrogen species in the growth of GaN by RF–MBE.* Journal of Crystal Growth, 2006. **292**(2): p. 221-226.

184. Jordan, D.C., C.T. Burns, and R.B. Doak, *Corona discharge supersonic free-jet for III–V nitride growth via A 3Σu+ metastable nitrogen molecules.* Journal of Applied Physics, 2000. **89**(2): p. 883-892.

185. Gilmore, F.R., R.R. Laher, and P.J. Espy, *Franck–Condon Factors, r-Centroids, Electronic Transition Moments, and Einstein Coefficients for Many Nitrogen and Oxygen Band Systems.* Journal of Physical and Chemical Reference Data, 1992. **21**(5): p. 1005-1107.

186. Boivin, R.F. and E.E. Scime, *Control of nitrogen species in helicon plasmas.* Plasma Sources Science and Technology, 2005. **14**(2): p. 283-292.

187. Piper, L.G., *Reevaluation of the transition-moment function and Einstein coefficients for the N2(A 3Σ+u–X 1Σ+g) transition.* The Journal of Chemical Physics, 1993. **99**(5): p. 3174-3181.

188. Jones, R.D. and K. Rose, *Thermal stability of InN.* Journal of Physics and Chemistry of Solids, 1987. **48**(6): p. 587-590.

189. Duan, X.M. and C. Stampfl, *Vacancies and interstitials in indium nitride: Vacancy clustering and molecular bondlike formation from first principles.* Physical Review B, 2009. **79**(17): p. 174202.

190. Chen, F.Z., et al., *Low and room temperature photoabsorption cross sections of NH3 in the UV region.* Planetary and Space Science, 1998. **47**(1): p. 261-266.

191. Wróbel, A.M., et al., *Silicon Carbonitride Films by Remote Hydrogen-Nitrogen Plasma CVD from a Tetramethyldisilazane Source.* Journal of The Electrochemical Society, 2004. **151**(11): p. C723-C730.

192. Carrasco, E., et al., *Neutral and ion chemistry in low pressure dc plasmas of H2/N2 mixtures: routes for the efficient production of NH3 and NH4+.* Physical Chemistry Chemical Physics, 2011. **13**(43): p. 19561-19572.

193. Bockel, S., et al., *A spectroscopic study of active species in DC and HF flowing discharges in - and Ar - - mixtures.* Plasma Sources Science and Technology, 1996. **5**(3): p. 567-572.

194. Oliva, R., et al., *Raman scattering by the E2h and A1(LO) phonons of InxGa1−xN epilayers (0.25 < x < 0.75) grown by molecular beam epitaxy.* Journal of Applied Physics, 2012. **111**(6): p. 063502.

195. Kontos, A.G., et al., *Micro-Raman characterization of InxGa1-xN/GaN/Al2O3 heterostructures.* Physical Review B, 2005. **72**(15): p. 155336.

196. Kim, J.G., et al., *Observation of A1(LO), E2(high) and B1(high) phonon modes in Inx Ga1–xN alloys with x = 0.11–0.54.* physica status solidi c, 2011. **9**(3-4): p. 730-732.

197. Hernández, S., et al., *Raman-scattering study of the InGaN alloy over the whole composition range.* Journal of Applied Physics, 2005. **98**(1): p. 013511.

198. Ager, J.W., et al., *Multiphonon resonance Raman scattering in InxGa1-xN.* Physical Review B, 2005. **72**(15): p. 155204.

199. Correia, M.R., et al., *Raman study of the A1(LO) phonon in relaxed and pseudomorphic InGaN epilayers.* Applied Physics Letters, 2003. **83**(23): p. 4761-4763.

200. People, R. and J.C. Bean, *Calculation of critical layer thickness versus lattice mismatch for GexSi1−x/Si strained-layer heterostructures.* Applied Physics Letters, 1985. **47**(3): p. 322-324.

201. Pereira, S., et al., *Structural and optical properties of InGaN/GaN layers close to the critical layer thickness.* Applied Physics Letters, 2002. **81**(7): p. 1207-1209.

202. Zhao, W., et al., *Theoretical study on critical thicknesses of InGaN grown on (0001) GaN.* Journal of Crystal Growth, 2011. **327**(1): p. 202-204.

203. Pereira, S., et al., *Strain and composition distributions in wurtzite InGaN/GaN layers extracted from x-ray reciprocal space mapping.* Applied Physics Letters, 2002. **80**(21): p. 3913-3915.

204. Wang, H., et al., *Cathodoluminescence study on in composition inhomogeneity of thick InGaN layer.* Thin Solid Films, 2010. **518**(17): p. 5028-5031.

205. Selke, H., et al., *Compositional inhomogeneities in InGaN studied by transmission electron microscopy and spatially resolved cathodoluminescence.* Materials Science and Engineering: B, 1999. **59**(1): p. 279-282.

206. Correia, M.R., et al., *Direct evidence for strain inhomogeneity in InxGa1−xN epilayers by Raman spectroscopy.* Applied Physics Letters, 2004. **85**(12): p. 2235-2237.

207. Kar, A., et al., *Evidence of compositional inhomogeneity in InxGa1−xN alloys using ultraviolet and visible Raman spectroscopy.* Journal of Applied Physics, 2008. **104**(7): p. 073502.

208. Behr, D., et al., *Evidence for compositional inhomogeneity in low In content (InGa)N obtained by resonant Raman scattering.* Applied Physics Letters, 1998. **73**(2): p. 241-243.

209. Wieser, N., et al., *Compositional fluctuations in GaInN/GaN double heterostructures investigated by selectively excited photoluminescence and Raman spectroscopy.* Applied Physics Letters, 1999. **74**(26): p. 3981-3983.

210. Lazić, S., et al., *Resonant Raman scattering in strained and relaxed InGaN/GaN multi-quantum wells.* Applied Physics Letters, 2005. **86**(6): p. 061905.

211. Tütüncü, H.M., G.P. Srivastava, and S. Duman, *Lattice dynamics of the zinc-blende and wurtzite phases of nitrides.* Physica B: Condensed Matter, 2002. **316-317**: p. 190-194.

212. Davydov, V.Y. and A.A. Klochikhin, *Electronic and vibrational states in InN and InxGa1−xN solid solutions.* Semiconductors, 2004. **38**(8): p. 861-898.

213. Kaczmarczyk, G., et al., *Lattice dynamics of hexagonal and cubic InN: Raman-scattering experiments and calculations.* Applied Physics Letters, 2000. **76**(15): p. 2122-2124.

214. Talwar, D.N., et al., *Optical properties of plasma-assisted molecular beam epitaxy grown InN/sapphire.* Optical Materials, 2014. **37**: p. 1-4.

215. Serrano, J., et al., *InN Thin Film Lattice Dynamics by Grazing Incidence Inelastic X-Ray Scattering.* Physical Review Letters, 2011. **106**(20): p. 205501.

216. Kuball, M., et al., *Resonant Raman spectroscopy on InN.* physica status solidi (a), 2005. **202**(5): p. 763-767.

217. Doppalapudi, D., et al., *Phase separation and ordering in InGaN alloys grown by molecular beam epitaxy.* Journal of Applied Physics, 1998. **84**(3): p. 1389-1395.

218. Li, S.X., et al., *Fermi-level stabilization energy in group III nitrides.* Physical Review B, 2005. **71**(16): p. 161201.

219. Poliani, E., et al., *Nanoscale Imaging of InN Segregation and Polymorphism in Single Vertically Aligned InGaN/GaN Multi Quantum Well Nanorods by Tip-Enhanced Raman Scattering.* Nano Letters, 2013. **13**(7): p. 3205-3212.

220. Schörmann, J., et al., *Molecular beam epitaxy of phase pure cubic InN.* Applied Physics Letters, 2006. **89**(26): p. 261903.

221. Tabata, A., et al., *Raman phonon modes of zinc blende InxGa1−xN alloy epitaxial layers.* Applied Physics Letters, 1999. **75**(8): p. 1095-1097.

222. Casallas-Moreno, Y.L., et al., *High cubic phase purity and growth mechanism of cubic InN thin-films by Migration Enhanced Epitaxy.* Thin Solid Films, 2018. **647**: p. 64-69.

223. Jumpei, K., et al., *High-quality cubic and hexagonal InN crystals studied by micro-Raman scattering and electron backscatter diffraction.* Journal of Physics D: Applied Physics, 2016. **49**(15): p. 155106.

224. Daniel Seidlitz, et al., *Optoelectronic and structural properties of InGaN nanostructures grown by plasma-assisted MOCVD.* Proc.SPIE, 2015. **9571**.

Acknowledgement

I want to express my gratitude to a lot of kind and friendly people who have helped me along the way of my dissertation. In particular:

- My both advisors Prof. Dr. Axel Hoffmann and Prof. Dr. Nikolaus Dietz, who have given me the opportunity to work on the exploration of a novel growth concept (MEPA-MOCVD) for the fabrication of group III-nitrides at Georgia State University in Atlanta and the characterization with state of the art nanoscopic characterization tools such as TERS at Technical University Berlin. Both deserve my gratitude for their scientific and personal support during my dissertation. I am also thankful that I could present my work at conferences and exchange knowledge with other scientists.
- Prof. Dr. Michael Lehmann for being the chairman of the thesis committee.
- Prof. Dr. Axel Hoffmann for reviewing this thesis.
- Prof. Dr. Janina Maultzsch for reviewing this thesis.

- Prof. Dr. Abate and his group for providing s-SNIN measurements.
- Mark Vernon for his support and many fruitful discussions in the MOCVD laboratory.
- Indika Senevirathna for FTIR measurements and analysis.
- Brendan Garnett Cross and Zaheer Ahmad for FTIR and AFM measurements.
- Sampath Gamage and Rasanga Samaraweera for introducing me into CVD lab and Raman measurement setup.
- Vladislav S. Yakovlev for many conversations during lunch and coffee breaks at Ebrik coffee room.
- Pete Walker and his colleagues from the instrument shop for their technical support and manufacturing of parts for the MOCVD system.
- Emanuele Poliani and Maximilian Ries for their support of many hours in the TERS lab together as well as the long and the inspiring discussions about the TERS results together with Markus Wagner.
- The office colleagues, Christoph Tyborski, Felix Kampmann, and Stefan Kalinowski for a great working atmosphere, but also refreshing and joyful moments.
- The daily lunch group with many amusing conversations.
- Anja Sandersfeld for her help and management of all the bureaucracy.
- Everybody, who reviewed my thesis in respect of spelling and grammar.

- The AG Hoffmann for the very pleasant atmosphere during the last one and a half years, especially Stefan Kalinowski, Christoph Tyborski, Felix Kampmann, Dirk Heinrich, Harald Scheel, Thomas Kure, Felix Nippert, Ludwig Greif, Stefan Jagsch, Alexander Mittelstädt, Andrei Schliwa, Hans Tornatzky, Narine Ghazaryan and Markus Wagner.
- Zhe Chuan Feng and his group for their help with XRD measurements.
- I also acknowledge the financial support of the Air Force Office of Scientific Research Award# FA9550-10-1-0097 and GSU-RPE.

Last but not least, my deepest gratitude goes to my parents and my family for their unconditional support during my dissertation.